Experimental Application and Numerical Study of Reflectometry in the Alcator C-Mod Tokamak

by

Yijun Lin

B.S. (1993), M.S. (1996), Department of Modern Physics
University of Science and Technology of China

Submitted to the Department of Physics
in partial fulfillment of the requirements for the degree of

Doctor of Philosophy

at the

MASSACHUSETTS INSTITUTE OF TECHNOLOGY

June 2001

Author .....
Department of Physics
May 30, 2001

Certified by .....
Dr. James H. Irby
Research Scientist, Experimental and Group Leader
Thesis Supervisor

Certified by .....
Dr. Earl S. Marmar
Senior Research Scientist
Thesis Supervisor

Accepted by .....
Thomas J. Greytak
Professor, Associate Department Head for Education

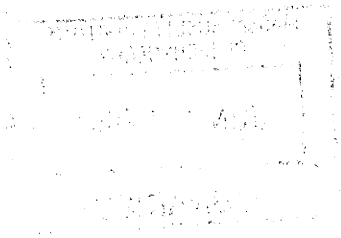

Experimental Application and Numerical Study of Reflectometry in the Alcator C-Mod Tokamak

by

Yijun Lin

Submitted to the Department of Physics
on May 30, 2001, in partial fulfillment of the
requirements for the degree of
Doctor of Philosophy

Abstract

The amplitude modulated ordinary-mode reflectometer in the Alcator C-Mod tokamak is used to study the quasi-coherent (QC) continuous edge fluctuations in enhanced D_α (EDA) H-modes. Reflectometer data show that the QC fluctuations are localized near the center of the density pedestal. The radial width (FWHM) is usually in the range of $0.1 - 0.3$ cm. The width increases with the increase of resistivity η. The line-integrated fluctuation level approximately scales with $(\nu^* q_{95}^2)^{0.56}$. This result indicates that higher q_{95}, higher density, and lower temperature are favored for the QC fluctuations. Neither the location nor the width changes significantly in an EDA H-mode period, while the frequency and level vary.

A 2-D full-wave code has been developed to simulate and quantitatively interpret reflectometry signals. The code uses the finite-difference time-domain method to solve Maxwell's equations in two dimensions. Perfectly-matched layers are used as the boundary. The Huygens source technique is used to generate Gaussian beams and separate the reflected waves from the total field.

Simulations based on realistic 2-D geometry of the Alcator C-Mod reflectometer provide a calibration curve by which we can relate the QC fluctuations in reflectometry signals to plasma density fluctuations. Results indicate that the line-integrated fluctuation level derived from reflectometry is similar to that measured by the phase contrast imaging system. Simulations also indicate that plasma curvature extends the reflectometry response to fluctuations of high poloidal wavenumber. A preliminary study indicates that reflectometry can be used to estimate the correlation length of the turbulence in Alcator C-Mod provided that the fluctuation level is small.

Thesis Supervisor: Dr. James H. Irby
Title: Research Scientist, Experimental and Group Leader

Thesis Supervisor: Dr. Earl S. Marmar
Title: Senior Research Scientist

Acknowledgments

It is a great pleasure to acknowledge with gratitude my debt to my supervisors, Dr. Jim Irby and Dr. Earl Marmar. I am very fortunate to have their support and guidance throughout my thesis research.

My thanks also go to Prof. Miklos Porkolab for being my thesis reader and his course of waves in plasmas. I also thank Prof. John Belcher for being my thesis reader and many helpful discussions as my academic advisor.

I thank Dr. Raffi Nazikian of Princeton Plasma Physics Laboratory. His intelligence and humor are greatly appreciated. Thanks are also due to Prof. Ian Hutchinson for his wonderful courses and many good suggestions on my thesis research.

I thank Alcator C-Mod scientists for their help on my research, Drs. Steve Wolfe, Martin Greenwald, Amanda Hubbard, Dmitri Mossessian, Brian LaBombard, Joe Snipes, John Rice, Rejean Boivin, Paul Bonoli, Catherine Fiore, John Goetz, Bob Granetz, Bruce Lipschultz, Spencer Pitcher, Jim Terry, and Steve Wukitch.

I would like to extend my thanks to engineers and technicians in Alcator C-Mod, especially to Frank Silva, Jim Rosati, Rick Murray, Ed Fitzgerald, Willy Burke, Bill Parkin, and Joe Bosco. Thanks also go to our computer guys, Josh Stillerman, Tom Fredian, Don Nelson, and Felix Kreisel.

I thank my fellow graduate students (and recent PhDs) at the Plasma Science and Fusion Center who have made my graduate student years enjoyable, Eric Nelson-Melby, Alex Mazurenko, Dr. Yongkyoon In, Dr. Thomas Sunn Pederson, Chris Boswell, Dr. Jim Reardon, Dr. Dimitrios Pappas, Sanjay Gangadhara, Dr. Rob Nachtrieb, William Davis Lee, Taekyun Chung, Howard Yu, Natalia Kresheninnikova, Kirill Zhurovich, Xiang Wang, Zhen Zhang, and Jian Ke. I thank Dr. Paul Stek for leading me into the field of reflectometry.

Many thanks to Anne Battis and Bruce Goodchild being my host family.

My deepest gratitude goes to my wife, Yili, for her patience and unfailing love throughout all these years. I thank my parents for their determination to support their children to pursue the best education. To them I dedicate my thesis.

Contents

1 Thesis goals and outline **16**

1.1 The Alcator C-Mod tokamak 16

1.2 Reflectometry 16

1.3 Enhanced D_α (EDA) H-mode 18

1.4 Thesis goals 20

1.5 Thesis outline 20

2 Introduction **21**

2.1 Nuclear fusion and tokamak 21

2.1.1 Nuclear fusion 21

2.1.2 Plasma, magnetically-confined fusion and tokamak 22

2.1.3 Basics of tokamak plasma physics 25

2.1.4 Plasma diagnostics 27

2.1.5 Transport, turbulence, and H-mode 27

2.2 The Alcator C-Mod tokamak 29

2.2.1 Machine parameters 29

2.2.2 Plasma diagnostics 32

2.2.3 EFIT 34

2.2.4 Research themes in Alcator C-Mod 35

2.2.5 H-mode and EDA H-mode 36

2.2.6 H-mode pedestal research 36

2.2.7 Plasma rotation 37

3 Reflectometry theory and principles **38**

3.1 Electro-magnetic (EM) waves in cold plasmas 38

3.1.1 Dispersion relations 39

3.1.2 Ordinary (O-mode) waves in plasmas 41

3.2 Reflectometry electron density profile measurement 45

3.2.1 Profile inversion 45

3.2.2 Amplitude modulated (AM) reflectometry 46

3.3 Reflectometry fluctuations interpretation 49

3.3.1 Analytic models 49

3.3.2 Numerical models 54

3.4 Optical distance fluctuations 56

3.5 Radial correlation length of turbulences 58

4 Reflectometer system in Alcator C-Mod **60**

4.1 Overview 60

4.2 Electron density profile measurements 62

4.2.1 Millimeter wave and IF systems 62

4.2.2 Profile inversion 66

4.2.3 System optimization 67

4.2.4 Experimental density profiles 69

4.3 Fluctuation measurement 71

4.4 Observed experimental fluctuations 74

4.4.1 Phase runaway phenomenon 74

4.4.2 Fluctuations in L-mode and H-mode 76

4.4.3 Quasi-coherent (QC) edge fluctuations in EDA H-modes . . . 76

5 Study of EDA H-modes **81**

5.1 General observations 81

5.2 Theoretical models 83

5.2.1 Resistive ballooning mode 83

5.2.2 Drift ballooning mode 85

5.3 QC fluctuations: location, radial width, and level 85
5.3.1 Fluctuations of optical distance 86
5.3.2 Location, width, and level estimates 92
5.3.3 Comparison with Langmuir probe observations 95
5.3.4 Comparison with plasma parameters 100
5.4 Evolution of the QC fluctuations in an EDA H-mode 105
5.4.1 Evolution of mode location, width, and level 106
5.4.2 Frequency behavior in the laboratory frame 111

6 2-D full-wave reflectometry simulation code 115
6.1 Calculation in the main field region 116
6.2 Perfectly-matched-layer absorption boundary 119
6.3 Huygens source technique 122
6.4 Gaussian beam 127
6.5 Reflectometry received signal 128
6.6 Simulation on multiple-frequency reflectometry 131

7 Numerical study of reflectometry 132
7.1 Simulation parameters of Alcator C-Mod reflectometer 132
7.2 QC fluctuation level 133
7.2.1 Model density profile and fluctuation 133
7.2.2 Simulation results 136
7.2.3 Experimental observations 139
7.3 Plasma curvature effect 143
7.3.1 Analytic result from a phase screen model 144
7.3.2 2-D full-wave simulation result 148
7.4 Simulation of radial correlation measurement 154
7.4.1 Simulation parameters 154
7.4.2 Reflectometry responses at different turbulence correlation lengths 156
7.4.3 Reflectometry responses at different turbulence levels 157

8 Conclusions and future work **162**

8.1 Conclusions 162

8.2 Future work on the reflectometer 164

8.2.1 Upgrade to measure radial correlation length 164

8.2.2 Dual O-X mode reflectometry 167

8.2.3 Reflectometry imaging 167

8.3 Future physics studies by reflectometry in Alcator C-Mod 168

8.3.1 Advanced tokamak physics study 168

8.3.2 ICRF physics study 169

List of Figures

1-1 Reflectometry concept 17

1-2 EDA H-mode 19

2-1 A schematic drawing of a tokamak 24

2-2 The Alcator C-Mod tokamak. 31

2-3 Density diagnostics in Alcator C-Mod 33

3-1 Notations for the EM wave 40

3-2 Dispersion relation of the O-mode and X-mode waves 42

3-3 The exact solution of 1-D wave equation 43

3-4 The principle of AM reflectometry 47

3-5 Microwave scattering in 2-D 52

4-1 The reflectometer in Alcator C-Mod (side view) 61

4-2 The reflectometer in Alcator C-Mod (front view) 62

4-3 Layout of the mm-wave part of the reflectometry system measuring electron density profiles 63

4-4 Layout of the IF part of the reflectometry system measuring electron density profiles. 65

4-5 Temperature control of a Gunn diode oscillator 68

4-6 Electron density profiles in L-mode 70

4-7 Layout of the mm-wave part of the upgraded 88 GHz channel 72

4-8 Layout of the IF part of the upgraded 88 GHz channel 73

4-9 Phase runaway phenomenon in reflectometry signal fluctuations . . . 75

4-10 Contours of reflectometer fluctuations at an L-H transition 77
4-11 Fluctuation spectra in L-mode and H-mode 78
4-12 Quasi-coherent fluctuations during an EDA H-mode 79

5-1 QC fluctuations in a relatively low density EDA H-mode 87
5-2 QC fluctuations in a high density EDA H-mode 88
5-3 Plasma parameters of shot 1000914006 89
5-4 Fluctuations of optical distance vs. time 90
5-5 Auto-power spectra of optical distance fluctuations 91
5-6 QC fluctuation level in terms of optical distances of different reflectometry channels 92
5-7 Electric fields obtained from the 1-D wave equation 94
5-8 Least-squares fit of $\tilde{d}_{num}$ and $\tilde{d}$ 96
5-9 Inferred QC fluctuation location and radial width of a RF heated EDA H-mode discharge 97
5-10 Langmuir probe observation of the QC fluctuations in an ohmic EDA discharge 98
5-11 Inferred QC fluctuations location and width of the ohmic EDA H-mode discharge from reflectometry measurements 99
5-12 Comparison of the probe and reflectometry measurements of QC fluctuations 101
5-13 Inferred location of the QC fluctuations vs. temperature at the center of pedestal 102
5-14 Inferred width of the QC fluctuations radial width vs. $T_e^{-1.5}$ at the center of the pedestal 103
5-15 The line integrated QC mode level vs. $\nu^* q_{95}^2$ 104
5-16 The QC fluctuation level in terms of the fluctuation of optical distance in an EDA H-mode 107
5-17 The evolution of QC fluctuations location, radial width, and frequency in lab frame in an EDA H-mode 108

5-18 Comparison of QC fluctuation levels obtained from reflectometry and PCI 109
5-19 Growth rate of the QC fluctuations 110
5-20 Observed QC frequency and global plasma parameters vs. time . . . 112
5-21 Peak frequency of the QC fluctuations in steady EDA periods vs. W_p/I_p 113

6-1 Computation box of the 2-D full-wave reflectometry simulation code . 116
6-2 FDTD mesh in the main field region and PML boundary 118
6-3 Four-component conductivities of the PML boundary 121
6-4 PML boundary absorption efficiency test 123
6-5 Huygens source technique 124
6-6 A plane wave generated using the Huygens sources technique and PML boundary 126
6-7 Examples of Gaussian beam generated by the Huygens sources technique 129

7-1 An EDA H-mode discharge 134
7-2 Density profile derived from the visible continuum array measurement 135
7-3 Electric field contours from the simulation result 137
7-4 Simulation results of reflectometry phase responses vs. fluctuation levels 137
7-5 Phase runaway phenomenon and nonlinearity to high fluctuation level 138
7-6 Electric field distribution at the horn aperture for different fluctuation levels 139
7-7 Raw fluctuations data from PCI and reflectometry 88 GHz channel . 140
7-8 Comparison of the phase fluctuation level $\Delta\phi$ of reflectometry and line-integrated fluctuation level measured by PCI 141
7-9 Comparison of the line-integrated fluctuation levels of reflectometry and PCI 142
7-10 Phase screen model including curvature 144
7-11 Analytic result of curvature effect 147
7-12 Curvature effects on a single-horn system 149
7-13 Curvature effects on a two-horn system 150

7-14 Electric field contours showing the curvature effects 152
7-15 Curvature effects on reflectometer response 153
7-16 Turbulence with different correlation lengths 156
7-17 Reflectometry phase correlation γ_ϕ and turbulence correlation γ_n . . . 157
7-18 Reflectometry $L_{r,\phi}$ vs. turbulence $L_{r,n}$ 158
7-19 Reflectometry amplitude correlation γ_A and turbulence correlation γ_n 158
7-20 Reflectometry $L_{r,A}$ vs. turbulence $L_{r,n}$ 159
7-21 Reflectometry $L_{r,A}$ at different turbulence level 160
7-22 Reflectometry $L_{r,\phi}$ at different turbulence level 160

8-1 Layout of the mm-wave part of 132 GHz and 140 GHz channels . . . 165
8-2 Layout of the IF part of the 132 and 140 GHz channels 166
8-3 Reflectometry accessibility to ITB 170

List of Tables

2.1 Parameters of the Alcator C-Mod tokamak 30

2.2 A list of n_e and T_e diagnostics in the Alcator C-Mod tokamak 32

4.1 Choices of signal frequencies 64

Chapter 1

Thesis goals and outline

1.1 The Alcator C-Mod tokamak

The Alcator C-Mod tokamak is the third Alcator tokamak operated at the MIT Plasma Science and Fusion Center following the successful Alcator A and Alcator C. Alcator C-Mod is a compact tokamak (minor radius $a \simeq 0.22$ m and major radius $R_0 \simeq 0.67$ m) with high magnetic field ($B_0 \leq 8$ T), high plasma density ($\bar{n}_e \leq 4 \times 10^{20}$ m^{-3}), high current density ($I_p \leq 1.4$ MA), and dedicated ion cyclotron radio frequency (ICRF) wave heating. It has a shaped plasma and divertor configuration. Alcator C-Mod is one of the two current major tokamaks focusing on the research of fusion plasma in the US. Research themes include plasma transport, ICRF heating, divertor physics, magneto-hydrodynamics (MHD), and advanced tokamak physics.

1.2 Reflectometry

A major part of this thesis is the understanding of reflectometry and its application in Alcator C-Mod measuring plasma density fluctuations and profiles. Reflectometry is a technique similar to radar (Fig. 1-1). Microwaves are launched to the plasma and reflected at critical surfaces. The location of the critical surface is determined by the microwave frequency and electron density n_e (and sometimes also magnetic field). As a result, we can reconstruct density profiles by measuring group delays of multiple

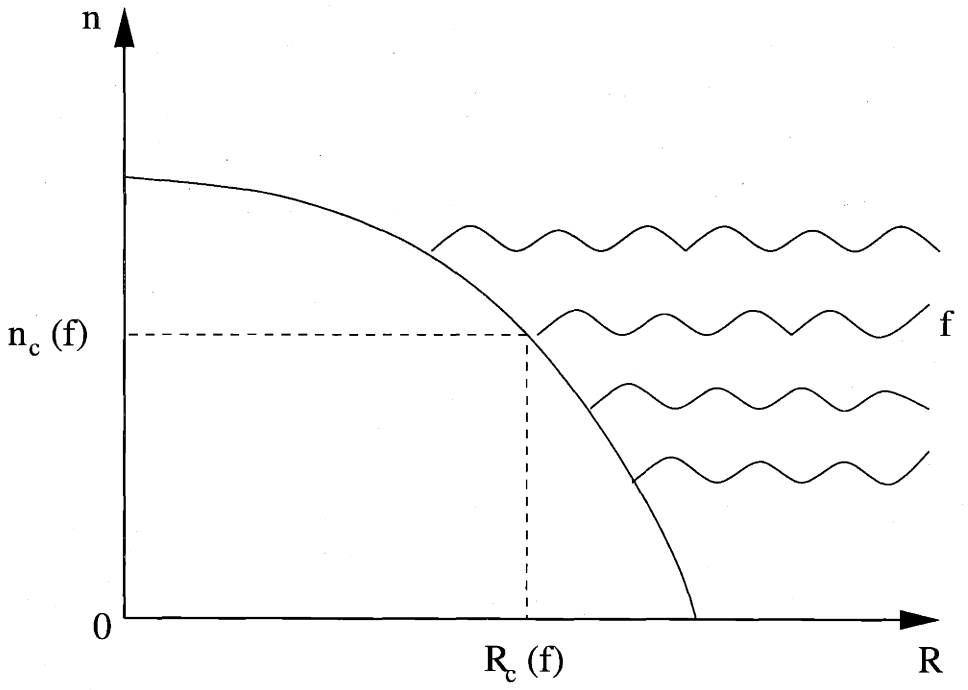

Figure 1-1: Reflectometry concept. Microwaves with different frequencies are launched to the plasma and reflected at different critical surfaces, $n = n_c(f)$ and $R = R_c(f)$. The group delays of these waves are used to reconstruct plasma density profiles. The fluctuations of the microwave signals can be used to study the location, level, and radial correlation length of density fluctuations.

frequencies. Density fluctuations along the wave-path (more weighted near the critical surface in many cases) are embedded in the signal fluctuations of the reflectometry microwaves, therefore we can also study density fluctuations using reflectometry. By studying the fluctuations of microwave signals reflected at different critical surfaces, we can also estimate the radial correlation length of turbulence. Both fluctuation level and correlation length are important in understanding the effect of turbulence on plasma transport.

The interpretation of reflectometry application on density profile measurements is well established. However, there is incomplete understanding of how to relate the signal fluctuations of reflectometry to plasma density fluctuations, or the correlation length of reflectometry signals in terms of the correlation length of turbulence. Besides the experimental application, part of this thesis is devoted to developing a two-dimensional (2-D) full-wave code to simulate the reflectometry process and study specific cases in Alcator C-Mod.

1.3 Enhanced D_α (EDA) H-mode

A key issue for the research of fusion plasma is to understand and predict plasma transport. Particles and energy leave confined plasma generally much faster than that predicted by classical and neo-classical theories. Micro-turbulences are believed to be the culprit of these (sometimes enormous) discrepancies.

Plasma confinement has a baseline level — Low-confinement mode or L-mode. L-mode plasma may suddenly enter a High confinement mode — H-mode — when parameters are favored, such as sufficient auxiliary heating power, high edge temperature, and/or shaped and diverted plasma (Ref. [1]). Confinement in an H-mode is typically a factor of 2 better than that in an L-mode. Since its discovery in the ASDEX tokamak (Ref. [2]), several types of H-mode have been observed. For example, based on the edge localized modes (ELMs) activity in H-modes, we classify H-modes into ELMy and ELM-free H-mode, etc. In Alcator C-Mod, we observed a particular H-mode dubbed as enhanced D_α (EDA) H-mode (first reported in Ref. [3]).

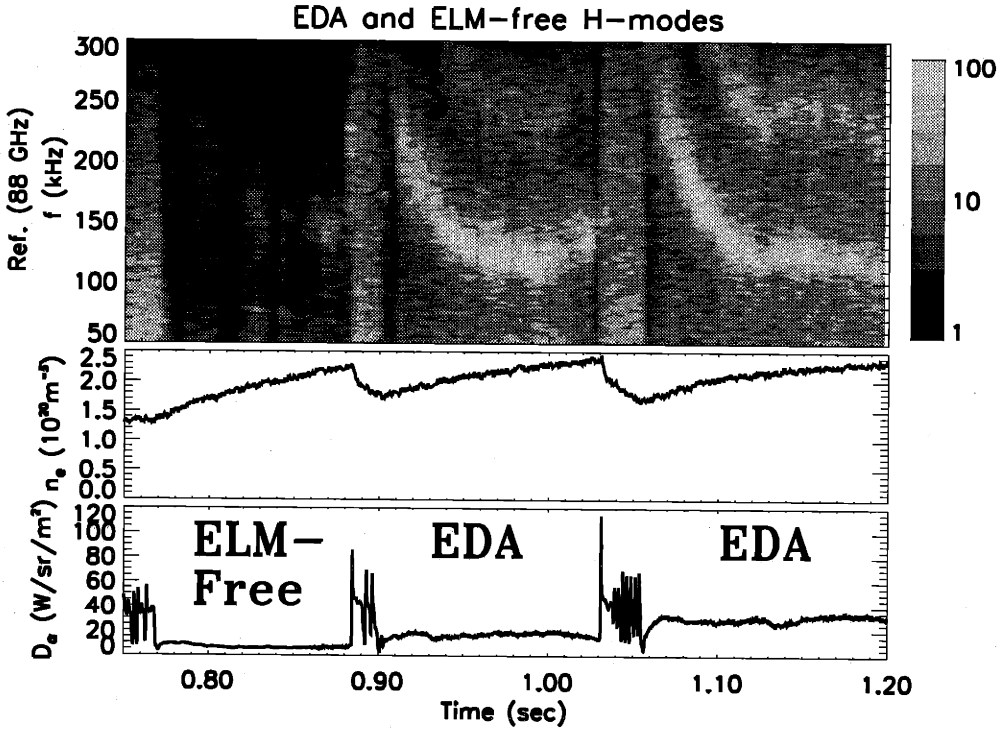

Figure 1-2: In an EDA H-mode, the D_α signal gradually increases after the sudden signature drop at the L-H transition. An ELM-free period and two EDA H-mode periods are shown. Also shown are the contour plot of the 88 GHz reflectometry signal fluctuations and line-averaged electron density measured by two-color interferometer. Continuous quasi-coherent fluctuations appear in the EDA periods, but they do not exist in the ELM-free period.

In a typical EDA H-mode, the D_α signal gradually increases after the sudden signature drop at the L-H transition (Fig. 1-2). Like in ELM-free H-modes, there is usually no apparent ELM activity in EDA H-mode periods. The enhanced D_α signal suggests a more active plasma edge than in ELM-free H-modes. Plasma energy confinement in EDA H-modes is close to that in ELM-free H-modes, but particle confinement (especially impurities) confinement is below the ELM-free H-modes level. As a result, an EDA H-mode plasma can reach steady state with good energy confinement. This particular characteristic makes the EDA H-mode a promising operation regime for future reactor-size machine.

In EDA H-modes, continuous edge quasi-coherent fluctuations (also shown in Fig. 1-2) are observed by the reflectometer along with several other diagnostics in Alcator C-Mod. Experimental study of these fluctuations using reflectometry and interpretation of the reflectometry signals are the major goals of this thesis.

1.4 Thesis goals

The thesis goals are the experimental application of reflectometry on Alcator C-Mod and numerical study of reflectometry. The reflectometer reported in Ref. [4] was upgraded to be more sensitive to fluctuations. Work has been concentrated on the study of the quasi-coherent fluctuations in EDA H-modes. This work has been in collaboration with Princeton Plasma Physics Laboratory (PPPL).

A 2-D full-wave reflectometry simulation code has been developed based on an earlier code (Ref. [5]). The new code has been used to study the reflectometry measurements on density fluctuation level and correlation length.

1.5 Thesis outline

The thesis is arranged as follows. Chapter 2 introduces some basics of plasma physics and the Alcator C-Mod tokamak. Chapter 3 is a review of reflectometry theory including wave propagation in cold plasmas, geometric optics approximation, principles of density profile measurements, and models for the interpretation of reflectometry fluctuation level and signal correlation length. Descriptions of the reflectometer in Alcator C-Mod and some typical experimental observations are presented in Chapter 4. Chapter 5 presents the experimental study of the quasi-coherent density fluctuations in EDA H-modes using the reflectometer. The new 2-D full-wave reflectometry simulation code, including computation methods and testing results, is described in Chapter 6. Chapter 7 shows simulation results on the quasi-coherent fluctuation level, plasma curvature effects, and interpretation of correlation length. In Chapter 8, conclusions and recommendations for future work are presented.

Chapter 2

Introduction

2.1 Nuclear fusion and tokamak

2.1.1 Nuclear fusion

Nuclear fusion is a process in which two (or more) nuclei fuse into one heavier nucleus and energy is released in the form of high energy particles and radiation. Nuclear fusion is the principal energy source for most stars including the Sun. Because of their relatively large cross sections and low reaction temperatures, the most important fusion reactions for nuclear fusion research are

$$\mathrm{D} + \mathrm{D} = {}^{3}\mathrm{He}\ (0.82\ \mathrm{MeV}) + \mathrm{n}\ (2.45\ \mathrm{MeV}), \tag{2.1}$$

$$\mathrm{D} + \mathrm{D} = \mathrm{T}\ (1.01\ \mathrm{MeV}) + \mathrm{p}\ (3.03\ \mathrm{MeV}), \tag{2.2}$$

$$\mathrm{D} + \mathrm{T} = {}^{4}\mathrm{He}\ (3.52\ \mathrm{MeV}) + \mathrm{n}\ (14.06\ \mathrm{MeV}). \tag{2.3}$$

Compared with the $\sim$ 1 eV energy released in a typical chemical reaction, nuclear fusion can release a factor of 10^6 more energy using the same amount of fuel.

However, it is not an easy task to create and maintain nuclear fusion processes. Fusion happens only when the distance between the two reactant nuclei is in the order of strong interaction scale ($\leq 10^{-14}$ m). The two nuclei, both having positive charges, must overcome the extremely high Coulomb potential barrier in order to

reach such an infinitesimal distance. The only way to overcome the Coulomb barrier is to accelerate the nuclei so that they have high kinetic energy ($\geq$ several kilovolts) before they collide. Alternatively, we need to have extremely high temperatures. The fusion rate is proportional to the reaction cross section and density square. To be energetically favorable the fusion reaction rate has to be higher than the energy loss from plasma. Thus there is a criterion for self-sustainable fusion reaction — the Lawson criterion (Ref. [6]). For D-T reaction, we have the Lawson criterion (Ref. [7])

$$n\tau > 10^{20}\ \mathrm{m}^{-3}\mathrm{sec} \tag{2.4}$$

at ion temperature $T_i \simeq 10$ keV (1 eV $\simeq 1.16 \times 10^4$ ^{0}C), where n is the particle density, and τ is the energy confinement time.

To meet the Lawson criterion, two distinct paths toward controlled nuclear fusion have been studied. One path is to improve energy confinement time τ, but with relatively low particle density n; the other one is using high density n, but with short τ. The fusion research based on the first path leads to magnetically-confined fusion (MCF), which is the area that this thesis research is working on. The second path leads to inertially confined fusion (ICF). Both approaches have made significant progress in the past half century.

2.1.2 Plasma, magnetically-confined fusion and tokamak

Plasma is the fourth state of matter after the familar liquid, solid, and gas. It is basically a neutral gas of charged particles: ions and electrons.

In a magnetic field, due to the Lorentz force $\vec{F} = Ze\vec{v} \times \vec{B}$, a particle with charge Ze moves freely along the field line and gyrates with a Larmor radius (gyro-radius) ρ, and cyclotron frequency (gyro-frequency) ω_c, given by

$$\rho = \frac{mv_\perp}{ZeB}\ ,\ \ \omega_c = \frac{ZeB}{m}. \tag{2.5}$$

This helical motion results in a confinement of charged particles in the two dimensions

perpendicular to the magnetic field. Fusion experiments using magnetic fields are thus called magnetically-confined fusion experiments. Early experiments with open-ended devices, such as magnetic mirrors, Z-pinches, and θ-pinches, were proved impractical for reactor purpose due to rapid energy and particle losses in the less confined third dimension. Several types of more successful devices with closed magnetic field, such as tokamaks, stellerators, reversed field pinches, and spheromaks, have been developed.

The picture of the simple helical motion is drastically modified where either electric field exists in addition to the magnetic field or the magnetic field has gradient or curvature. With an additional electric field, the charged particle drifts in the direction perpendicular to both the magnetic field and electric field with a drift velocity

$$\vec{V}_{E\times B} = \frac{\vec{E}\times\vec{B}}{B^2}. \tag{2.6}$$

This drift is called the $\vec{E}\times\vec{B}$ drift, in which both ions and electrons drift in the same direction. When the magnetic field is curved with the radius of curvature, $\vec{R}_c$, and has gradient, $\nabla\vec{B}$, the charged particle undergoes another type of drift

$$\vec{V}_{R_c} + \vec{V}_{\nabla B} = \frac{m}{Ze}\frac{\vec{R}_c\times\vec{B}}{R_c^2 B^2}\left(v_\parallel^2 + \frac{1}{2}v_\perp^2\right), \tag{2.7}$$

where $v_\parallel$ and $v_\perp$ are the velocities parallel and perpendicular to the magnetic field respectively. Because ions and electrons are moving in opposite directions under this drift, the electric field generated by charge separation may induce an $\vec{E}\times\vec{B}$ drift and push plasma away from the confined region on a very short time scale. It has been recognized early on that a magnetically-confined device must have special magnetic field configurations to overcome these drifts.

A tokamak (shown in Fig. 2-1) is a donut shape device. It has external coils to generate a toroidal magnetic field and drive plasma current. The plasma current also creates poloidal magnetic field. The toroidal field, poloidal field, and externally applied vertical field together can produce the special magnetic field configuration required to achieve plasma equilibrium and stability. The superposition of these

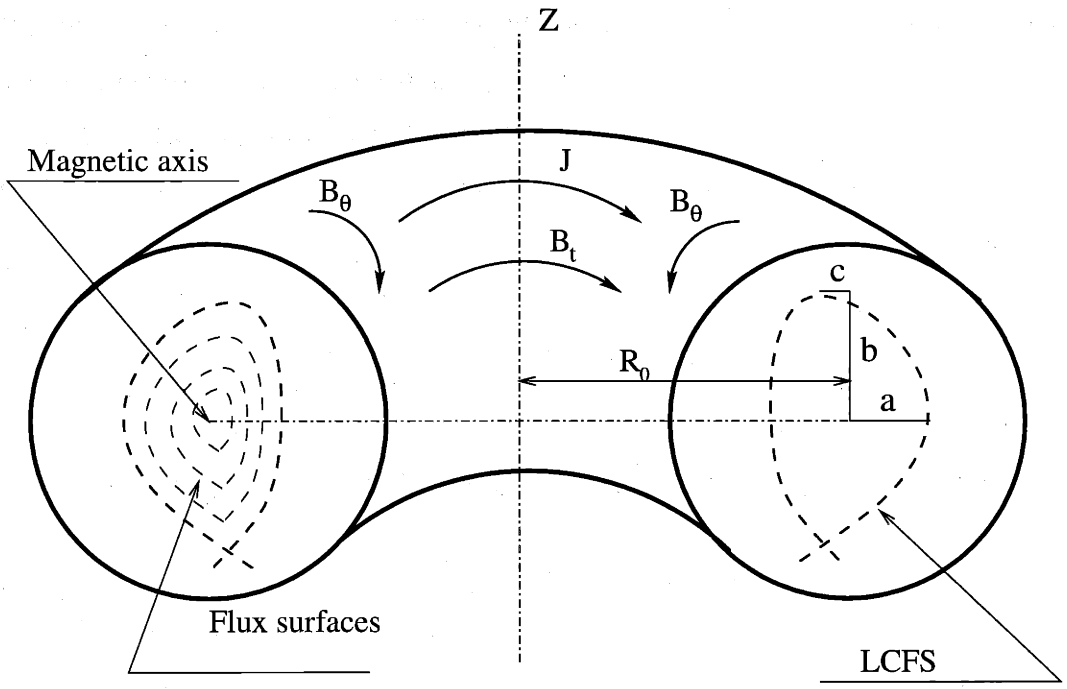

Figure 2-1: A schematic drawing of a tokamak. Plasma is confined by a complicated magnetic field, which includes an externally applied toroidal field and a poloidal field created by plasma current. To the first order, plasma pressure, temperature, and density are constant on a flux surface. The last closed flux surface (LCFS) is also drawn. For a non-circular shape plasma, we define elongation, $\kappa = b/a$, and triangularity, $\delta = c/a$.

fields creates helical field lines, which allow particles to short out the vertical electric field induced by $\vec{V}_{R_c}$ and $\vec{V}_{\nabla B}$, thus avoid the radial $\vec{E} \times \vec{B}$ drift. It also prevents instabilities by averaging over favorable (inner) and unfavorable (outer) magnetic field regions. Plasma is created by electrical breakdown of the fueling gas, which is deuterium for most plasma discharges in Alcator C-Mod. The plasma is then heated by the plasma current—ohmic heating[1]. In most modern tokamaks, auxiliary heating by radio frequency (RF) waves and/or high energy neutral beam injection is also used to achieve high plasma temperature.

[1]Since plasma resistivity decreases with plasma temperature, $\eta \propto T_e^{-3/2}$, ohmic heating alone is not adequate to achieve Lawson criterion.

2.1.3 Basics of tokamak plasma physics

A very important feature of the plasma state is the collective motion of particles because of the long range nature of the electro-magnetic force. The shortest time scale for plasma collective motion is the frequency of electrons natural oscillation, or the plasma frequency

$$\omega_{pe} = \left(\frac{n_e e^2}{\epsilon_0 m_e}\right)^{1/2}, \tag{2.8}$$

where n_e is the electron density. The ion and electrons Larmor radii, ρ_i and ρ_e, represent the smallest scale lengths for motion perpendicular to the magnetic field. The Alfven speed

$$C_A = \left(\frac{B^2}{\mu_0 n m_i}\right)^{1/2} \tag{2.9}$$

is approximately the fastest speed of magneto-hydrodynamic (MHD) phenomena.

Many other parameters will occur later in the thesis. For example, the diamagnetic frequency

$$\omega_* = \frac{T_e}{eB}\left(\frac{d\ln n}{dr}\right)^{-1}, \tag{2.10}$$

is related to drift instabilities. The safety factor

$$q \simeq \frac{rB_t}{RB_\theta}, \tag{2.11}$$

where B_θ is the poloidal magnetic field, B_t is the toroidal magnetic field, R is the major radius, and r is the minor radius, shows how many times field lines twist before close. It is important in determining the stability and location of MHD phenomena. A more accurate definition of q is based on the poloidal fluxes. In most practical cases, the q value at the flux surface that encloses 95% of total poloidal magnetic flux, q_{95}, is used to represent the q value at the plasma edge. The ratio of plasma pressure and magnetic pressure is defined as $\beta = 2\mu_0 p/B^2$, which shows the efficiency of plasma confinement. The dimensionless collisionality, ν^*, is defined as

$$\nu^* = \nu_{ei}\epsilon^{-3/2} qR/V_{Te} \tag{2.12}$$

where $V_{Te} = (T_e/m_e)^{1/2}$ is the electron thermal speed, $\epsilon = r/R$ is the inverse aspect ratio, and ν_{ei} is the electron-ion collision rate. ν^* is used to classify different regimes of transport characteristics in neo-classical theory.

Plasma equilibrium and stability are described by MHD (short time scale) and kinetic theory (relatively long time scale). Plasmas usually behave like ideal conducting fluids and satisfy the ideal MHD equations (Ref. [8]):

$$\frac{\partial \rho}{\partial t} + \nabla \cdot \rho \vec{v} = 0, \tag{2.13}$$

$$\rho \frac{d\vec{v}}{dt} = \vec{J} \times \vec{B} - \nabla p, \tag{2.14}$$

$$\frac{d}{dt}\left(\frac{p}{\rho^\gamma}\right) = 0, \tag{2.15}$$

$$\vec{E} + \vec{v} \times \vec{B} = 0, \tag{2.16}$$

$$\nabla \times \vec{E} = -\frac{\partial \vec{B}}{\partial t}, \tag{2.17}$$

$$\nabla \times \vec{B} = \mu_0 \vec{J}, \tag{2.18}$$

$$\nabla \cdot \vec{B} = 0, \tag{2.19}$$

where plasma is described as a single-component fluid with mass density, ρ, and velocity, $\vec{v}$. A practical result from these equation is that plasma is "frozen" on $\vec{B}$ field lines. To the first order, plasma density, temperature, and pressure are constant on a magnetic flux surface.

The plasma axisymmetric equilibrium in a tokamak is described by a second order nonlinear partial differential equation — Grad-Shafranov equation (Ref. [8]):

$$\Delta^* \psi = -\mu_0 R^2 \frac{dp}{d\psi} - F\frac{dF}{d\psi}, \tag{2.20}$$

where p is the plasma pressure, $-F/2\pi$ is poloidal current, $\psi/2\pi$ is the poloidal magnetic flux, and operator Δ^* is given by

$$\Delta^* \psi = R^2 \nabla \cdot \left(\frac{\nabla \psi}{R^2}\right) = R\frac{\partial}{\partial R}\left(\frac{1}{R}\frac{\partial \psi}{\partial R}\right) + \frac{\partial^2 \psi}{\partial Z^2}. \tag{2.21}$$

2.1.4 Plasma diagnostics

To understand fusion grade plasmas, many special diagnostic techniques have been developed (see Ref. [9] on this topic). Lasers are used to measure electron density, temperature, and fluctuations. CCD cameras, bolometers, and X-ray imaging systems are used to measure a wide range of plasma radiation. Coils are installed to measure magnetic fields and plasma current. There are many other diagnostics measuring plasma heating power, fusion neutron rate, plasma motion velocity, and impurities. A major part of this thesis is devoted to understanding reflectometry and its application in Alcator C-Mod.

2.1.5 Transport, turbulence, and H-mode

One of major challenges in fusion research is to minimize particle and energy transport. A confined plasma is never at an ideal thermal equilibrium, therefore transport cannot be avoided. However, to reduce the transport effects to a minimum so as to improve the confinement time τ is essential.

A transport process can be described by the following equation

$$\frac{\partial Y}{\partial t} = -\nabla(D \cdot \nabla)Y + S, \tag{2.22}$$

where Y can be either plasma particle density or energy density, D (sometimes χ is used for thermal transport coefficient) is the transport coefficient, and S is the particle or energy source. There are so called classical and neoclassical transport theories to estimate the transport coefficients (see Ref. [10]). The classical theory is based on diffusion across a constant magnetic field by the collisional change of the gyro center. The neo-classical theory also takes into account tokamak toroidal geometry, helical deformation of equilibria, and toroidal magnetic field ripple, etc. However, these theoretical results are far away from the experimental results. Under special circumstances, the observed value of the ion thermal transport coefficient, χ_i, can be a few times the neoclassical theoretical predictions. But the experimental density transport coefficient, D, and electron thermal transport coefficient, χ_e, typically

exceed the neoclassical theory by two orders of magnitude.

Presently there is no "first principles" theory that is capable of predicting the observed transport. Turbulence with a spectrum of short wave length modes, whose amplitudes determined by various nonlinear mode-mode and mode-particle couplings, is thought to be responsible for the enhancement of the transport above the neoclassical theory (Ref. [11]). Electrostatic drift waves, which are driven by the non-uniformity in spatial distribution and the temperature of particles, can have dominant contribution to χ_e. The ion temperature gradient mode is also thought to play an important role. Near plasma edge, micro-tearing mode, ripple modes, and resistive ballooning modes can all have contributions. Detailed physics is still far from being comprehensively understood because of the complexity of the problem. Part of this thesis research is to study plasma turbulence using reflectometry.

The tokamak plasma has two distinct regimes in terms of plasma confinement. The good confinement state is called the high confinement mode (H-mode) compared to the baseline level (L-mode). The H-mode was first seen in the ASDEX tokamak in 1982 (Ref. [2]), and it has since been observed in many tokamaks with auxiliary heating and divertor configuration. Signatures of the H-mode include a sudden drop of deuterium Balmer α ($3p \rightarrow 2s$) line, D_α, emission and increases in density, temperature, and plasma stored energy. The "first principles" physics of this process is not well understood. A heating power threshold exists above which the H-mode occurs. This threshold is determined by plasma density, plasma volume, magnetic field strength, temperature, and other parameters. ITER[2] H-mode database shows a power threshold (Ref. [12])

$$P_{th}[\mathrm{MW}] = (0.45 \pm 0.10) B[\mathrm{T}] \bar{n}_{e_{20}}^{0.75} R^2[\mathrm{m}] (0.6 \bar{n}_{e_{20}} R^2[\mathrm{m}])^{\alpha}, \tag{2.23}$$

where $\bar{n}_{e_{20}}$ is the line-averaged electron density in units of 10^{20} m^{-3}, and α is a fitting parameter, $\alpha \leq 0.25$. The L-H transition also requires a critical edge temperature

[2]It was a big next step tokamak aiming to study burning and ignition plasmas. However, due to premature physics and reduced budget, a reduced size machine, ITER-feat, is now being considered instead.

(for example, see Refs. [13][14])

$$T_{e,crit} \sim B^{\alpha} n^{-\gamma}, \tag{2.24}$$

where $1/2 < \alpha < 2$ and $0 < \gamma < 2/3$. The causes of such L-H transition thresholds have been studied for many years, but they are still not well understood (see Ref. [1] for a recent review).

In an H-mode, both plasma particle and energy confinements are typically about a factor 2 better than those in an L-mode. A transport barrier forms near the plasma edge. The barrier results from a suppression of convective eddies by sheared $\vec{E}_r \times \vec{B}$ poloidal rotation (see a review article Ref. [15]). Plasma density and temperature profiles form a pedestal shape near the edge due to the barrier. An internal transport barrier (ITB) may also appear in the core plasma when special heating or current drive techniques are applied (for example, Ref. [16]). Although H-mode operation can achieve a better confinement, some types of H-mode are not suitable for steady state operation. For example, edge localized mode (ELM)-free H-mode can accumulate large amount of impurities (Ref. [17]). The radiation from impurities may cause large plasma energy loss and trigger the H to L back transition. In H-modes with ELMs (ELMy H-modes), which have several types corresponding to different ELM characteristics, the ELMs deposit bursty heat loads to the divertor plate, which is not favorable for future reactor size device (Ref. [18]). A new type of H-mode discovered in Alcator C-Mod is called enhanced D_α (EDA) H-mode. It will be discussed in detail in next Section.

2.2 The Alcator C-Mod tokamak

2.2.1 Machine parameters

The Alcator C-Mod tokamak is the third Alcator tokamak built at MIT following Alcator A and Alcator C[3]. Like the two previous tokamaks, Alcator C-Mod, which

[3]Commissioned in 1973 and 1979, respectively.

Table 2.1: Parameters of the Alcator C-Mod tokamak

Parameter	Symbol	Typical value
Major radius	R_0	0.67 m
Minor radius	a	0.22 m
Elongation	κ	1.6
Triangularity	δ	0.5
Toroidal B field	B_{t0}	$\leq$ 8.0 T
Plasma current	I_p	$\leq$ 1.5 MA
ICRF heating	P_{RF}	$\leq$ 8 MW
Average density	$\bar{n}_e$	$\leq 10^{21}$ m^{-3}
Central electron temperature	T_{e0}	$\leq$ 5 keV

had its first plasma in 1993, is also a compact tokamak with high magnetic field ($B_0 \leq 8.0$ T), and high plasma density. Unlike its precedents, Alcator C-Mod has a shaped plasma and a divertor. Some major parameters of Alcator C-Mod are shown in Table 2.1. Compared with other major tokamaks in the world, such as DIII-D, JET, Tore-Supra, JT-60U, and ASDEX-Upgrade, Alcator C-Mod operates in a unique parameter space of high field, high density, and very high power density.

From the engineering point of view, the tokamak consists of several major parts: the vacuum chamber, toroidal field coils, poloidal field coils, power system and cryogenic system (Fig. 2-2). The vacuum chamber is stainless steel and covered with plasma facing components made of molybdenum. There are nine 20 cm wide horizontal ports for access to the plasma. The toroidal coils are able to produce up to an 8 Tesla field at the center of the vacuum chamber. Poloidal coils are used to drive plasma current, and control plasma position and shape. Poloidal coils include 3 ohmic coils and 4 equilibrium coils. The power system includes an alternator, which can store about 2 GJ of energy in the fly-wheel and deliver as much as 500 MJ during a typical plasma discharge. The coils are cooled by liquid nitrogen so that the toroidal magnetic coils have higher conductivity than that at room temperature, and dissipative heat can also be easily dissipated. The time required to cool down, in most cases, determines the interval between discharges, which is typically about 20 minutes. All experimental data are acquired by an advanced data system called MDS-plus.

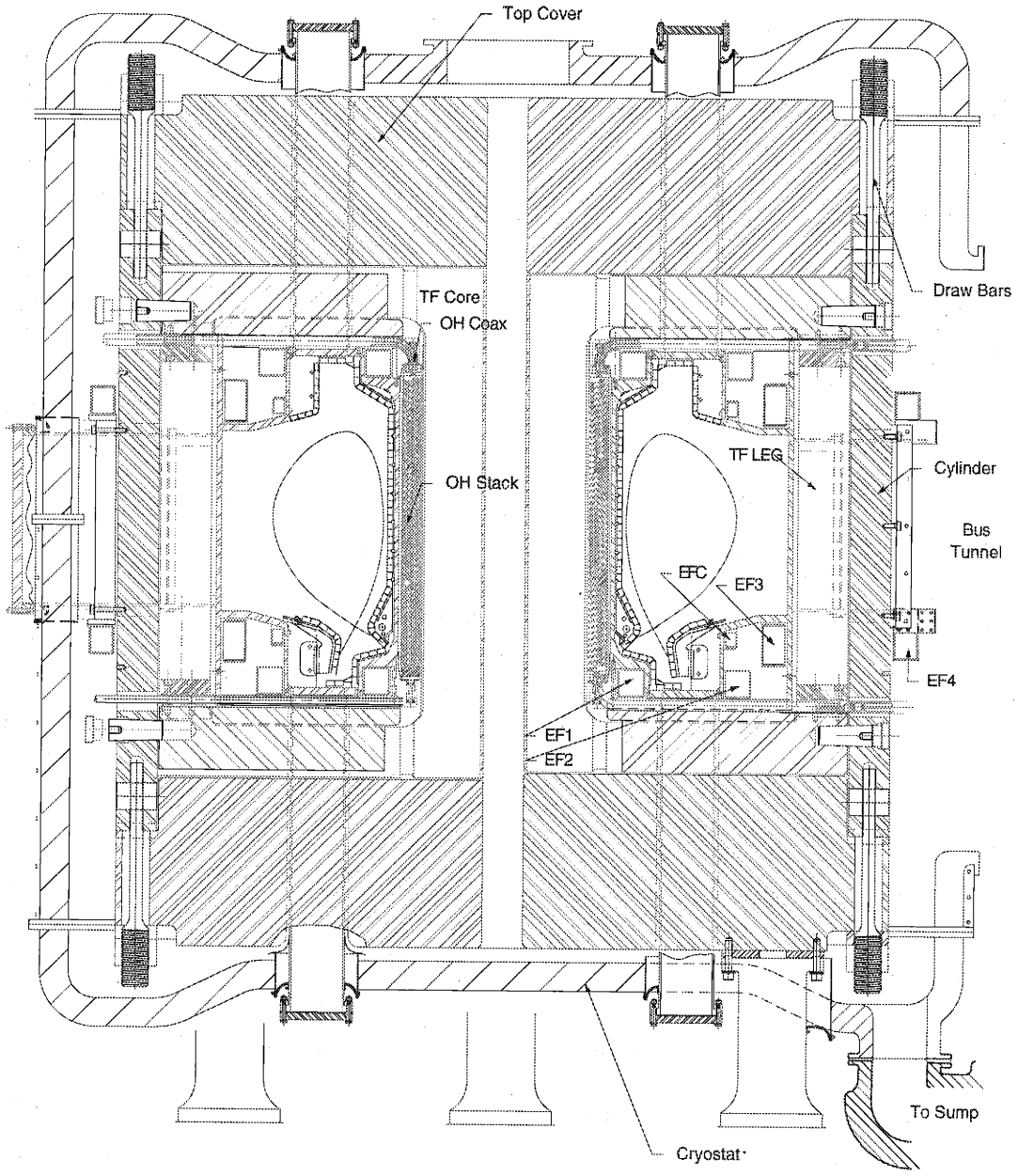

Figure 2-2: The Alcator C-Mod tokamak.

Table 2.2: A list of n_e and T_e diagnostics in the Alcator C-Mod tokamak

Parameter	Diagnostics	Principle
n_e	Two color interferometer (TCI) and tangential TCI	Refractive index line-integral
$n_e\sqrt{Z}$	Visible continuum array	Bremstrahlung emissivity with known T_e profile
n_e, $\tilde{n}_e$	Reflectometer	Microwave reflection group delay
$\int \tilde{n}_e dl$	Phase contrast imaging (PCI)	Refractive index line-integrated fluctuations
n_e, T_e	Core and edge Thomson scattering systems	Laser scattering from free electrons
T_e	Electron cyclotron emission (ECE)	ECE
n_e, T_e	Langmuir probes	Particle collection

2.2.2 Plasma diagnostics

Table 2.2 shows typical plasma density, density fluctuations, and temperature diagnostics in Alcator C-Mod. The reflectometer, phase contrast imaging (PCI) system, Langmuir probes, and edge thomson scattering (TS) system are shown in Fig. 2-3. The reflectometer views at the mid-plane, and measures plasma density profiles and fluctuations near the edge. Swept Langmuir probes usually measure plasma at the scrape-off-layer (SOL). They are able to penetrate the last closed flux surface (LCFS) only in ohmic discharges. PCI measures line-integrated electron density fluctuations, $\int \tilde{n}_e dl$, along its vertical chords. The edge TS system measures density and temperature profiles from a small plasma volume near the top edge. The two-color interferometer (TCI) measures line-integrals of electron density, $n_{el} = \int n_e dl$. TCI also provides density profiles through Abel inversion. The visible continuum array views with high spatial resolution at the mid-plane, and measures the profiles of $n_e\sqrt{Z}$, where Z is the the effective charge.

Other measured plasma parameters include plasma radiation (bolometry, spectroscopy, X-ray, and bremstrahlung radiation), magnetic fields (toroidal B_t and magnetic field fluctuations), loop voltage, plasma current I_p, ICRF heating power, fusion neutron rate, plasma velocity, ion temperature, and impurity inventory. There are

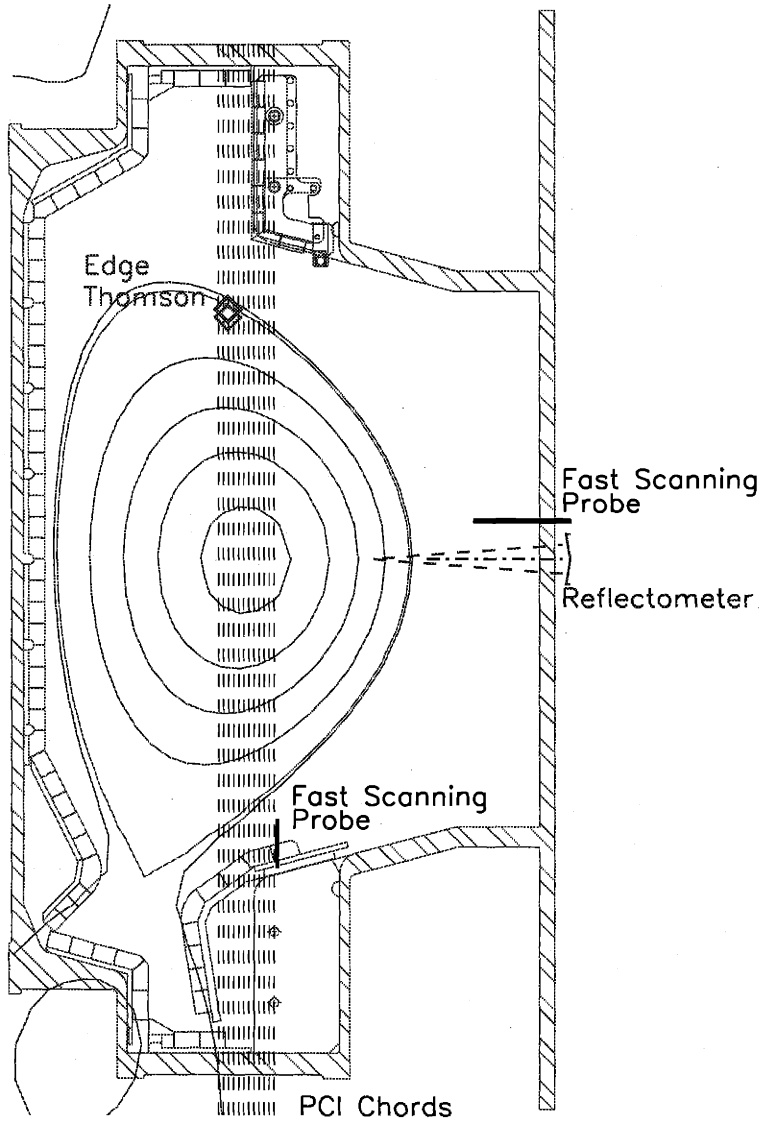

Figure 2-3: Several density diagnostics in Alcator C-Mod. The reflectometer views at the mid-plane and measures plasma edge. Langmuir probes measure plasma at the scrape-off-layer (SOL). PCI measures the line-integrated density fluctuations along its laser paths. The edge Thomson scattering system measures density profiles at the upper plasma edge.

also some diagnostics that mainly measure the edge plasma for divertor research.

2.2.3 EFIT

Many important plasma parameters are actually calculated by a plasma equilibrium code — EFIT (Refs. [19][20]). EFIT solves the Grad-Shafranov equation (Eq. 2.20) for the magnetic equilibrium by performing a least-squares fit to measurements of the poloidal field, B_p, and flux, ψ, at the vessel wall, together with measurements of the plasma current and active coil currents. The flux functions p' and FF', which determine the toroidal current in the plasma, are obtained in parametrized form. Currents flowing in passive conductors (the vacuum vessel and structure) are also inferred from the fit. From this solution, the code then self-consistently reconstructs the plasma shape, current density, q profile, and stored energy, etc. EFIT is run automatically between shots, providing equilibria at 20 ms intervals for the duration of the discharge. These reconstructions are then used for the mapping of various diagnostics to a common "flux space" geometry.

For the automatic analyses between shots, only external magnetic and current measurements are used as inputs to the code. Consequently, only a small number of free parameters (typically 5) describing the flux functions p' and FF' can be determined; the resulting reconstruction is incapable of reproducing detailed profile features, such as the H-mode pedestal. For more detailed studies, "kinetic" data, including temperature and density profile measurements from various diagnostics, are also used to further constrain the pressure profile, and additional physics considerations, e.g. the neoclassical Ohm's law, may be introduced to constrain the net parallel current density. With these additional inputs, more complicated parametrizations may be employed for the flux functions, permitting more accurate equilibria to be reconstructed.

2.2.4 Research themes in Alcator C-Mod

The Alcator C-Mod team plays an important role in many major fusion plasma research areas. Research themes in Alcator C-Mod include transport study, ICRF heating, divertor and edge plasma, MHD, and advanced tokamak physics. The work in this thesis mainly contributes to the study of plasma transport and confinement.

ICRF heating is based on the ion-cyclotron resonance of ions with electro-magnetic waves at the ion-cyclotron frequency. If we choose the correct wave polarization, such a resonance can transfer wave energy to the ions. In practice, we introduce a minority species (hydrogens or helium-3) in the bulk deuterium plasma. The launched waves (fast waves) have a frequency equal to the cyclotron frequency of the minority ions, but the wave polarization is determined by the bulk deuterium plasma. As a result, the wave energy is absorbed by the minority ions. Electrons and bulk deuterium ions are heated through collisional processes with the minority ions. In Alcator C-Mod, the RF antennas are capable of providing total RF power up to about 6 MW to the plasma. These antennas usually operate at 80 MHz, that is, the ion-cyclotron frequency for hydrogen ions (protons) at $B \simeq 5.4$ T. ^{3}He minority is used at $B \simeq 8$ T and 80 MHz RF frequency to heat the plasma. Research on ICRF heating includes engineering development and physics. Waves and plasma interaction, RF power absorption, mode conversion, and RF current drive are some of the active areas of RF physics research.

The research of edge plasma concentrates on the divertor and SOL plasma. SOL is the region outside the last closed flux surface (LCFS). Particles in SOL exit to the divertor and leave the main plasma. Neutrals and neutral impurities entering the SOL are ionized and pumped into the divertor away from the main plasma. Along the path to the strike point, the particles are cooled and sputtering effects at the striking point are reduced. Interaction between the plasma and surface material, atomic processes, and transport of impurities and neutrals are some directions in this research area.

2.2.5 H-mode and EDA H-mode

The physics research of this thesis mainly contributes to the study of plasma confinement: H-mode and enhanced D_α (EDA) H-mode. In Alcator C-Mod, we have a type of H-mode called EDA H-mode (Fig. 1-2). The name is derived from the D_α emission enhancement after the L-H transition. EDA H-modes have similar energy confinement to that in ELM-free H-modes, but weaker impurity confinement. Like ELM-free H-modes, EDA H-modes do not have apparent ELMs. With these particular features, EDA H-modes are potential candidates for steady state reactor-relevant tokamak operation.

There is a favored parameter regime for EDA H-modes: higher safety factor ($q_{95} \geq 3.5$), relative higher density ($\bar{n}_e \geq 1.2 \times 10^{20}$ m^{-3}), and larger triangularity ($\delta \geq 0.35$) (see Ref. [21] and references therein for details). A smaller ion mass (for example, hydrogen) also helps to reach EDA. The boundary of EDA H-mode and ELM-free H-mode has been shown to be a "soft" boundary in contrast to the "hard" threshold of L-H transition.

The reduced particle (especially impurities) confinement is probably caused by high wavenumber continuous edge quasi-coherent fluctuations, which have been observed by the reflectometer (Refs. [4][22]), PCI (Ref. [23]), the Langmuir probes (Ref. [24]), and magnetic coils installed in a probe head (Ref. [25]). These fluctuations usually have poloidal wavenumbers about $2-6$ cm^{-1} and frequencies of $50-250$ kHz in the lab frame. They are localized in the pedestal region, and their existence coincides the D_α enhancement in EDA H-mode. The experimental measurement and study of the behavior of these quasi-coherent fluctuations using the reflectometer will be discussed in detail.

2.2.6 H-mode pedestal research

In an H-mode plasma, the pedestal region, which acts as the boundary condition for transport equations, affects the bulk plasma confinement. In Alcator C-Mod, this region is extremely narrow. The density pedestal width is ≤ 0.5 cm, and the

temperature pedestal width is $\leq$ 0.8 cm. The width of X-ray radiation pedestal is even narrower ($\sim$ 1 mm). In this region, pressure gradient (and probably electric field shear) is very large. Pedestal study is to reveal the mechanism of such an extreme phenomenon, for example, its correlation with plasma current, heating power, magnetic field configuration and plasma stored energy. This large gradient may also be one of the necessary conditions that trigger the quasi-coherent fluctuations seen in EDA H-modes. More details of the progress of pedestal physics research can be found in Ref. [26].

2.2.7 Plasma rotation

In Alcator C-Mod, a self-accelerating core plasma toroidal rotation is observed even without direct momentum input (Refs. [27] and [28]). The rotation is co-current in H-mode and counter-current in L-mode. It is observed by both Argon spectroscopy and magnetic fluctuations. The rotation velocity increases with plasma stored energy and decreases with plasma current. With off-axis ICRF heating, the central toroidal rotation significantly decreases together with the formation of an ITB (Ref. [29]). Some theoretical work has been developed to understand such a toroidal momentum generation (for example, Ref. [30]), but the mechanism has not been fully understood.

The reflectometry fluctuation measurements, which are made in the lab frame, are subject to the Doppler shift due to plasma motion. In order to understand density fluctuations in the plasma frame, we need to transform the lab frame measurement into the plasma frame using the measured plasma velocity. Conversely, one can infer plasma velocity from reflectometry fluctuation measurements provided we have a knowledge of the spatial structure of the fluctuations. The poloidal velocity measurement near plasma edge will be available in the near future using the recently installed diagnostic neutral beam (DNB) (Ref. [31]).

Chapter 3

Reflectometry theory and principles

Reflectometry is a plasma diagnostic technique similar to radar. Microwaves are launched into the plasma and reflected at the critical surfaces, which are determined by the frequencies of the microwaves, plasma density, and magnetic field. By receiving the reflected microwave signals and comparing them with the launched waves, one can infer plasma density profiles, density fluctuations, and the correlation length of turbulences.

In this Chapter, the theory and principles of reflectometry are presented. First we introduce the propagation of electro-magnetic waves in cold plasmas. Then the techniques for density profile measurements are briefly discussed. A major part of this Chapter is the interpretation of fluctuations and correlations of the reflectometry signal. Some existing analytic and numerical models are also discussed.

3.1 Electro-magnetic (EM) waves in cold plasmas

In reflectometry, we need only consider cold plasma in dealing with the propagation of electro-magnetic (EM) waves. The cold plasma approach does not consider any effects of plasma temperature, which in most cases only add a negligible correction in the calculation of critical density ($\delta n_c/n_c \sim 5 \times 10^{-3} Te[\text{keV}]$) (Ref. [4]). The frequency

range of microwaves in reflectometry is usually about a factor of $(m_i/m_e)^{1/2}$ larger than ion plasma frequency ($f_{pi} = \omega_{pi}/2\pi$), and a factor of (m_i/m_e) larger than ion cyclotron frequency ($f_{ci} = \omega_{ci}/2\pi$), therefore ion species effects are also ignored.

3.1.1 Dispersion relations

We can derive the dispersion relation for electro-magnetic waves in a homogeneous and collisionless plasmas based on Maxwell's equations combined with the motion of electrons (for example, Refs. [32] and [33]). Using the notation shown in Fig. 3-1, the magnetic field is in $\hat{z}$ direction, and the wave lies in $x-z$ plane. The wave propagates at an angle of θ relative to $\vec{B}$. The perturbed electric field is described as

$$\vec{E}_1 = \vec{E}_1(\vec{k},\omega)\exp[i(\vec{k}\cdot\vec{r}-\omega t)], \tag{3.1}$$

which is the solution of the following equation

$$\vec{N}(\vec{N}\cdot\vec{E}_1) - N^2\vec{E}_1 + \overline{K}\cdot\vec{E}_1 = 0, \tag{3.2}$$

where $\vec{N} = c\vec{k}/\omega$ is the index of refraction, and $\overline{K}$ is the dielectric tensor. Eq. 3.2 can be written in a matrix form:

$$\begin{bmatrix} K_{xx}-N^2\cos^2\theta & K_{xy} & K_{xz}+N^2\cos\theta\sin\theta \\ K_{yx} & K_{yy}-N^2 & K_{yz} \\ K_{zx}+N^2\cos\theta\sin\theta & K_{zy} & K_{zz}-N^2\sin^2\theta \end{bmatrix} \cdot \begin{bmatrix} E_{1x} \\ E_{1y} \\ E_{1z} \end{bmatrix} = 0, \tag{3.3}$$

where

$$K_{yy} = K_{xx} = 1 + \frac{\omega_{pe}^2}{\omega_{ce}^2-\omega^2}, \tag{3.4}$$

$$K_{xy} = -K_{yx} = \frac{i\omega_{ce}}{\omega}\frac{\omega_{pe}^2}{\omega_{ce}^2-\omega^2}, \tag{3.5}$$

$$K_{zz} = 1 - \frac{\omega_{pe}^2}{\omega^2}, \tag{3.6}$$

$$K_{yz} = K_{zy} = K_{xz} = K_{zx} = 0, \tag{3.7}$$

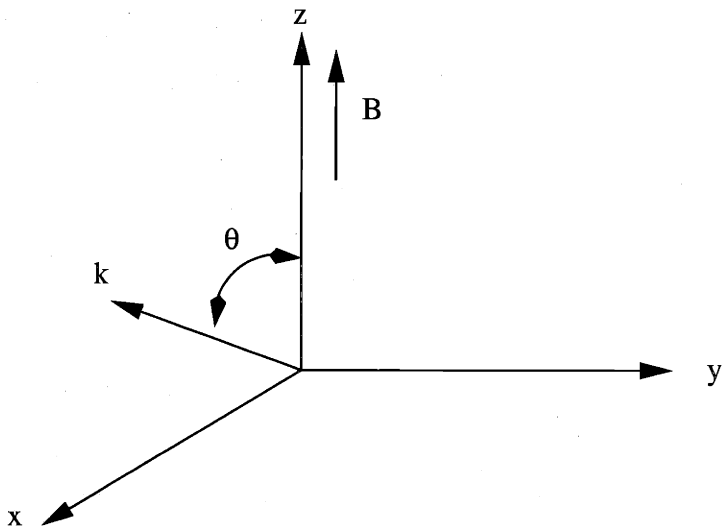

Figure 3-1: Notations for the EM wave

$\omega_{pe} = (n_e e^2/\epsilon_0 m_e)^{1/2}$ is the plasma frequency, and $\omega_{ce} = eB/m_e$ is the electron cyclotron frequency.

For an EM wave propagating perpendicular to the magnetic field ($\theta = 90^0$), which is the usual case for the reflectometry application, Eq. 3.3 is reduced to

$$\begin{bmatrix} K_{xx} & K_{xy} & 0 \\ K_{yx} & K_{yy} - N^2 & 0 \\ 0 & 0 & K_{zz} - N^2 \end{bmatrix} \cdot \begin{bmatrix} E_{1x} \\ E_{1y} \\ E_{1z} \end{bmatrix} = 0. \tag{3.8}$$

The dispersion relation is obtained by setting the determinant of the matrix in Eq. 3.8 equal to zero:

$$\begin{vmatrix} K_{xx} & K_{xy} & 0 \\ K_{yx} & K_{yy} - N^2 & 0 \\ 0 & 0 & K_{zz} - N^2 \end{vmatrix} = 0. \tag{3.9}$$

There are two roots of this equation depending upon the direction of the perturbed electric field:

- If $\vec{E}_1 \parallel \vec{B}$, the wave is called ordinary (O-mode) wave. The dispersion relation

for an O-mode wave is

$$N^2 = 1 - \frac{\omega_{pe}^2}{\omega^2}. \tag{3.10}$$

- If $\vec{E}_1 \perp \vec{B}$, the wave is called extra-ordinary (X-mode) wave. The dispersion relation for an X-mode wave is

$$N^2 = 1 - \frac{\omega_{pe}^2}{\omega^2}\left(\frac{\omega^2 - \omega_{pe}^2}{\omega^2 - \omega_{uh}^2}\right), \tag{3.11}$$

where $\omega_{uh} = \left(\omega_{pe}^2 + \omega_{ce}^2\right)^{1/2}$ is the upper hybrid frequency.

An EM wave can propagate in the region where $N^2 > 0$, but it is evanescent where $N^2 < 0$. The wave is reflected at the critical (cutoff) surface where $N^2 = 0$. Reflectometry is particularly interested in the cutoff condition. Explicitly, the cutoff conditions for O-mode and X-mode waves are

- $\omega = \omega_{pe}$ for O-mode,
- $\omega = \frac{1}{2}\omega_{ce} \pm \left(\frac{1}{4}\omega_{ce}^2 + \omega_{pe}^2\right)^{1/2}$ for X-mode, where the plus sign corresponds to the right hand cutoff (RHC), and the minus sign corresponds to the left hand cutoff (LHC).

Microwave accessibility is determined by plasma parameters such as electron density profile and magnetic field profile (Fig. 3-2). Since the reflectometer in Alcator C-Mod is currently an O-mode reflectometer, the following discussion focuses on O-mode waves.

3.1.2 Ordinary (O-mode) waves in plasmas

It is not adequate to only know where the critical surfaces are. The wave solution along the whole wavepath must be known in order to reconstruct plasma information. This Section discusses the exact analytic solution for linear density profile and the geometric approximation in dealing with the propagation of O-mode waves.

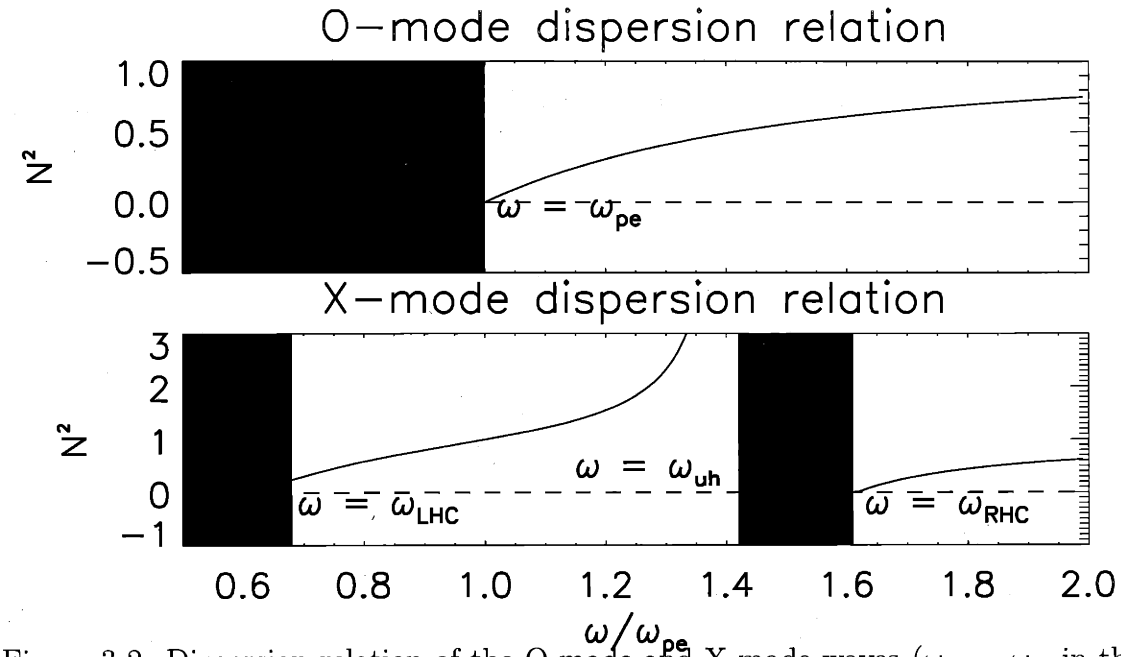

Figure 3-2: Dispersion relation of the O-mode and X-mode waves ($\omega_{pe} = \omega_{ce}$ in this figure). The shaded are the evanescent (forbidden) areas. The critical layers are also labeled.

Exact solution for linear density profile

In an inhomogeneous medium, the electric field distribution of an O-mode wave is described by the following time independent equation

$$\frac{d^2E_1(x)}{dx^2} + \frac{\omega^2}{c^2}N^2(\omega, x)E_1(x) = 0, \tag{3.12}$$

where $\vec{B} = B\hat{z}$, $\vec{E}_1 \parallel \vec{B}$, $n_e = n_e(x)$, and the wave propagates in the direction of $\hat{x}$, $\vec{k} = k\hat{x}$.

Eq. 3.12 has an exact analytic solution if the density profile is linear: $n = n_c x/x_c$, where n_c and x_c are the critical density and position respectively (Ref. [34]). By making the substitution

$$\xi = \left(\frac{\omega^2}{c^2 x_c}\right)^{1/3}(x - x_c), \tag{3.13}$$

we obtain the solution of Eq. 3.12:

$$E(\xi) = \frac{3A}{\pi}\int_0^\infty \cos\left(\frac{x'^3}{3} - \xi x'\right)dx', \tag{3.14}$$

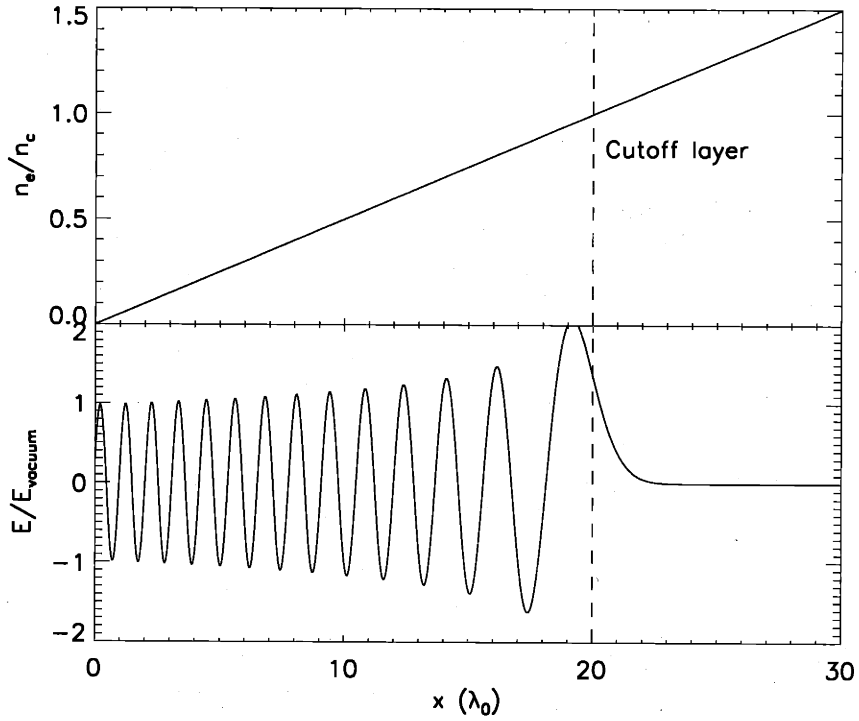

Figure 3-3: The solution of 1-D wave Eq. 3.12. $x_c = 20\lambda_0$, where λ_0 is the vacuum wavelength of the incident wave.

where A is a constant. For $\xi \gg 1$, i.e., at the places that are many wavelengths away from the cutoff surface, the electric field becomes

$$E(\xi) = \frac{3A}{\sqrt{\pi}}\xi^{-1/4}\cos\left(\frac{2}{3}\xi^{3/2} - \frac{\pi}{4}\right). \tag{3.15}$$

Fig. 3-3 shows a plot of the solution in the case of $x_c = 20\lambda_0$, where λ_0 is the vacuum wavelength of the incident wave. The argument inside the cosine of Eq. 3.15 can be re-written in a suggestive form

$$\frac{2}{3}\xi^{3/2} - \frac{\pi}{4} = \int_x^{x_c} k(x)dx - \frac{\pi}{4}. \tag{3.16}$$

This result indicates that the launched wave and reflected wave have a phase difference that is equal to the phase change calculated by integrating the local index of refraction

minus a $\pi/2$ offset. This statement is also approximately valid for density profiles other than the linear density profile as shown by the geometric optics approximation discussed below.

Geometric optics approximation

Note that Eq. 3.12 has the same form as the 1-D Schröedinger equation in quantum mechanics

$$\frac{d^2\Psi}{dx^2} + \frac{2m}{\hbar}[E - V(x)]\Psi = 0, \tag{3.17}$$

where E is particle total energy, V is the potential function, and Ψ is the quantum wave function. In order to approximately solve various quantum mechanic problems, the WKBJ (Wentzel, Kramers, Brillouin, and Jeffrey) approximation was developed (see Ref. [35] for applications in quantum mechanics). The main result of the WKBJ approximation is that the local wavenumber of an EM wave can be approximately determined by the local index of refraction. Therefore, the approximation is also called geometric optics approximation.

For O-mode waves, the geometric optics approximation holds provided that

$$\frac{\lambda}{2\pi} \ll L_n, \tag{3.18}$$

where λ is the local wavelength of the reflectometry wave, and $L_n = \left(\frac{1}{n}\frac{dn}{dr}\right)^{-1}$ is the scale length of density gradient. Eq. 3.18 says that the approximation is valid wherever the variation of density profile is small in a distance equal to one wavelength divided by 2π.

Where the geometric optics approximation is valid, the solution of the electric field has an approximate form

$$E(x) = E_0(x)\exp\left[-i\frac{\omega}{c}\Phi(x)\right], \tag{3.19}$$

$$\Phi(x) = \pm\left[\int_{x_0}^{x} N(x)dx - \frac{\pi}{4}\right], \tag{3.20}$$

and we can obtain the phase difference of the launched and reflected waves at the

plasma edge

$$\phi = -\frac{\pi}{2} + \frac{2\omega}{c}\int_{x_c}^{x_{edge}} N(x)dx. \tag{3.21}$$

Eq. 3.21 suggests that the phase difference of the reflected wave and launched wave is determined by an integral of the local index of refraction along the wavepath. This is the basic equation for many applications of reflectometry.

3.2 Reflectometry electron density profile measurement

3.2.1 Profile inversion

Eq. 3.21 gives an approximate phase difference ϕ between the launched and reflected waves. Because ϕ is calculated by an integral, there can be infinite density profiles that can produce identical ϕ. In order to obtain density profiles in a range of $0 \leq n_e \leq n_0$ using reflectometry, we need to know ϕ or the group delay $d\phi/df$ for all waves that have critical densities in the range of $0 \leq n_e \leq n_0$.

For O-mode reflectometry, given $d\phi/df$, the density profile, shown in positions of critical surfaces, is readily available (Refs. [36] [9]):

$$R_c(f_0) = R_{edge} - \int_0^{f_0} \frac{c}{2\pi}\frac{d\phi}{df}\frac{df}{\sqrt{f_0^2 - f^2}}, \tag{3.22}$$

and the relation between the critical density and frequency is given by

$$n_c(f_0) = \left(\frac{f_0}{89.8}\right)^2, \tag{3.23}$$

where f_0 is in GHz, and $n_c(f_0)$ is in units of 10^{20} m^{-3}.

This simple method using Abel inversion shown in Eq. 3.22 is invalid for X-mode reflectometry, where critical surfaces are determined by both electron density and magnetic field. In order to obtain a density profile, one should use a matrix inversion method based on Eq. 3.21 (see Ref. [37] and references therein). This matrix solving

method is similar to that used in X-ray tomography, and it is also applicable for O-mode reflectometry.

O-mode reflectometry is not able to measure hollow density profiles because the O-mode wave is reflected at the first critical surface. Moreover, O-mode reflectometry always needs other diagnostics to provide density profiles at the very plasma edge, where the critical frequency approaches to zero. The right hand cutoff (RHC) X-mode reflectometer is able to detect hollow profiles, and measure density profiles independently if the frequency range covers the electron cyclotron frequency at the plasma edge, $f_{ce,edge}$. In fusion experiments with low or moderate magnetic field, RHC X-mode is often used because of a lower frequency range than that of O-mode, for example, reflectometer in the DIII-D tokamak (Ref. [38]). However, due to the high magnetic field in Alcator C-Mod, RHC X-mode requires a minimum frequency of about 110 GHz (roughly speaking, $f_{min} \geq f_{ce,edge}[\mathrm{GHz}] \simeq 28 B_{edge}[\mathrm{T}]$), which was not a practical choice due to the significantly higher cost of millimeter wave components at higher frequency[1].

3.2.2 Amplitude modulated (AM) reflectometry

As shown in the previous Section, we need to measure the phase change or group delay of waves in a range of frequencies in order to obtain a density profile. Many techniques, such as AM (amplitude modulated), DP (differential phases), FM (frequency modulated), and ultra-short pulses, have been developed to simultaneously measure phases or group delays of multiple frequencies (see Ref. [39] for a review). Only the AM technique (Ref. [40]), which is currently used for the Alcator C-Mod reflectometer, is discussed below in detail.

AM reflectometry is a simple technique to measure group delay (Fig. 3-4). A typical AM reflectometry system consists of several channels at discrete frequencies. In each channel, a microwave source with frequency f_0 (baseband) is amplitude modulated by a low frequency RF signal (Δf). The amplitude modulation produces two waves with a small frequency difference $f_{U,L} = f_0 \pm \Delta f$. The higher frequency band

[1]Since $f_{pe} \propto \sqrt{n_e}$, $f_{RHC} \propto B$, and typical plasma density $n_e \propto B$, we have $f_{RHC}/f_{pe} \sim \sqrt{B}$.

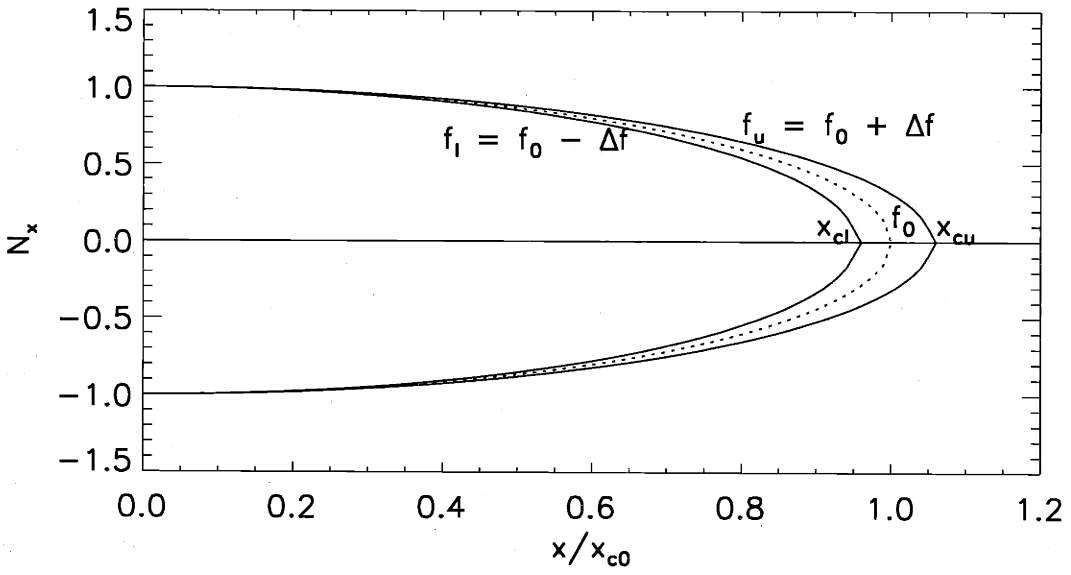

Figure 3-4: The principle of AM reflectometry. A wave with frequency f_0 is amplitude modulated to two waves with f_u and f_l, which are reflected at different critical surfaces $x = x_{cl}$ and $x = x_{cu}$. The phase changes in these waves are used to calculate group delay. This figure shows the case of a linear density $n_e/n_c = x/x_c$ and O-mode reflectometry.

(plus sign) is called the upper sideband (USB), and the lower frequency band (minus sign) is called the lower sideband (LSB). Both waves are launched to the plasma. Their phase changes are denoted as ϕ_u and ϕ_l. By measuring the difference of ϕ_u and ϕ_l, $\Delta\phi = \phi_u - \phi_l$, we can approximately obtain the group delay at frequency f_0:

$$\frac{d\phi(f_0)}{df} \simeq \frac{1}{2}\left(\frac{\Delta\phi}{\Delta f}\right) = \frac{\phi_u - \phi_l}{2\Delta f}. \tag{3.24}$$

With $d\phi/df$ at several frequencies, we can calculate the electron density profile using Eq. 3.22.

Compared with other techniques, the AM technique has advantages in the simplicity of design, reliability in group delay measurement, and high temporal resolution. An AM reflectometer reduces the system complexity by avoiding frequency modulation and a reference leg. By simply measuring the phase difference of two waves, the AM system has a simple transmission system because the phase difference is not

affected by the wave mode structure in the transmission line. Plasma information is carried in the modulation RF frequency. Therefore, the frequency stabilization of the microwave sources are not as critical as in other techniques. In a swept frequency system, complicated methods are used to follow and extract phase information (for example, see Refs. [41][42]). In AM reflectometry, the reflectometry phase are directly measured, and $2n\pi$ ambiguity in the returned phase can be eliminated or easily followed. The temporal response of AM reflectometry is generally only limited by the filter band-width of the detecting system. In contrast, a high temporal resolution is difficult to achieve in FM reflectometry because the response is mainly determined by the frequency sweeping rate of the microwave source.

AM reflectometry also has some disadvantages. A trade-off among the modulation frequency Δf, radial correlation of plasma turbulence, and phase detector resolution must be made. The distance between the two critical surfaces should be so small, typically within one radial correlation length of the turbulence, that most temporal and spatial turbulence can cancel due to the common phase shift in the USB and LSB (Ref. [39]). However, a smaller Δf also gives a smaller $\Delta\phi$, and demands a higher phase resolution from the phase detector. Too large a modulation frequency may also introduce too many fringe jumps in $\Delta\phi$, which may cause difficulty in eliminating $2n\pi$ phase ambiguity. The AM technique cannot discriminate against some spurious signal sources, such as multiple reflections from the vacuum chamber, from the measured signals due to its limited range resolution (Ref. [43]). We must test for and then exclude the spurious signals with in-vessel calibration tests. A third issue is spatial calibration. A fiducial point with known group delay must be established. The reflection at the inner wall normally provides this fiducial point. Nonetheless, in spite of these disadvantages, AM reflectometry has been successfully used in many fusion experiments as one of the principal or auxiliary density profile diagnostics (for example, see Refs. [4][22][40][44][45][46]).

3.3 Reflectometry fluctuations interpretation

Reflectometry has been widely used to monitor and measure density fluctuations in fusion experiments. For this purpose, the system is usually set up to work at a fixed set of frequencies. The amplitudes and phases of the reflected signals are continuously recorded. Plasma density fluctuations produce fluctuations in the reflectometry signals. However, the interpretation of the reflectometry signals in terms of density fluctuations is a complicated issue. We should answer the following questions before using reflectometry as a quantitative fluctuation diagnostic technique:

1. How localized is the reflectometry measurement?
2. How can the measured signal fluctuations be quantified in terms of the density fluctuations?
3. How do real experimental issues, such as microwave beam width, plasma curvature, and antenna pattern, affect the measurement?

In this Section, some existing analytic treatments and numerical models on this issue are discussed.

3.3.1 Analytic models

1-D model

In the 1-D treatment, density fluctuations only have radial wavenumbers. Although it is rarely the case in experiments, a discussion is still helpful.

An early study in Ref. [47] showed that for long-wavelength fluctuations, the phase fluctuations in the reflectometry signal, $\tilde{\phi}$, is simply related to $\tilde{n}/n$ and density scale length, L_n, at the critical surface layer. The phase response falls significantly as the fluctuation wavelength approaches the free space wavelength λ_0, and the location of the maximum response moves out in front of the critical surface following the Bragg condition: $k_f(x) = 2k_{wave}(x)$, where k_f is the radial wavenumber of the fluctuation, and k_{wave} is the local wavenumber of the O-mode reflectometry wave. Generally,

it concluded that O-mode reflectometry only measures phenomena with radial scale larger than $\lambda_0^{2/3} L_n^{1/3}$.

For a linear density profile, $n = n_c x/L$, the scattered electric field due to a radial fluctuation at an observation point $x = x_0$ can be obtained in an analytic form (Ref. [48]):

$$E_s = -i2\pi k_0^{8/3} L^{-1/3} \left[\mathrm{Ai}(\xi_0) - i\mathrm{Bi}(\xi_0)\right] \int d\xi \, \frac{\tilde{n}(\xi)}{n} \mathrm{Ai}^2(\xi) \ , \quad \xi = k_0^{2/3} L^{-1/3} x, \tag{3.25}$$

and

$$\phi = -2\pi (k_0 L)^{2/3} \int d\xi \frac{\tilde{n}(\xi)}{n} \mathrm{Ai}^2(\xi), \tag{3.26}$$

where Ai and Bi are Airy functions.

By assuming a localized density perturbation:

$$\tilde{n}(x) = n_0 \exp[(x - x_f)^2 / w_f^2] \cos[k_f (x - x_f)], \tag{3.27}$$

where w_f is the width of the perturbation, x_f is the location, and k_f is the radial wavenumber of the fluctuation, the response in 1-D strongly depends upon k_f, w_f, and x_f. We define a local wavenumber of the incident wave at the critical surface

$$k_A = 0.63 k_0^{2/3} L^{-1/3}. \tag{3.28}$$

For fluctuations with $k_f < 2k_A$, the Bragg scattering condition can never be satisfied. Thus, if only such small wavenumber perturbations exist in the plasma up to the critical surface, the oscillations very close to the critical surface should dominate the reflectometry response, and the phase response is

$$\tilde{\phi} \simeq 2\pi \frac{n_0}{n_c} \left(\frac{L/\lambda_0}{k_f/k_0} \right) \mathcal{F}, \tag{3.29}$$

where $\mathcal{F}$ is a numerical factor close to 1.

For fluctuations with wavenumbers $2k_A < k_f < 2k_0$, the reflectometry responses depend on the perturbation width w_f relative to a critical perturbation width $w_c =$

Lk_f/k_0^2. The maximal response is from the Bragg scattering point or nearby. Detailed discussion can be found in Ref. [48].

The 1-D analytic result on the linear density profile suggests that the reflectometry measurement is not always localized. The critical surface oscillations dominate when $k_f < 2k_A$. In other cases, Bragg scattering from locations other than the critical surface may dominate. From the diagnostic point of view, Bragg scattering is not benign because we do not know the Bragg scattering positions. Fortunately, under real experimental conditions, especially when a sharp density gradient near the critical surface exists, the condition $k_f < 2k_A$ is not as large a constraint as one sees in the simple 1-D theory. With a steeper gradient, we have a larger k_A as defined in Eq. 3.28. For example, in typical Alcator C-Mod H-mode plasmas, $L \simeq 0.4$ cm, and $k_0 \sim 20$ cm^{-1}, we have $k_A \simeq 6$ cm^{-1}. Earlier results from CO_2 scattering measurements on Alcator C showed a turbulence spectrum with $k_f \leq 12$ cm^{-1} (Ref. [49]). An estimate using $\overline{k}_f \rho_s = 0.1 - 0.3$, where $\rho_s = \sqrt{T_e/m_i}/eB$ is the ion gyro-radius, and $\overline{k}_f$ is the half width of the turbulent spectrum, gives a realistic range: $\overline{k}_f \leq 10$ cm^{-1}. The condition $k_f < 2k_A$ is therefore well satisfied.

For density profiles other than linear, the simplest interpretation of fluctuations of the reflectometry signal in 1-D can be obtained from the geometric optics approximation, which is rewritten here as:

$$\phi = -\frac{\pi}{2} + \frac{2\omega}{c}\int_{R_c}^{R_{edge}} N(R)dR, \tag{3.30}$$

where R_{edge} is the major radius of the plasma edge, and R_c is the critical surface position. Under this approximation, the fluctuations in the reflectometer signal only consist of phase fluctuations, which are mostly from the oscillations of the critical surface. There is no fluctuation in the signal level of the microwave. Although this is never the exact case in experiments, it is the simplest calculable interpretation provided that we know the density profile (and also the magnetic field profile for X-mode). This approximation can still be fairly good after including 2-D effects as shown in Chapter 7.

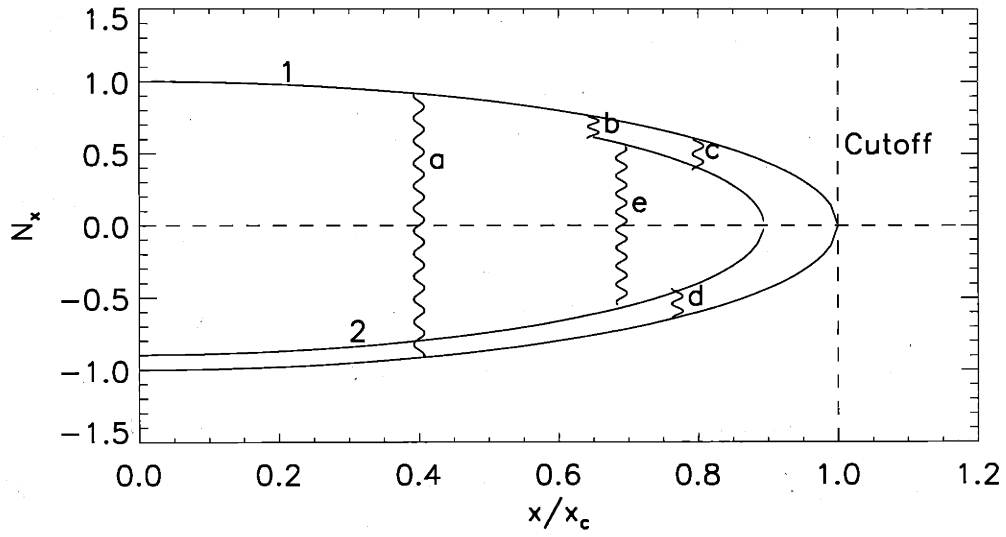

Figure 3-5: Microwave scattering in 2-D. Plotted is the x-component of the index of refraction $N_x = k_x c/\omega$. In the 1-D case, only scattering as shown in curve a is allowed at $2k_{x,loc} = k_f$. However, in 2-D, infinite possibilities exist because of the free choice of $k_{y,loc}$. For example, scattered waves can go along curves b, c, d and e, etc.

2-D analytic study

Analytic studies become very difficult in 2 dimensions. One such study is reported in Ref. [50]. Some interesting points from this 2-D analysis are discussed here.

Generally, the scattering is still dominated by the places where 2-D Bragg conditions are matched. The scattered signal increases with smaller fluctuations wavenumber. The main reason for such an increase is the increase in the coherence length (or resonance region, see Fig. 3-5), which is due to the fact that there are now many more scattering possibilities than in the 1-D situation. The theory indicates that a long distance to the critical surface is unfavorable for reflectometry application because the microwave signal may subject to strong small angle scattering along the wave path.

The study was done on a finite width plane wave-front and linear density profile, $n = n_c x/L$. With y as the poloidal direction and x as the radial direction, we assume

a density fluctuation

$$\tilde{n} = n_0 \exp\left[-ik_x(x-x_f) - \left(\frac{x-x_f}{w_f}\right)^2\right] \times \cos k_\perp (y-y_0), \tag{3.31}$$

where k_x is the radial wavenumber of the reflectometry wave, and $k_\perp$ is the poloidal wavenumber. We also assume the source electric field distribution of

$$f(u) = 2\pi^{1/2} W \exp\left(-\frac{u^2 W^2}{2}\right), \tag{3.32}$$

where u is the spectral number[2]. The scattered signal amplitude and phase are then given by:

$$\begin{aligned} A_s &= \frac{2\sqrt{2}i\pi^{3/2}e^2}{mc^2} P_i^{1/2} n_0 \frac{w_f W l^{3/4} \cos k_\perp y_0}{(L-x_f)^{1/2} L^{1/4}} \\ &\quad \exp\left[-\frac{k_\perp^2 W^2}{4}\left(2-\frac{x_f}{L}\right) - \frac{1}{8} w_f^2 k_\perp^4 W^2 \left(\frac{l}{L}\right)^{3/2} + i\Phi\right], \end{aligned} \tag{3.33}$$

$$\Phi = \frac{4}{3}\left(\frac{L}{l}\right)^{3/2} + k_\perp^2 l^{3/2} L^{1/2}\left(\frac{1}{2} + \frac{L-x_f}{L} - \frac{1}{8}\frac{w_f^2}{L^2} k_\perp^2 W^2\right), \tag{3.34}$$

where $l = (c^2 L/\omega^2)^{1/3}$ is the Airy scale length, and P_i the incident power. Eqs. 3.33–3.34 are valid if $W^2 < 2Lc/\omega$ and $w_f > l$. For poloidal fluctuations with longer wavelength, $k_\perp W < 1$, the signal becomes smaller when the position of the fluctuations moves towards the plasma boundary:

$$A_s \propto (L-x_f)^{-1/2}. \tag{3.35}$$

In the other region, $k_\perp W > 1$, the response is

$$A_s \propto \exp\left[-\frac{k_\perp^2 W^2}{4}\left(2-\frac{x_f}{L}\right)\right], \tag{3.36}$$

which indicates that reflectometry sensitivity drops exponentially to zero for fluctuations with large $k_\perp$. By including curvature of the plasma and curvature of the

[2]Notations are different than those used in the reference.

incident wave wave-front, the reflectometry response can be much larger than those predicted above (Ref. [51]). The curvature effect makes the result of the 2-D analytic study less important. The curvature effect is studied in Chapter 7.

3.3.2 Numerical models

Random phase screen model

The random phase screen model (RPSM) was developed at the Princeton Plasma Physics Lab (PPPL) (Refs. [52][53]). It has been used to interpret reflectometry measurements on the Tokamak Fusion Test Reactor (TFTR). In RPSM, plasma fluctuation effects on the mm-waves are reduced to a modulation on a phase screen. The modulation of the phase screen satisfies the geometric optics approximation:

$$\phi = 2k_0 \int_{x_{edge}}^{x_c} \epsilon^{1/2}\, dx, \tag{3.37}$$

where ϵ is plasma permittivity with fluctuations included, and k_0 is the vacuum wavenumber of the incident mm-wave. In a tokamak, x is in the direction of major radius R, x_c is the critical surface, and $x = x_{edge}$ at the plasma edge. The phase screen is located at

$$x_s = x_{edge} - \int_{x_{edge}}^{x_c} \epsilon^{-1/2}\, dx, \tag{3.38}$$

that is, the effective optical distance away from the plasma edge. From the correlation of reflected signals between two closely spaced phase screens, RPSM can estimate density fluctuation levels and correlation lengths.

We assume the spectrum of the radial density correlation has the form

$$\Gamma_n(k_x) = \sigma_n^2 \frac{k_x}{w_x^2} \exp(-k_x^2/\Delta k_x^2), \tag{3.39}$$

where σ_n is the root-mean-square (rms) of the density fluctuations. If the radial

correlation length is much shorter than the scale length of permittivity, we obtain

$$\Gamma_\phi(k_x) \simeq 4\pi k_0^2 L_\epsilon \frac{\sigma_n^2}{n_0^2 \Delta k_x^2} \exp(-k_x/\Delta k_x^2), \tag{3.40}$$

where Γ is the Fourier transformation of the radial correlation γ. This equation can be used to estimate the radial correlation length, which is discussed in Section 3.5. By measuring Γ_ϕ, we can infer σ_n and γ_n using Eq. 3.40.

RPSM concludes that reflectometry should work well if the amplitude variation in the reflectometry signal is small. A necessary condition is $\gamma_\phi \geq \gamma_E$, where γ_ϕ and γ_E are the correlation functions of phase and complex electric field respectively. The interpretation should be made with caution when there are strong amplitude variations in the reflectometry signal, which indicates a high level of density fluctuation or a long distance from the phase screen to the receiver. In the case of very large density fluctuations, the reflectometry signal spectrum may fall off as $1/f^2$.

RPSM does reproduce many phenomena seen in experiments such as loss of coherent reflection, strong amplitude variations, and the $1/f^2$ spectrum. However, this model implicitly assumes an infinite width of the incident wave. This treatment may lead to an overly restrictive criterion for reflectometry application. For example, the observation limit on $k_\perp$ based on the diffraction length study may not be applicable for some reflectometry geometry.

Distorted mirror model

A more simplified model is the distorted mirror model (Ref. [54]). The reflectometry process is modelled as a simple reflection from a distorted mirror. All plasma effects and fluctuations in the wavepath are approximated by the distortion of the mirror. The model has been used to study beam size effect (Ref. [55]), transmitter/receiver asymmetry (Ref. [56]), and correlation length measurements (Ref. [57]). Concerning the beam size effect, the model implies that the reflectometer can provide undistorted fluctuations measurements with $k_\perp w < \pi/5$, and will have virtually no response to fluctuations with $k_\perp w > \pi/2$, where w is the beam half width. The receiver and

transmitter asymmetry may also produce asymmetry in the power spectrum and induce phase runaway (Ref. [56]). Results based on this model are mostly qualitative because of its over-simplified assumptions.

L-C network model

The L-C network model is based on the equivalent view that the plasma behaves like an L-C network as far as microwave propagation is concerned. A 2-D simulation code based on such an equivalence has been developed (Ref. [58]). This code is able to deal with quite realistic geometry and experimental plasma profiles. It has been used to simulate reflectometry in the W7-AS stellerator, and to study the cause of phase runaway phenomenon.

2-D full-wave reflectometry simulation

J. H. Irby *et al* developed a 2-D full-wave simulation code, and studied the 2-D effects in reflectometry applications (Ref. [5]). The code solves Maxwell's equations with the assumption of cold plasma. A radiative boundary is used to match the computation domain and the vacuum. Simulation results based on this code first showed that including 2-D effects to interpret the reflectometry signal is very important. Part of my thesis work involved developing an upgraded version of this simulation code and using the new code to study reflectometry fluctuations. A detailed description of the upgraded code is presented in Chapter 6.

3.4 Optical distance fluctuations

An AM reflectometer can continuously measure the fluctuations of group delay. These fluctuations can be viewed as the fluctuations of optical distance, where optical distance is defined as the distance to a mirror that would produce the same phase shift as that of the plasma. The optical distance is proportional to the group delay $d\phi/df$. The following is a simple treatment of optical distance fluctuations versus density fluctuations using a 1-D model.

For O-mode reflectometry, the optical distance can be estimated from the 1-D geometric optics approximation

$$d_0 = \frac{c}{2\pi}\frac{d\phi}{df} = \int_0^{x_c} \frac{dx}{\sqrt{1-\frac{n_0(x)}{n_c}}} - \frac{\lambda_0}{4}, \tag{3.41}$$

where n_c is the critical density, $n_0(x)$ is the density profile, and λ_0 is the vacuum wavelength.

We study the reflectometry response by adding a density perturbation

$$\tilde{n}(x) = \begin{cases} \delta n & x_0 - \Delta x < x < x_0 \\ 0 & \text{otherwise} \end{cases}, \tag{3.42}$$

where: $x_0 - 1/2\Delta x$ is the location of the center of this perturbation, $\Delta x \ll x_c$ is the width of the perturbation, and $\delta n \ll n_c$ is the average perturbation level in the region. Writing the optical distance after the perturbation as $d = d_0 + \tilde{d}$, we have

$$\tilde{d} \simeq \begin{cases} \frac{\sqrt{2}L_n^{3/2}}{2\Delta x^{1/2}}\frac{\delta n}{n_c} & x_0 \sim x_c \\ \frac{\Delta x}{2[1-n(x_0)/n_c]^{-3/2}}\frac{\delta n}{n_c} & \text{otherwise} \end{cases}, \tag{3.43}$$

where $L_n = |d\ln n/dx|^{-1}$ is the density scale length at the critical layer.

Eq. 3.43 shows that the optical distance fluctuations are much more sensitive to fluctuations near the critical layer provided that $L_n \gg \Delta x$, that is, the fluctuation is localized. If we assume that $\tilde{d}$ is mostly due to fluctuations within $0.9n_c < n < n_c$ or equivalently $x_c - 0.1L_n < x < x_c$, we have

$$\tilde{d} \simeq 2.3\alpha_{2d}L_n\frac{\tilde{n}}{n_c}, \tag{3.44}$$

where $\tilde{n}$ should be understood as the average density fluctuation level in the region $x_c - 0.1L_n < x < x_c$. All 2-D effects are included in the factor α_{2d}. In Chapter 5, we use the optical distance fluctuations to study the location, radial shape, and level of the quasi-coherent fluctuations in EDA H-modes.

3.5 Radial correlation length of turbulences

Reflectometry has been used to measure the radial correlation length of plasma micro-turbulence (for example, see Refs. [53][59]). In this application, multiple frequency microwaves are launched to the plasma, and the correlation of the reflected signals are measured. We infer the radial correlation length of turbulence, $L_{r,n}$, from the signal correlation. With the knowledge of $L_{r,n}$, we can estimate the transport coefficient based on a mixing length approximation $D \sim L_{r,n}^2/t_e$, where $t_e \sim 1/\omega^*$ is the typical turbulence correlation time. Many simplified 1-D and 2-D models have been developed to interpret the correlation measured by reflectometry.

The early study in Ref. [47] concluded that correlation reflectometry can only measure correlation length less than $4\lambda_0$ due to small-wavelength turbulence effects. Another study in Ref. [60] showed that correlation reflectometry must use quadrature information. If the wave attenuation is not strong, then the measured correlation is at the critical surface. Otherwise, it is from the layer where the fluctuation wavelength is half of the local microwave wavelength. The localization is never less than the vacuum wavelength. The phase correlation is high, regardless of the correlation length of the fluctuations, unless either the wave attenuation is large or else the fluctuation correlation function is non-monotonic, corresponding to narrow-band turbulence. A 2-D analysis on the issue of the radial correlation study has also been carried out (Ref. [61]). Preliminary results show that the length of the wavepath is important for a localized measurement due to small angle scattering. The shorter the path length, the better the signal coherence function matches that of density turbulence.

In numerical studies, both RPSM and the distorted mirror model have been used to study the correlation length. In Ref. [53], RPSM was used to interpret TFTR results. That study concluded that the correlation of reflectometry signal $\gamma_E \simeq \gamma_n$ provided that the fluctuation level is small, $\sigma_\phi \ll 1$, where γ_n is the density correlation function, and σ_ϕ is the equivalent rms level of the fluctuations at the phase screen. When the density fluctuation level is high, $\sigma_\phi^2 > 2.5$, the measured correlation length is about a factor of $1/\sigma_\phi$ smaller than the density correlation length.

In Ref. [57], the distorted mirror model was used to study the response of a radial correlation reflectometer to turbulent plasma fluctuations. The radial correlation lengths computed from phase fluctuations, $L_{r(\phi)}$, and from power fluctuations, $L_{r(P)}$, show variations with the poloidal k-spectra width, the surface fluctuation amplitudes (weak and strong turbulence), and the microwave beam width. $L_{r(P)}$ is always smaller than the true correlation length $L_{r(true)}$ (computed from the layer fluctuations), by a factor up to 2, depending only on the fluctuation amplitude. $L_{r(\phi)}$, however, is much larger than $L_{r(true)}$ for weak fluctuations, and drops with increasing fluctuation amplitude to less than $L_{r(true)}$. $L_{r(\phi)}$ also varies with the beam width and poloidal k-spectra, while $L_{r(P)}$ does not.

The analytic and numerical studies above show that the interpretation of the radial correlation measured by reflectometry is very complicated. There might be a short-cut to solve this issue. In Refs. [62] and [63], experiments were performed to compare signal correlations of reflectometry to density correlations measured by Langmuir probes. A comparison between reflectometry signal amplitude, signal phase, and homodyne signal showed that the homodyne signal correlation gives the best fit to the density correlation measured by the probe (Ref. [63]). It also indicated that the reflectometry measurement is also very localized at the critical surface. However, the applicability of these results to other experiments is doubtful. For example, an arbitrary linear offset of in the phase of the reflectometry signal, which can be introduced by changing the location of the antenna(s), might nonlinearly affect the homodyne signals as well as the correlation.

Chapter 4

Reflectometer system in Alcator C-Mod

4.1 Overview

The reflectometer in the Alcator C-Mod tokamak is an amplitude modulated (AM) reflectometer working in O-mode [4] [22]. It consists of five channels with center frequencies at 50, 60, 75, 88, and 110 GHz. The corresponding critical electron densities are in the range of 0.31×10^{20} m$^{-3} \leq n_e \leq 1.50 \times 10^{20}$ m^{-3}. Schematic views of the reflectometer are shown in Fig. 4-1 and Fig. 4-2. The reflectometer uses a two antenna scheme — waves are launched by transmitting horn antennas (XMTRs) and received by separate receiving horn antennas (RCVRs). Compared to single-antenna systems, this two-antenna arrangement reduces multiple reflections and spurious wave coupling between the launched and reflected waves. There are three XMTR/RCVR pairs. The 50 GHz and 60 GHz channels share an antenna pair as do the 75 GHz and 88 GHz channels. The 110 GHz channel has its own antenna pair. The intersections of the XMTRs and RCVRs are at the mid-plane of the tokamak vacuum vessel, which is approximately the mid-plane of a typical plasma. The XMTRs are aligned -5^0 relative to the mid-plane, while the RCVRs are aligned at $+5^0$. In order to meet the O-mode launching condition $\vec{E} \parallel \vec{B}$, where $\vec{E}$ is the mm-wave electric field, and $\vec{B}$ is the total magnetic field in the plasma, the horn antennas are also twisted to match a

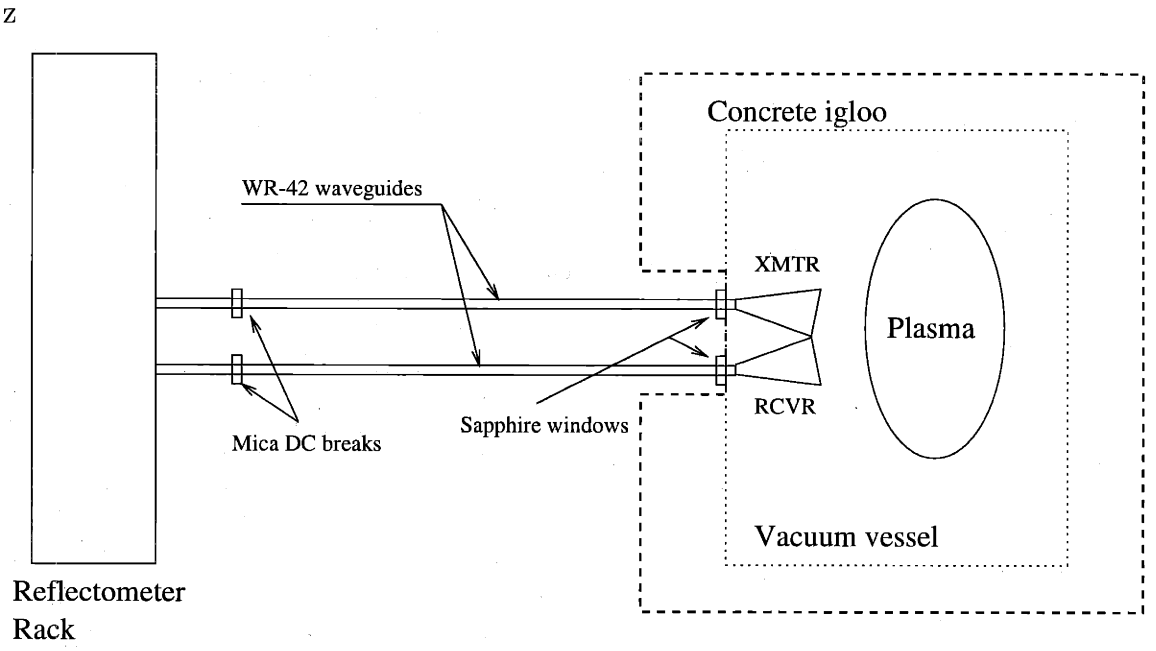

Figure 4-1: The reflectometer in Alcator C-Mod (side view, not in scale). The distance from the reflectometer rack to the horn antennas is about 3.3 m.

typical magnetic field pitch angle at the plasma edge. More details of the design of the reflectometer can be found in Ref. [4].

The millimeter waves are generated by Gunn diode oscillators, which are frequency stabilized through temperature control. We use WR-15 waveguides for the 50 and 60 GHz channels, WR-12 for the 75 and 88 GHz channels, and WR-10 for the 110 GHz channel. After coming out of the rack, these mm-waves are tapered into WR-42 over-moded waveguides and propagate towards the tokamak. Waves reach the XMTRs after passing sapphire vacuum windows. Mica DC breaks are inserted in the WR-42 waveguides to separate the reflectometer electrical ground and the machine ground. Connections between the CAMAC in the reflectometer rack and computers in the control room are through optical fibers. The electrical power for the reflectometry system is provided by an insulated transformer. As a result, the reflectometry system is electrically floating, which helps prevent damage to mm-wave components from potential electrical shocks during plasma discharges.

The reflectometer is able to measure plasma density profiles by measuring group delays in all five channels. All five channels are also able to measure fluctuations of

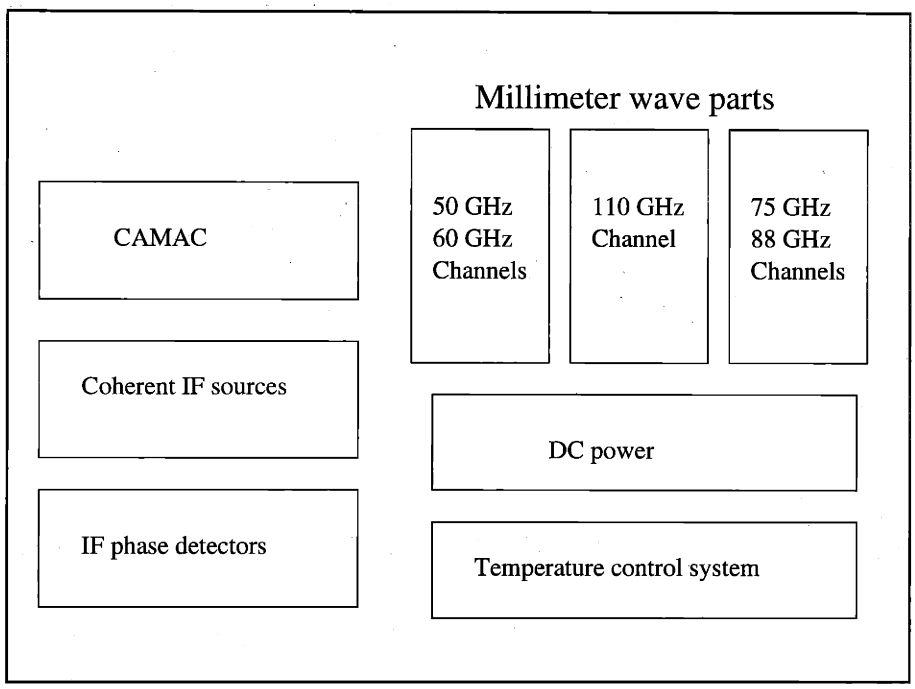

Figure 4-2: The reflectometer in Alcator C-Mod (front view).

group delay. The 88 GHz channel of the reflectometer also measures the baseband fluctuations.

Some experimental observations are presented in this Chapter. Further studies on these experimental phenomena can be found in following Chapters.

4.2 Electron density profile measurements

4.2.1 Millimeter wave and IF systems

An AM reflectometer continuously measures the group delay of millimeter waves to the critical surface on a time scale much faster than that of the dominant plasma turbulence. The modulation frequency can be chosen at the expense of phase resolution so that less than one fringe needs to be tracked during the time of interest (see Section 3.2.2).

The layout of the mm-wave part of each channel (except for the 88 GHz channel) is schematically shown in Fig. 4-3. The microwave source with a baseband frequency f_0,

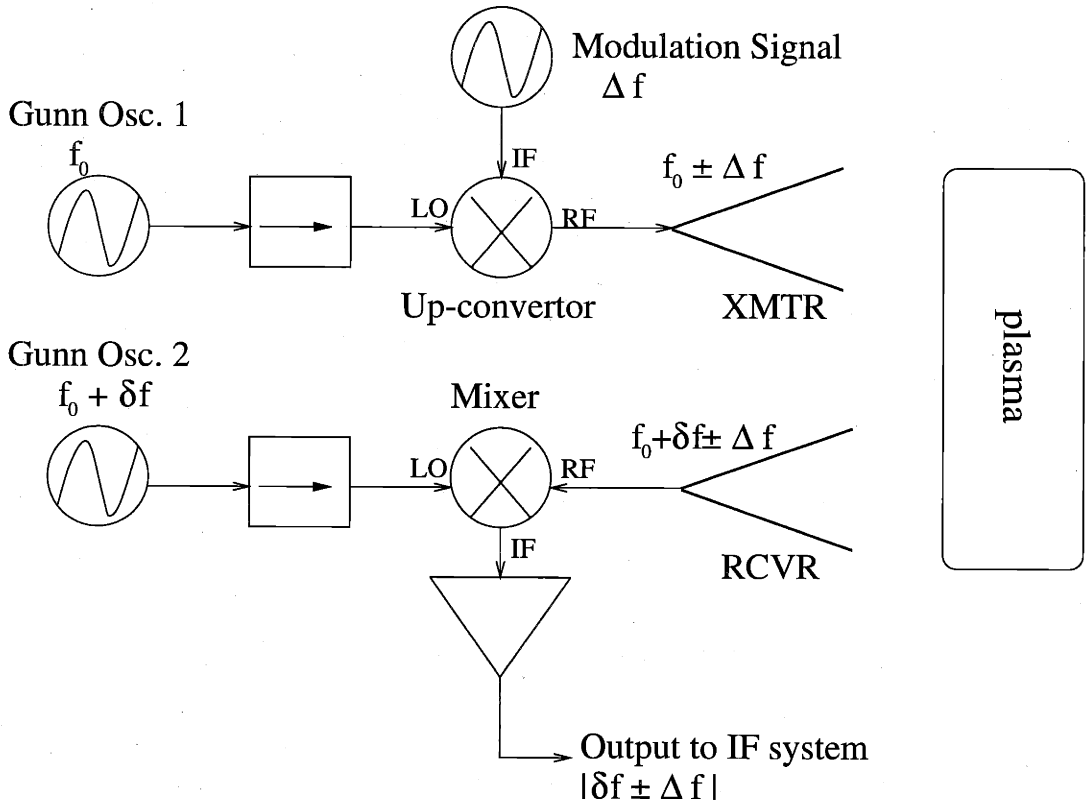

Figure 4-3: Layout of the mm-wave part of the reflectometry system measuring electron density profiles. The group delay is obtained by measuring the phase difference between the upper $(\delta f + \Delta f)$ and lower sidebands $(|\delta f - \Delta f|)$.

usually at about the 13 dbm level[1], is amplitude modulated by a modulation signal of frequency Δf before being launched into the plasma. Here, $f_0 = 50, 60, 75, 110$ GHz and the modulation frequency, Δf, can be manually chosen to be 132.5, 265, or 500 MHz. As a result of the AM process, the launched wave mostly consists of the two sideband signals, $f_0 \pm \Delta f$, while the base band signal, f_0, is suppressed. After being received by the receiving antenna, the reflected wave is mixed with a signal, $f_0 + \delta f$, from the other Gunn oscillator. We choose the frequency δf as a function of Δf as shown in Table 4.1. The frequency difference, δf, is chosen such that one of the output IF signal frequencies, $|\delta f + \Delta f|$ or $|\delta f - \Delta f|$, is in the optimum operation range $(510 - 560$ MHz) of the limiting amplifier in the IF detecting system, which is described below.

[1] 1 dbm = 1 mW and 13 dbm = 20 mW

Table 4.1: Choices of signal frequencies

Choice	1	2	3
Modulation frequency Δf (MHz)	132.5	235	500
Gunn frequency difference δf (MHz)	397.5	295	30
IF frequency f_{IF} (MHz)	235	500	970
Reference frequency f_{ref} (MHz)	30	30	30
Optical distance per fringe (cm)	56.6	28.3	15

The phase difference of the two IF signals, $\delta f \pm \Delta f$, is measured by the IF system shown in Fig. 4-4. The two sidebands are separated by band-pass filters. One band (S_1), $\delta f + \Delta f$, is mixed with an input coherent signal, f_{IF}, and two signals are generated, $\delta f + \Delta f + f_{IF}$ (S_3) and $|\delta f + \Delta f - f_{IF}|$ (S_4). The signal of f_{IF} is derived from the same quartz oscillator as the modulation signal Δf. The other sideband (S_2), $|\delta f - \Delta f|$, is amplified by a limiting amplifier, which has a 10 dbm constant output power. By mixing S_2 and S_4, we get signal S_5, which carries the differential phase of the two side bands at the frequency of $|2\Delta f - f_{IF}| = f_{REF}$. Signal S_5 is compared with another coherent signal with the same frequency $f_{REF} = 30$ MHz through an I/Q detector, which has phase accuracy better than $\pm 3^0$ at 30 MHz. The I/Q detector produces the sine and cosine of the phase difference $\Delta\phi$. The group delay, $\tau(f_0)$, for the millimeter wave of frequency f_0 can be estimated as: $\tau(f_0) \simeq \Delta\phi/2\Delta f$.

One shortcoming of this scheme is that we must have a fiducial point to eliminate the offset in $\Delta\phi$. In some AM reflectometers, this task is done by inserting a mirror in front of the antennas in two-antenna systems (Ref. [45]) or using a shutter in the case of single-antenna systems (Ref. [44]). For the Alcator C-Mod reflectometer, we use the group delay measured before the plasma discharge to get such a calibration by assuming that this signal is reflected at the inner vacuum wall. There is non-linearity between the group delay and the distance of reflection, which may be due to coupling of the reflected waves between the horns. Because of the long distance ($\geq$ 40 cm) from the inner wall to the critical surfaces during plasma discharges, this calibration is not ideal.

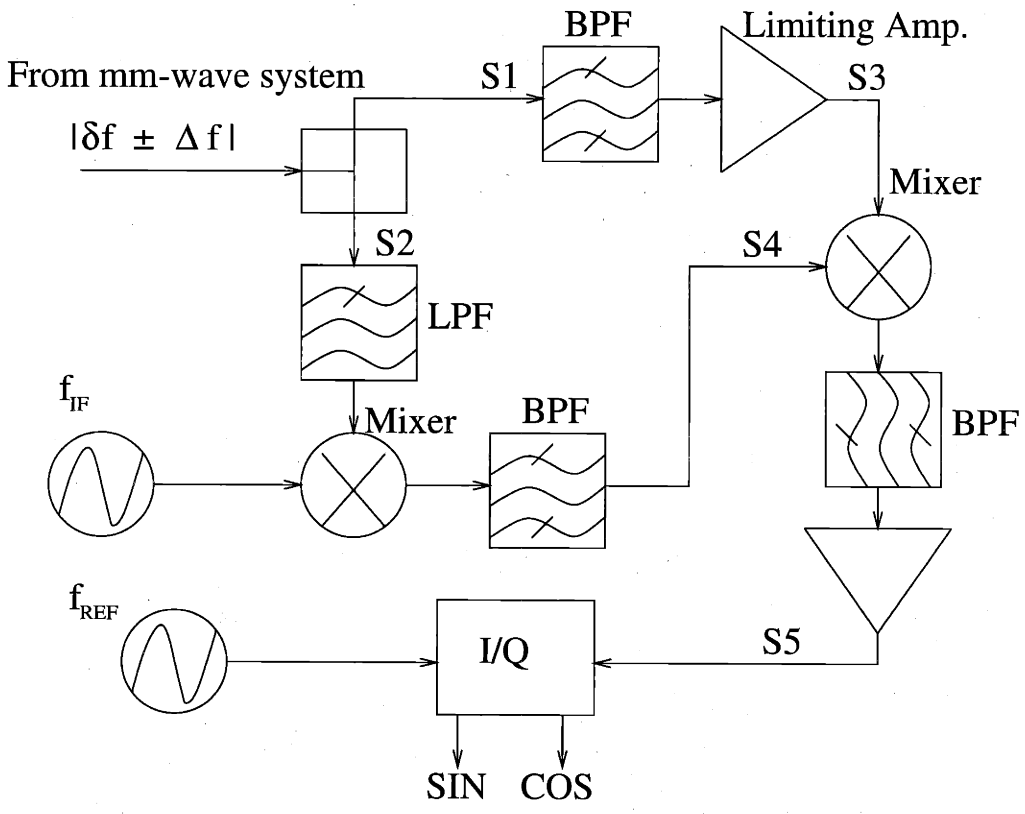

Figure 4-4: Layout of the IF part of the reflectometry system measuring electron density profiles. The phase difference of the two sidebands are measured by an I/Q phase detector.

4.2.2 Profile inversion

We calculate optical distances from measured group delays

$$R_{op} = R_{inner} + \frac{c}{4\pi}\left(\frac{\Delta\phi_{inner} - \Delta\phi}{2\Delta f}\right), \tag{4.1}$$

where R_{inner} is the major radius of the inner vacuum wall, $\Delta\phi_{inner}$ is the measured phase difference before the plasma discharge, and c is the speed of light in vacuum.

Using the optical distances of all five channels, the density profile can be reconstructed. We should determine beforehand the position R_{edge}, where plasma density is zero. Technically, R_{edge} does not significantly affect the density profile in the range higher than the lowest critical density ($n_c = 0.31 \times 10^{20}$ m^{-3} for the 50 GHz channel). The critical surface position of an O-mode wave with frequency f is given by:

$$R(f) = R_{edge} + \int_0^f \frac{R_{op}(f') - R_{edge}}{(f^2 - f'^2)^{1/2}}\, df', \tag{4.2}$$

which is equivalent to Eq. 3.22. For the reflectometer in Alcator C-Mod, the integral above is estimated by interpolating among the measured five optical distances. Using the relation between O-mode cutoff frequency and electron density

$$n_e(f) = \left(\frac{f[\text{GHz}]}{89.8}\right)^2 \times 10^{20}\ \text{m}^{-3}, \tag{4.3}$$

we can obtain the plasma density profile $n = n(R)$ using Eq. 4.1 and Eq. 4.2.

The optical distance, $R_{op}(f')$, at f' toward f is more weighted in determining the critical surface position $R(f)$ as shown in Eq. 4.2, but the contribution from $R_{op}(f')$ at $f' < f$ is not negligible. We write $R(f)$ in the following form

$$R_{edge} - R(f) \simeq \alpha \times [R_{edge} - R_{op}(f)], \tag{4.4}$$

where the factor α ($0 < \alpha < 1$) is determined by the shape of the density profile. For a density profile having an exponential shape, α is close to 1. In contrast, $\alpha = \pi/2 - 1 \simeq 0.6$ for a linear profile. Therefore, a change in the optical distance of

a single reflectometry channel does not indicate an equal amount of change in the position of its critical surface.

4.2.3 System optimization

Frequency stabilization of Gunn oscillators

The IF system (Fig. 4-4) uses narrow bandwidth filters and limiting amplifiers. This measuring scheme restricts the allowable frequency drift of the Gunn diode oscillators to be less than ± 5 MHz. The frequency of a Gunn oscillator depends on the bias voltage, varactor voltage, and temperature. Since all applied voltages are well controlled, frequency drift is mainly due to a change in ambient temperature. The drift can be as high as 10 MHz/^{0}C for Gunn oscillators in the frequency range of $50 \leq f \leq 110$ GHz, which will make the system unreliable even under small variations in room temperature. A method that controls the temperature and stabilizes the Gunn oscillators frequencies has been implemented as part of a collaboration with PPPL.

Fig. 4-5 shows the method used. A thermo-electric chip (TEC) is mounted onto an aluminum block, which is in thermal contact with the Gunn oscillator. The resistance of the thermistor in the aluminum block varies with temperature. The response of the thermistor is used to control the TEC, which can heat as well as cool the Gunn oscillator. The feed-back temperature control system controls the temperature of the Gunn oscillator to within $\pm 0.1^0$C, and stabilizes the frequency to within ± 2 MHz during a run day. This range is sufficient to keep all IF signals within allowable passbands.

Optimizing the modulation frequency

The modulation signal frequency, Δf, must be chosen carefully. It cannot be too large or fringe jumps would be difficult to follow, but it cannot be so small as to seriously limit reflectometer spatial resolution.

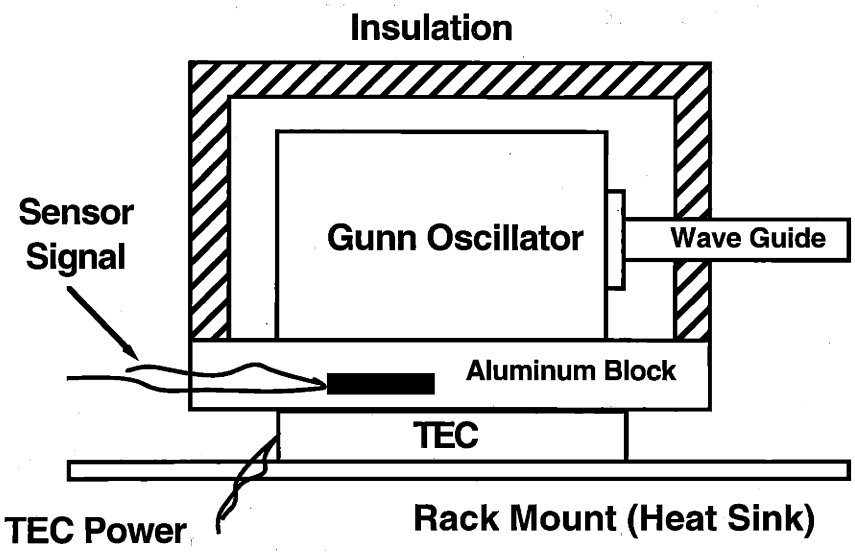

Figure 4-5: Temperature control of a Gunn diode oscillator. Depending on the feedback signal from the temperature sensor, the thermo-electric chip (TEC) heats or cools the aluminum block, which is in thermal-contact with the Gunn oscillator. The temperature is controlled, thus the frequency is stabilized.

The optical distance corresponding to one fringe jump (2π) is

$$\mathrm{OPD} = \frac{1}{4}\left(\frac{c}{\Delta f}\right). \tag{4.5}$$

Different modulation signals give different OPDs (see Table 4.1 in the previous Section). The modulation frequency $\Delta f = 132.5$ MHz was used in year 1998 and 1999 campaigns. At this frequency, OPD $\simeq 56.6$ cm, which is more than twice the plasma minor radius, $a \simeq 23$ cm. The reflectometry phase change in a plasma discharge was usually less than one fringe so that phase ambiguity was avoided. However, it turned out that other problems became serious. Using a smaller Δf, the sensitivity of phase measurement is also smaller. A $\pm 3^0$ uncertainty in $\Delta\phi$ leads to ± 0.5 cm uncertainty in optical distance. It was also found that magnetic fields, especially the field from equilibrium coil EF-4 (see Fig. 2-2), can cause phase shifts as large as 10^0, which is equivalent to ~ 1.5 cm shift in optical distance. This magnetic field effect may be due to the fact that some components are made of ferromagnetic material, which changes

characteristics with magnetic field[2].

In the year 2000 campaign, the modulation frequency was set to 500 MHz. At this frequency, the magnetic field effect on optical distance was reduced to approximately 0.5 cm. However, for $\Delta f = 500$ MHz, OPD = 15 cm, which is smaller than the plasma diameter. Fringe jumps now appear in the data. The fringe jumps in the low frequency channels can be eliminated by simply assuming that their critical surfaces are less than an OPD away from the plasma edge. However, we cannot always automatically eliminate phase ambiguity in the high frequency channels, 88 GHz and 110 GHz, without manual intervention.

4.2.4 Experimental density profiles

After considering most possible sources of error, such as calibration difficulty, profile inversion accuracy, mechanical vibration of waveguides, and magnetic field effects, the reflectometer density profiles have system uncertainty of about $0.5 - 1.0$ cm in $R(n)$. The reflectometer is good for measuring density profiles in L-mode periods (Fig. 4-6). The density profiles obtained by reflectometry do not have adequate spatial resolution to resolve the H-mode pedestal, which may have a scale length as small as 0.5 cm (Ref. [64]).

A radially movable calibration plate could alleviate the calibration problem, as suggested in Ref. [4]. Improvement on the waveguide structure can make the system less vulnerable to mechanical vibrations and coupling effects at the horns. After the recent installation of two high spatial resolution edge electron density profile diagnostics — edge Thomson scattering system (Ref. [65]) and visible continuum emissivity array (Ref. [66]), these upgrades have had a low priority. The reflectometer, therefore, is now mostly used to study fluctuations.

[2]The B field at the reflectometer rack is estimated in the range of $0.01 - 0.1$ T during discharges.

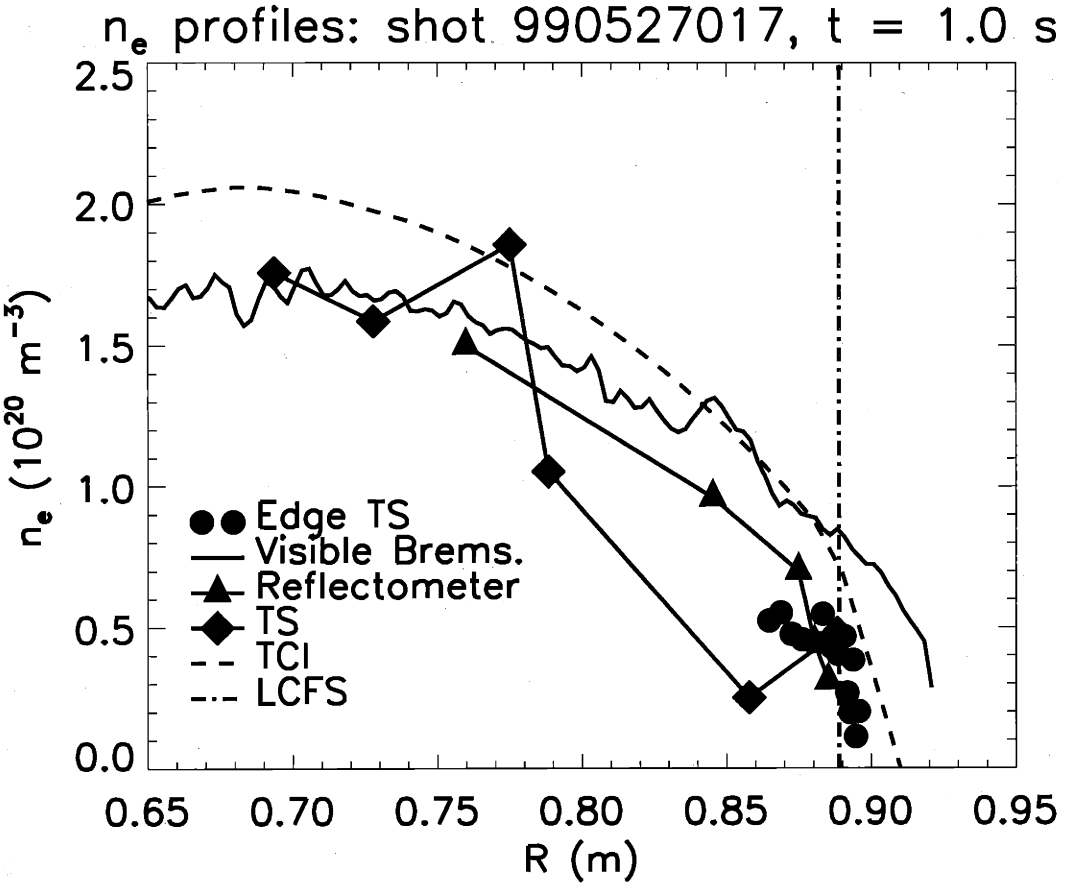

Figure 4-6: Electron density profiles in L-mode. The inverted reflectometry density profile, with five points corresponding to the positions of the critical surface for the five channels, is shown together with profiles derived from visible continuum emissivity array, two-color interferometer, and Thomson scattering systems.

4.3 Fluctuation measurement

AM reflectometry measures the phase difference, $\Delta\phi$, between the upper (USB) and lower (LSB) sidebands of the AM waves. This differential phase scheme is an advantage for density profile measurements, but it reduces fluctuation sensitivity compared to the baseband technique because correlated fluctuations found in the USB and LSB signals are subtracted. In order to better study density fluctuations, the USB and LSB signals should be separated and measured independently. In collaboration with PPPL, the 88 GHz channel has been upgraded to have such capability (Ref. [22]).

As shown in Fig. 4-7, in addition to the IF output with frequency $\delta f \pm \Delta f$, a signal with the frequency difference of the two Gunn oscillators, δf, is also produced. This signal is used to separate the USB and LSB signals in the IF system (Fig. 4-8). Instead of only measuring the phase difference, $\Delta\phi = \phi_{USB} - \phi_{LSB}$, the phases of the USB and LSB signals, ϕ_{USB} and ϕ_{LSB}, are measured independently. No limiting amplifier is used in the IF system, thus both amplitude and phase fluctuations of the reflected signals can be studied. The I/Q detectors produce the sine and cosine of the reflected signal: $A\cos\phi$ and $A\sin\phi$.

For a modulation frequency of $\Delta f = 132.5$ MHz, δf is chosen to be $\delta f \simeq 515$ MHz. For a modulation frequency of $\Delta f = 500$ MHZ, $\delta f \simeq 540$ MHz. The reference signal, f_{REF}, is 500 MHz for the fluctuation I/Q detectors. The two 500 MHz signals from the two sidebands are also down-converted to 30 MHz, and their phase difference is measured with a 30 MHz I/Q detector just as those used in all other channels.

In each plasma discharge, we take fluctuation data in a time window of 0.5 second with a sample rate of 1 MHz. The sampling window is controlled by a general fast window control program, which also controls other fluctuation diagnostics, including magnetic coils, ECE, and X-rays. The digitizers (Aurora 14) have 12-bit accuracy (4096 steps in the range of ± 2.5 V). A small portion of the 512 kilobytes memory of each digitizer channel is used to store system noise level before and after the plasma discharge.

The upgraded 88 GHz reflectometer channel has contributed significantly to the

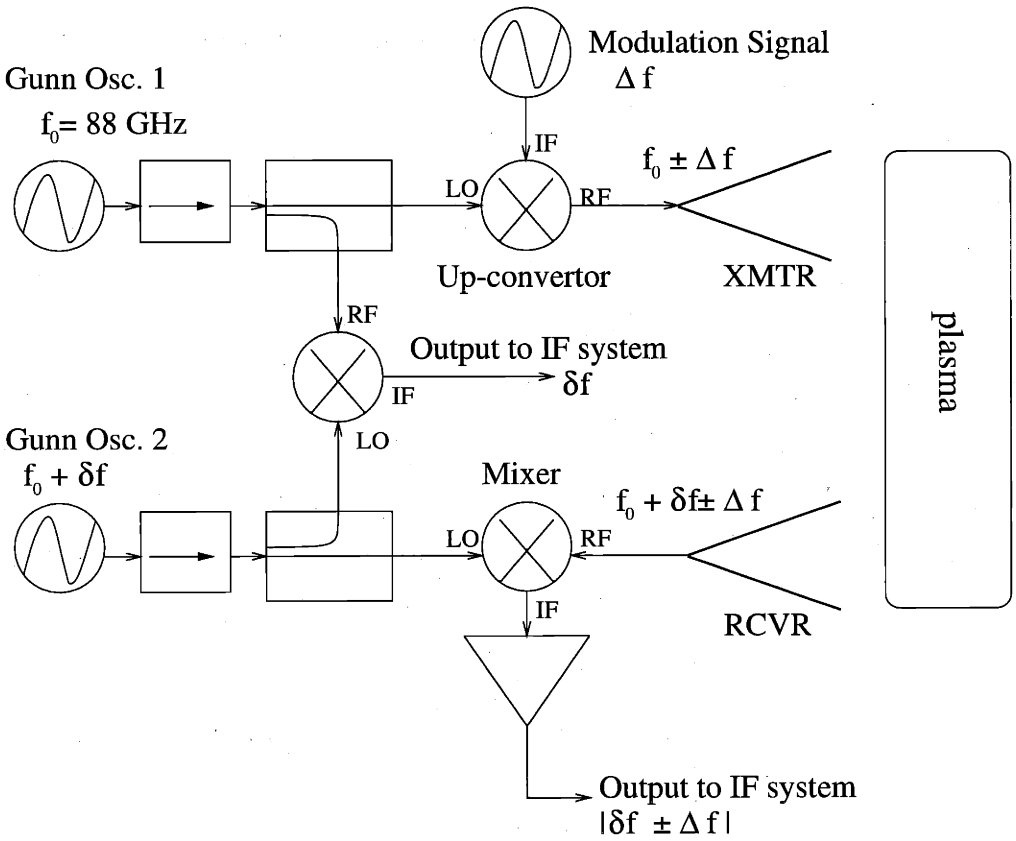

Figure 4-7: Layout of the mm-wave part of the upgraded 88 GHz channel. A signal δf derived by mixing signals from the two Gunn oscillators is used to separate the USB and LSB.

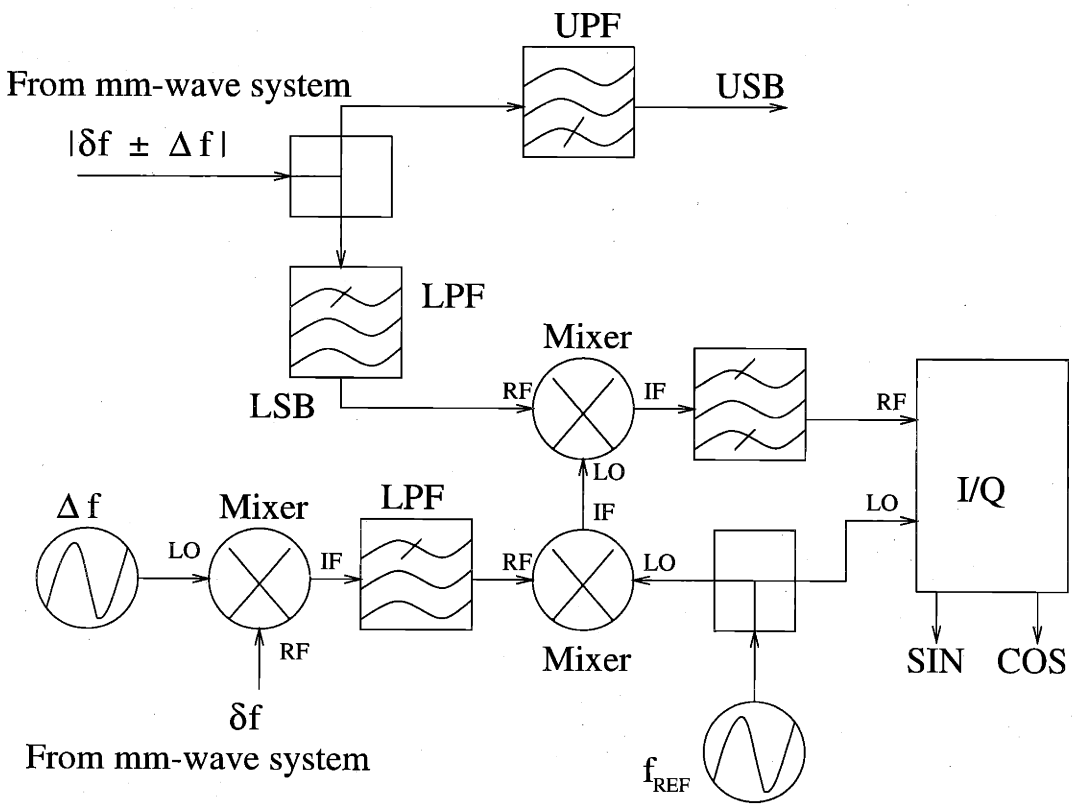

Figure 4-8: Layout of the IF part of the upgraded 88 GHz channel. The phases of the sidebands are measured independently. Only the LSB part is shown in the figure while the USB part is similar. $f_{REF} = 500$ MHz. (PPPL design)

study of H-modes and EDA H-modes. Because this channel is more sensitive to fluctuations than the other reflectometer channels, and its critical surface ($n_c = 0.96 \times 10^{20}$ m^{-3}) is usually in the H-mode pedestal region, this channel continuously monitors edge density fluctuations.

Other channels are also used to measure fluctuations. The fluctuations in these channels are group delay fluctuations, or equivalently, fluctuations of optical distance. Since the measured fluctuations are the phase difference fluctuations between two-closely spaced mm-wave frequencies, the sensitivity is expected to be smaller than that of the 88 GHz channel. However, these channels may give a better qualitative view of fluctuations in cases where the fluctuation level exceeds the linear response region of the 88 GHz channel.

4.4 Observed experimental fluctuations

This Section shows some examples of experimental observation of reflectometry signal fluctuations, such as the phase runaway phenomenon, fluctuation suppression in L-H transition, and the continuous quasi-coherent edge fluctuations associated with EDA H-modes.

4.4.1 Phase runaway phenomenon

In the 1-D approximation, as discussed in Chapter 3, the phase fluctuations, $\tilde{\phi}$, in the reflectometry signal are approximately equal to the geometric optical phase fluctuations, while the signal amplitudes are constant. In fact, the signal amplitudes do vary significantly. This variation contribute to a phenomenon called phase runaway.

During a phase runaway, the complex reflectometry signal, $A(t)\,[\cos\phi(t) + i\sin\phi(t)]$, is not oscillating around a static point in the complex plane. Instead, as shown in Fig. 4-9, the measured signal is "circling" around the origin point $(0, 0)$, and the signal phase no longer satisfies the 1-D geometric optics approximation.

Many studies have addressed the causes of the phase runaway phenomenon (for example, Refs. [56][58]). An insufficient sampling rate may cause phase runaway.

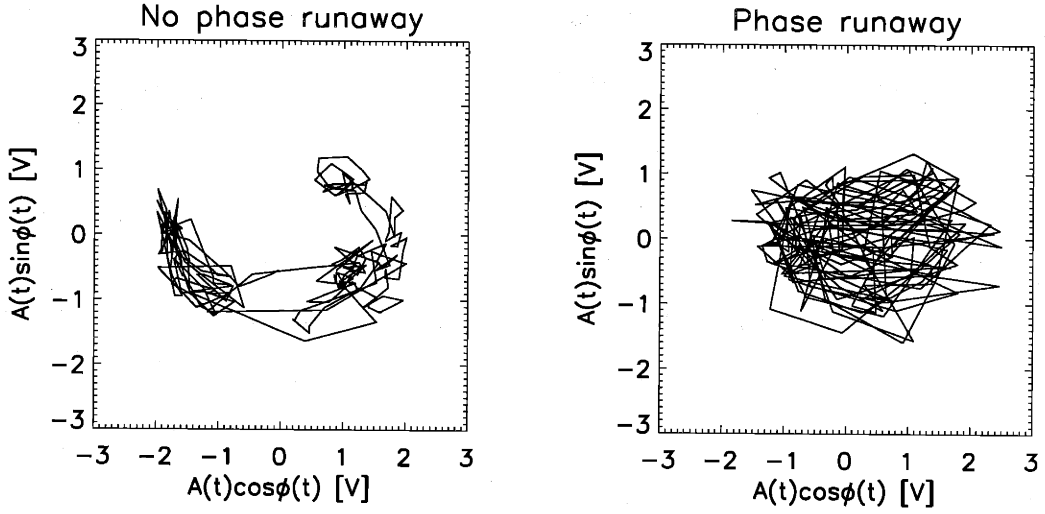

Figure 4-9: Phase runaway phenomenon in reflectometry signal fluctuations. Data are taken from the USB signal of the 88 GHz channel for shot 990921020. No phase runaway appears in the left figure, which plots data at $0.9 < t < 0.9002$ sec. The right figure plots data at $1.1 < t < 1.1002$ sec, and it shows significant phase runaway. There are 200 data points in both figures.

However, phase runaway may not be completely avoided by simply increasing the sampling rate (Ref. [67]). Phase runaway can also be caused by asymmetric responses in the reflectometry system to fluctuations of positive and negative $\vec{k}$ (Ref. [58]). Such asymmetry induces a net phase increase or decrease in time. Although the XMTR and RCVR antennas are symmetric relative to the mid-plane of the vacuum vessel for the Alcator C-Mod reflectometer, asymmetry can still arise due to a plasma shape variation. Large density fluctuation levels can also cause phase runaway.

Phase runaway makes it difficult in how to unambiguously retrieve plasma information. There are several ways to alleviate this problem (for example, Ref. [68]). Any such methods, however, need to assume some fluctuation characteristics based on other experimental measurements or theoretical predictions. One may simply assume that the phase change between any two adjacent data points is smaller than π, and eliminate phase uncertainties. This assumption only works part of the time for the Alcator C-Mod reflectometer. In some cases as shown in Ref. [69], the homodyne signal, $A\cos\phi$, may be a better representation of plasma fluctuations than either sig-

nal amplitude, A, or phase, ϕ. Though it does avoid the difficulty in dealing with phase runaway, this treatment is only qualitative.

4.4.2 Fluctuations in L-mode and H-mode

The time evolution of spectra for typical reflectometry fluctuations during a L-H transition is shown in Fig. 4-10. In L-mode, the fluctuations are very broadband. After the sudden L-H transition, the spectrum shape changes (Fig. 4-11). The low frequency part of the fluctuations in H-mode is more suppressed compared to the fluctuations in L-mode.

Care must be taken in the interpretation of the change in the fluctuation level, however. The plasma density profile also changes significantly after the L-H transition. In L-mode, the profile is usually parabolic. After the transition, a pedestal shape is formed. As a result, the critical surface has moved farther out than that before the L-H transition. Nonetheless, the difference in spectrum shapes of L-mode and H-mode does indicate that the plasma fluctuations in L-mode and H-mode may be dominated by different types of turbulence. Studies on some other fusion devices using reflectometry and other diagnostics suggested that the turbulence spectra in L and H modes satisfy different power laws of correlation, which may be related to the self-organized criticality phenomenon (Refs. [70] and [71]).

4.4.3 Quasi-coherent (QC) edge fluctuations in EDA H-modes

During EDA H-modes, we see continuous quasi-coherent (QC) fluctuations in the reflectometry fluctuation signals (Fig. 4-12) (Ref. [22]).

Fig. 4-12 shows time histories of a discharge with three H-mode periods. The second and the third H-modes are EDA H-modes as can be seen by the enhancement of the D_α signal level after the sudden drop at the L-H transition. QC fluctuations appear in the spectra of reflectometry fluctuations. In this discharge, the lab-frame frequency of these fluctuations starts at about 250 kHz, and ramps down to about 100 kHz during the steady EDA H-mode periods.

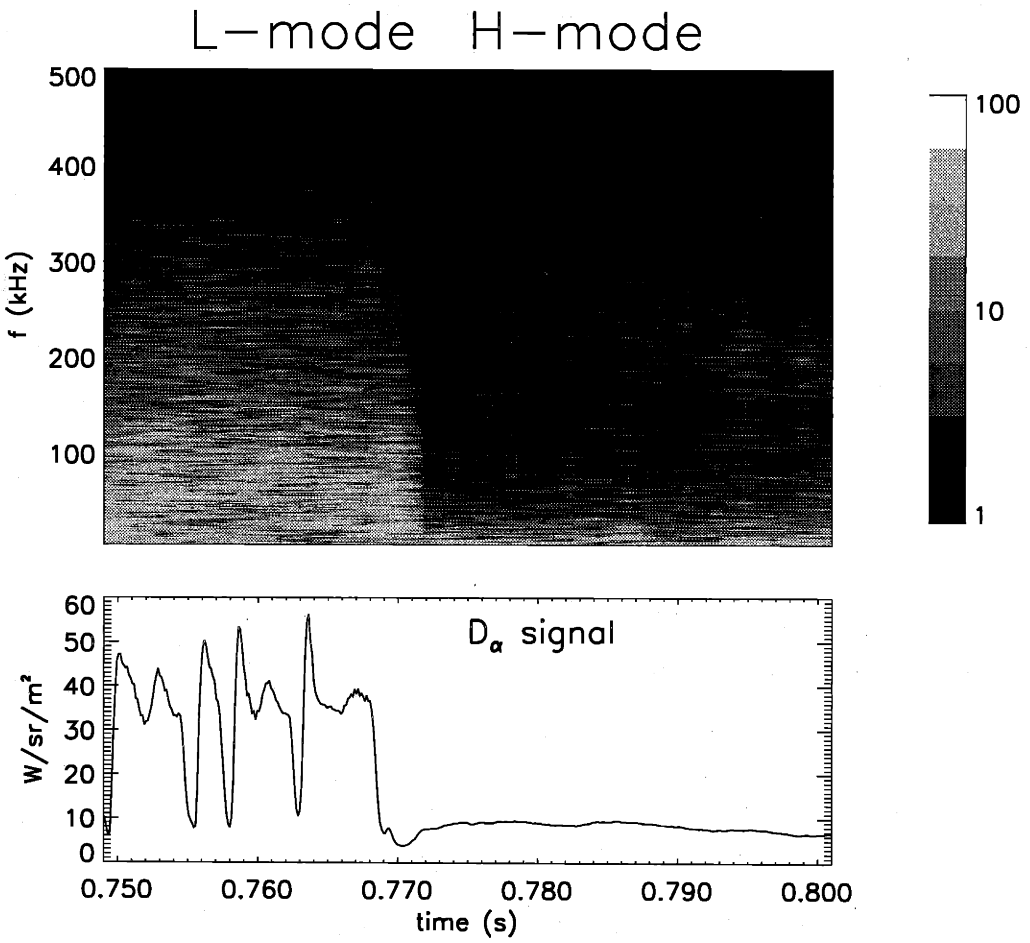

Figure 4-10: Contours of reflectometer fluçtuations at an L-H transition. Data are from shot 990921020. The spectra are calculated from the complex signal, $A(t)[\cos\phi(t) + i\sin\phi(t)]$. The color bar shows the relative value.

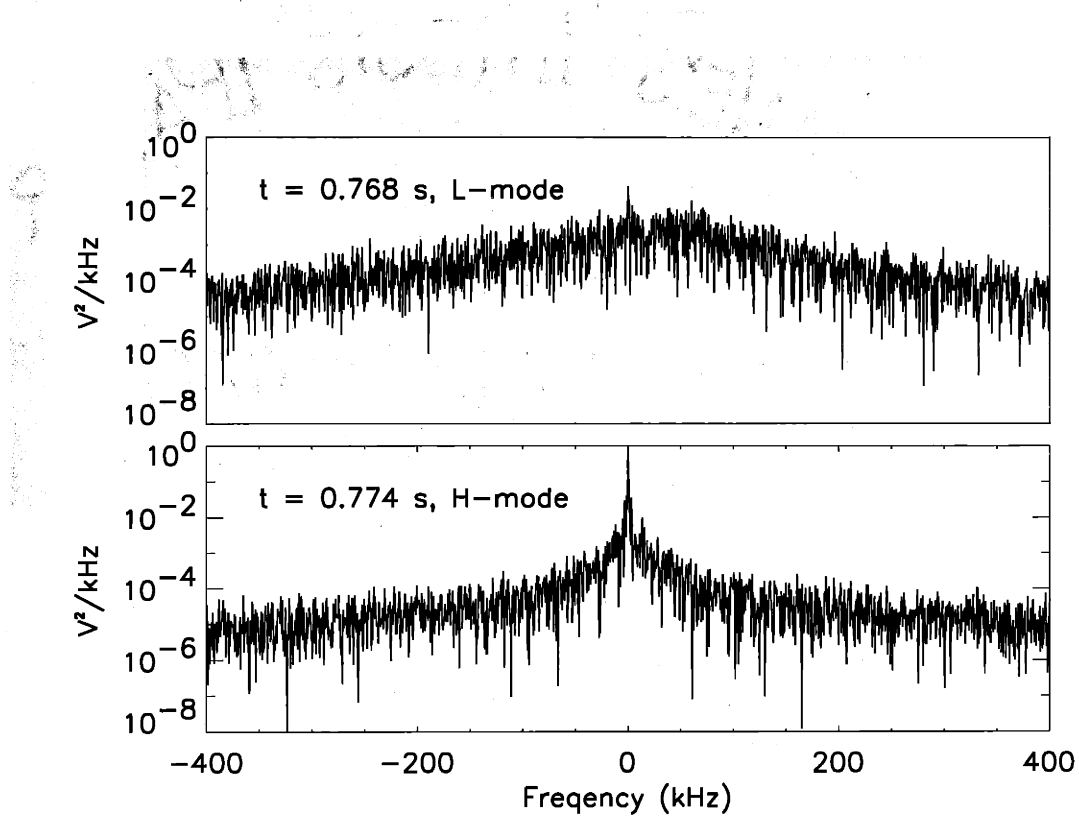

Figure 4-11: Fluctuation spectra in L-mode and H-mode. The same shot as in Fig. 4-10. It shows that the low frequency part of the fluctuations in H-mode are suppressed relative to the fluctuations in L-mode. The system noise level before plasma discharge is $\sim 10^{-7}\mathrm{V}^2/\mathrm{kHz}$.

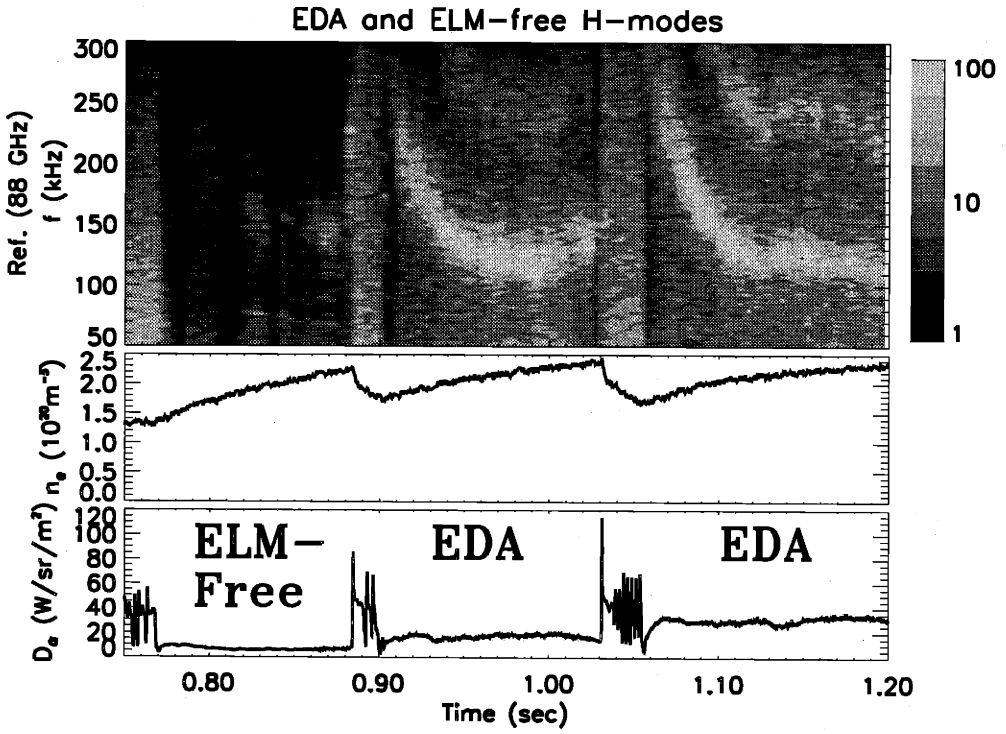

Figure 4-12: Quasi-coherent fluctuations during an EDA H-mode. Quasi-coherent fluctuations appear in the two EDA H-mode periods while they do not appear in the ELM-free H-mode. The discharge is the same as that in Fig. 4-10.

These QC fluctuations are also observed by the PCI system (Ref. [23]), Langmuir probes (Ref. [24]), and a magnetic coil installed on a fast-scanning probe head (Ref. [25]). It has been shown that these fluctuations affect the characteristics of particle transport in EDA H-modes. They are considered to be the *signature* of EDA H-modes (see Refs. [21][72][73]). A detailed description of these fluctuations as seen by the reflectometer are discussed in Chapter 5. Numerical studies of the reflectometry measurement of these fluctuations are presented in Chapter 7.

Chapter 5

Study of EDA H-modes

In this Chapter, we study the quasi-coherent continuous edge fluctuations in EDA H-modes using the Alcator C-Mod reflectometer. General observations of these fluctuations are given in Section 5.1. In Section 5.2, two theoretical models, the resistive ballooning mode and the drift-ballooning mode, are reviewed. In Sections 5.3 and 5.4, we analyse these fluctuations based on reflectometry measurements and compare these results with theoretical models.

5.1 General observations

As shown in Fig. 4-12 of Chapter 4, continuous quasi-coherent (QC) fluctuations are the signature of EDA H-modes (Ref. [21]). These fluctuations have been shown to drive particle transport near the plasma edge (Ref. [73]). To understand these QC fluctuations has become the key to understand the EDA H-mode. Several diagnostics have observed these fluctuations. Reflectometry provides localized measurement of fluctuation levels in both ICRF heated and ohmic EDA H-mode discharges. The PCI system gives the k and ω spectra of line-integrated density fluctuations. PCI does not provide spatially localized information about these fluctuations. Langmuir probes can have localized measurements only in ohmic discharges, but not in ICRF heated discharges due to the potentially destructive RF pickup and heat load. Results from the PCI and probe are briefly discussed below.

PCI studies have shown that the poloidal wavenumber of the QC fluctuations is affected by electron temperature at the pedestal, $k_\theta \rho_s = 0.1 - 0.3$, where $\rho_s = m_i T_e^{1/2}/eB$ and T_e is obtained at the middle of pedestal (Ref. [74]). The fluctuation level is found to be affected by temperature and pedestal width, $\tilde{n}_e/n_e \propto \rho_s/\Delta_n$, where Δ_n is the density pedestal width. The coherence of the fluctuations is in the range of $\Delta f/f = 0.05 - 0.2$.

Studies of ohmic EDA H-modes, using biased Langmuir probes, which measure both density fluctuations $\tilde{n}_e$ and plasma potential fluctuations $\tilde{\phi}_p$, have shown that the QC fluctuations drive significant particle flux $\Gamma_n \leq 10^{22}$ m^{-2}s (Ref. [73]). Though this estimate is preliminary, and certain assumptions are made about spatial distribution of the fluctuations, it suggests that these fluctuations could account for the difference of particle transport between ELM-free and EDA H-modes. Probe measurements also indicate that these fluctuations may be localized in the pedestal region with radial widths as narrow as $1 - 2$ mm. However, perturbation of the plasma by the intrusive probe cannot be discounted with certainty.

Studies based on the measurement by a magnetic coil installed on a fast-scanning Langmuir probe in several ohmic EDA H-mode discharges showed that QC fluctuations have a significant magnetic component with $dB/dt \sim 200$ T/s, which corresponds to $\tilde{B} \sim 5 \times 10^{-4}$ T (Ref. [25]). This result was obtained by an extrapolation of the radial distribution of the magnetic fluctuation level well outside the separatrix with a radial scale length of approximately 1.5 cm. The magnetic probe was located at about 2 cm from the pedestal region. The study also indicated a density fluctuation level $\tilde{n}_e/n_e \simeq 30\%$ and particle driven flux $\Gamma_n \sim 4 \times 10^{22}$ m^{-2}.

Studies on the boundary of EDA and ELM-free H-modes showed a favored parameter regime at higher $q_{95} \geq 3.5$, higher triangularity, higher plasma density, and lower plasma ion mass (Refs. [21][24][72][73]). The physical origin of these fluctuations is still under study through a collaboration of experiment, theory development, and numerical simulation based on gyro-kinetic equations.

5.2 Theoretical models

We shall review here the available theoretical models. Since these fluctuations are in a high k regime, the probable candidates are those involving micro-instabilities rather than large scale MHD instabilities. In this Section, we briefly discuss two theories — resistive ballooning modes and drift ballooning modes — and compare them with the experimental observation.

5.2.1 Resistive ballooning mode

Ballooning instability arises at high plasma pressure. This instability is closely related to the plasma toroidicity and develops by the displacements of plasma flux tubes. The ballooning instability only appears at the outer contour of the plasma. This instability sets a limit on the highest β that a tokamak can achieve. However, even if the ideal ballooning instability is prevented, resistive ballooning modes (RBM) can also exist at the edge of the tokamak plasmas (Refs. [75][76][77]). The linear resistive ballooning mode growth rate, γ, is given by ($\gamma \ll \omega_*$):

$$\gamma = \frac{\gamma_0^3}{\omega_*^2}, \tag{5.1}$$

where

$$\gamma_0^3 = \frac{\alpha^2}{2}\frac{n^2 q^2}{\tau_\eta \tau_A^2}, \tag{5.2}$$

$\alpha = -2Rq^2(dp/dr)/B^2$ is the ballooning parameter, n is the mode toroidal number, $\tau_A = Rq\sqrt{1+2q^2}/sC_A$ is the Alfven time, C_A is the Alfven speed, $s = (r/q)(dq/dr)$ is the shear parameter, and $\tau_\eta = \mu_0 r^2/\eta$ is the resistive diffusion time with η the plasma resistivity. The diamagnetic frequency is $\omega_* = (nq/r)(\rho_i V_{Ti}/L_n)$, with ρ_i the ion Larmor radius, $V_{Ti} = \sqrt{T_i/m_i}$ the ion thermal speed and L_n the characteristic density gradient scale length. The radial width of a single mode resistive ballooning fluctuation is determined by the resistive layer thickness (Ref. [78])

$$W = \left(\frac{\eta}{4S}\frac{\gamma q^2}{n^2 q'^2}\right)^{1/4}, \tag{5.3}$$

under the condition of $r/m > W$, where $S = \tau/\tau_{hp}$ is the Lundquist number, τ_{hp} is the poloidal Alfven time, $\tau_{hp} = R_0(\mu_0 m_i n_i)^{1/2})/B_0$, and m is the poloidal mode number.

A collisional resistive ballooning mode exists only when

$$\gamma > \frac{C_s}{Rq} = \omega_s, \tag{5.4}$$

where C_s is the sound speed, $C_s^2 = \Gamma p/n_i m_i$, and Γ is the adiabatic index. Preliminary studies by Dr. D. Mossessian (Ref. [79]) have shown that this condition may be satisfied in the pedestal region of EDA H-modes. In contrast, in ELM-free H-modes, this condition can be satisfied only at the pedestal foot.

The growth rate of the resistive ballooning mode is sensitive to the parameter $\nu^* q^2$ (Ref. [80]). The criterion in Eq. 5.4 is approximately equal to a threshold on $\nu^* q^2$, where

$$\nu^* = \nu_{ei}\epsilon^{-3/2} qR/V_{Te} \tag{5.5}$$

is the dimensionless collision frequency, and $V_{Te} = (T_e/m_e)^{1/2}$ is the electron thermal speed, $\epsilon = r/R$ is the inverse aspect ratio, and ν_{ei} is the electron-ion collision rate. It shows that a higher density, lower pedestal temperature, and higher q are favored for the RBM mode. These conditions coincide with some of the requirements for EDA H-modes presented in Section 2.2.4.

Nonlinear simulations including toroidal geometry have also been carried out for the resistive ballooning mode (Refs. [78][81]). It is found that the mixing length approximation is valid in estimating the saturated mode level. The mixing length approximation attempts to relate the properties of fully evolved turbulence to the characteristic scales of the underlying linear instability by semi-quantitatively balancing nonlinearity with the linear drive (Ref. [82]). In this approach, we assume resistive ballooning modes saturate when the pressure fluctuation mixes the pressure gradient over the radial extent of each poloidal sub-harmonic (Ref. [76]). As a result, we have the saturated mode level, $\langle \tilde{p}^2 \rangle^{1/2}/p \sim \Delta_p/L_p$, where $\tilde{p}$ is the pressure fluctuation, Δ_p is the radial correlation length, and L_p is the scale length of the pressure

gradient. We can also estimate the diffusivity using the mixing length approximation, $D \sim \Delta_p^2/\tau_c$, where τ_c is the decorrelation time of the fluctuations.

5.2.2 Drift ballooning mode

In Ref. [83], the L-mode to H-mode boundary in Alcator C-Mod has been shown to agree well with the results from a 3-D simulation code based on the Braginskii equations developed by B. Rogers and J. Drake. In Ref. [84], the 3-D simulations were used to study the stability of tokamak plasma edge pedestal. It was found that the stability criterion for the ballooning instability at the pedestal is less stringent than ideal MHD theory predicted because of the ion diamagnetic drift and the finite radial localization of the pedestal pressure. A stability limit is given as $\beta < \beta_c$, where $\beta_c = (\alpha_c/3q^2)\,(\delta_R/R)$, $\delta_R \simeq \rho_i^{2/3} R^{1/3}$, and α_c is ideal MHD ballooning mode threshold. Under marginal conditions, this mode has a poloidal wavenumber of $k_\theta \simeq \delta_R^{-1}$, a radial envelope $\sim \delta_R (> \delta)$, and real frequency $\omega \sim C_s/\sqrt{\delta_R R}$, where δ is the pedestal half-width, and R is the major radius. The model also predicted a $m^{1/2}/q$ dependence of the criterion of the mode instability (Ref. [73]). The simulation generated a similar quasi-coherent feature of fluctuations near the marginal stability condition.

Using estimated parameters at the pedestal center, $T_i \simeq 200$ eV, $B \simeq 4$ T, and $R \simeq 0.9$ m, we have $\delta_R \simeq 0.13$ cm. However, we should be cautious since the criterion, $\delta_R > \delta$, where δ is the pedestal half-width, is not satisfied by typical Alcator C-Mod parameters.

5.3 QC fluctuations: location, radial width, and level

For most examples of EDA H-modes we have studied ($P_{RF} \leq 4$ MW and $I_p \leq 1.2$ MA), the quasi-coherent fluctuations are observed by the 75 GHz, 88 GHz and 110 GHz reflectometry channels ($0.69 \times 10^{20} \leq n_e \leq 1.5 \times 10^{20}$ m^{-3}). In some EDA discharges with relatively low density, these fluctuations are also clearly seen by the

60 GHz channel ($n_c = 0.45 \times 10^{20}$ m^{-3}) as shown in Fig. 5-1. In contrast, for some EDA discharges at high density, the fluctuations are not observed on any of the reflectometry channels, while they still clearly show up in PCI signals (Fig. 5-2). A probable explanation is that the fluctuations are localized inside the critical surfaces of all the reflectometry channels for these discharges. For discharges like that shown in Fig. 5-1, where at least three reflectometry channels clearly see the QC fluctuations, we are able to estimate the radial location, width, and level for the mode.

5.3.1 Fluctuations of optical distance

We use the fluctuation's optical distance, $\tilde{d}$, to estimate the density fluctuation level $\tilde{n}$ of the QC fluctuations. Optical distance is defined as the distance to the location of a mirror that has the same effect on the signal as that of the plasma. Optical distance fluctuations are derived from the fluctuations of the measured phase difference $\Delta\phi$ of the USB and LSB $\Delta\tilde{\phi}$:

$$\tilde{d} = \frac{c}{4\pi}\left(\frac{\Delta\tilde{\phi}}{2\Delta f}\right), \tag{5.6}$$

where Δf is the modulation frequency for the AM system. Optical distances are measured in four of the five reflectometry channels[1].

Fig. 5-3 shows plasma parameters of the discharge in Fig. 5-1. At $1.15 \leq t \leq 1.3$ sec, the plasma is in an EDA H-mode while at $1.04 \leq t \leq 1.13$ sec, the plasma is in an ELM-free H-mode. Fig. 5-4 shows the raw fluctuation data of optical distances from the reflectometry channels at 60 GHz, 75 GHz, 88 GHz and 110 GHz, at 1.2 sec into the discharge. Clear quasi-coherent oscillations ($\simeq$ 100 kHz) are apparent in all four signals. Fig. 5-5 shows the auto-power spectra of the fluctuations of optical distance shown in Fig. 5-4. The QC fluctuation is shown as a strong peak in the spectra around frequency $f_{QC} \simeq 100$ kHz. We can estimate the level of the QC fluctuations in terms of the optical distance fluctuations $\tilde{d}$ by integrating the power spectra around f_{QC}. The result is shown in Fig. 5-6, where $\tilde{d}$ versus the critical

[1]The 50 GHz channel was not set up for fluctuation measurements because of the limit on available digitizer channels in the 1999 and 2000 campaigns. Because its wave frequency is too low to penetrate the LCFS, we have never observed the QC fluctuations from this channel.

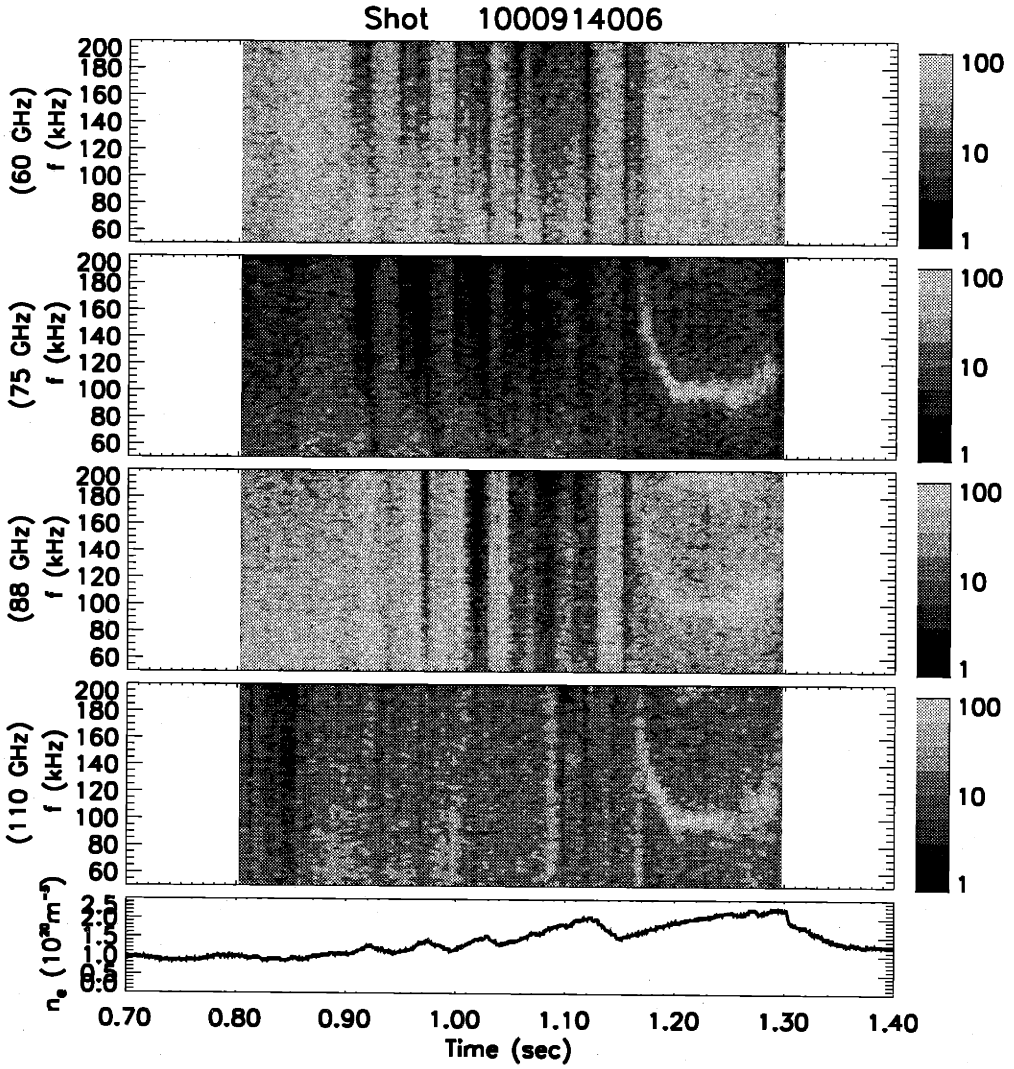

Figure 5-1: Quasi-coherent fluctuations in a relatively low density EDA H-mode ($\bar{n}_e \simeq 2.2 \times 10^{20}$ m^{-3}). The fluctuations appear in the 60, 75, 88 and 110 GHz reflectometry channels during the EDA H-mode period ($1.15 \leq t \leq 1.3$ s). The contour scale in each panel is normalized to its maximal level (= 100).

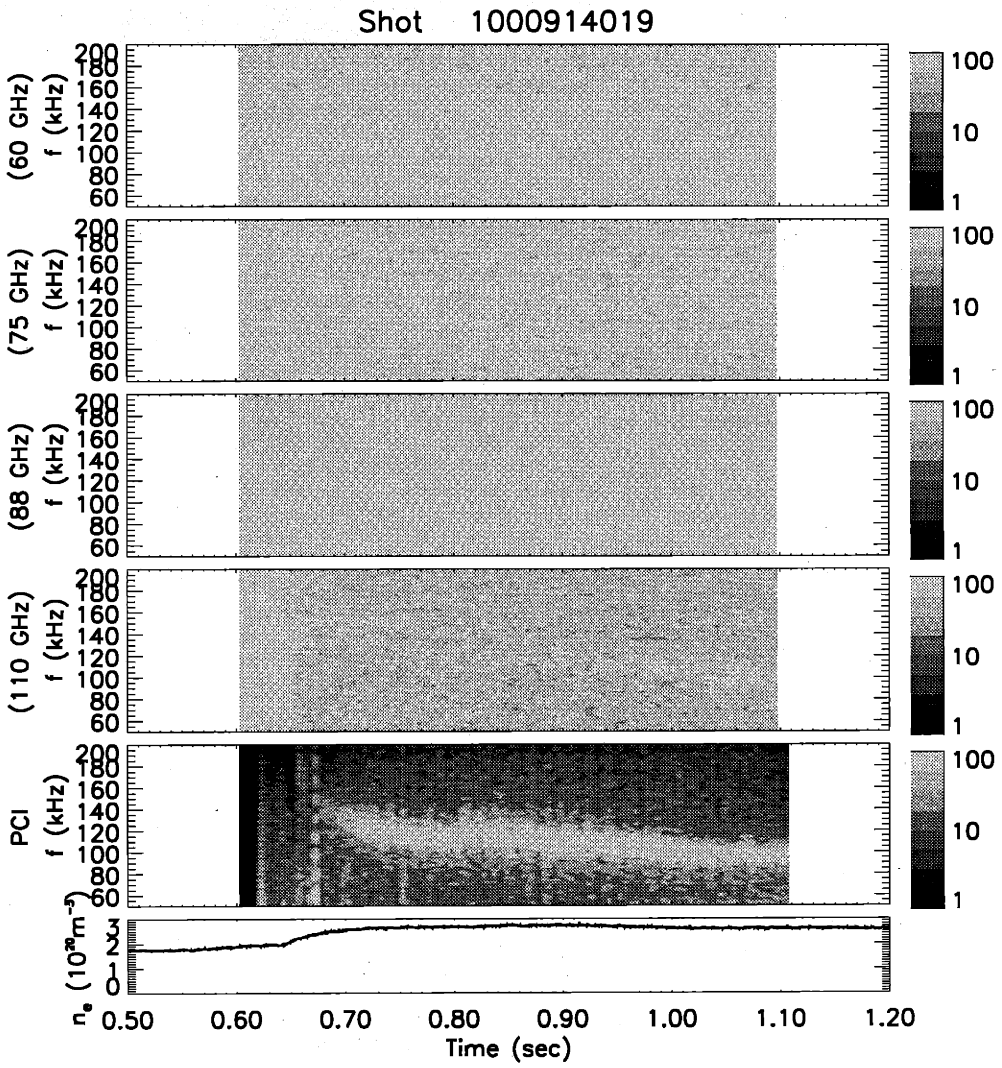

Figure 5-2: QC fluctuations in a high density EDA H-mode ($\bar{n}_e \simeq 2.6 \times 10^{20}$ m^{-3}). In this discharge, though the QC fluctuations are clearly shown in the PCI signal, they can be only weakly seen in the 110 GHz channel.

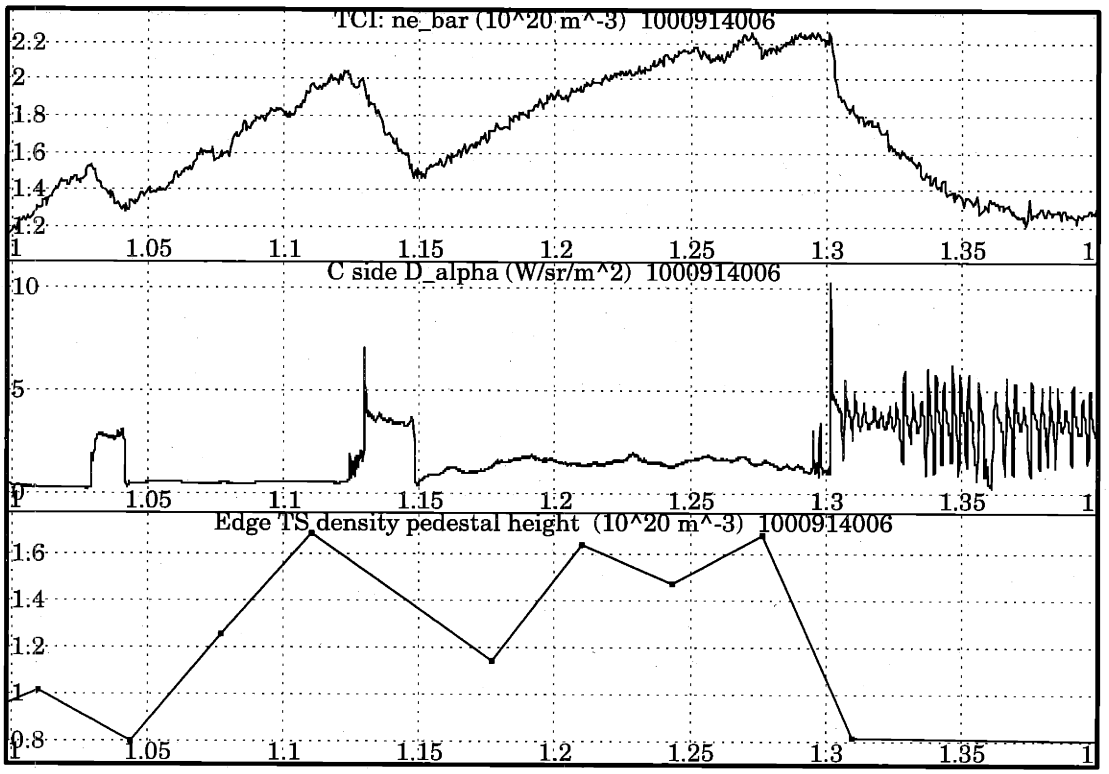

Figure 5-3: Plasma parameters of shot 1000914006. At $1.15 \leq t \leq 1.3$ sec, the plasma is in an EDA H-mode. The line-averaged density from TCI, D_α signal level and density pedestal height from edge TS measurement are shown in the figure. Other plasma parameters are $I_p \simeq 800$ kA, $B_{t0} \simeq 5.4$ T, total ICRF power input $P_{RF} \simeq 2.6$ MW, and $q_{95} \simeq 4.9$.

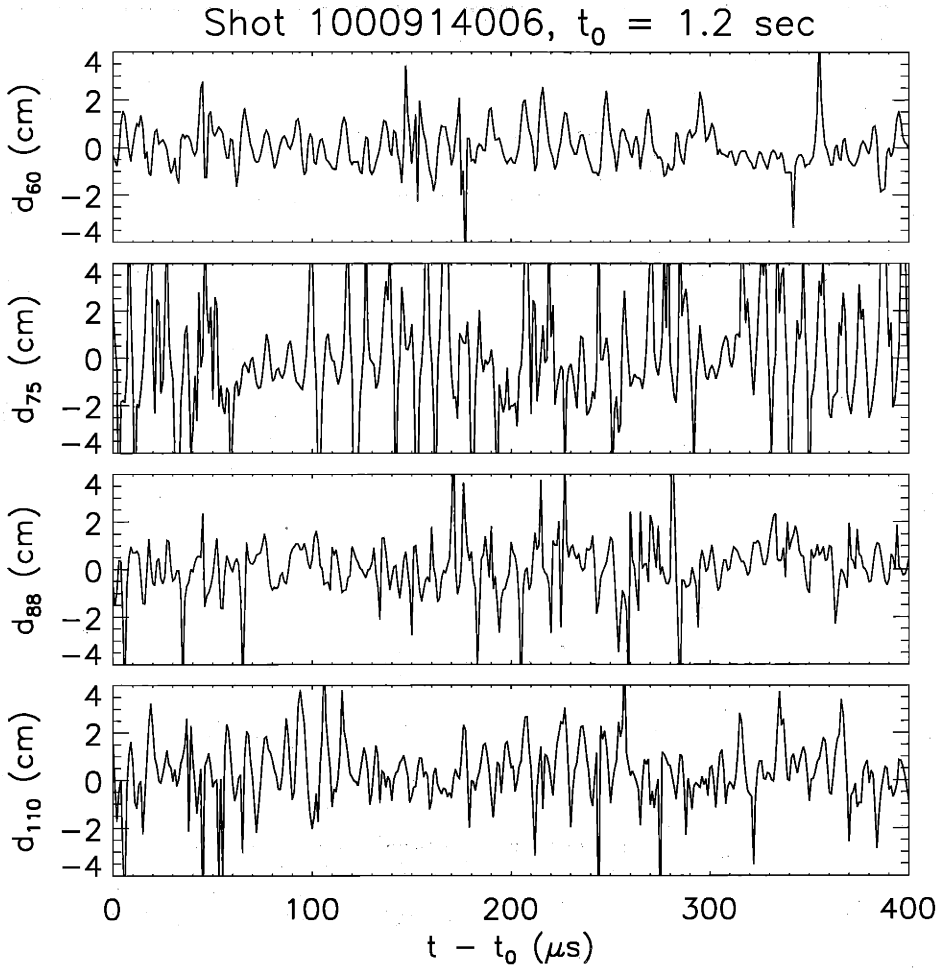

Figure 5-4: Fluctuations of optical distance vs. time from four reflectometry channels. Clear quasi-coherent oscillations ($\simeq$ 100 kHz) exist in all four signals. Data are taken at $t_0 \simeq 1.2$ sec with a sampling rate of 1 MHz.

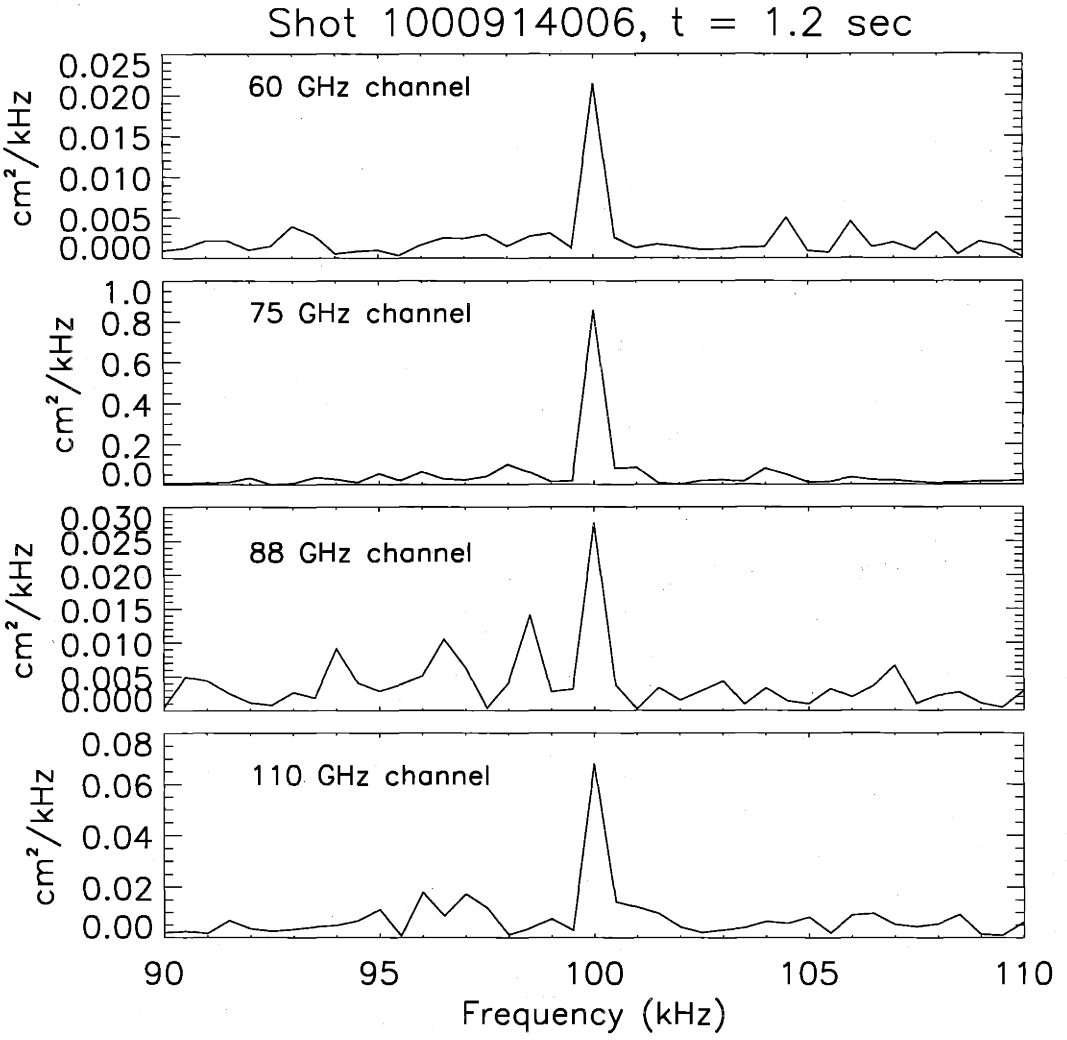

Figure 5-5: Auto-power spectra of optical distance fluctuations from four reflectometer channels. The QC fluctuation is shown as a peak around $f_{QC} \simeq 100$ kHz. Each spectrum is the average of FFT spectra performed on two adjacent 2000-point datasets.

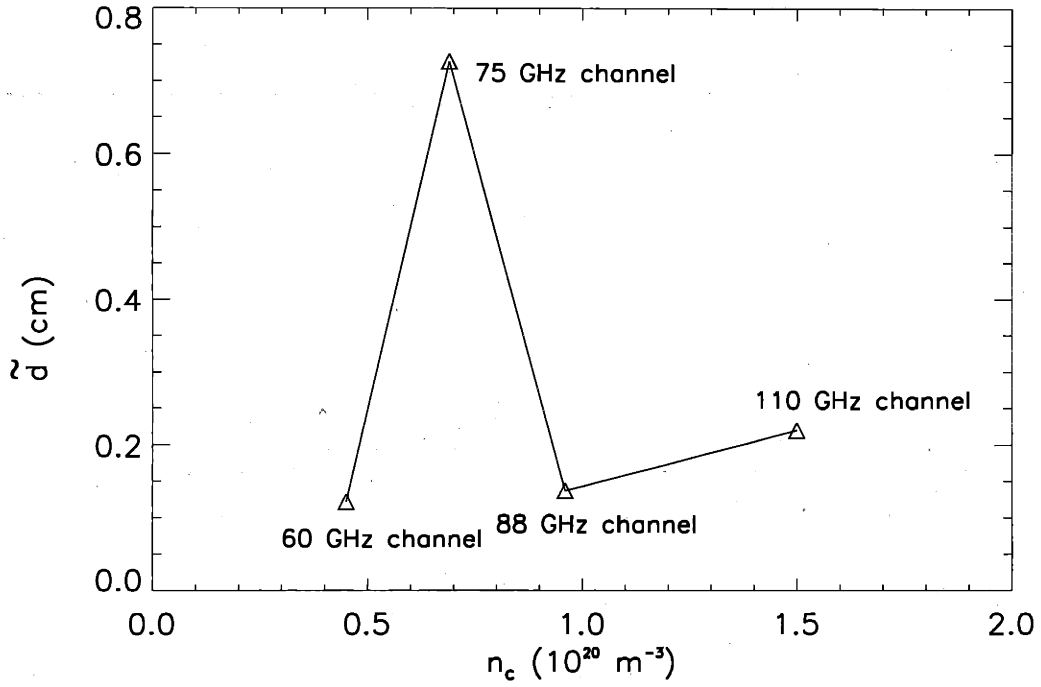

Figure 5-6: QC fluctuation level in terms of optical distances $\tilde{d}$ of different reflectometry channels.

densities of different reflectometry channels is plotted.

5.3.2 Location, width, and level estimates

In order to estimate the corresponding $\tilde{n}_e/n_e$ from the experimentally measured $\tilde{d}$, we need to numerically solve the 1-D second-order differential equation — Eq. 3.12, which is rewritten here as

$$\frac{d^2E}{dR^2} + \frac{\omega^2}{c^2}N^2(\omega, R)E(R) = 0, \tag{5.7}$$

where R is the major radius, $N^2 = 1 - n_e(R)/n_c$, and c is the speed of light in vacuum. We calculate the numerical optical distances, $\tilde{d}_{num}$, for each reflectometry channel by solving the equation for a given density profile with modelled fluctuation level, location, and radial shape. The characteristics of the QC fluctuations are

estimated from the parameters that give a best least squares fit between $\tilde{d}_{num}$ and $\tilde{d}$ while scanning the three dimensional parameter space — location, width, and level. The least squares fit is made to minimize δ given by:

$$\delta = \left[\frac{\sum \left(\tilde{d}_{num} - \tilde{d} \cdot C \right)^2}{\langle C^2 \tilde{d}^2 \rangle} \right]^{1/2}, \tag{5.8}$$

where

$$C = \frac{\sum \tilde{d}^2_{num}}{\sum \tilde{d} \cdot \tilde{d}_{num}}, \tag{5.9}$$

which satisfies $\partial\delta/\partial C = 0$, and $\sum$ sums over reflectometry channels. Using the data in Fig. 5-6 as an example, the method is described in detail below.

We construct a density profile with a *tanh* shape using experimental data given by the edge TS system:

$$n_e \simeq \frac{n_h}{2} \left[1 + \tanh\left(\frac{R - R_{ped}}{Ped_w} \right) \right], \tag{5.10}$$

where R_{ped} is the center of the pedestal, n_h is the pedestal height, and Ped_w is the full-width of the pedestal. For data shown in Fig. 5-6, we have $n_h \simeq 1.6 \times 10^{20}$ m^{-3} and $Ped_w \simeq 0.5$ cm. We also assume a fluctuation with a Gaussian radial shape:

$$\tilde{n}_e/n_e = n_f \exp\left[-\frac{4 \ln 2}{W^2} (R - R_{QC})^2 \right], \tag{5.11}$$

where R_{QC} and n_f are the central location and magnitude of the QC mode respectively, and W is the full width at half magnitude (FWHM) of the fluctuations.

Fig. 5-7 shows the density profile and electric fields of different reflectometry channels, which are obtained by numerically solving Eq. 5.7 at $n_f = 0$. The critical surfaces of the four channels are at well-separate positions in the pedestal region. By comparing the fluctuation behaviors in all four channels, we can infer the fluctuation level and spatial characteristics.

We scan the three parameters, n_f, R_{QC}, and W, and find the set of parameters that gives the minimum δ. Fig. 5-8 shows a 3-D plot of $1/\delta$ at $n_f = 0.6$ vs. the mode

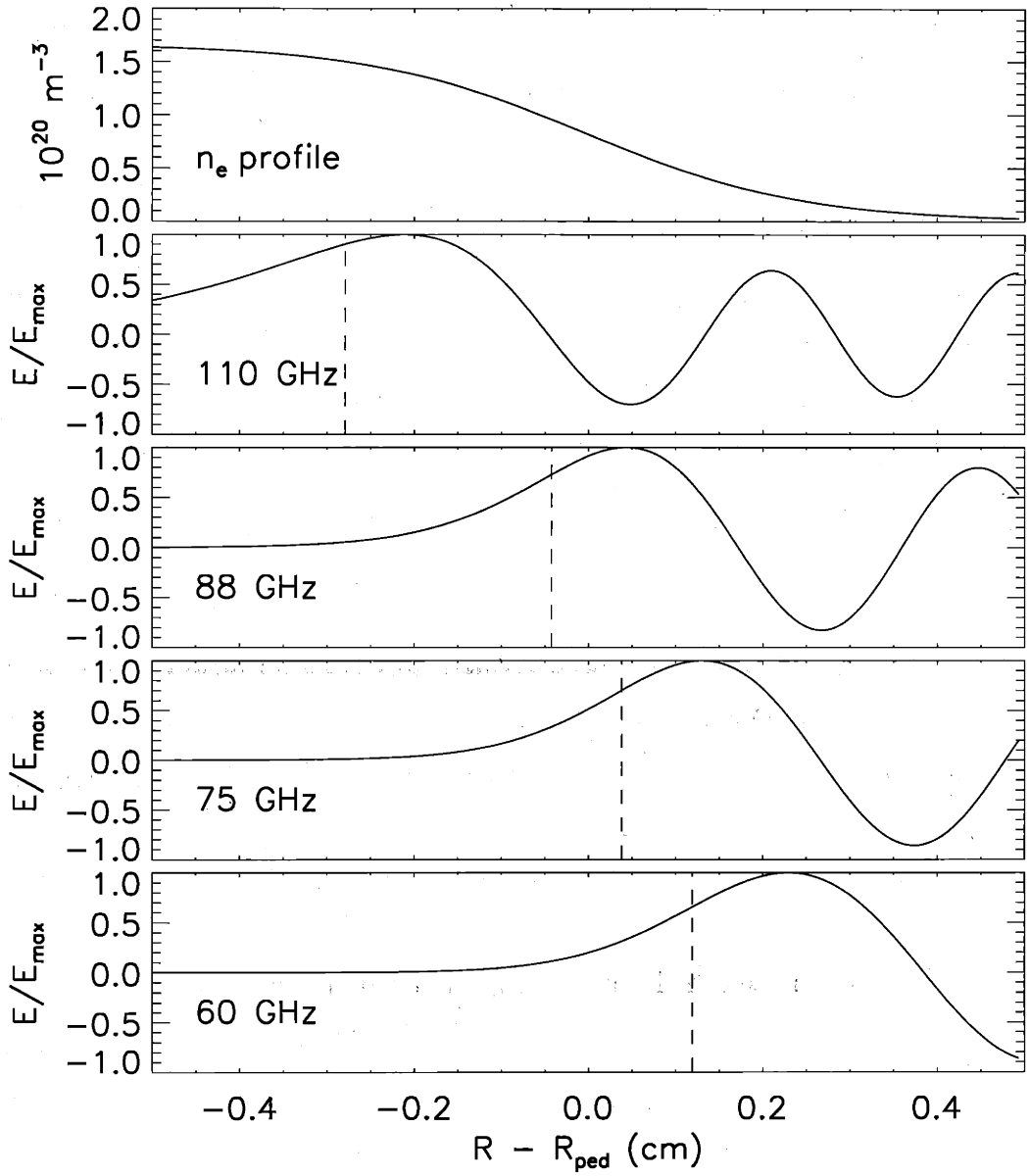

Figure 5-7: The density profile and electric fields of different reflectometry channels. The vertical dash-lines are the critical surface positions.

location and width. The peak in the upper figure corresponds to the best fit, while the lower figure compares the numerically calculated $\tilde{d}_{num}$ versus $\tilde{d}$ obtained from experimental measurements. Fig. 5-9 shows the density profile and the estimated QC fluctuations location, width, and level from the best fit. This fit gives a fluctuation level, $\tilde{n}_e/n_e \simeq 0.6$, $R_{QC} - R_{ped} \simeq 0.10 \pm 0.05$ cm, and $W \simeq 0.10 \pm 0.04$ cm. The error bars in R_{QC} and W are estimated assuming a $\pm 10\%$ uncertainty of the TS pedestal height, n_h. Because of the uncertainty in the effects of reflectometry geometry, we are not certain of the absolute fluctuation level.

5.3.3 Comparison with Langmuir probe observations

Langmuir probes (in A-port and F-port) are able to measure the density fluctuations, $\tilde{n}_e$, and plasma potential fluctuations, $\tilde{\phi}_p$, in ohmic discharges. In some discharges, the A-port probe penetrated to a depth where a significant decrease of the QC fluctuation level was observed. Fig. 5-10 shows one of these cases (shot 1000928017, $t \simeq 1.16$ sec). The top panel of the figure shows $\tilde{\phi}_p$ in volts, which clearly shows the radial shape of the QC fluctuation.

Simultaneously, the QC fluctuations are observed by all four reflectometer channels. Fig. 5-11 shows the density fluctuations level, $\tilde{n}_e/n_e$, derived from reflectometry. Due to the large instrumental uncertainty (about 40%-50%) in the density profile measured by the probe (Fig. 5-10), we still use the density profile measured by the edge TS, which gives a density pedestal height of $n_h \simeq 2.1 \times 10^{20}$ m^{-3}, and pedestal full width $Ped_w \simeq 0.5$ cm. The figure shows that the QC fluctuations are localized at about $R - R_{ped} \simeq 0.10 \pm 0.03$ cm with a magnitude of $\tilde{n}_e/n_e \simeq 0.3$, and $W \simeq 0.10 \pm 0.02$ cm.

Depending on the model of physical origin of QC fluctuations, which is still under study, the two quantities — $\tilde{n}_e/n_e$ and $\tilde{\phi}_p$ — can scale differently with plasma parameters. However, the width of these fluctuations should be similar and insensitive to different models[2]. The fluctuation's radial width inferred from reflectometer

[2]If $\tilde{n}_e/n_e \propto \left(\tilde{\phi}_p\right)^{\gamma}$, then we have $W_n \simeq W_\phi/\sqrt{\gamma}$. For acoustic type mode, $\gamma \simeq 1$.

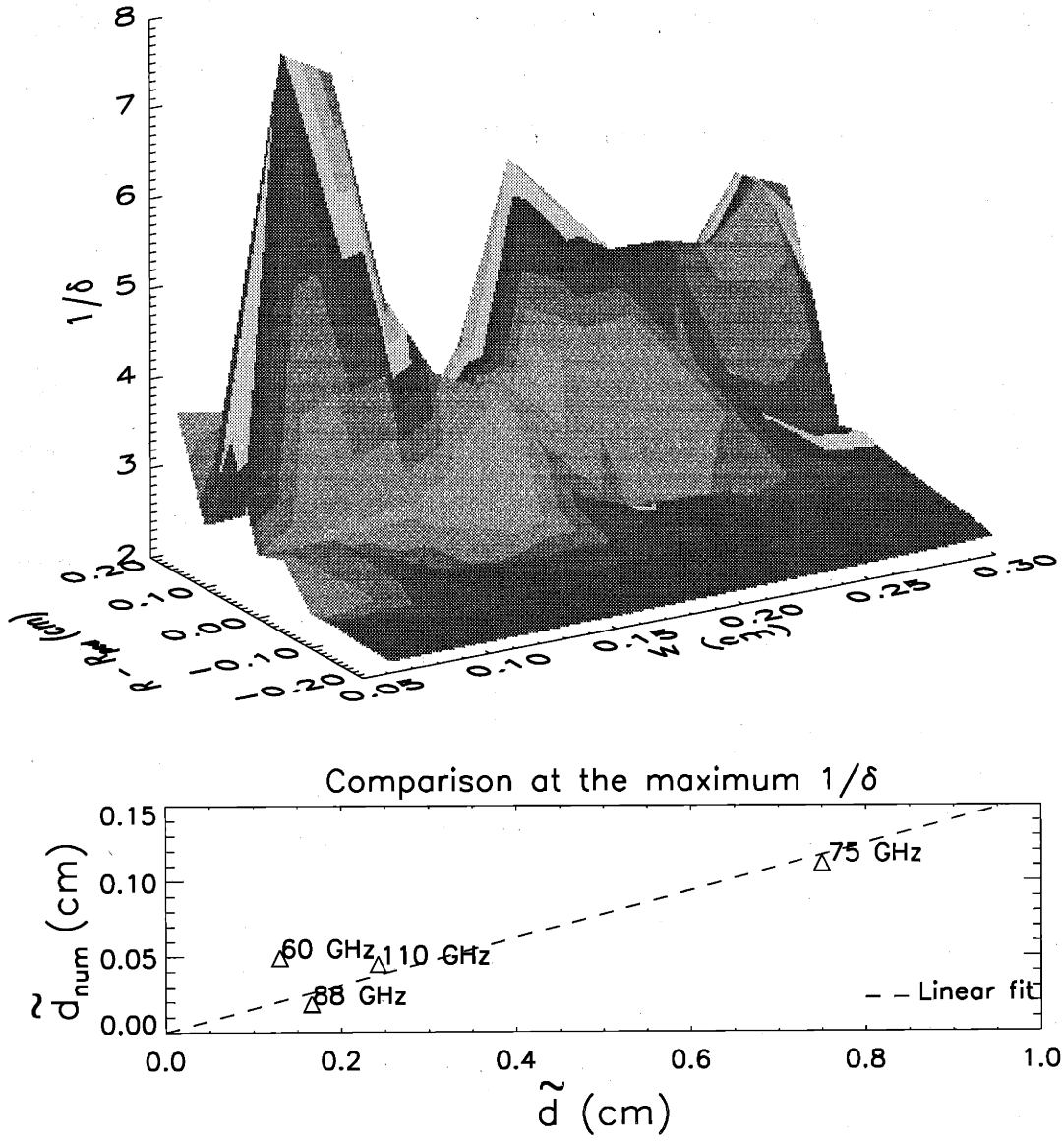

Figure 5-8: The least-square fit of $\tilde{d}_{num}$ and $\tilde{d}$. δ is defined in Eq. 5.8. The peak in $1/\delta$ corresponds to the best fit. The lower figure compares the numerically calculated $\tilde{d}_{num}$ versus reflectometry measured $\tilde{d}$.

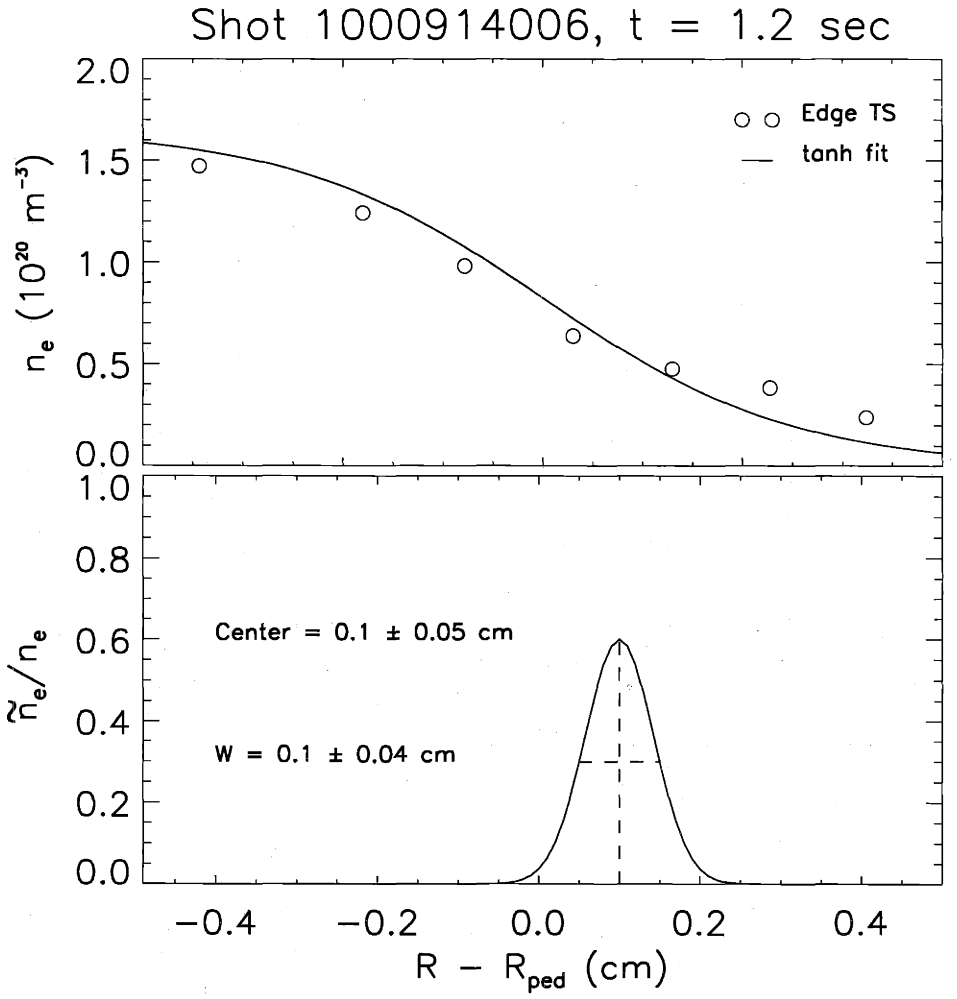

Figure 5-9: Inferred QC fluctuation location and radial width. Fig. (a) is the density measured by the edge Thomson scattering system. A *tanh* density profile with a height $n_h = 1.6 \times 10^{20}$ m^{-3} and width $\mathrm{Ped_w} = 0.5$ cm is also plotted; Fig. (b) shows the estimated fluctuation level, location and shape. The best fit between $\tilde{d}_{num}$ and $\tilde{d}$ gives the fluctuations level, $\tilde{n}_e/n_e \simeq 0.6$, center at $R_{QC} - R_{ped} \simeq 0.10 \pm 0.05$ cm, and $W \simeq 0.10 \pm 0.04$ cm.

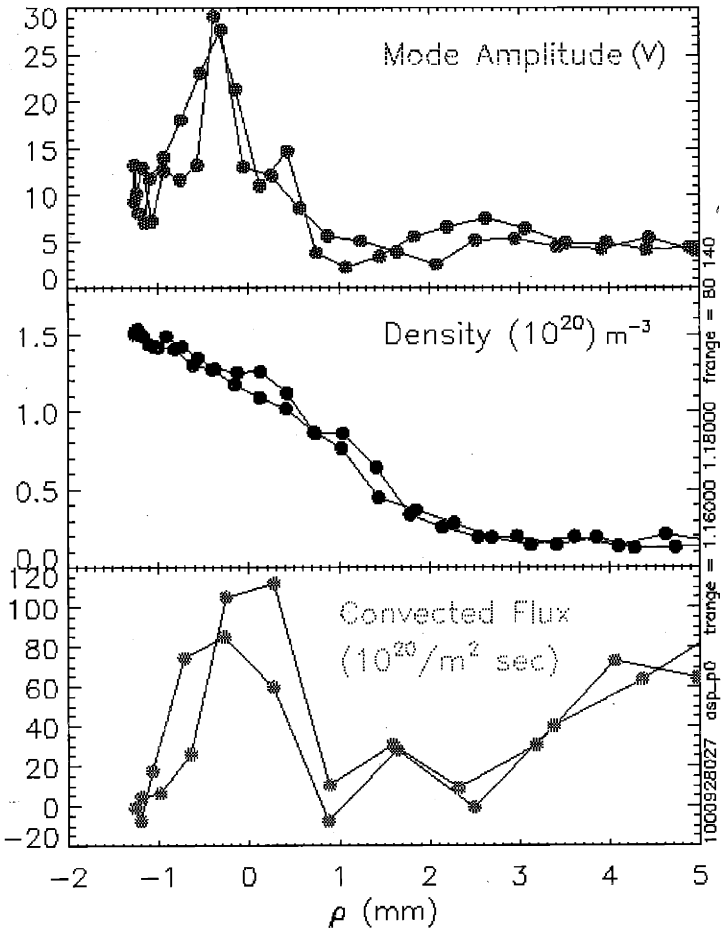

Figure 5-10: Langmuir probe observation of the QC fluctuations in an ohmic EDA discharge (shot 1000928017, $t = 0.16$ sec). The top panel shows the plasma potential fluctuation $\tilde{\phi}_p$ in volts. The middle panel is the density measured by the probe and the bottom panel is the derived particle flux. The horizontal axis is in $\rho = R - R_{LCFS}$ (Ref. [73]).

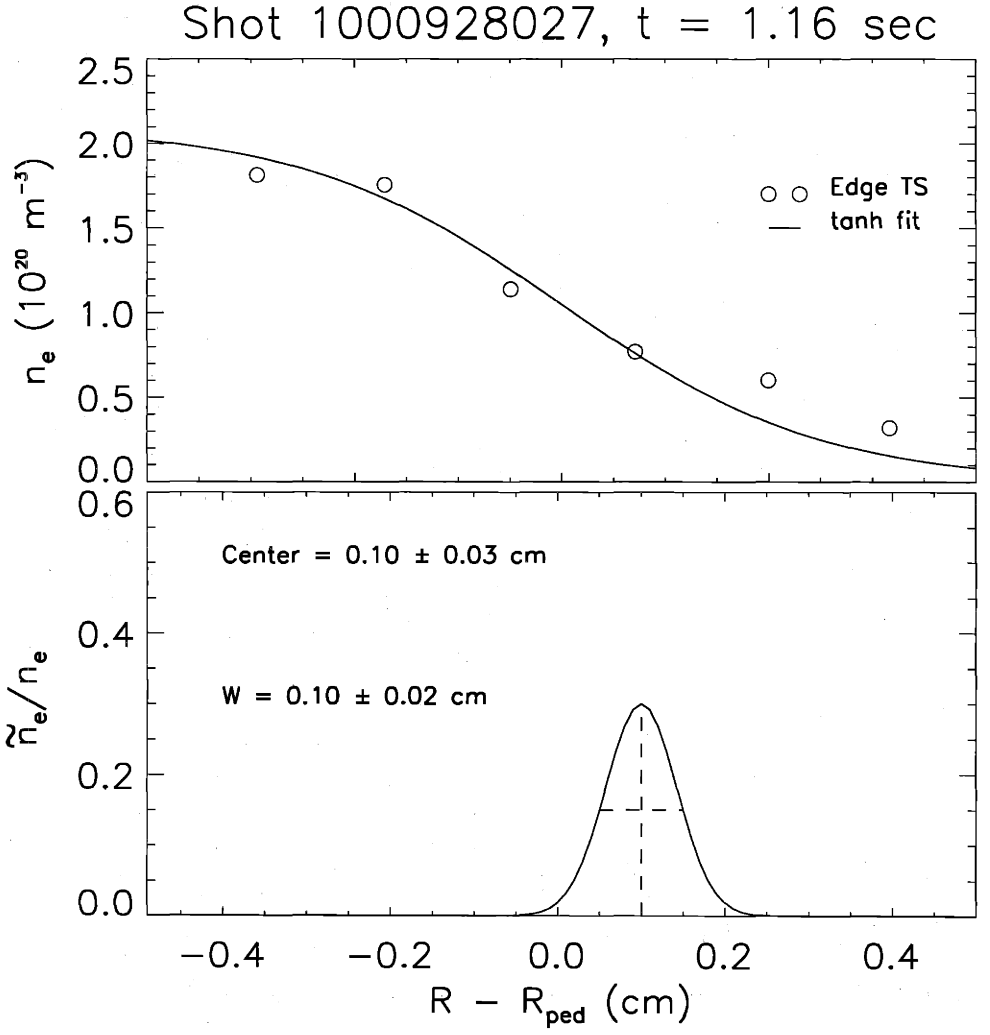

Figure 5-11: Inferred QC fluctuations location and width of the ohmic EDA H-mode discharge. The upper figure is the *tanh* density profile; the lower figure shows the inferred fluctuation location and radial shape relative to the pedestal center. The Gaussian fit gives a center at $R - R_{ped} \simeq 0.10 \pm 0.03$ cm, $W = 0.11 \pm 0.02$ cm, and magnitude $\tilde{n}_e/n_e \simeq 0.5$.

measurement is indeed very close to that from the Langmuir probe result as shown in Fig. 5-12. In this figure, we use the edge TS density profile mapped onto the mid-plane by EFIT to estimate the position of pedestal center, R_{ped}, and transfer $R-R_{ped}$ into $\rho = R - R_{LCFS}$. The reflectometer result is shown as a Gaussian fit, which gives the best fit to the experimental data. The critical surfaces are also shown. The fluctuation shape is shifted 2.3 mm outward to match that obtained from the probe measurement. The 2.3 mm shift is within the uncertainty of EFIT in determining the LCFS position and flux surface mapping ($\leq$ 5 mm). Probe data are the averages of the two (in and out) traces shown in the uppermost panel of Fig. 5-10. The size of the probe tip in the radial direction is about 0.7 mm.

5.3.4 Comparison with plasma parameters

In this Section, we choose a set of EDA H-mode discharges from experiments dedicated to the EDA H-mode study. These discharges cover a range of global plasma parameters, such as $2.8 \leq q_{95} \leq 5.6$, $0.7 \leq I_p \leq 1.4$ MA, and both Ohmic and RF heated shots. We study the correlations of the fluctuation location and radial width with plasma parameters at the pedestal.

Fig. 5-13 shows the radial location of the QC fluctuations relative to the center of the pedestal, R_{ped}, versus electron temperature at the center of the pedestal T_e, which is estimated to be half of the height of the temperature pedestal measured by edge TS. Each point in the figure represents a time point in a steady EDA H-mode period. The location is generally very close to the pedestal center with a small shift toward the lower part of the pedestal at $R_{QC} - R_{ped} \simeq 0.1$ cm. The location does not change within the uncertainty of the reflectometry observation.

Fig. 5-14 shows the width of the QC fluctuation, W, versus $T_e^{-1.5} \propto \eta$. The width is in the range of $0.1-0.3$ cm. This range is close to that shown by the drift-ballooning simulation (Section 5.2.2). The width increases with the increase of η. This weak correlation is similar to the $\eta^{1/4}$ scaling shown in Eq. 5.3, which is derived from linear resistive ballooning mode theory.

Fig. 5-15 compares the line integrated QC fluctuation level from reflectometry and

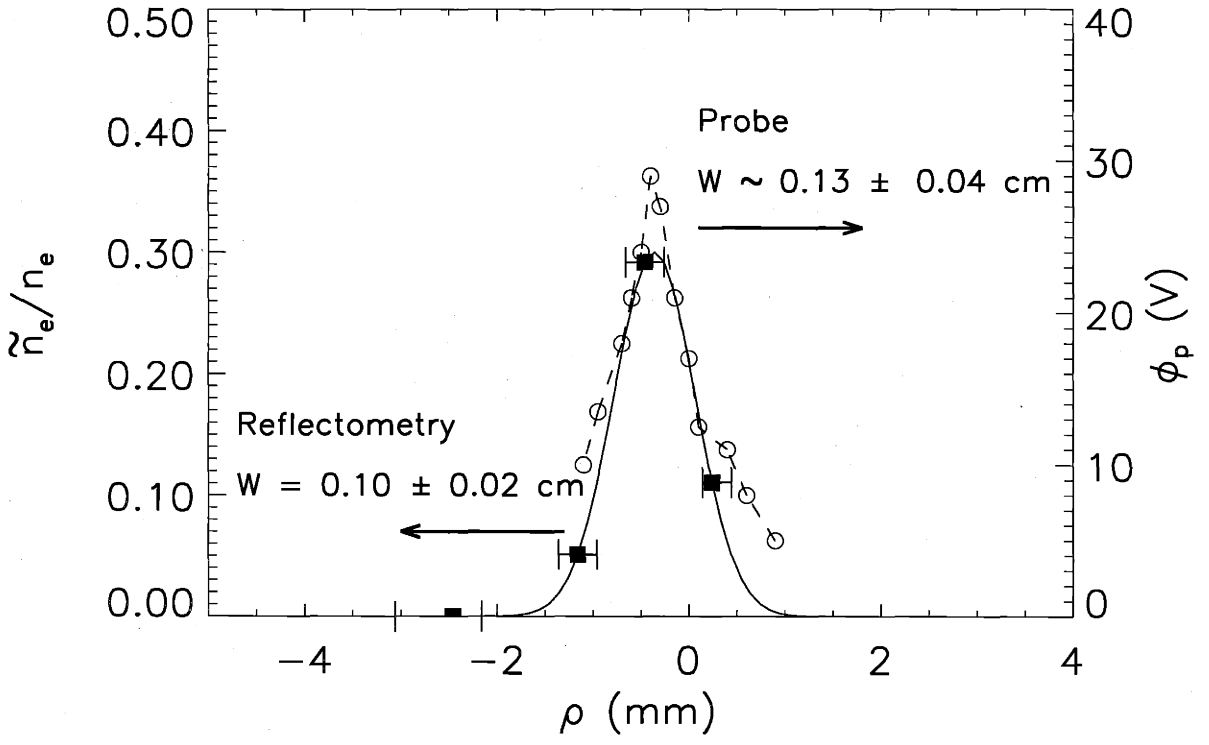

Figure 5-12: Comparison of the probe and reflectometry measurement. The normalized fluctuations are plotted together. The center of the reflectometry fluctuations are shifted 2.3 mm outward to match the probe result. The filled squares are the critical surface locations (110 GHz, 88 GHz, 75 GHz, and 60 GHz respectively from left to right). The radial shapes from both diagnostics are similar.

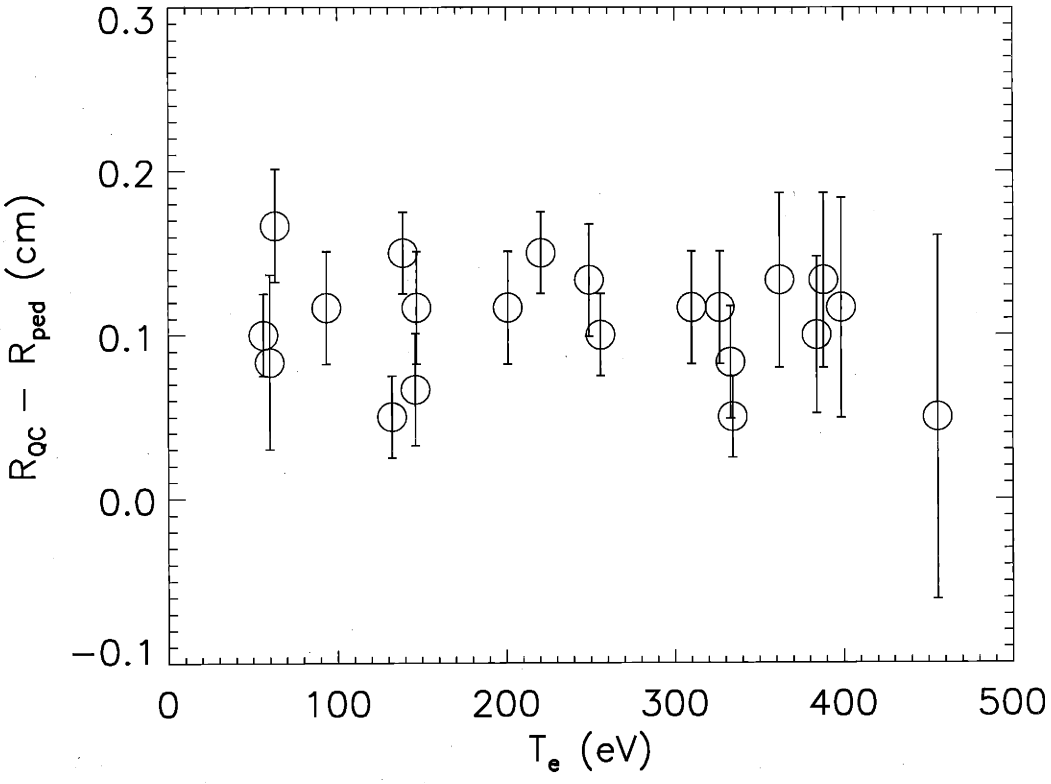

Figure 5-13: Inferred location of the QC fluctuations vs. temperature at the center of pedestal.

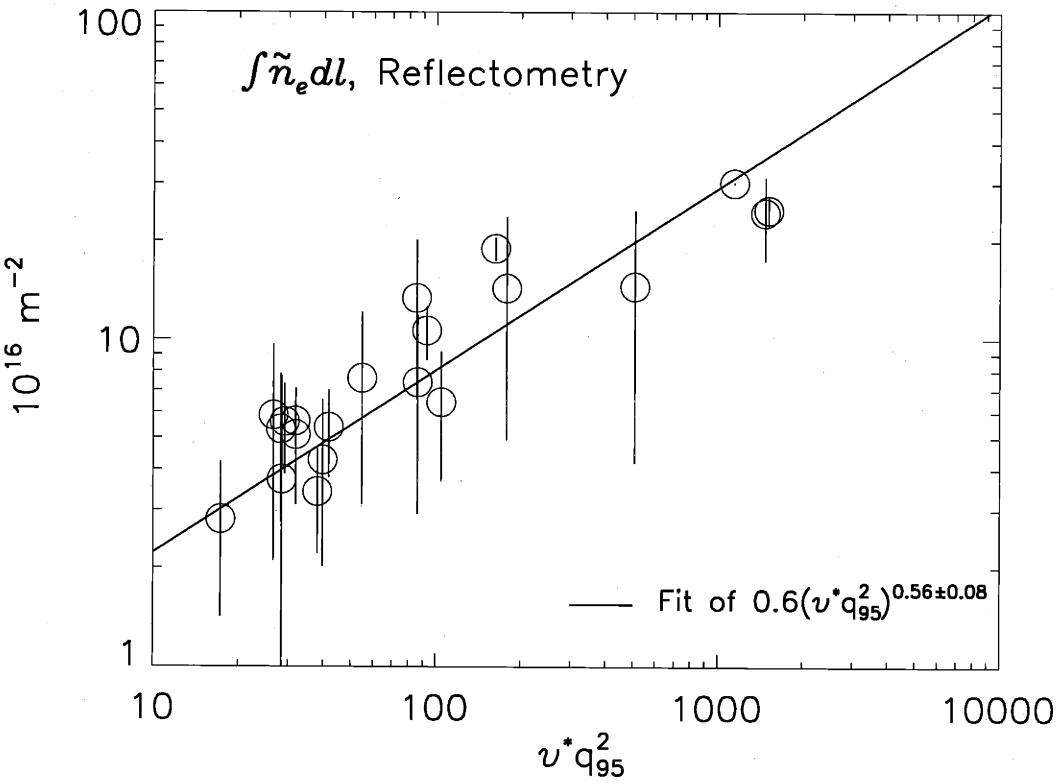

Figure 5-15: The line integrated QC mode level vs. $\nu^* q_{95}^2$. The plot is in Log-Log scale. A scaling of $\int \tilde{n}_e dl \sim (0.6 \pm 0.2) \times 10^{16} \, (\nu^* q_{95}^2)^{0.56\pm0.08}$ m^{-2} is over-plotted.

$\nu^* q_{95}^2$, which is a parameter determining resistive mode growth rate in linear theory (see Section 5.2.1). The dimensionless collisionality, ν^*, is evaluated using plasma parameters at the center of the pedestal and with q substituted by q_{95}. Fig. 5-15 shows a strong relation of the mode level — the saturated mode level — vs. the parameter $\nu^* q_{95}^2$. A scaling of $\int \tilde{n}_e dl \sim (0.6 \pm 0.2) \times 10^{16} \, (\nu^* q_{95}^2)^{0.56\pm0.08}$ m^{-2} is found. The linear theory cannot predict the saturated mode level, which is mostly determined by nonlinear processes. The finding in Fig. 5-15, however, indicates that $\nu^* q_{95}^2$ can also be an important parameter affecting the saturated mode level. In Ref. [78], it is shown that the mixing length approximation is still good in estimating the saturated level of resistive ballooning modes. Under the mixing length approximation, we have $\langle \tilde{p}^2 \rangle^{1/2}/p \sim \Delta_p/L_p$, and $D \sim \Delta_p^2/\tau_c$, where $\tilde{p}$ is pressure fluctuations, Δ_p is the

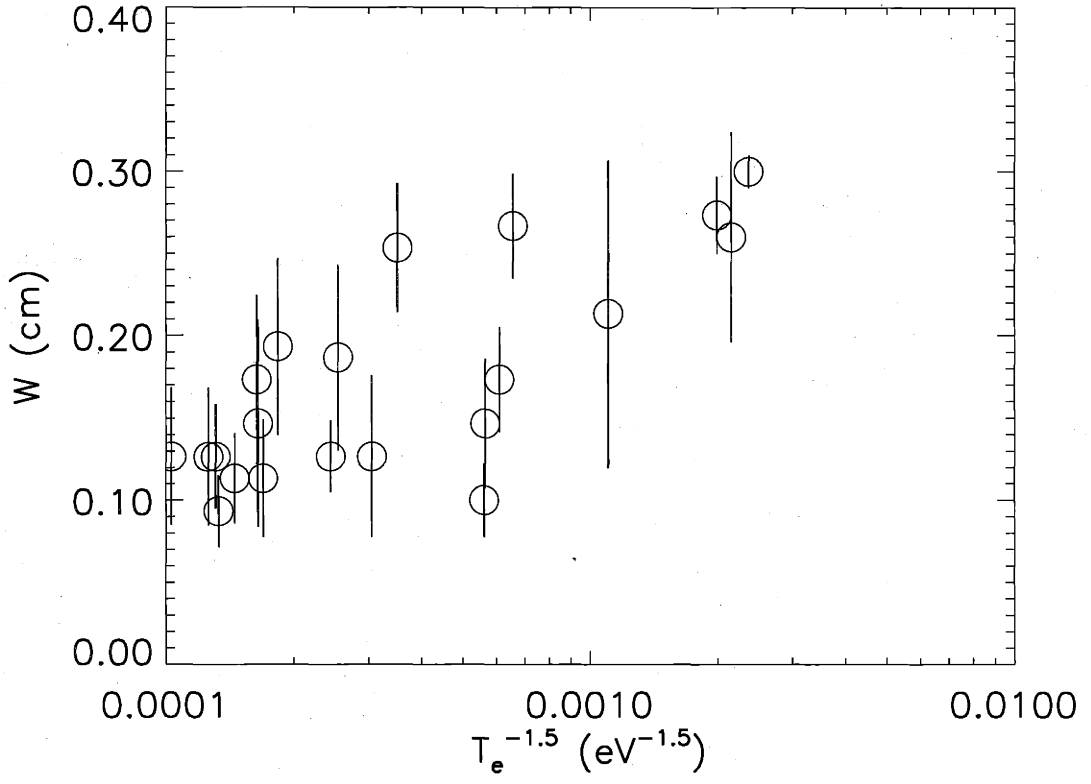

Figure 5-14: Inferred width of the QC fluctuations radial width vs. $T_e^{-1.5} \propto \eta$ at the center of the pedestal.

this Section we will answer whether the location, radial width and fluctuations level also vary as significantly as the lab frame frequency in an EDA H-mode period. We will also study how the frequency varies with plasma parameters.

5.4.1 Evolution of mode location, width, and level

Fig. 5-16 shows the evolution of the QC fluctuations in terms of the fluctuation of optical distance $\tilde{d}$ of four reflectometry channels in the EDA H-mode period shown in Fig. 5-1. The peak frequency of the fluctuations is also shown.

Fig. 5-17 shows the location and width of the QC fluctuations inferred from the reflectometer. The location (shown in the uppermost panel) is nearly constant relative to the center of pedestal throughout the whole period. The radial width (shown in the middle panel) varies within the uncertainty during the entire EDA period. The mode frequency as shown in the lowermost panel changes from about 200 kHz at the start of EDA to about 100 kHz from during the steady EDA period.

Fig. 5-18 shows the line-integrated fluctuation level from the reflectometer and PCI. Both levels increase significantly in the start of EDA. The level from the reflectometer stays at a relatively constant level within the uncertainty during the steady EDA period, and then decreases near the end of the EDA H-mode period. The level from PCI is smaller than that estimated from the reflectometer. Two causes that have not been considered may account for such discrepancy. The optical distance is sensitive to the length of wave path, which is affected by reflectometer geometry. The other reason may be due to the fact that these two diagnostics measure the QC fluctuations at different places. If the mode is ballooning-like, the level at the outer edge of mid-plane (poloidal angle $\theta \simeq 0$), where reflectometry measures, should be larger than the level at $\theta \simeq \pm 90^0$, where PCI is sensitive. We should be cautious in comparing the absolute levels here[3].

In Fig. 5-19, we estimate the mode growth rate from reflectometer data. The

[3]In Chapter 7, the fluctuation level will be estimated using a 2-D full-wave simulation and the baseband signal fluctuations of the 88 GHz channel. The result obtained shows a difference less than the instrumental uncertainties.

radial correlation length of the pressure fluctuations, D is the diffusivity, and τ_c is the decorrelation time of the fluctuations. The pressure gradient length $L_p \sim L_n \sim Ped_w$ are similar in different EDA discharges (Ref. [64]). If we assume that τ_c also varies insignificantly, and $\tilde{p}/p \sim \tilde{n}_e/n_e$, the scaling shown in Fig. 5-15 indicates that the QC fluctuations may have larger transport effects at discharges with higher value of $\nu^* q_{95}^2$ at the pedestal.

In most Alcator C-Mod H-mode plasmas, the pedestal temperature is related to the pedestal density and input power, $T_{e,0.9} \propto (P_{in}/\bar{n}_e)^{0.5\pm0.1}$ (Ref. [73]), where $T_{e,0.9}$ is the temperature at the flux surface enclosing 90% poloidal magnetic flux. Since $\nu^* \propto n_e/T_e^2$, the result that $\nu^* q_{95}^2$ scales with the QC mode level suggests a lower density limit for EDA H-modes at the same power input. Such a density limit has been observed in experiments (also see Ref. [73]). An edge temperature threshold $T_{e,crit}$ must be exceeded to obtain H-modes (Refs. [13][14]). The result above also suggests that it may be difficult to obtain EDA H-modes in tokamaks that have a high $T_{e,crit}$.

In summary, the QC fluctuations are mostly localized near the center of density pedestal with a small shift toward the lower part of the pedestal. The radial width of these fluctuations, W, is usually in the range of $0.1-0.3$ cm. W increases with the increase of η. The line-integrated fluctuation level approximately scales with $(\nu^* q_{95}^2)^{0.56}$. The result indicates that higher q_{95}, higher density, and lower temperature are favored for the QC fluctuations. Both drift-ballooning mode and resistive ballooning mode can be a candidate of the QC fluctuations.

5.4 Evolution of the QC fluctuations in an EDA H-mode

Experimental data in the previous Section were taken from the steady EDA H-mode periods, when most plasma parameters are relatively constant. As clearly shown in Fig. 5-1, the observed fluctuation frequency in the lab frame can vary significantly. In

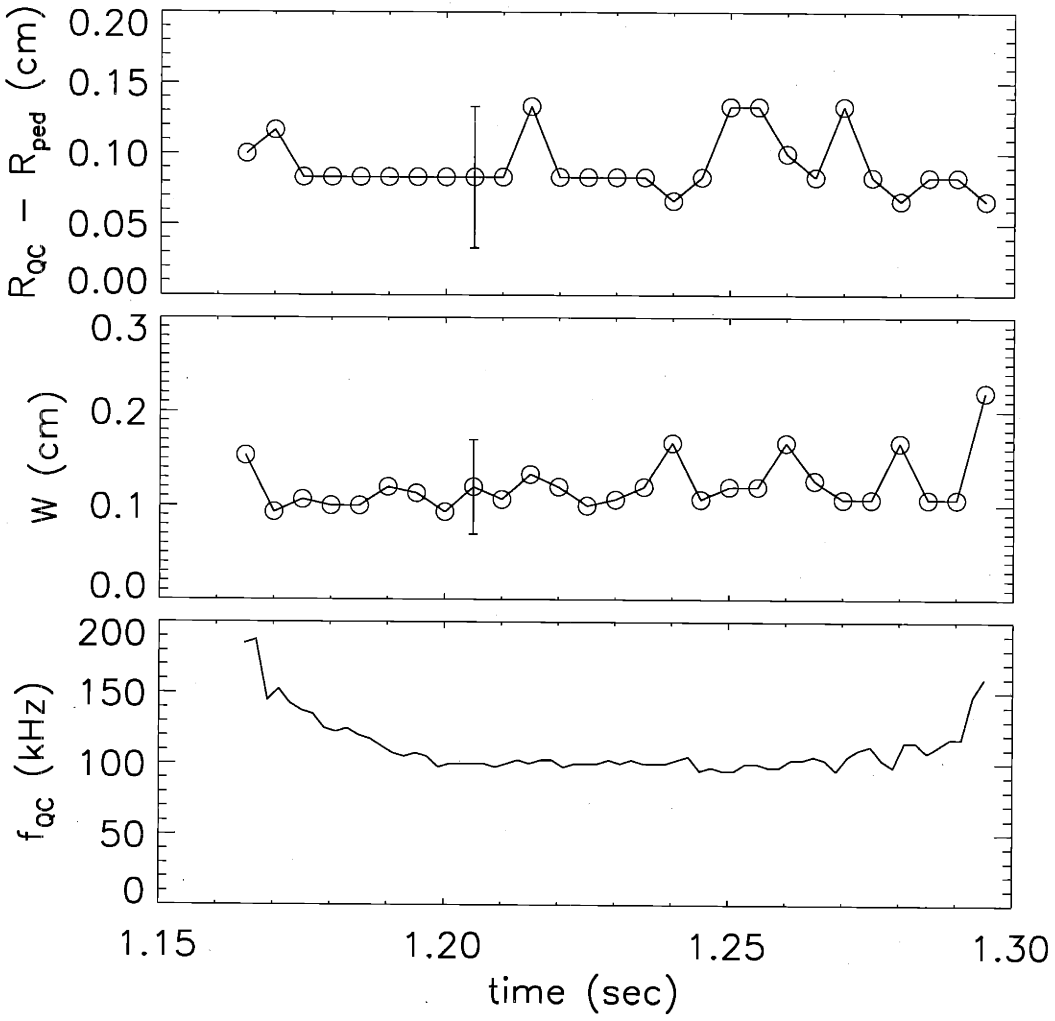

Figure 5-17: The evolution of QC fluctuations location, radial width, and frequency in lab frame in an EDA H-mode. Both location and width are nearly constant in the whole EDA period, while the frequency in the lab frame changes significantly.

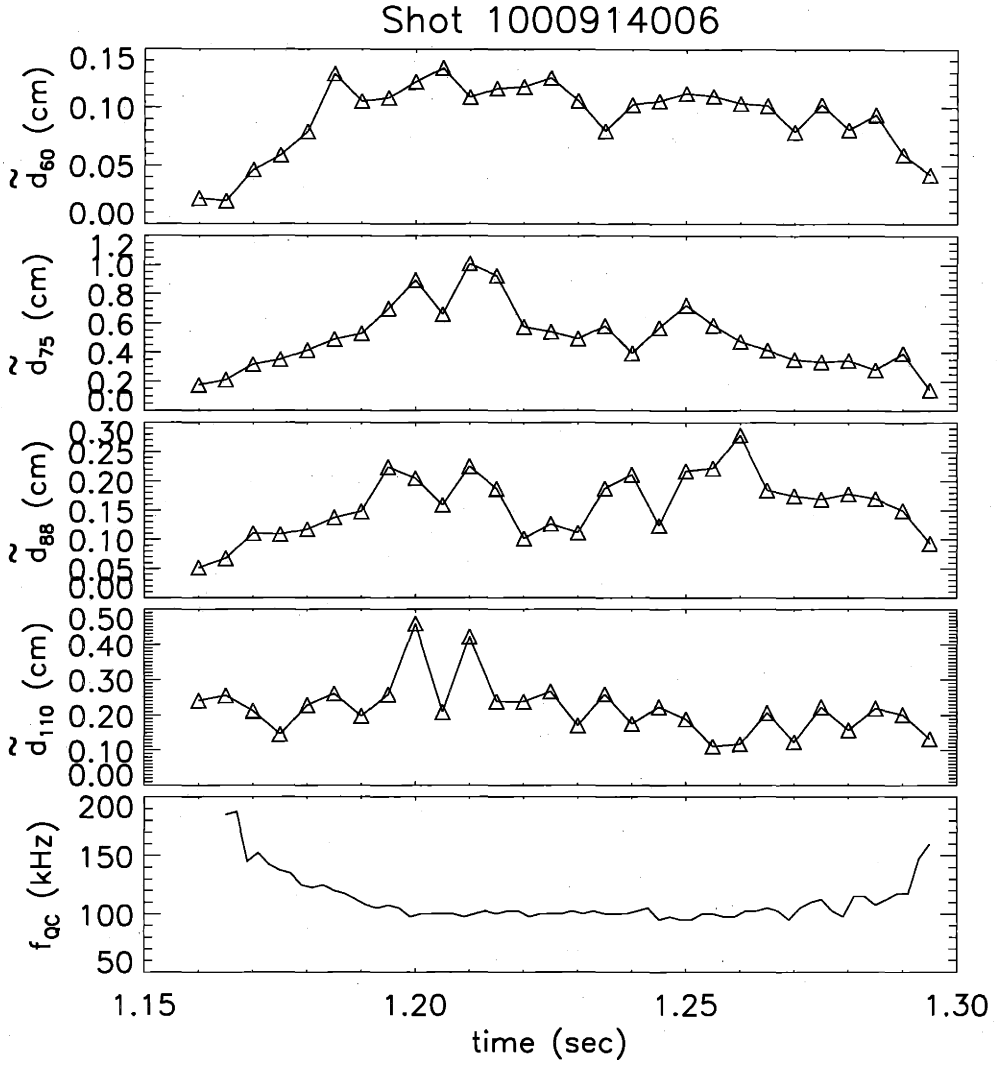

Figure 5-16: The QC fluctuation level in terms of the fluctuation of optical distance $\sqrt{\langle \tilde{d}^2 \rangle}$ measured by four reflectometry channels (60, 75, 88 and 110 GHz) are shown versus time in the EDA H-mode period of Fig. 5-1. The peak frequency of the fluctuations is shown in the bottom panel.

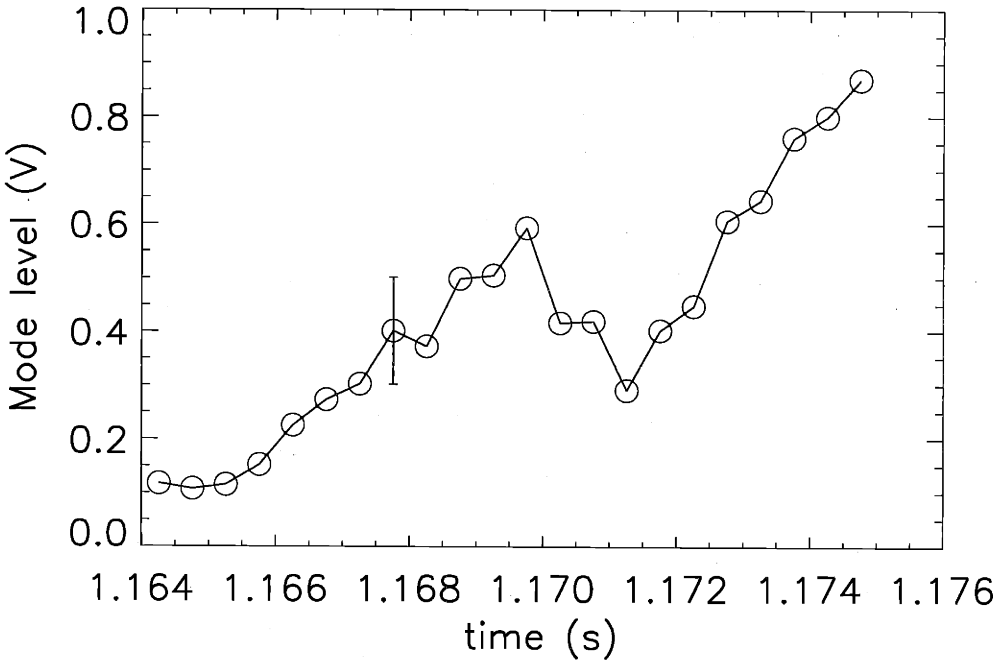

Figure 5-19: Growth rate of the QC fluctuations. The mode level is estimated from the baseband fluctuation signal, $A\cos\phi$, of the 88 GHz channel. At $t < 1.164$ s, the QC fluctuations are not identifiable from the reflectometry data. The growth rate is about 200 s^{-1} at $1.64 \leq t \leq 1.69$ s.

mode level is estimated from the homodyne signal, $A\cos\phi$, of the 88 GHz channel baseband fluctuations. At $t < 1.164$ s, the QC fluctuations are not identifiable from the reflectometry data. Using data in the period of $1.64 \leq t \leq 1.69$ s, we estimate a growth rate about 200 s^{-1}. We should be cautious that this growth rate may not be the linear growth rate. Instead, nonlinear effects may play an important role in determining the mode level in this period. It is difficult to pinpoint the very beginning of the mode because of the large frequency change and small mode level.

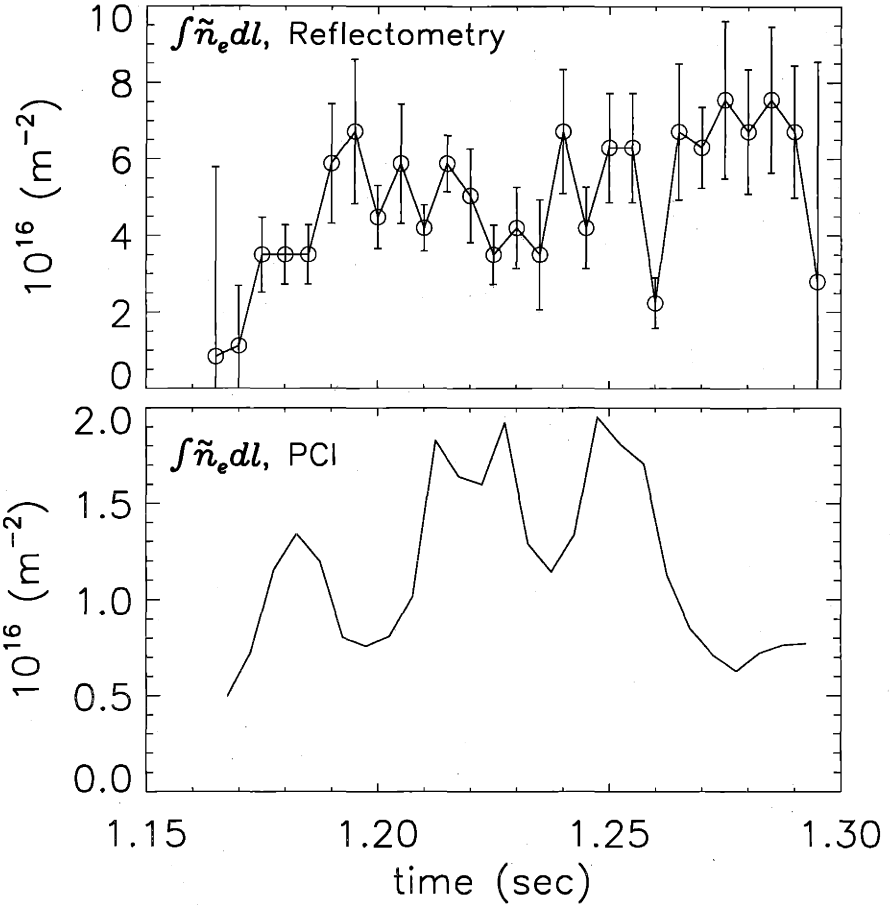

Figure 5-18: Comparison of QC fluctuation levels obtained from reflectometry and PCI.

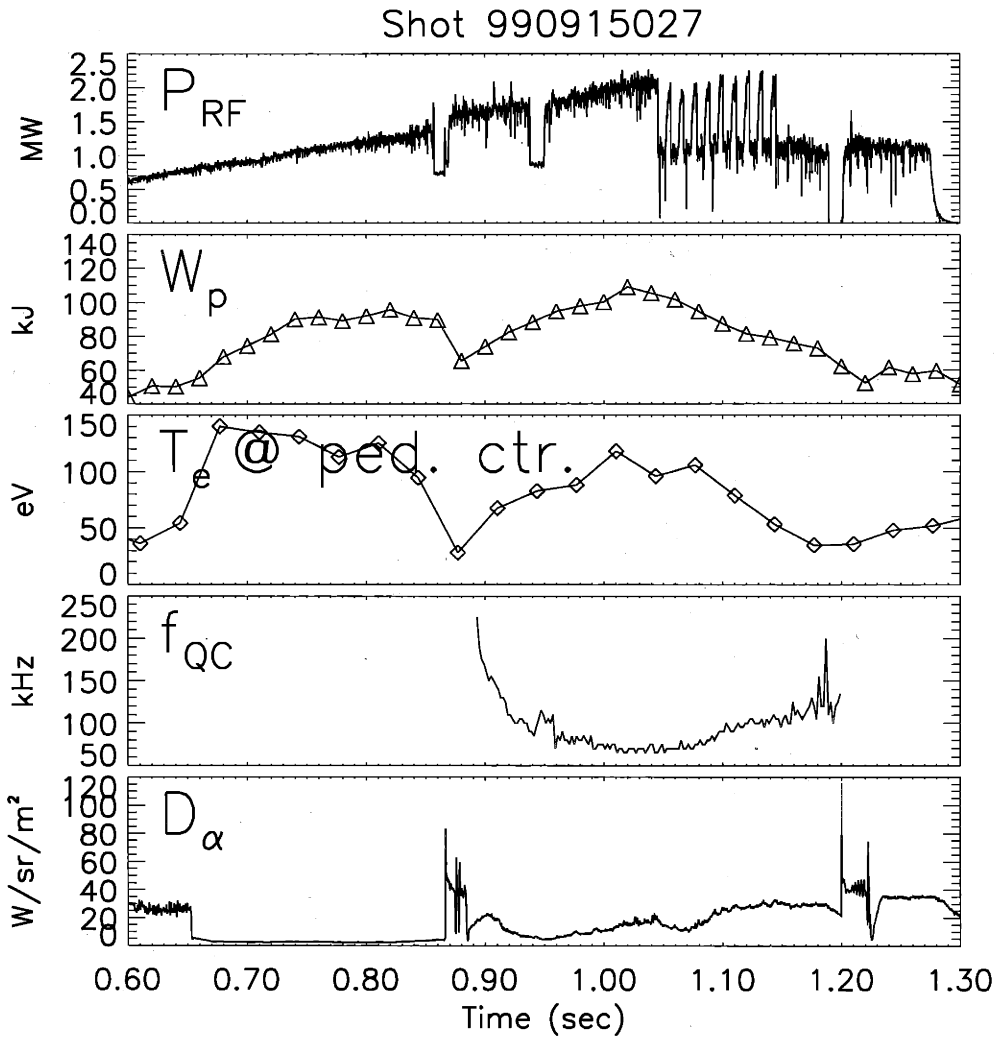

Figure 5-20: Observed QC frequency and global plasma parameters vs. time. The higher stored energy and pedestal temperature, the lower the frequency.

5.4.2 Frequency behavior in the laboratory frame

The reflectometry measurement is a lab frame measurement. A bulk plasma motion with velocity $\vec{v}$ will induce a Doppler shift in the observed frequency of the fluctuation,

$$f_{QC} = f_{plasma} + \vec{k} \cdot \vec{v}/2\pi \tag{5.12}$$

where f_{plasma} is the frequency of the fluctuation in plasma frame. It shows that the observed frequency change in the lab frame is determined by f_{plasma}, $\vec{k}$ and $\vec{v}$. Without direct measurement of $\vec{v}$, we are not able to ascertain the frequency change in the plasma frame. In this Section, we present some preliminary observations on the frequency behavior of the QC fluctuations.

As shown in earlier figures, for example, Fig. 5-1, we see that the peak frequency of the QC fluctuations changes significantly in the EDA period. The frequency seems to scale with plasma stored energy (Fig. 5-20). The higher the stored energy, the smaller the frequency. The frequency might also change together with the pedestal temperature as indicated in this figure.

Fig. 5-21 shows a plot of f_{QC} versus plasma stored energy over plasma total current (W_p/I_p). Each point represent a time point in a steady EDA period. If we assume that f_{plasma} is small or near zero, and the mode k is relative constant for different discharges, Fig. 5-21 might indicate that the poloidal velocity at the pedestal center may correlate with W_p/I_p, as has been seen for the core toroidal rotation (Refs. [27][28]). To test this hypothesis, a direct measurement of plasma velocity at the pedestal is needed. The measurement will be available from charge exchange recombination spectroscopy (CXRS) on the diagnostic neutral beam (DNB) (Ref. [31]).

Summary

The QC fluctuations are mostly localized near the center of density pedestal with a small shift toward the lower part of the pedestal. The radial width of these fluc-

tuations, W, is usually in the range of $0.1 - 0.3$ cm. W is weakly correlated with the resistivity, η, at the center of the pedestal. W increases with the increase of η. The line-integrated fluctuation level approximately scales with $(\nu^* q_{95}^2)^{0.55}$. The result indicates that higher q_{95}, higher density, and lower temperature are favored for the QC fluctuations. Neither the location nor the width changes significantly in an EDA H-mode period, while the frequency and level vary. Both theoretical models on resistive ballooning mode and drift ballooning mode show promising agreements with experimental results.

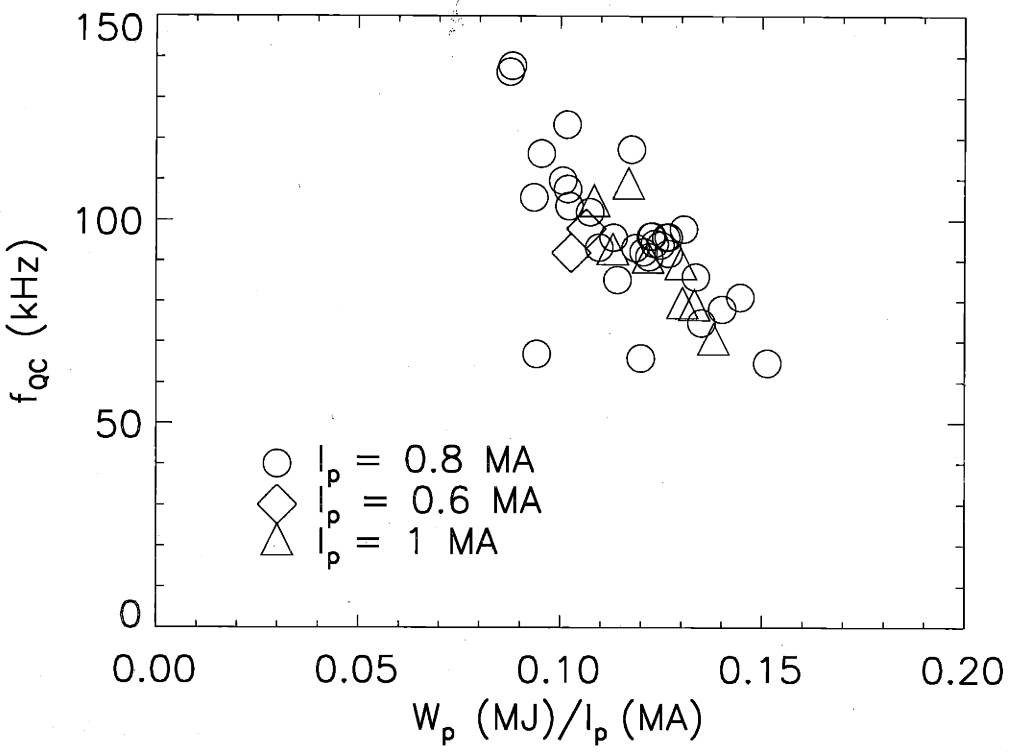

Figure 5-21: Peak frequency of the QC fluctuations in steady EDA periods vs. W_p/I_p.

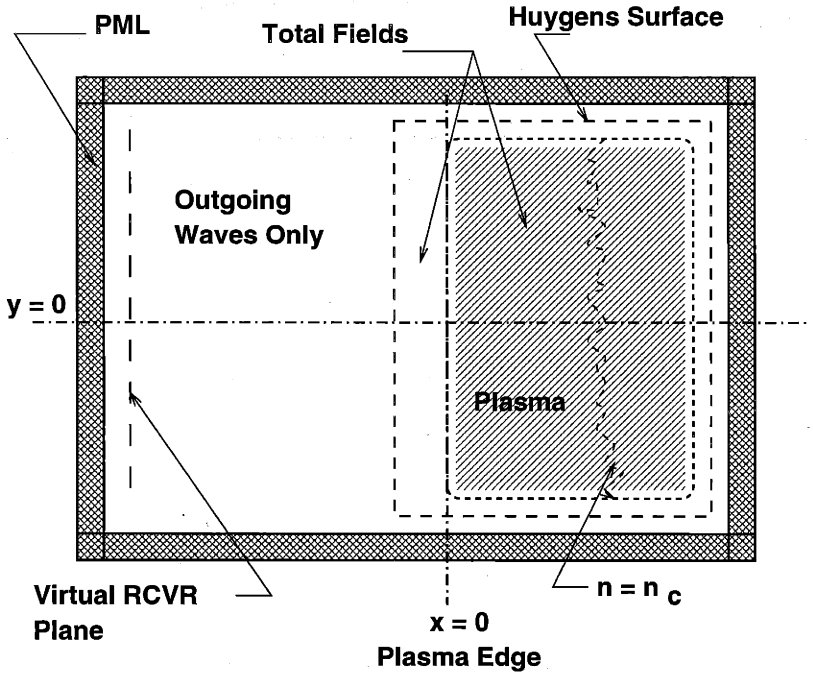

Figure 6-1: Computation box of the 2-D full-wave reflectometry simulation code. It consists of PML boundary, Huygens surface, plasma, receiving plane, and vacuum region. Incident waves are generated from sources on the Huygens surface, and reflected waves from plasma are recorded at the receiving plane.

simulate Gaussian beams incident on realistic 2-D plasma geometry.

The 2-D computation box of the new code is illustrated in Fig. 6-1. In this setup, $\vec{e}_x$ is in the direction of $-\vec{R}$ for the Alcator C-Mod reflectometer, and $\vec{e}_y$ is in the $\vec{Z}$ direction of conventional tokamak coordinates. The computation box consists of the main field region, perfectly-matched-layer (PML) boundary, Huygens surface, plasma, receiving plane, and vacuum region. The 2-D full-wave code is described in detail in this Chapter.

6.1 Calculation in the main field region

The 2-D full-wave code has been developed based on an earlier code (Ref. [5]) to simulate O-mode ($\vec{E} = E_z(x,y)\vec{e}_z \parallel \vec{B}$) reflectometry fluctuation signals. We start

Chapter 6

2-D full-wave reflectometry simulation code

Reflectometry has been widely used to measure plasma density fluctuations in magnetically confined fusion experiments. However, the interpretation of the fluctuations in reflectometry signals in terms of plasma fluctuations is still incomplete, as is the interpretation of the radial correlation of turbulences (see discussion in Chapter 3). The critical density of the 88 GHz mm-wave channel ($n_c = 0.96 \times 10^{20}$ m^{-3}) of the O-mode reflectometer in Alcator C-Mod is usually in the H-mode pedestal region, which has a sharp density gradient (density scale length ≤ 0.5 cm). The WKBJ approximation fails in this region. The quasi-coherent fluctuations seen in EDA H-modes have poloidal wavenumber $k_\perp \sim 2 - 6$ cm^{-1} as measured by PCI. This range of wavenumber corresponds to $\lambda_\perp / w_b \sim 1$, where w_b is the half width of $1/e$ intensity of the incident reflectometry mm-wave beam. A model including the beam profile, plasma density profile, and curvature must be used to confidently interpret the reflectometry fluctuation measurements in Alcator C-Mod.

A new code based on the earlier 2-D full-wave simulation code (Maxwell code) (Ref. [5]) has been developed. Studies using the Maxwell code first demonstrated the importance of 2-D effects in interpreting reflectometry measurements. The new code incorporates additional electro-magnetic field computation techniques such as perfectly-matched-layer boundary and the Huygens source technique. It is able to

from normalized Maxwell's equations under the cold plasma approximation:

$$\frac{\partial H_x}{\partial t} = -\frac{\partial E_z}{\partial y}, \tag{6.1}$$

$$\frac{\partial H_y}{\partial t} = \frac{\partial E_z}{\partial x}, \tag{6.2}$$

$$\frac{\partial J_z}{\partial t} = \frac{n_e}{n_c}\pi E_z, \tag{6.3}$$

$$\frac{\partial E_z}{\partial t} = -4\pi J_z + \frac{\partial H_y}{\partial x} - \frac{\partial H_x}{\partial y}, \tag{6.4}$$

where lengths are normalized to the vacuum wavelength of the incident beam λ_0 ($\lambda_0 \simeq 0.34$ cm for the 88 GHz microwave), and times are normalized to the microwave period $\tau_0 = 1/f_0$. The critical density n_c is $(f_0/89.8)^2 \times 10^{20}$ m^{-3} with f_0 in GHz. These normalized units are used throughout this Chapter[1]

We use the standard finite-difference time-domain (FDTD) method as described in Ref. [85] to calculate electric and magnetic fields. The FDTD grid-mesh is shown in Fig. 6-2. We assign electric field ($E_z[i,j]$), current density ($J_z[i,j]$), and electron density ($n_e[i,j]$) at the center of each grid square $[i,j]$, where $x = (i+1/2)\Delta x$, $y = (i+1/2)\Delta y$, $i,j = 0,1,2...$, and Δx, Δy are the grid sizes, but assign magnetic fields, H_x and H_y, at the sides of the grid square, labeled as $H_x[i,j-1/2]$ and $H_y[i-1/2,j]$. It should be pointed out that the calculation would be unstable if one calculated all quantities at the same locations. Using a version of the Yee algorithm (Ref. [85] and references therein), iterations from time $t = n\Delta t$ to $t = (n+1)\Delta t$ are

$$J_z^{n+1}[i,j] = J_z^n[i,j] + \pi\Delta t E_z^n[i,j] n_e[i,j]/n_c, \tag{6.5}$$

$$H_x^{n+1}[i,j-1/2] = H_x^n[i,j-1/2] - \left\{E_z^n[i,j] - E_z^n[i,j-1]\right\}\Delta t/\Delta y, \tag{6.6}$$

$$H_y^{n+1}[i-1/2,j] = H_y^n[i-1/2,j] + \left\{E_z^n[i,j] - E_z^n[i-1,j]\right\}\Delta t/\Delta x, \tag{6.7}$$

$$\begin{aligned} E_z^{n+1}[i,j] = {} & E_z^n[i,j] - 4\pi\Delta t J_z^{n+1}[i,j] \\ & + \left\{H_y^{n+1}[i+1/2,j] - H_y^{n+1}[i-1/2,j]\right\}\Delta t/\Delta x \\ & - \left\{H_x^{n+1}[i,j+1/2] - H_x^{n+1}[i,j-1/2]\right\}\Delta t/\Delta y. \end{aligned} \tag{6.8}$$

[1]Constants like ϵ_0 and μ_0 are set to unity, and we treat the problem as a general wave propagation problem.

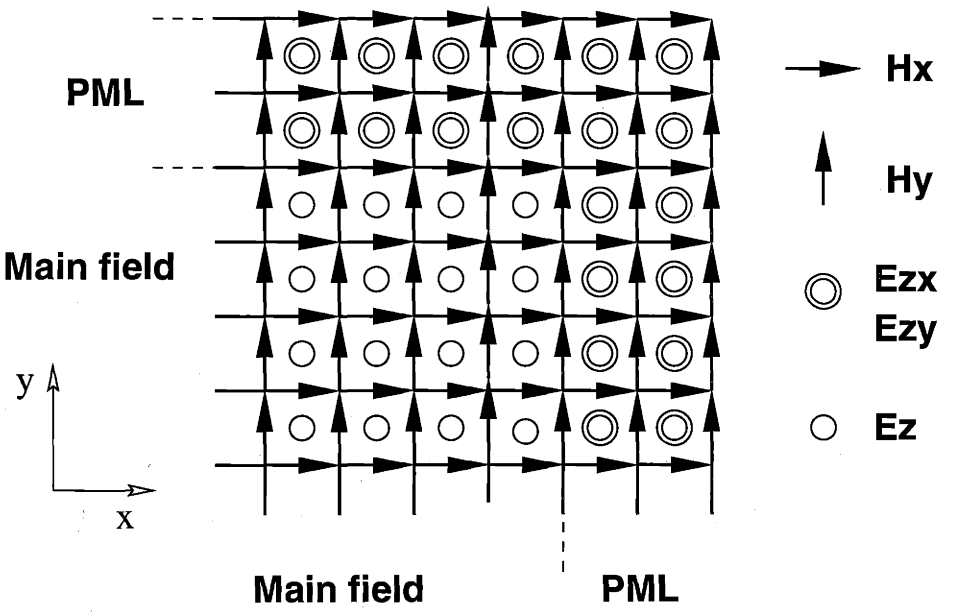

Figure 6-2: FDTD mesh in the main field region and PML boundary. Note that E_z nodes and H_x, H_y nodes are not at the same locations. E_z nodes become E_{zx} and E_{zy} nodes in PML boundary, while $E_z = E_{zx} + E_{zy}$ at the interface.

We should consider the grid-dispersion error and code stability when choosing Δx, Δy, and Δt. We usually choose $\Delta x = \Delta y$. The grid-dispersion error is in the order of $(\Delta x/\lambda_0)^2$. A sufficient condition for computational stability is the Courant criterion. For simulation in 2-D, the Courant criterion is

$$\frac{\Delta x}{\Delta t} > \frac{c}{\sqrt{2}}, \tag{6.9}$$

which implies that the time step Δt has to be less than the shortest wave traveling time between two adjacent grids in order to satisfy causality. Typically, the grid size $\Delta x = \Delta y = 0.1\lambda_0$ and time step $\Delta t = 0.05\tau_o$ are used in our simulation so as to obtain adequate precision and also ensure computational stability.

6.2 Perfectly-matched-layer absorption boundary

Full-wave simulation needs appropriate boundary conditions. Setting all field values equal to zero at the boundary of the computation box creates a boundary of ideal conductor. It is valid only if we use a very large computation box or study an ultra-short time scale (for example, a pulse). Using a periodic boundary condition, which implies that the incident beam has an infinite size, is not realistic either. As a result, full-wave simulations typically use a boundary that absorbs the waves propagating out of the computation domain. An ideal absorption boundary should have a matched impedance with the medium (usually vacuum) outside the computation box so that no wave reflection occurs at the boundary. Instead of a radiative absorption boundary as used in the Maxwell code, the new code uses a better absorption boundary — perfectly-matched-layer (PML) boundary (Ref. [86]).

A PML is made of a virtual medium in which electric and magnetic fields satisfy the following modified Maxwell's equations:

$$\frac{\partial H_x}{\partial t} = -\frac{\partial (E_{zx}+E_{zy})}{\partial y} - 4\pi\sigma_y^* H_x, \tag{6.10}$$

$$\frac{\partial H_y}{\partial t} = \frac{\partial (E_{zx}+E_{zy})}{\partial x} - 4\pi\sigma_x^* H_y, \tag{6.11}$$

$$\frac{\partial E_{zx}}{\partial t} = \frac{\partial H_y}{\partial x} - 4\pi\sigma_x E_{zx}, \tag{6.12}$$

$$\frac{\partial E_{zy}}{\partial t} = -\frac{\partial H_x}{\partial y} - 4\pi\sigma_y E_{zy}, \tag{6.13}$$

where σ and σ^* are electric and magnetic conductivities respectively. $E_z = E_{zx} + E_{zy}$ at the intersection with the main field. If we set $\sigma = \sigma^* = 0$, we recover the "real" Maxwell's equations in vacuum. If $\sigma_x^* = \sigma_y^* = 0$, but $\sigma_x = \sigma_y \neq 0$, the medium is just a usual conductive medium.

A PML medium is described by a four-component conductivity, $(\sigma_x, \sigma_x^*; \sigma_y, \sigma_y^*)$. As proved in Ref. [86], the reflectivity of EM waves at the interfaces of two PML media satisfies the following rules:

- Reflection is null at an interface normal to $\hat{x}$ lying between a vacuum and a

$(\sigma_x, \sigma_x^*; 0, 0)$ PML medium, or between a $(0, 0; \sigma_y, \sigma_y^*)$ medium and a $(\sigma_x, \sigma_x^*; \sigma_y, \sigma_y^*)$ medium.

- Reflection is null at an interface normal to $\hat{y}$ lying between a vacuum and a $(0, 0; \sigma_y, \sigma_y^*)$ PML medium, or between a $(\sigma_x, \sigma_x^*; 0, 0)$ medium and a $(\sigma_x, \sigma_x^*; \sigma_y, \sigma_y^*)$ medium.

The PML boundary is built to obtain null reflection for normal incident waves according to the two rules above. Fig. 6-3 shows that each side or corner of the PML boundary has a different four-component conductivity. We should set $\sigma = \sigma^* = 0$ at the outer boundary of the PML to match the condition of vacuum, but set σ and σ^* at the inner boundary of PML to match the medium in the main field region, which is also vacuum in most cases. Therefore, we choose a parabolic conductivity profile:

$$\sigma(\rho) = \sigma_{max} \left[1 - \left(\frac{\rho - \delta/2}{\delta} \right)^2 \right]^2, \tag{6.14}$$

where δ is the thickness of the PML, $\rho = 0$ at the inner boundary, and $\rho = \delta$ at the outer boundary. A thickness $\delta = 2\lambda_0$ is usually chosen in our simulation.

The modified Maxwell's Eqs. 6.10–6.13 at each part of the PML boundary are also solved by the FDTD method together with special treatments based on the field continuity at PML–PML interfaces and interfaces between the PML boundary and the main field region.

The absorption efficiency of a PML boundary is determined by the boundary thickness, δ, and conductivity profiles. The reflectivity of the PML boundary in our normalized units is

$$\mathcal{R} \simeq \exp\left(-2\cos\theta \int_0^\delta 4\pi\sigma(\rho)\, d\rho \right), \tag{6.15}$$

where θ is the wave incident angle onto the boundary, and $\sigma^* = \sigma$. Eq. 6.15 suggests that a thicker PML boundary with larger σ and σ^* has better absorption. However, a thicker PML boundary also requires more grids in the full-wave simulation, and reduces the simulation efficiency. Large σ (or σ^*) may also create sharp gradient in σ (or σ^*) profile, which may induce wave scattering. As a result, there is an optimum

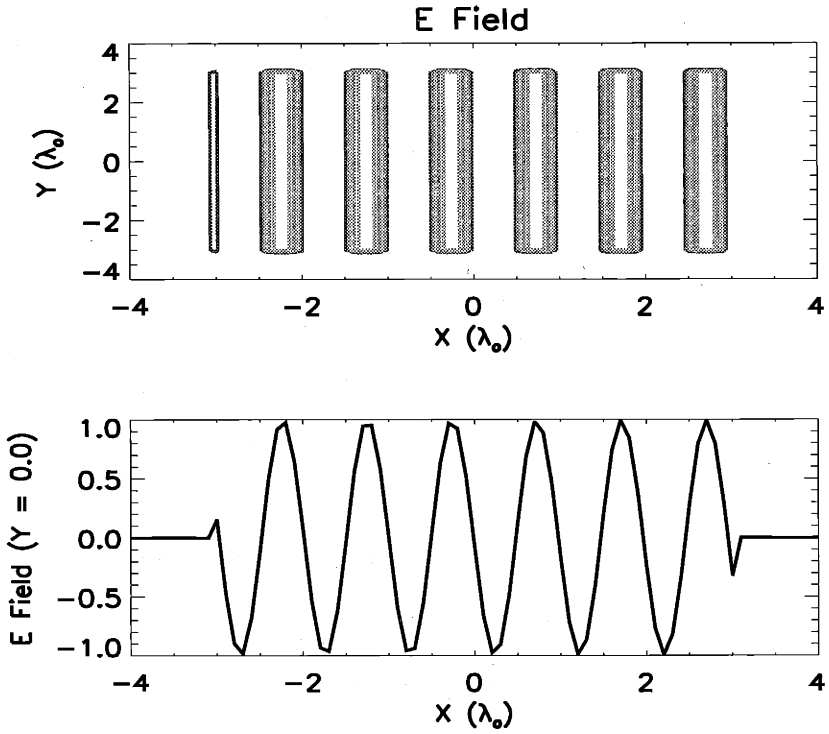

Figure 6-6: A plane wave propagating in vacuum. The plane wave is generated using the Huygens sources technique and PML boundary. The upper figure shows contours of the electric field. The Huygens surface is the rectangle with the lower-left corner at $(-3\lambda_0, -3\lambda_0)$ and the upper-right corner at $(3\lambda_0, 3\lambda_0)$. The wave propagates in $+\vec{x}$ direction. Note that fields outside the Huygens surface are nearly zero ($< 0.1\%$) as shown in the lower figure.

The second advantage suggests that we can avoid numerical horns, which are used in 2-D total-field reflectometry simulation such as the Maxwell code.

Fig. 6-6 shows contours of the electric field of a plane wave propagating in vacuum. The plane wave is generated using the Huygens source technique together with the PML boundary. Note that the amplitude of the electric field outside the Huygens surface are less than 0.1% of the amplitude of the plane wave. The value 0.1%, instead of an exactly zero, comes from the discrete nature of the FDTD method, where $\vec{M}_s^h$ nodes and $\vec{J}_s^h$ nodes do not overlap and the Huygens surface S has a finite thickness.

In the simulation code, the Huygens surface is a rectangle constructed around the plasma (see Fig. 6-1). Plasma densities $n_e(x, y)$ are derived from experimental

$$\frac{\partial H_y}{\partial t} = \frac{\partial E_z}{\partial x} - 4\pi M^h_{s,y}, \tag{6.20}$$

$$\frac{\partial J_z}{\partial t} = \frac{n_e}{n_c}\pi E_z, \tag{6.21}$$

$$\frac{\partial E_z}{\partial t} = -4\pi J_z + \frac{\partial H_y}{\partial x} - \frac{\partial H_x}{\partial y} - 4\pi J^h_{s,z}. \tag{6.22}$$

We have following relations regarding the newly-created EM fields on the two sides of surface S:

$$\vec{n} \times (\vec{E}_1 - \vec{E}_2) = -\vec{M}^h_s, \tag{6.23}$$

$$\vec{n} \times (\vec{H}_1 - \vec{H}_2) = \vec{J}^h_s, \tag{6.24}$$

where $\vec{E}_1$ and $\vec{H}_1$ are electric and magnetic fields just inside surface S, and $\vec{E}_2$ and $\vec{H}_2$ are fields just outside S. Comparing with the definition of $\vec{J}^h_s$ and $\vec{M}^h_s$ in Eq. 6.17 and Eq. 6.18, we find a solution for Eq. 6.23 and 6.24:

$$\vec{E}_1 = \vec{E}^{inc}, \tag{6.25}$$

$$\vec{H}_1 = \vec{H}^{inc}, \tag{6.26}$$

$$\vec{E}_2 = 0, \tag{6.27}$$

$$\vec{H}_2 = 0. \tag{6.28}$$

This solution must be the only physical solution as required by the uniqueness theorem. Therefore, the fields inside surface S generated by $\vec{M}^h_s$ and $\vec{J}^h_s$ are identical to those radiated from source P, but the EM fields everywhere outside surface S are zero. Now, we put the plasma into the Huygens surface, and again generate the EM fields from $\vec{M}^h_s$ and $\vec{J}^h_s$. As shown above, the fields inside the Huygens surface are identical to those generated by source P, but the fields outside of the Huygens surface S now consist only those from the reflected waves. In general, the Huygens source technique has two advantages:

1. Create waves for which sources do not have explicit analytic expressions;

2. Separate the reflected waves from the total fields.

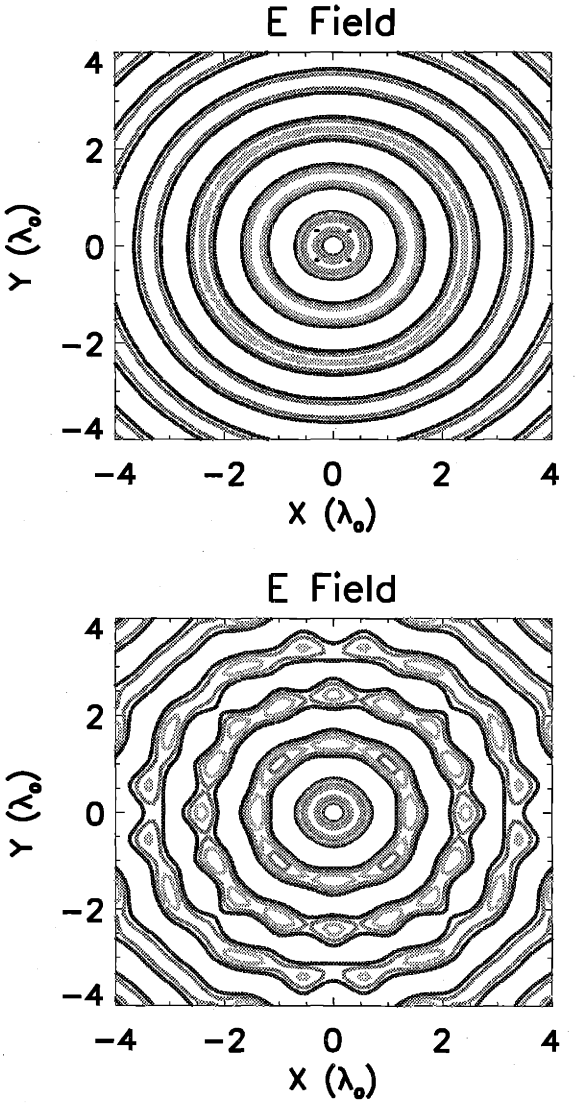

Figure 6-4: PML absorption efficiency test. Waves are generated by a point source at the center, $J_z = 10\sin(2\pi t/\tau_0)$, and propagate in vacuum. The upper figure shows the case of the optimum PML ($4\pi\sigma_{max} = 45$), while the lower figure shows a poor PML boundary with $4\pi\sigma_{max} = 1$. A standing wave pattern is built up in the lower figure ($t = 100\tau_0$) due to the insufficient absorption capability of the boundary.

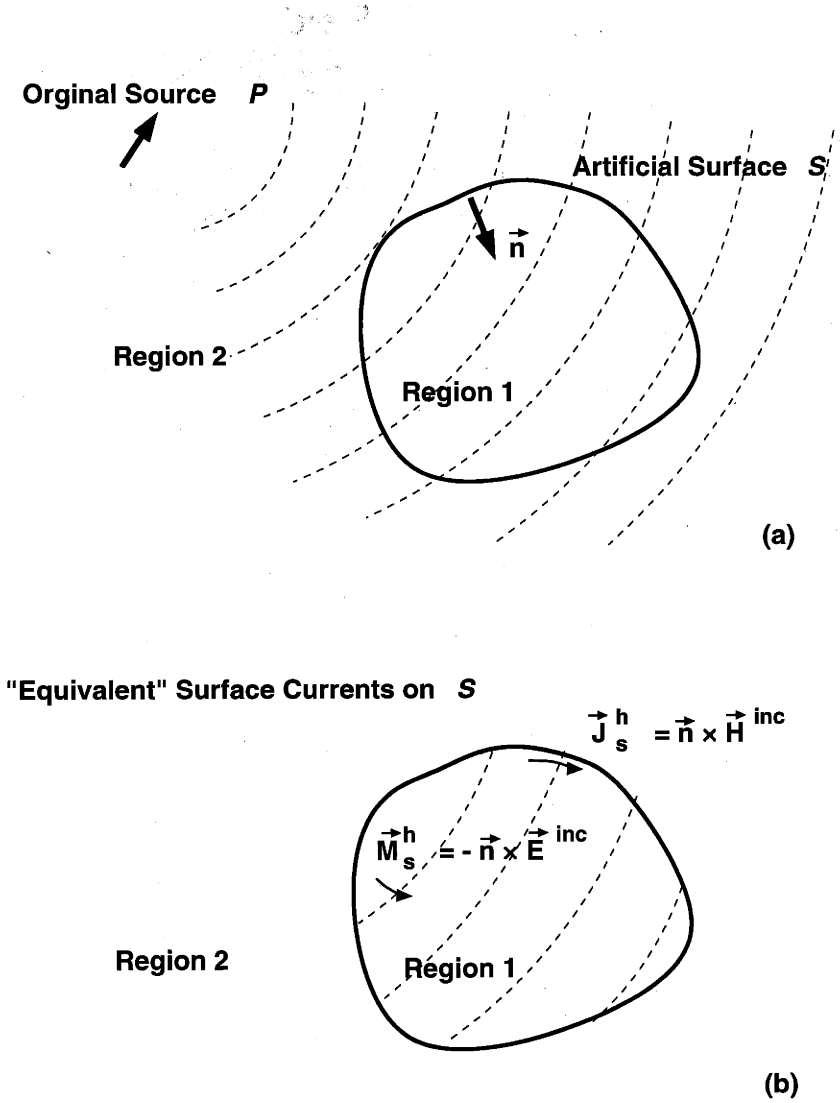

Figure 6-5: Huygens source technique. Huygens current sources on the surface S in Fig. (b) substitute the original source P in Fig. (a). Identical fields in region 1 are produced as with source P, but zero fields in region 2 if no plasma is present. If plasma introduced in region 1, fields in region 2 will be scattered (reflected) fields only.

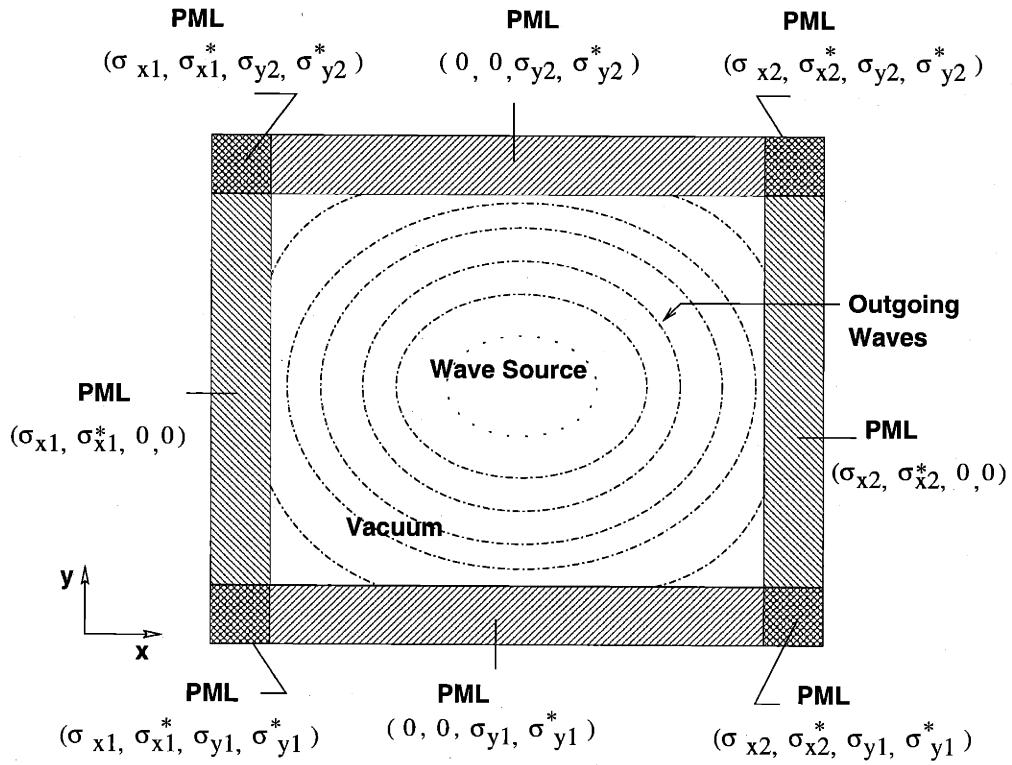

Figure 6-3: The four-component conductivities $(\sigma_x, \sigma_x^*; \sigma_y, \sigma_y^*)$ of the PML boundary are different at different parts of the boundary. The absorption efficiency of PML is determined by the boundary thickness and conductivity profiles.

choice of δ and σ.

Substituting our conductivity profiles (Eq. 6.14) into Eq. 6.15, we can estimate the reflectivity of the PML boundary in our code,

$$\mathcal{R} \simeq \exp\left[-\frac{4}{3}\left(4\pi\sigma_{max}\right)\cos\theta\right]. \tag{6.16}$$

A value $4\pi\sigma_{max} = 45$ has been selected to have the best absorption through numerical tests. Fig. 6-4 shows the difference of the optimum PML boundary and a PML boundary that does not have sufficient absorption capability. Numerical tests showed that the optimum PML boundary in our code has a reflection coefficient less than 0.1% for incidence angles up to 83^0. Eq. 6.16 indicates that the reflectivity is close to 1 (no absorption) for near grazing incidence, $\theta \rightarrow 90^0$. This is not a concern for the simulation because these waves are absorbed by other PMLs. For instance, a

wave propagating towards the left boundary with a near grazing angle will finally arrive at the top or bottom PML boundary with a near normal incident angle where it will be "perfectly" absorbed. Therefore, the PML boundary ensures the reliability of simulation on a long time scale.

6.3 Huygens source technique

Some types of wave, such as a pure plane wave, cannot be generated by finite current sources. Moreover, in principle, reflectometry only measures waves propagating towards the receiver instead of the total fields in Maxwell's equations. We use the Huygens source technique (Ref. [87]) to generate incident waves and also to separate reflected waves from the total fields.

The Huygens source technique is based on the uniqueness theorem of electrodynamics: The EM fields inside a closed surface is uniquely determined by the EM fields on the surface. The technique is illustrated in Fig. 6-5. Here, we have a wave source P in region 2 and plasma in region 1, and we want to calculate the scattered (and reflected) fields by the plasma in region 2. We draw a closed surface S — Huygens surface — around region 1. If the fields from the source P on the Huygens surface, $\vec{E}^{inc}$ and $\vec{H}^{inc}$, are known or analytically calculable in the absence of plasma, such as plane waves, Gaussian beams, and spherical waves, we can obtain Huygens electric surface current density, $\vec{J}_s^h$, and magnetic surface current density, $\vec{M}_s^h$, on surface S:

$$\vec{J}_s^h = \vec{n} \times \vec{H}^{inc}, \tag{6.17}$$

$$\vec{M}_s^h = -\vec{n} \times \vec{E}^{inc}, \tag{6.18}$$

where $\vec{n}$ is an inward unit vector normal to S. Then, we remove the original source P, and generate EM waves using the following Maxwell's equations incorporating $\vec{M}_s^h$ and $\vec{J}_s^h$:

$$\frac{\partial H_x}{\partial t} = -\frac{\partial E_z}{\partial y} - 4\pi M_{s,x}^h, \tag{6.19}$$

$$w^2 = w_0^2\left[1+\left(\frac{\lambda x}{\pi w_0^2}\right)^2\right], \tag{6.33}$$

$$R = x\left[1+\left(\frac{\pi w_0^2}{\lambda x}\right)^2\right], \tag{6.34}$$

$$r^2 = z^2+y^2, \tag{6.35}$$

$\lambda = 2\pi/k$, w_0 is the beam waist, and E_0 is the beam amplitude. The magnetic field of the Gaussian beam is assumed to have the same value as the electric field in our normalized units. To generate a Gaussian beam, we calculate the Huygens source, $\vec{M}_s^h$ and $\vec{J}_s^h$, using Eq. 6.31 and Eqs. 6.17-6.18.

Fig. 6-7 shows two examples of Gaussian beam generated using the Huygens sources technique. Beam waist $w_0 = 4\lambda_0$, and it is located at the position of $x = -10\lambda_0$. The left Huygens surface is at $x = -\lambda_0$. Fig. 6-7-(a) and Fig. 6-7-(b) show a Gaussian beam propagating in vacuum. In Fig. 6-7-(c) and Fig. 6-7-(d), the incident beam is at a 5^0 angle relative to the x-direction towards a plasma, which has an elliptical shape with a center $x = 30\lambda_0$ and elongation $\kappa = 1.6$. Contours of electron density, $n_e(x,y)/n_c$, are also over-plotted in Fig. 6-7-(c). The interference pattern between the incident beam and reflected waves only appears inside the Huygens surface ($x > -\lambda_0$). In the region outside the Huygens surface ($x < -\lambda_0$), the electric fields only consist of those of the reflected waves.

6.5 Reflectometry received signal

The reflectometry received signal is the integrated electric field at the receiving aperture. We use the following approach to obtain reflectometry signals from the simulated 2-D electric field, $E_z(x,y,t)$.

The plasma is assumed to be static for each run of the simulation. The propagation time of the generated waves is long enough so that steady state is reached. Usually, a simulation time $t_s \simeq 3t_g$ is sufficient to reach such steady state, where t_g is the 1-D group delay from the Huygens surface to the receiving plane. In order to save CPU time and memory, all fields, E_z, H_x and H_y, in the simulation are in float (or double

measured profiles at the mid-plane and mapped to 2-D by assuming that n_e is constant on flux surfaces. The left side of Huygens surface is chosen to have a distance of λ_0 to the plasma edge. A Huygens surface must enclose all "scatterers". Therefore, we allow the plasma density to drop exponentially down to zero at the upper and lower plasma boundaries. Although this setup differs from the reality, it does not undermine the simulation result as long as the height of the computation box is much larger than the incident beam width[2].

6.4 Gaussian beam

We use a Gaussian beam to approximate the reflectometer antenna radiation near the plasma. This approximation is valid as long as the radiation level in the major lobe of the antenna pattern is much larger than that in the side-lobes. A Gaussian beam is the fundamental mode solution of waves in a homogeneous medium under the paraxial approximation. Starting from the wave equation

$$\nabla^2 E + k^2 E = 0, \tag{6.29}$$

writing $E = u(x, y, z) \exp(-jkx)$, and using the paraxial approximation,

$$\frac{\partial^2 u}{\partial x^2} << \frac{\partial^2 u}{\partial y^2} + \frac{\partial^2 u}{\partial z^2}, \tag{6.30}$$

we have the solution of a Gaussian beam propagating in the $+\hat{x}$ direction

$$E = \frac{E_0}{w}\sqrt{\frac{2}{\pi}} \exp\left[-j(kx - \Phi) - r^2\left(\frac{1}{w^2} + \frac{jk}{2R}\right)\right], \tag{6.31}$$

where

$$\Phi = \arctan\left(\frac{\lambda x}{\pi w_0^2}\right), \tag{6.32}$$

[2]It also implies that the code is not good at simulating plane-wave incidence.

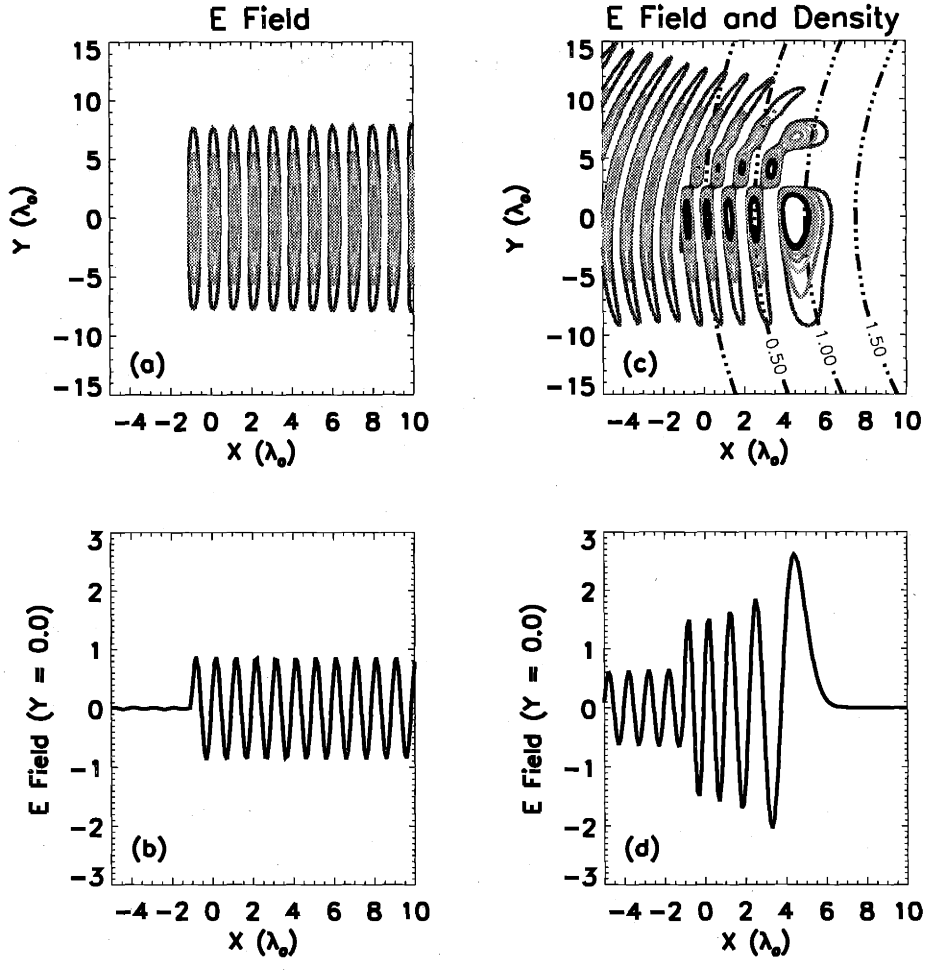

Figure 6-7: Examples of Gaussian beam generated by the Huygens sources technique. Beam waist $w_0 = 4\lambda_0$, and it is located at $x = -10\lambda_0$. The left Huygens surface is at $x = -\lambda_0$. Fig. (a) and Fig. (b) show a Gaussian beam in vacuum. In Fig. (c) and Fig. (d), plasma has an elliptical shape, center $x = 30\lambda_0$, $\kappa = 1.6$, and the incident beam is at a 5^0 angle relative to the $+x$-direction. The contours of electron density, $n_e(x, y)/n_c = 0.0, 0.5, 1.0$ and 1.5, are also over-plotted in Fig. (c).

precision) format instead of complex fields as in usual field denotation:

$$E_z(x,y,t) = \Re\left[\mathcal{E}(x,y,t)\right], \tag{6.36}$$

where $\mathcal{E}$ is the complex electric field. The complex field distribution at the end of the simulation, $\mathcal{E}(x,y,t_s)$, can be approximately obtained from E_z after steady state is reached:

$$\mathcal{E}(x,y,t_s) \simeq E_z(x,y,t_s) + jE_z(x,y,t_s - \tau_0/4), \tag{6.37}$$

Given a plasma density profile, we extract the reflectometry signal, E_{rcvr}, from the snapshot of $\mathcal{E}(x,y,t_s)$ considering the real geometry of the receiving horn antenna. A horn antenna has a directivity function, which restricts its receiving angle. Mathematically, a directivity function is equivalent to a filter of $\mathcal{E}(x,y,t_s)$ in Fourier transformed k-space. The detected reflectometer signal is the integral of the complex electric field, $\mathcal{E}(x,y,t_s)$, across the receiving horn aperture after passing through this horn directivity, $\mathcal{D}(k_x,k_y)$. We model the complex reflectometry signal E_{rcvr} as:

$$\begin{aligned} E_{rcvr} &= Ae^{j\phi} \\ &= \frac{1}{2\pi}\int_{Aperture} dl \int dk_x \int dk_y\ \mathcal{D}(k_x,k_y)e^{j(k_x x + k_y y)} \\ &\quad \int dx \int dy\ \mathcal{E}(x,y,t_s)e^{-j(k_x x + k_y y)}, \end{aligned} \tag{6.38}$$

where A is the amplitude of the reflectometry signal, and ϕ is the signal phase. Therefore, for a given plasma density distribution, we have a corresponding reflectometry signal E_{rcvr}. By combining results from many runs with identical initial beam condition but different phases of plasma fluctuations or different turbulence structures, we can reconstruct a picture of E_{rcvr} versus plasma fluctuations.

6.6 Simulation on multiple-frequency reflectometry

In order to simulate reflectometry measurements of radial correlation length, we should compare the reflectometry signals from multiple frequencies (multiple critical surfaces). Eqs. 6.1–6.4 uses normalized units λ_0 and $\tau_0 = 1/f_0$. We can simulate a wave with a different frequency f_1 using the same grid and time steps after modifying Eqs. 6.39–6.42 to

$$\frac{\partial H_x}{\partial t} = -\frac{\partial E_z}{\partial y}, \tag{6.39}$$

$$\frac{\partial H_y}{\partial t} = \frac{\partial E_z}{\partial x}, \tag{6.40}$$

$$\frac{\partial J_z}{\partial t} = \left(\frac{1}{\alpha}\right)\frac{n_e}{n_{c0}}\pi E_z, \tag{6.41}$$

$$\frac{\partial E_z}{\partial t} = -4\pi\alpha J_z + \left(\frac{\partial H_y}{\partial x} - \frac{\partial H_x}{\partial y}\right), \tag{6.42}$$

where $\alpha = f_1/f_0$ is the ratio of the two frequencies, and n_{c0} is the critical density for frequency f_0. After this modification, we can compare reflectometry signals of different frequencies at the same time and location. Studies of reflectometry measurements of radial correlation length are presented in Chapter 7.

Chapter 7

Numerical study of reflectometry

In Chapter 5, we studied the QC fluctuations in EDA H-modes using the fluctuations of optical distance. However, we were not able to adequately assess the QC fluctuation level. In order to get further insights of these fluctuations, we need to quantitatively interpret the fluctuation of reflectometry signals in terms of electron density fluctuations. In Section 7.2, the code described in Chapter 6 will be used to simulate the reflectometry with realistic Alcator C-Mod geometry and experimental density profiles (also see Ref. [88]). This study not only provides a calibration curve of the reflectometry response versus the fluctuation level, but it also suggests that plasma curvature may enhance the reflectometry responses to fluctuations with short poloidal wavelength. This super-resolution is further studied in Section 7.3. Section 7.4 shows a preliminary study of reflectometry application on measuring the radial correlation length.

7.1 Simulation parameters of Alcator C-Mod reflectometer

The 2-D full-wave reflectometry simulation code described in Chapter 6 can in principle deal with any 2-D geometry of reflectometry and plasma. In order to simulate the reflectometry measurements in Alcator C-Mod, we input realistic parameter.

For the 88 GHz channel of Alcator C-Mod reflectometer, the vacuum wavelength is $\lambda_0 \simeq 0.34$ cm. We assume the mm-wave near the plasma can be described as a Gaussian beam with the beam waist $w_0 \simeq 2.2\lambda_0$ near the launch horn aperture, which is about $40\lambda_0$ away from the plasma edge. We use the same coordinates as those in Chapter 6. The wave beam has an angle $\theta_b = -5^0$ relative to $+\vec{e}_x$ (that is, $-\vec{R}$ direction).

The receiving horn views at an angle of $+5^0$ relative to $+\vec{e}_x$. The effective horn aperture size is assumed to be $6\lambda_0$. The receiving horn is modelled with 24 dB gain, that is, the peak sensitivity is $10^{2.4}$ times that of a 4π solid angle average. We construct the following 2-D directivity function:

$$\mathcal{D}(\vec{k}) \simeq \exp\left[-\frac{|\vec{k}-\vec{k}_{rcvr}|^2}{(0.01k_0)^2}\right], \tag{7.1}$$

where $k_0 = \lambda_0/2\pi$ is the incident wave wavenumber in vacuum, $\vec{k}_{rcvr}$ is in the optimal receiving direction of the horn antenna and $|k_{rcvr}| = k_0$, and $\vec{k} = k_x\hat{x} + k_y\hat{y}$ is the wave vector of the reflected wave. As described in Section 6.5, we use Eq. 6.38 to obtain the received reflectometry signal $E_{rcvr} = Ae^{j\phi}$ from the 2-D electric field distribution of the reflected waves considering the receiving horn antenna geometry and the directivity function $\mathcal{D}$.

7.2 QC fluctuation level

7.2.1 Model density profile and fluctuation

Fig. 7-1 shows a typical EDA H-mode discharge. The D_α enhancement starts at $t \simeq 0.70$ s shortly after the L-H transition at $t \simeq 0.69$ s. The D_α signal level and density profile reach a steady state after $t \geq 0.81$ s. We use a *tanh* fit for the experimental density profile derived from the high spatial resolution visible continuum

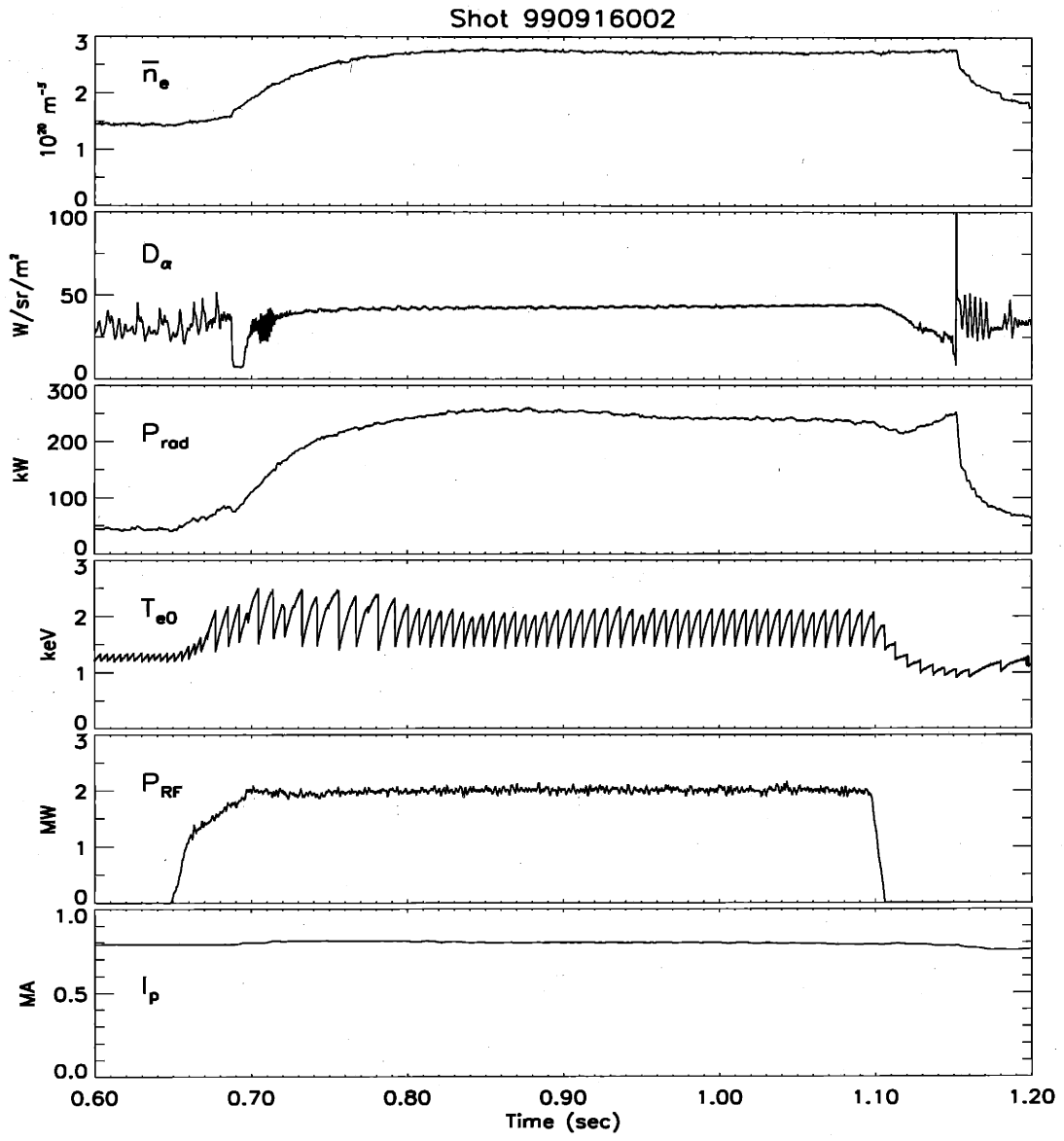

Figure 7-1: An EDA H-mode discharge. The D_α signal enhances shortly after the L-H transition at $t \simeq 0.69$ sec. The EDA H-mode enters a steady state at $0.81 \leq t \leq 1.0$ sec. P_{rad} is the total radiated power, T_{e0} is the core plasma temperature as measured by ECE, P_{RF} is the total ICRF heating powers, and I_p is the total plasma current.

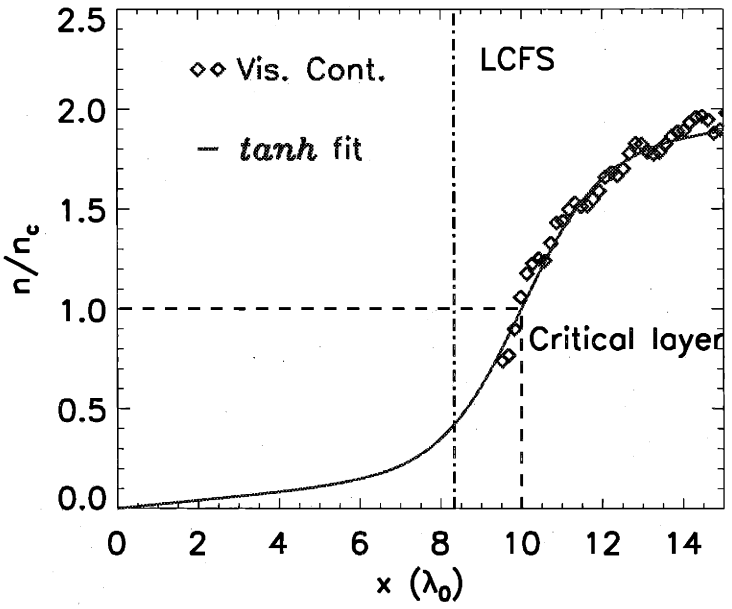

Figure 7-2: The density profile derived from the high-resolution visible continuum array measurement. We use the $x = 0$ point to be the zero density plasma edge for convenience. The profile has been shifted to our coordinates. The separatrix (LCFS) position is also shown. The wave vacuum wavelength $\lambda_0 = 0.34$ cm.

array (Ref. [66]) (Fig. 7-2):

$$n_e(x, y = 0) = 0.8 n_c \left[1 + 0.025 x/\lambda_0 + \tanh\left(\frac{x - 10\lambda_0}{2\lambda_0} \right) \right], \tag{7.2}$$

where $x = 0$ is the model plasma edge at the mid-plane ($y = 0$), and the critical density $n_c = 0.96 \times 10^{20}$ m^{-3} for 88 GHz microwave. As in Chapter 6, here $\hat{x}$ is in the $-\hat{R}$ direction, and $\hat{y}$ is in the $\hat{Z}$ direction in conventional tokamak coordinates. We use a circularly shaped density profile with the center at $X_P = 45\lambda_0$. The radius of curvature, X_P, is estimated from EFIT reconstructed flux surface[1].

In Chapter 5, we showed that the QC fluctuations are localized in the pedestal region. For the purpose of the numerical study, we introduce a poloidal fluctuation centered near the middle of the pedestal with a radial width about half of the pedestal

[1]A better result is $X_P \simeq 60\lambda_0 \simeq 20$ cm. However, as shown in Section 7.3, for the curvature radii in this range, the final result vary insignificantly.

full-width. The fluctuation has a perpendicular (poloidal direction $\hat{\theta}$ in tokamak coordinates) wavelength $\lambda_\perp = 4\lambda_0$ estimated from the PCI measurement:

$$\tilde{n}_e(x,y)/n_e = \eta \times \exp\left[-(x-9.5\lambda_0)^2\right]\cos\left(2\pi y/\lambda_\perp + \varphi_f\right), \tag{7.3}$$

where η is hereafter referred to as the quasi-coherent fluctuation level, and φ_f is the fluctuation phase. The actual form also includes the plasma curvature, that is, fluctuation levels are constant on flux surfaces. The fluctuation radial shape for $x > x_c \simeq 10\lambda_0$ is unimportant due to insignificant microwave penetration.

7.2.2 Simulation results

Fig. 7-3 shows part of the computation box with E_z contours and the density critical layer for the simulation. The computation box is $-17\lambda_0 \leq y \leq 17\lambda_0$ and $-42\lambda_0 \leq x \leq 16\lambda_0$. The left Huygens surface is at $x_H = -\lambda_0$. The E_z field at $x > x_H$ is the total field of the incident beam and the reflected waves while only reflected waves are propagating to the left at $x < x_H$. Interference patterns between the incident Gaussian beam and reflected waves are clear for $x > x_H$.

We run simulations for $0 \leq \varphi_f < 2\pi$, and obtain the reflectometry received signals $E_{rcvr}(\varphi_f) = A(\varphi_f)\exp\left[j\phi(\varphi_f)\right]$, where $A(\varphi_f)$ is the signal amplitude and $\phi(\varphi_f)$ is the signal phase. For φ_f varying from 0 to 2π, both A and ϕ finish a period. Note that in the 1-D geometric optics approximation, $\phi(\varphi_f)$ fluctuates around a constant in an approximately cosine form corresponding the $\cos\varphi_f$ in the fluctuation expression 7.3, while the amplitude A is constant in a period. Because the 1-D result is readily calculable (see Eq. 3.21), we can compare 2-D simulation results with the 1-D result [2].

Fig. 7-4 shows the phase response versus fluctuation level for three different cases. $\Delta\phi = \phi_{max} - \phi_{min}$ is the magnitude of reflectometer phase variation in one period of the fluctuation ($0 \leq \varphi_f < 2\pi$). The figure shows three curves corresponding to the 1-D numerical calculation based on geometric optics approximation, 2-D full-wave with

[2]This 1-D result is the phase fluctuation level of baseband reflectometry signal. It is different than the 1-D result of optical distance as used in Chapter 5.

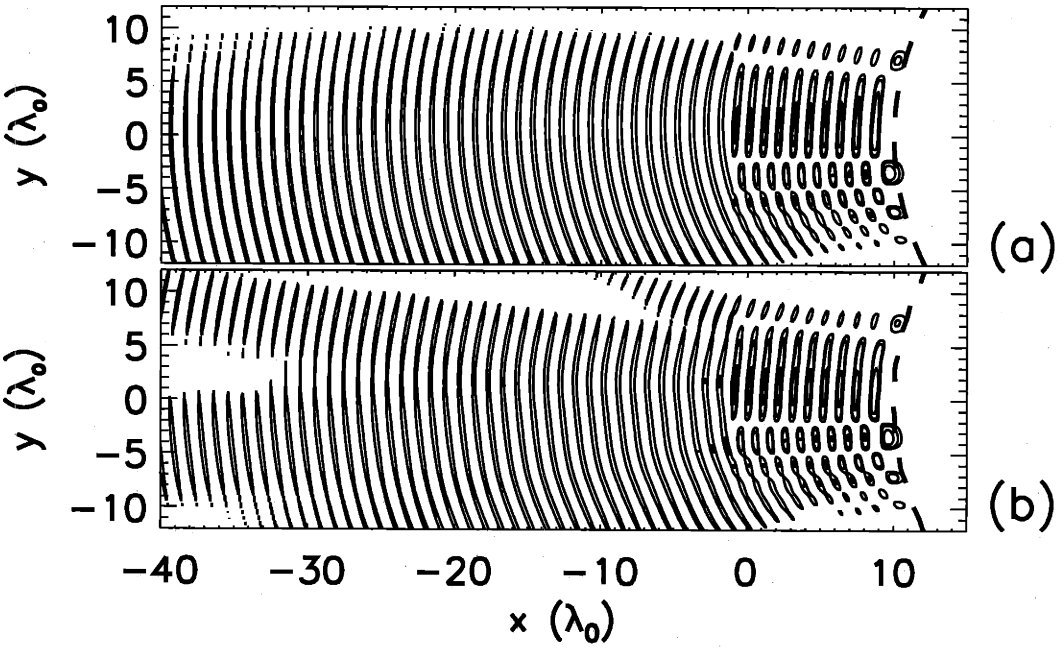

Figure 7-3: Electric field contours from the simulation result. Figure (a) is the case without fluctuations and figure (b) shows the case with $\eta = 0.05$. The cutoff surfaces are also shown as broken curves in the right of both figures.

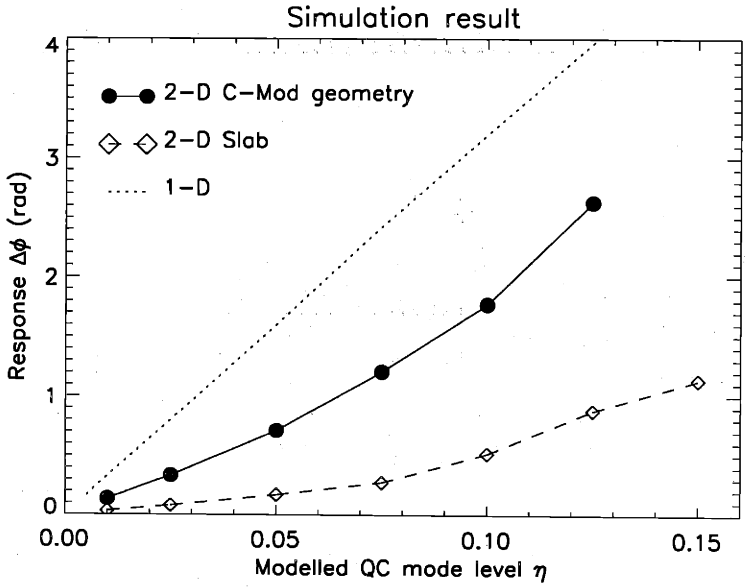

Figure 7-4: Simulation results of reflectometry phase responses vs. fluctuation levels. Results from the 1-D calculation, 2-D curved plasma and 2-D slab plasma simulation are shown. Note that curved plasma simulation result is closer to the 1-D result than the result from slab 2-D plasma simulation.

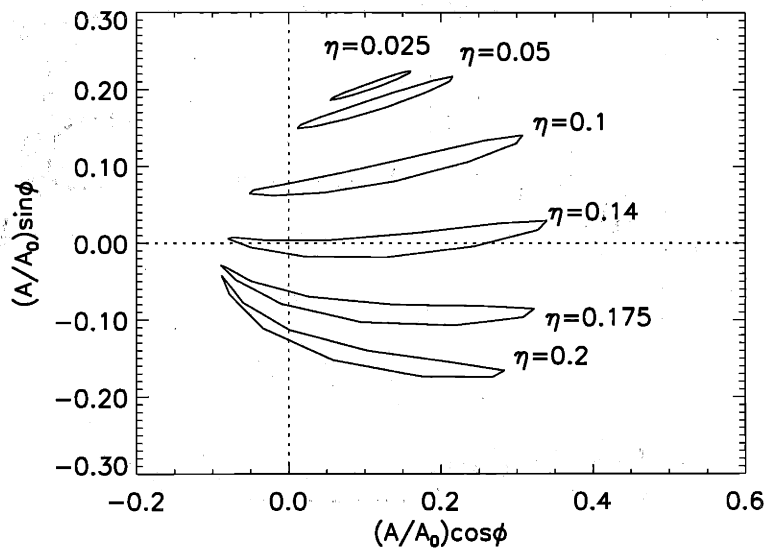

Figure 7-5: Phase runaway phenomenon and nonlinearity to high fluctuation level. The complex reflectometry responses are plotted for different fluctuation levels. For $0.12 < \eta < 0.15$, the response curve encloses the point $(0, 0)$, which induces phase runaway. It should also be noted that for higher η, the reflectometry response is no longer linear.

a slab plasma profile and 2-D full-wave with a curved plasma profile (the one closest to the experimental profile). There is a nearly linear relation between $\Delta\phi$ and η for $\eta \leq 0.1$ in the case of curved plasma simulation result. This result is smaller than the result from the 1-D calculation, but it is much larger than the simulation result of slab plasma geometry. The plasma curvature effect is discussed in detail in Section 7.3. The result from the simulation with plasma curvature provides a calibration curve through which we can infer the level of the quasi-coherent fluctuation in terms of the level of plasma density fluctuation.

For realistic 2-D geometry, there is a limit of the fluctuation amplitude that can be measured by reflectometry. Asymmetry in the measured spectrum introduces ellipticity in the complex plane of the reflectometer signals (Fig. 7-5). As the mode amplitude increases, the point $(0, 0)$ may be enclosed by the curve and the phase changes 2π for a fluctuations period, which leads to the phase runaway phenomenon as discussed in Chapter 4. For our simulation parameters, phase runaway occurs at

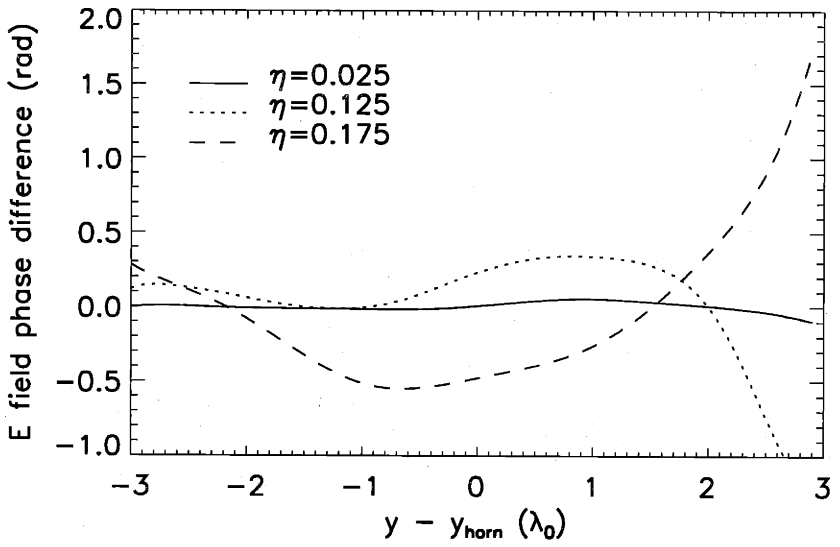

Figure 7-6: Electric field distribution at the horn aperture for different fluctuation level η. The electric field difference are calculated for $\varphi = 0$ and π. Note that it is nearly constant in the whole aperture for small η, but significantly variation for large η, which induces the non-linearity of the reflectometry response.

$0.125 < \eta < 0.15$ as shown in Fig. 7-5.

For even higher fluctuations the linearity between the reflectometer phase and fluctuation level breaks down due to large variations in the phase across the receiving horn aperture even when no phase runaway exists. Fig. 7-6 shows the phase difference across the horn aperture for two fluctuation phases $\varphi_f = 0$ and π at different fluctuation levels η. At low fluctuation level, the phase difference is nearly constant across the aperture. For high fluctuation levels, the variation is large due to strong scattering. The reflectometer signal no longer linearly represents the fluctuation level when the fluctuation level is high.

7.2.3 Experimental observations

The reflectometer signals are measured by I/Q phase detectors, which produce $Q(t) = A(t)\cos\phi(t)$ and $I(t) = A(t)\sin\phi(t)$. From these two signals, we can calculate the reflectometry signal amplitude $A(t)$ and phase $\phi(t)$.

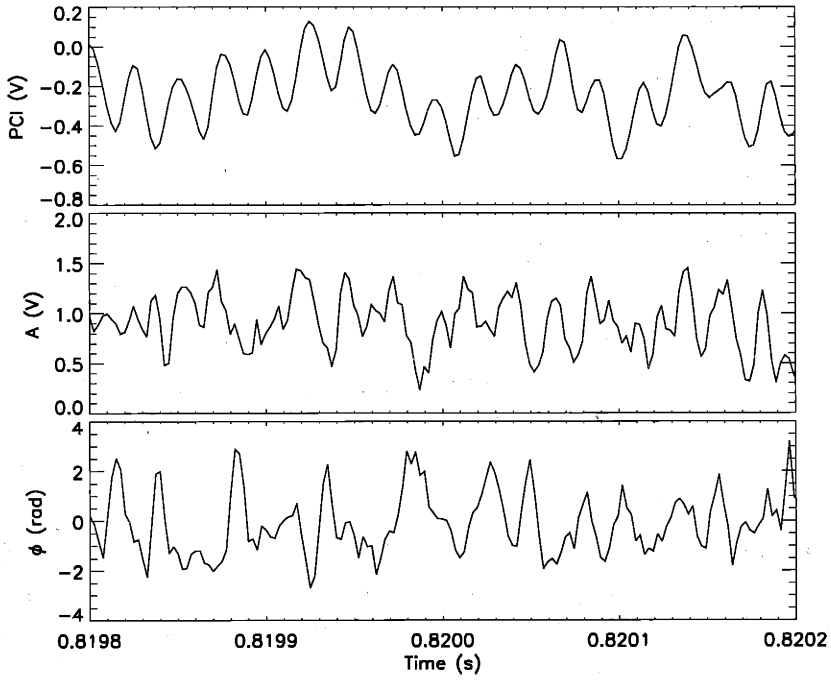

Figure 7-7: Raw fluctuations data from PCI and reflectometry 88 GHz channel in a short time window of the discharge show in Fig. 7-1. Note that a coherent fluctuation at about 100 kHz in all three plots. A is the reflectometry signal amplitude and ϕ is the signal phase. PCI data are taken from the center chord measurement.

Fig. 7-7 shows raw reflectometer data in a short time window of the discharge in Fig. 7-1. Clear quasi-coherent fluctuations are shown ($\simeq$ 100 kHz) in the PCI signal, reflectometry signal amplitude A and phase ϕ.

In order to quantitatively estimate the measured reflectometry signal phase, we should check the raw data carefully. The following procedure is used to obtain the power spectra of reflectometry phase and estimate the level of the quasi-coherent fluctuations in the experimental signal. Data in a 2 ms time window is divided into 4 sub-windows each 0.5 ms wide. In each sub-window, we calculate the raw phase data using $I(t)$ and $Q(t)$, then subtract the average. Also by assuming that the phase difference between any two adjacent points do not exceed $\pm\pi$, we can alleviate phase ambiguity in the data. When the turbulence and the quasi-coherent fluctuation level

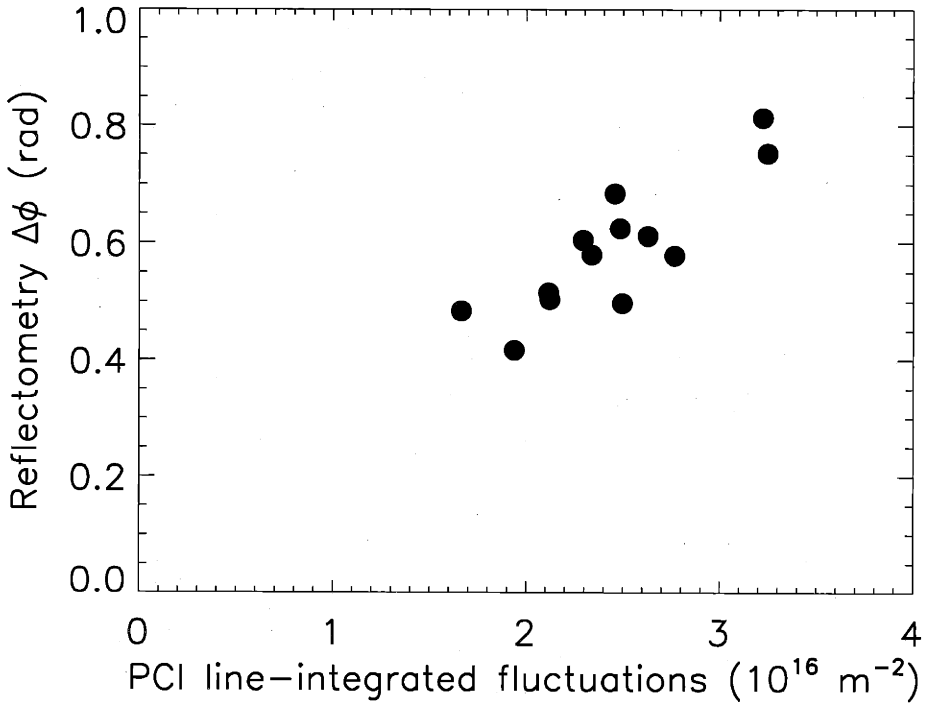

Figure 7-8: Comparison of the phase fluctuation level $\Delta\phi$ of reflectometry and line-integrated fluctuation level measured by PCI.

are small, we can then obtain raw phase data as shown in Fig. 7-7, which are clearly dominated by the quasi-coherent fluctuations. We calculate the auto-power spectrum for each of the four sub-windows. The power spectrum (auto-spectral density) of reflectometry signal phase at the 2 ms window is obtained by an average over the four sub-window using a method described in Ref. [89].

The quasi-coherent fluctuation levels in the reflectometry phase signal are estimated from integrated auto-spectral densities around the coherent peak frequency ($\pm$2 kHz), which occurs at $\sim$ 100 kHz in the time period $0.8 \leq t \leq 1.0$ s of the discharge shown in Fig. 7-1. Fig. 7-8 shows a plot of the quasi-coherent fluctuations level in $\Delta\phi$ measured by reflectometry versus the line-integrated fluctuations, $\int \tilde{n}_e dl$, measured by PCI. These data are taken from $0.8 \leq t \leq 1.0$ s of the discharge shown in Fig. 7-1. PCI signal levels are independently calibrated using acoustic waves before each discharge (Ref. [23]).

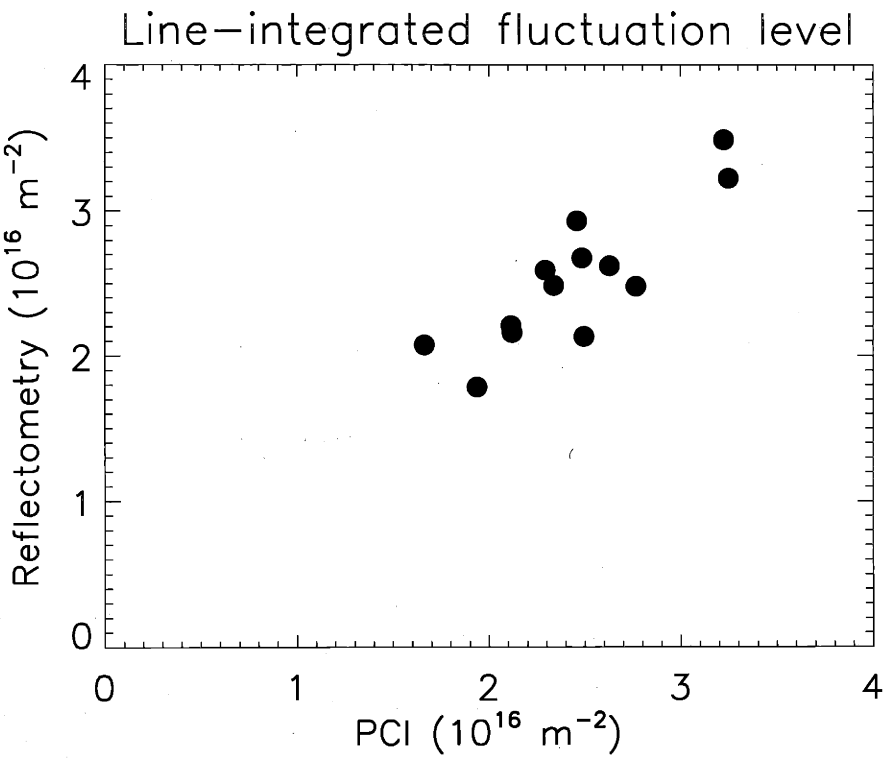

Figure 7-9: Comparison of the line-integrated fluctuation levels of reflectometry and PCI. The reflectometry results are obtained by comparing Fig. 7-8 and the 2-D simulation curve with curvature in Fig. 7-4.

Using the curve of 2-D simulation with curvature shown in Fig. 7-4, we can also calculate the line-integrated fluctuation level from reflectometry measurement. The result is shown in Fig. 7-9, where the line-integrated fluctuation levels from reflectometry and PCI are compared. A good agreement between PCI and reflectometry is shown in Fig. 7-9. Considering the uncertainties in estimating the mode location and width (see Section 5.3), we cannot distinguish the fluctuation level at the outer middle plane (poloidal angle = 0^0), where reflectometry is measuring, and the fluctuation level at poloidal angle at $\pm 90^0$), where PCI is sensitive.

7.3 Plasma curvature effect

Fig. 7-4 in the previous Section suggests that the reflectometry response from the 2-D full-wave simulation including plasma curvature is much larger than that from slab plasma geometry. In this Section, we do further analysis on this curvature effect, and show that the inclusion of the effect of plasma curvature can lead to a major modification of the spectral resolution compared to analysis based on slab geometry (also see Ref. [51]).

Various 2-D analytic and numerical models have been developed to interpret reflectometry responses to poloidal density fluctuations (see discussion in Chapter 3). These 2-D models or analytic studies are either based on slab plasma profiles (Refs. [52][90] [58][55][50]), or do not isolate and clarify the effect of plasma curvature where it is included (Ref. [5]). It is well known that the reflectometry sensitivity to poloidal fluctuation wavenumber, $k_\perp$, is limited by receiver location and incident beam width (or spot size). For a finite beam width it was shown that the geometric optics result in 1-D may apply for $k_\perp w \ll \pi/\sqrt{2}$, where w is $1/e$ radius of the incident beam intensity (Ref. [58]). For larger wavenumbers, it was suggested that a tilted receiver arrangement is necessary for measuring fluctuations with $k_\perp w \gg \pi/\sqrt{2}$. The issue of resolution has also been addressed using the distorted mirror model (Refs. [56][55]), assuming that the receiver and transmitter have similar aperture sizes. This analysis showed that the upper limit for the undistorted observation of the poloidal spectrum is $k_\perp w \leq \pi/5$. It was suggested in Ref. [55] that a tightly focused beam is better for fluctuations measurement in order to enhance the gain and improve the wavenumber response. A $1/e^2$ sensitivity criterion of the reflectometry, $k_\perp w < 2$, can be deduced from the result of a rigorous analysis based on slab geometry and linear density profiles (Ref. [50]).

The $k_\perp$ of the quasi-coherent fluctuations in EDA H-modes are in the range $k_\perp \simeq 2 - 6$ cm^{-1} as determined by the PCI system. On the other hand the reflectometer antenna spot size at the cutoff is estimated to be $w \sim 1-2$ cm, with receiver distance $d \simeq 20$ cm, horn antenna angles $\pm 5^0$ relative to the mid-plane. The observed system

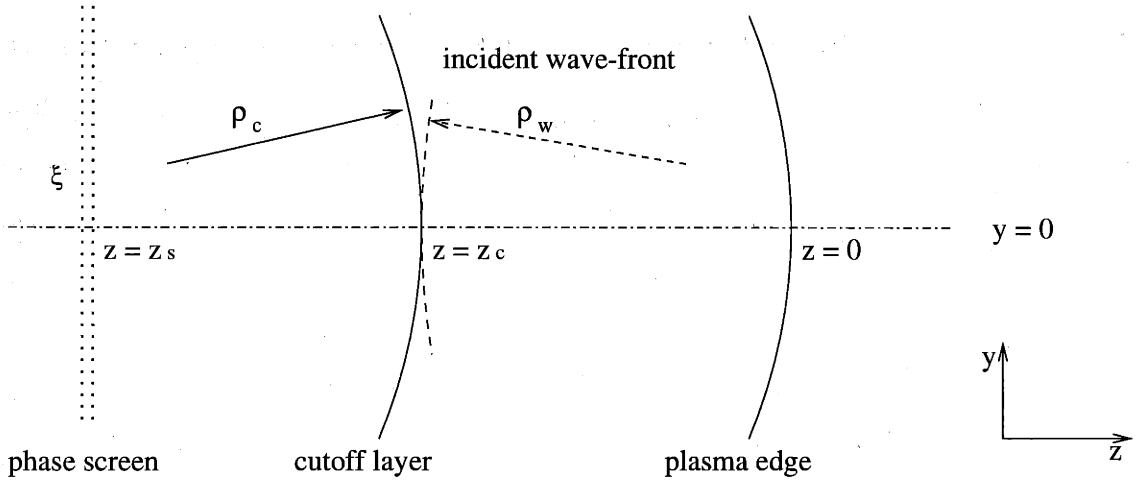

Figure 7-10: Phase screen model. Plasma turbulence is reduced to a modulation on the phase screen.

response appears to be much broader in $k_\perp$ than predicted from 2-D slab geometry analysis for these plasmas as shown in Section 7.2.

In this Section, we show that super-resolution of high $k_\perp$ fluctuations can indeed be achieved due to a magnification caused by plasma poloidal curvature and the curved wave-front of the incident waves. The phenomenon of super resolution is analyzed using a phase screen model for general cases and the results are supported by detailed numerical 2-D full-wave simulations for the specific case of the Alcator C-Mod tokamak.

We use a different coordinate system in this Section. Instead of the $x-y$ system used in Chapter 4 and the previous Section, we use $y-z$ system. Here $\hat{y}$ is the vertical direction $\hat{Z}$ in conventional tokamak notation, and $\hat{z}$ is the major radius $\hat{R}$ direction. The launched waves propagate in $-\hat{z}$ direction.

7.3.1 Analytic result from a phase screen model

To give a general insight into the curvature effect, we use a phase screen model including plasma curvature and wave-front curvature (Fig. 7-10). All plasma effects are reduced to the phase modulation induced by the phase screen.

The phase of the electric field at the screen is calculated by 1-D geometric optics:

$\phi_0 = 2k_0 \int_0^{z_c} \epsilon^{1/2}\, dz$, where ϵ is plasma permittivity, z_c is the critical layer, $z = 0$ at the plasma edge, and k_0 is the incident microwave vacuum wavenumber. The phase screen is located at $z_s = \int_0^{z_c} \epsilon^{-1/2}\, dz$, i.e., at the effective optical distance from the plasma edge. A poloidal plasma density fluctuation is modeled as a phase modulation with wavenumber $k_\perp$. The modulation magnitude, $\sigma_\phi = \langle(\phi - \phi_0)^2\rangle^{1/2}$, can also be calculated from 1-D geometric optics given the details of the density profile. Assuming a radius of curvature ρ_c of the cutoff layer and ρ_w of the incident wave-front at the cutoff layer, the complex electric field at the phase screen is approximately:

$$E_s(\xi) = \frac{1}{\sqrt{2\pi}w} \exp\left(-\frac{\xi^2}{2w^2}\right) \times \exp\left(\frac{ik_0\xi^2}{\rho}\right) \times \exp\left[i\sqrt{2}\sigma_\phi \cos(k_\perp \xi + \theta)\right], \quad (7.4)$$

where ξ is the coordinate on the phase screen, θ is the phase offset of the modulation at $\xi = 0$, $\rho = 2\rho_c\rho_w/(\rho_c + 2\rho_w)$ is the effective radius of curvature, and w is the $1/e$ radius of the Gaussian incident waves intensity ($\propto |E_s|^2$) distributed on the phase screen. The second term comes from the curvature effect assuming $w \ll \rho/2$. The third term denotes phase modulation by density fluctuations.

The electric field in all space, in principle, can be calculated using the Fresnel-Huygens formula:

$$\begin{aligned} E(y,z) &= \frac{1}{2\pi}\int_{-\infty}^{\infty} g(u) \exp\left[i(z - z_s)\sqrt{k_0^2 - u^2}\right] \exp(iuy)\, du, \quad (7.5)\\ g(u) &= \int_{-\infty}^{\infty} E_s(\xi) \exp(-iu\xi)\, d\xi. \end{aligned}$$

Only two dimensions of the formula is incorporated. In the regime where $\sigma_\phi \ll 1$, $k_\perp \ll k_0$, we estimate the rms level of the electric field over $-\pi < \theta < \pi$ on the axis $y = 0$. By integrating Eq. 7.5, we find:

$$\begin{aligned} E_{rms}(0,z) &= \frac{\langle|E - \langle E\rangle|^2\rangle^{1/2}}{|\langle E\rangle|} \simeq \sigma_\phi \exp\left[-\frac{k_\perp^2 w^2}{C_1}\left(1 - \frac{1}{2}C_2\right)\right], \quad (7.6)\\ C_1 &= 1 + \frac{4k_0^2 w^4}{\rho^2},\\ C_2 &= \frac{1 - 4d/\rho}{(1 - 2d/\rho)^2 + d^2/k_0^2 w^4}, \end{aligned}$$

where $d = z - z_s$ is the distance to the phase screen. The curvature effect is strongly embedded in parameter C_1 while C_2 is usually close to 1. In the case of $k_\perp \to 0$ or $w \to 0$, E_{rms} approaches σ_ϕ, which is the 1-D geometric optics limit. In the regime of weak curvature where $\rho \gg 2k_0w^2$, the curvature effect is negligible. Using $C_2 \simeq 1$, we get:

$$E_{rms}(0,z) \simeq \sigma_\phi \exp\left(-k_\perp^2 w^2/2\right), \quad \rho/2 \gg k_0 w^2. \tag{7.7}$$

The dependence on $\exp\left(-k_\perp^2 w^2/2\right)$ is identical to that deduced from the result in Ref. [50]. In contrast, in the regime of strong curvature where $w \ll \rho/2 \ll k_0w^2$,

$$E_{rms}(0,z) \simeq \sigma_\phi \exp\left[-\left(\frac{\rho}{2k_0w^2}\right)^2 \frac{k_\perp^2 w^2}{2}\right], \quad w \ll \rho/2 \ll k_0 w^2. \tag{7.8}$$

Eq. 7.8 shows that, with strong curvature, the electric field fluctuations due to a density fluctuation with wavenumber $k_\perp$ is as strong as for density fluctuation of much smaller wavenumber,

$$k'_\perp \simeq \left(\frac{\rho}{2k_0w^2}\right) k_\perp, \quad w \ll \rho/2 \ll k_0 w^2, \tag{7.9}$$

found in Eq. 7.7, which is the analytic result using slab plasma geometry and plane wave-front with finite beam size. As a result, the reflectometry response to poloidal fluctuations can be significantly broader in $k_\perp$ than the result without consideration of plasma curvature.

Fig. 7-11 shows E_{rms}/σ_ϕ calculated using Eq. 7.6 for different curvature radii. Fig. 7-11-(a) is the case of $\rho_w = 10$ cm while $\rho_w = 25$ cm is shown in Fig. 7-11-(b). Results of plasma curvature $\rho_c = \infty$, 25 and 15 cm are plotted. Other parameters used are realistic parameters for the Alcator C-Mod 88 GHz reflectometer channel, $k_0 \simeq 18.5$ cm^{-1}, $w \simeq 1.6$ cm, $d \simeq 20$ cm. All curves converge to the 1-D geometric optics limit, $E_{rms}/\sigma_\phi = 1$, for $k_\perp \to 0$. For large $k_\perp$, there can be orders of magnitude difference in E_{rms} for different ρ_c. E_{rms}/σ_ϕ in Fig. 7-11-(a) is also larger than those in Fig. 7-11-(b) with the same ρ_c because of a smaller ρ_w.

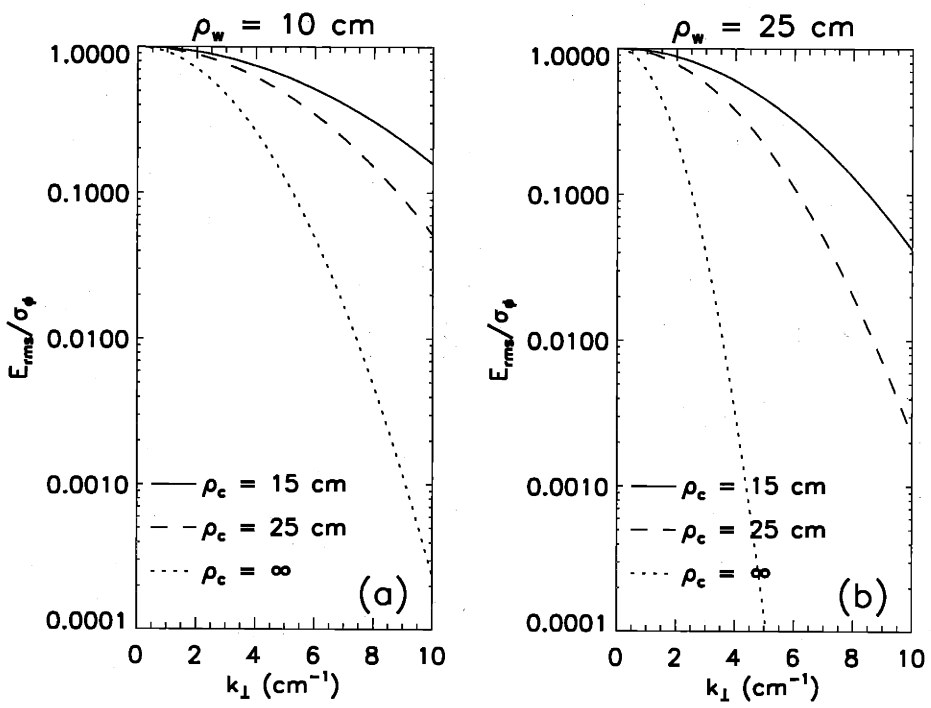

Figure 7-11: E_{rms}/σ_ϕ evaluated from Eq. 7.6 for different radii of plasma curvature: $\rho_c = \infty$, 25 and 15 cm. $k_0 \simeq 18.5$ cm^{-1}, $w \simeq 1.6$ cm, $d \simeq 20$ cm. Figure (a) shows the result of $\rho_w = 10$ cm and figure (b) shows the result of $\rho_w = 25$ cm.

7.3.2 2-D full-wave simulation result

A more realistic plasma curvature effect for O-mode reflectometry has been estimated using the 2-D full-wave simulation based on the experimental density profile and reflectometer geometry in the Alcator C-Mod tokamak. The plasma density profile is modelled with an EDA H-mode profile with pedestal width of 0.6 cm at $z < 0$:

$$n_{e0}(z)/n_c = 0.8\left[1 - 0.025z - \tanh\left(\frac{z+3.5}{0.6}\right)\right]. \tag{7.10}$$

where lengths are in cm, and $n_c = 0.96 \times 10^{14}$ cm^{-3} is the cutoff density for 88 GHz microwave (O-mode). The fluctuations are assumed to be localized in z but poloidally modulated:

$$\tilde{n}_e(z)/n_{e0} = 0.04 \times \exp\left[-\left(\frac{z+3.3}{0.35}\right)^2\right]\cos(k_\perp y + \theta). \tag{7.11}$$

Such fluctuations give a 1-D phase modulation level $\sigma_\phi \simeq 0.5$ rad. The total density is $n_e = n_{e0} + \tilde{n}_e$.

The electric field of the incident Gaussian beam in the vacuum region propagating in $-\vec{e}_z$ direction is described as (a time factor $e^{-i\omega t}$ is ignored):

$$E_b(y,z) \simeq \sqrt{\frac{2P}{\pi w_b^2}}\exp\left[-i\arctan\left(\frac{z-z_0}{k_0 w_0^2}\right) - y^2\left(\frac{1}{2w_b^2} + \frac{ik_0}{2\rho_b}\right)\right]\exp\left[-ik_0(z-z_0)\right], \tag{7.12}$$

where z_0 is the position of the beam waist and w_0 is the beam waist radius; the beam's $1/e$ intensity radius $w_b = w_0\left[1 + (z-z_0)^2/k_0^2 w_0^4\right]^{1/2}$, the radius of wave-front curvature $\rho_b = |z - z_0|\left[1 + k_0^2 w_0^4/(z-z_0)^2\right]$, P is the total incident power. We assume a Gaussian beam waist radius $w_0 \simeq 0.75$ cm at the launching horn aperture position ($z_0 \simeq 15$ cm), which has an optical distance $d \simeq 20$ cm to the cutoff layer based on the model density profile. We estimate $\rho_b \simeq 25$ cm and $w_b \simeq 1.6$ cm at the phase screen based on the propagation in vacuum.

Fig. 7-12 and Fig. 7-13 show the 2-D electric field distribution of $\rho_c = \infty, 25$, and 15 cm for a single-antenna system (Fig. 7-12) and a two-antenna (transmitter XMTR and receiver RCVR) system with angles of $\pm 5^0$ relative to $y = 0$ (Fig. 7-13). The plasma density fluctuations perturb the electric field distribution and

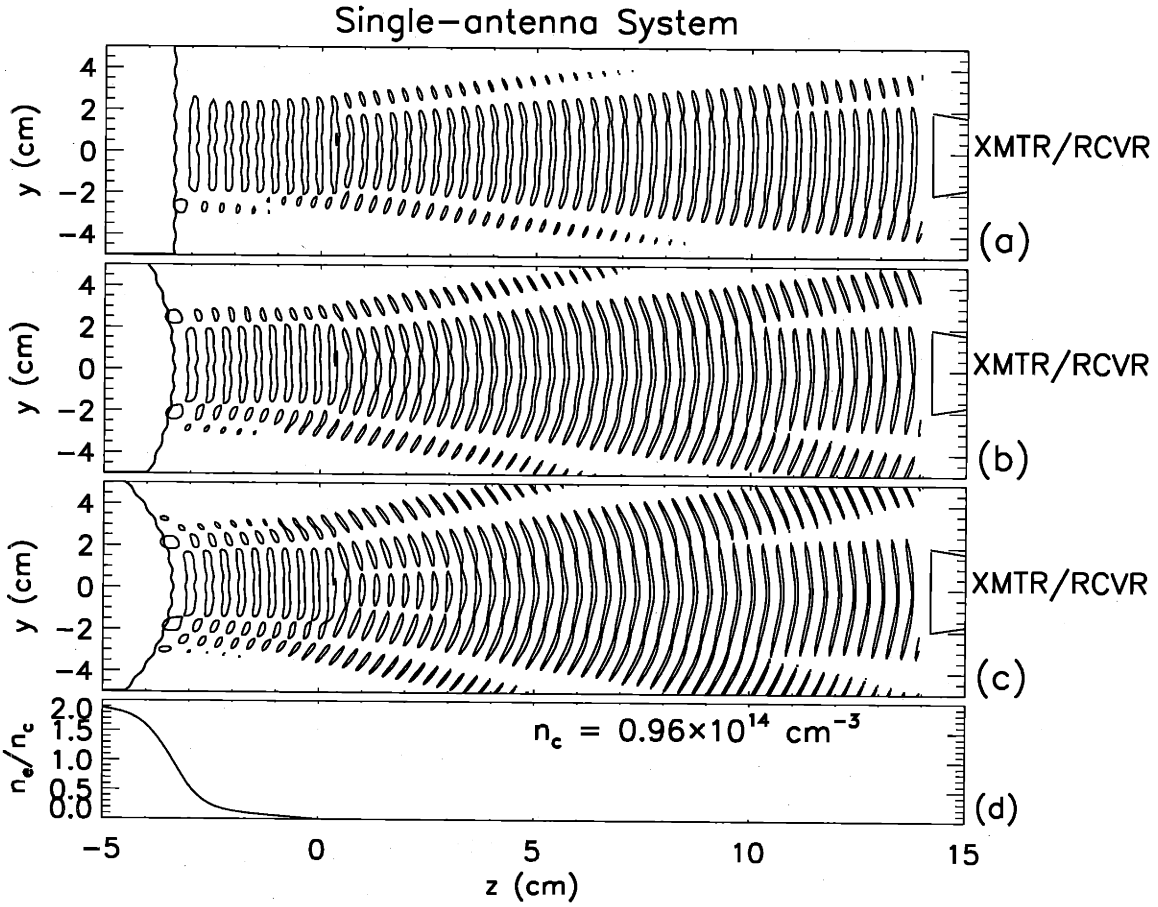

Figure 7-12: The distribution of the electric field for a single-antenna system. (a) slab geometry $\rho_c = \infty$, (b) curved plasma with $\rho_c = 25$ cm; (c) curved plasma with $\rho_c = 15$ cm. The cutoff layer and the antenna (XMTR/RCVR) are also drawn. The density profile at $y = 0$ is drawn in (d). The fluctuation $k_\perp = 6$ cm and $\sigma_\phi = 0.5$ rad.

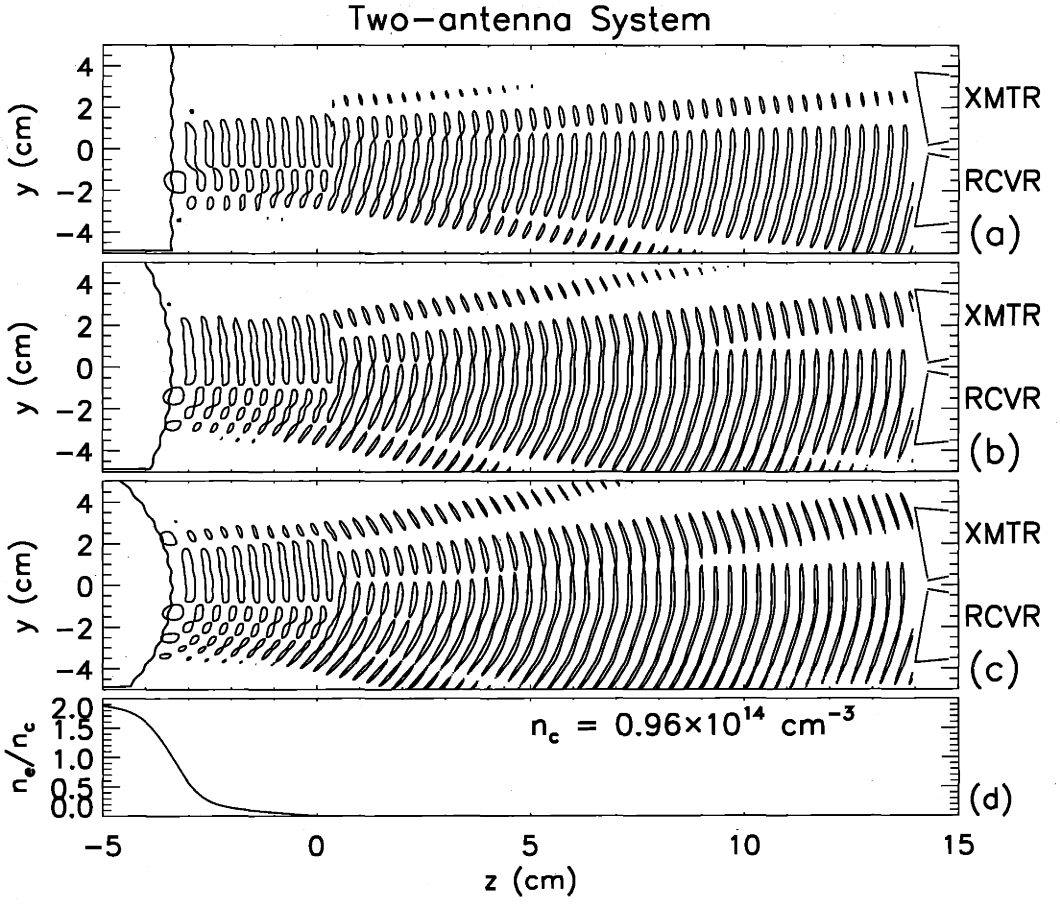

Figure 7-13: The distribution of the electric field for a two-antenna system. (a) slab geometry $\rho_c = \infty$; (b) curved plasma with $\rho_c = 25$ cm; (c) curved plasma with $\rho_c = 15$ cm. The cutoff layer and the antennas (transmitter XMTR and receiver RCVR) are also drawn. Antenna angles are $\pm 5^0$ relative to $y = 0$ axis. The density profile at $y = 0$ is drawn in (d). The fluctuation $k_\perp = 6$ cm and $\sigma_\phi = 0.5$ rad.

reflectometry derives the density fluctuations from the electric field perturbation. The electric field perturbation caused by the plasma density fluctuation is larger for smaller ρ_c. Fig. 7-14 shows an enlarged view of the region near the antenna of Fig. 7-12. In the simulation, we construct a Huygens surface at $z = 2\pi/k_0 \simeq 0.34$ cm, and generate Gaussian beams propagating towards the plasma at $z < 0$. The Huygens surface separates the reflected waves from the total field. As a result, the field in the region of $z > 0.34$ cm consists of only the reflected waves while the total electric field of the incident Gaussian beam and the reflected waves are shown in the region of $z < 0.34$ cm in both Fig. 7-12 and 7-13. The contour level is $E = \frac{1}{2}E_0$, where E_0 is the maximal electric field amplitude at the Gaussian beam waist. The plasma density profile at $y = 0$ is also shown. The fluctuation wavenumber is $k_\perp = 6$ cm^{-1} and the phase modulation level $\sigma_\phi \simeq 0.5$ rad. With smaller ρ_c, the reflected waves are more poloidally expanded, which results in less absolute power received by RCVR. The contours of $\Re(\tilde{E})/|E|$ are plotted, where $\tilde{E}$ is the difference of the electric fields with density fluctuations ($\sigma_\phi = 0.5$ rad) and without density fluctuations ($\sigma_\phi = 0$), and $|E|$ is the amplitude of the complex electric field. $\Re(\tilde{E})/|E|$ is poloidally modulated due to the poloidal density fluctuation. The perturbation level on the electric field is $\sigma_E = \langle|\tilde{E}|^2/|E|^2\rangle^{1/2}$, where average $\langle\ \rangle$ is defined in the region shown in the figure. The perturbation level increases for smaller ρ_c. $\sigma_E \simeq 0.13, 0.23$ and 0.28 is obtained for $\rho_c = \infty, 25$ and 15 cm respectively. This response is many orders of magnitude larger than expected from 2-D slab geometry analysis (Eq. 7.7), but much closer to the 1-D geometric optics limit, $\sigma_E \simeq \sigma_\phi \simeq 0.5$. The larger σ_E shown in the case of curved plasma than that in the cases of $\rho_c = \infty$ means higher sensitivity to density fluctuations.

Including the finite size of the receiving horn antenna, the rms level of reflectometer response over a fluctuation period, E_{rms} is slightly less than σ_E. Fig. 7-15 shows E_{rms}/σ_ϕ versus the poloidal wavenumber $k_\perp$. The results of the single-antenna system and two-antenna systems are similar. For typical quasi-coherent fluctuations in EDA H-modes, $k_\perp \sim 2-6$ cm^{-1}, the simulation result shows that the reflectometer response with curvature ($\rho_c = 15$ and 25 cm) is significantly higher than that of a slab profile

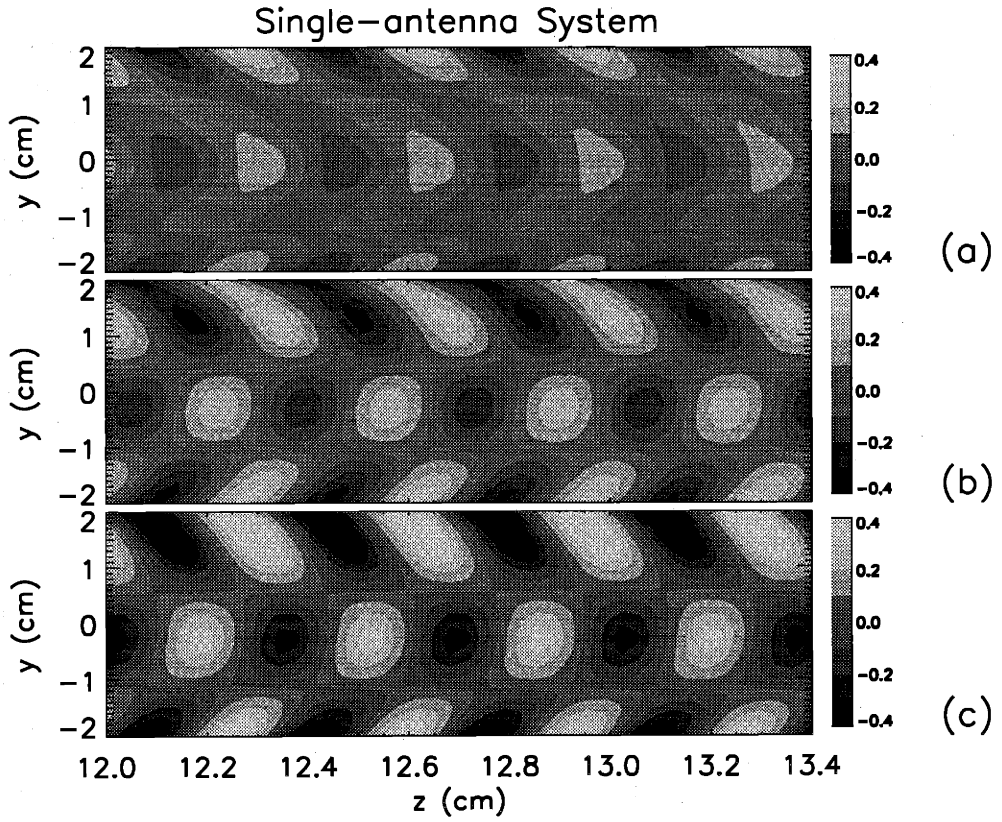

Figure 7-14: Electric field contours showing the curvature effects. $\Re(\tilde{E})/|E|$ in an enlarged region near the antenna for the single-antenna system in Fig. 7-12. (a) slab geometry $\rho_c = \infty$, (b) curved plasma with $\rho_c = 25$ cm. (c) curved plasma with $\rho_c = 15$ cm.

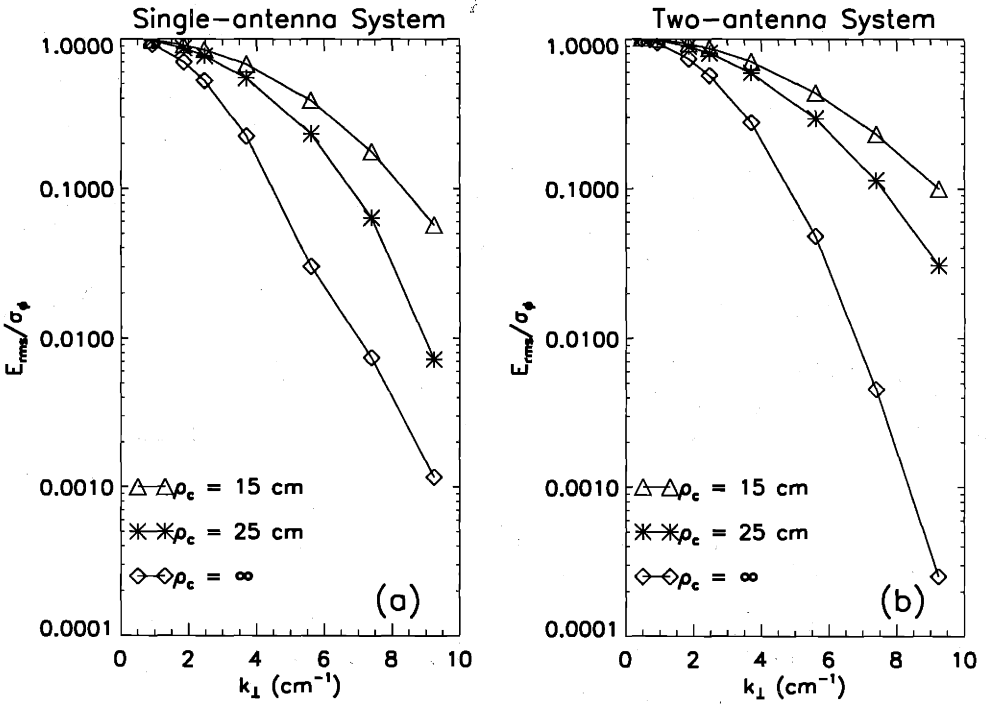

Figure 7-15: Curvature effects on reflectometer response. E_{rms}/σ_ϕ for different radii of curvature of plasma from the 2-D full-wave simulation. $\rho_c = \infty, 25, 15$ cm. Figure (a) is for the single-antenna system (Fig. 7-12) and figure (b) is for the two-antenna system (Fig. 7-13).

plasma with $\rho_c = \infty$. The simulation results are close to those in Fig. 7-11-(a), which are calculated from Eq. 7.6 using $\rho_w = 10$ cm. In contrast, the results in Fig. 7-11-(b), which is obtained using $\rho_w = \rho_b = 25$ cm, where ρ_b is the estimated Gaussian beam curvature radius at the phase screen based on propagation in vacuum, are much smaller than the simulation results. It indicates that the plasma effect on the wave-front curvature is not negligible when using the phase screen model (Eq. 7.6) to estimate the reflectometry sensitivity. It also indicates that plasma curvature plays an important role in determining the wave number resolution of the measurement.

In summary, plasma curvature is found to significantly extend the microwave reflectometry response to high $k_\perp$ fluctuations when the effective radius of curvature $\rho \ll 2k_0w^2$. The reflectometry responses to high $k_\perp$ poloidal fluctuations may be several orders of magnitude larger than the slab geometry result. Thus, the 1-D model may work better than 2-D slab geometry models for high $k_\perp$ fluctuations due to the curvature effect. At low $k_\perp$, however, the 1-D model and 2-D slab geometry models agree well, and plasma curvature does not affect the response.

7.4 Simulation of radial correlation measurement

As discussed in Chapter 3, the interpretation on radial correlation measurement has not been completely understood. In this Section, we present some preliminary results on this issue, which is obtained from the 2-D full-wave simulation for typical Alcator C-Mod plasmas.

7.4.1 Simulation parameters

Turbulence model

We use correlation length, correlation time, and the random phase approximation to model density turbulence. We start from an ideal Gaussian shape density correlation function

$$\gamma(\delta x, \delta y, \delta t) = \exp\left(-\frac{\delta x^2}{2L_{r,n}^2}\right)\exp\left(-\frac{\delta y^2}{2L_{r,n}^2}\right)\exp\left(-\frac{\delta t^2}{2L_t^2}\right), \qquad (7.13)$$

where $L_{r,n}$ is the turbulence correlation length[3], and L_t is the correlation time. The turbulence distribution in space and time $\zeta(x, y, t)$ is obtained from γ:

$$\zeta(x, y, t) = \mathcal{F}^{-1}\left[|\mathcal{F}(\gamma)|^{1/2} \exp(j\phi_{rand})\right] C, \tag{7.14}$$

where $\mathcal{F}$ and $\mathcal{F}^{-1}$ are the Fourier and inverse Fourier transformation on the two spatial dimensions plus the time dimension, ϕ_{rand} are random phases $0 \leq \phi_{rand} < 2\pi$, and C is a factor to tune the rms turbulence level, which is defined as

$$\zeta_{rms} = \left[\frac{\int dt \int dx \int dy\ \zeta^2(x, y, t)}{\int dt \int dx \int dy}\right]^{1/2}. \tag{7.15}$$

Density profile

We input the following linear density profile to our 2-D full-wave simulation code

$$n_e(x, y, t) = n_{c,88}(1 - x[\text{cm}]/4.8)\,[1 + \zeta(x, y, t)]\,, \tag{7.16}$$

where $n_{c,88} = 0.96 \times 10^{20}$ m^{-3} is the critical density of the 88 GHz wave. The 2-D density profile is curved with a curvature radius of 0.20 m.

Simulation setup

Given a density turbulence level ζ_{rms} and incident wave frequency f, we run simulations at 24 time points, $t = L_t/12, 2L_t/12, \ldots, 23L_t/12$ and obtain the corresponding reflectometry responses $E_{rcvr}(f, t)$ for density profiles $n_e(x, y, t)$. We run simulations with different frequencies around 88 GHz to model the correlation reflectometry. Other parameters are set up as those used in Section 7.1.

Varying correlation length $L_{r,n}$ or turbulence level ζ_{rms} affects the reflectometry measurement. The following Sections, we will show these two effects respectively.

[3]For simplicity, we assume radial and poloidal correlation lengths are identical.

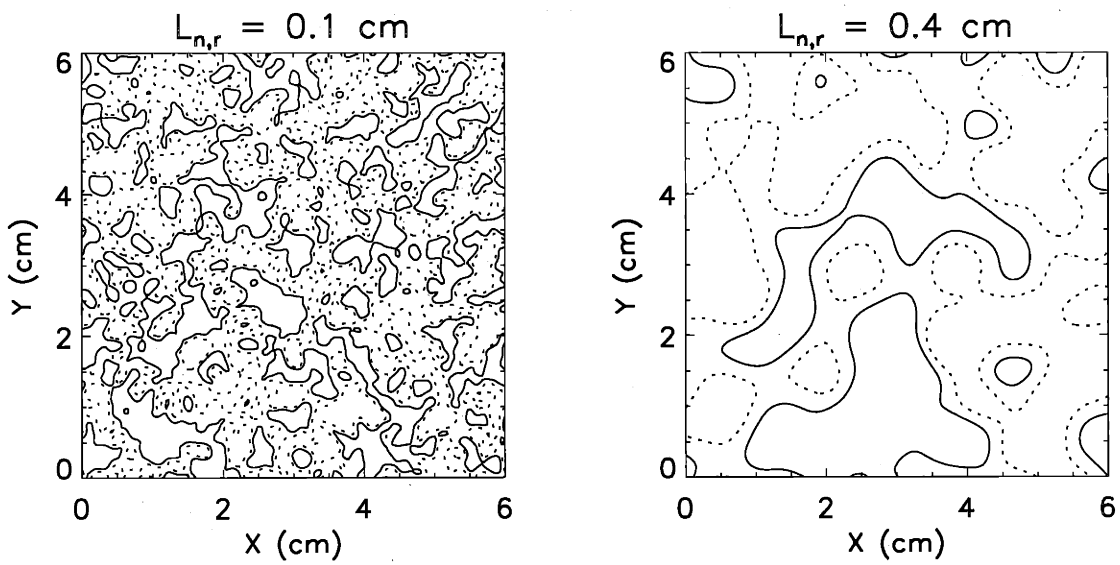

Figure 7-16: Turbulence with different correlation lengths. Two snap-shots of turbulence $\tilde{n}/n$ in part of the computation box is shown in contour plots. The left plot is the case of $L_{n,r} = 0.1$ cm and the right plot is of $L_{n,r} = 0.4$ cm. The contour levels are $-0.5\zeta_{rms}$ and $0.5\zeta_{rms}$.

7.4.2 Reflectometry responses at different turbulence correlation lengths

In this study, we run simulations with different density correlation lengths $0.1 \leq L_{r,n} \leq 0.8$ cm at a low turbulence level $\zeta_{rms} = 0.01$. This $L_{r,n}$ range is close to the estimated correlation length for typical Alcator C-Mod plasmas.

Fig. 7-16 shows two snap-shots of turbulence $\tilde{n}/n$ in part of the computation box. The left plot of the figure shows a turbulence with correlation length of $L_{n,r} = 0.1$ cm, and the right plot is of $L_{n,r} = 0.4$ cm.

Fig. 7-17 shows an example of the reflectometry signal phase (ϕ) correlation functions γ_ϕ and model density correlation γ_n. γ_ϕ and γ_n are plotted vs. the relative critical surface position $\Delta r = x_c(f) - x_c(f_0)$ with $f_0 = 88$ GHz. Gaussian fits with three free parameters (width, center and height) are performed on γ_ϕ and γ_n. In this specific case, the width of both fits are close. Fig. 7-18 shows the correlation length obtained from Gaussian fitted γ_ϕ and γ_n. The figure shows that generally $L_{r,\phi} \simeq L_{r,n}$ in the range $0.1 \leq L_{r,n} \leq 0.8$ cm at the weak turbulence level $\zeta_{rms} \simeq 0.01$. The large

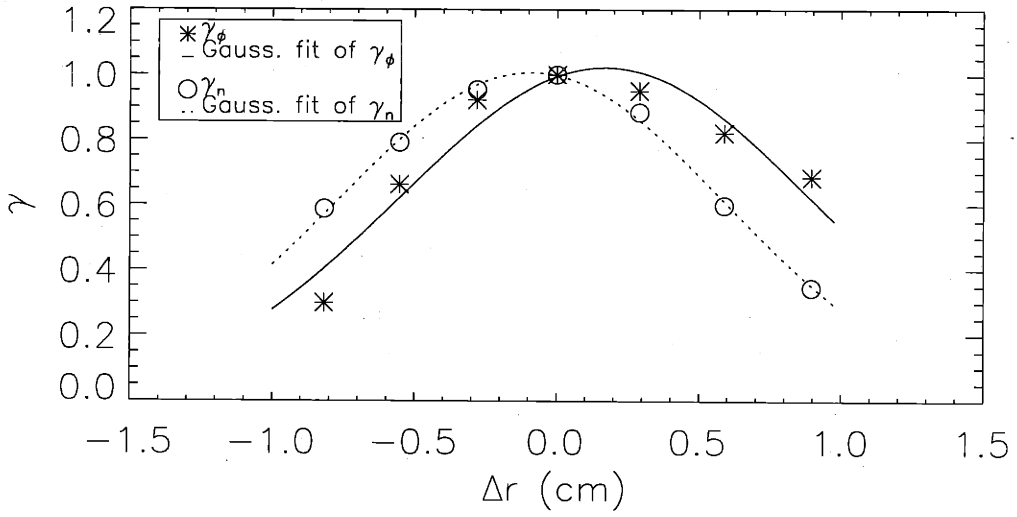

Figure 7-17: Reflectometry phase correlation γ_ϕ and turbulence correlation γ_n. Gaussian fits are performed on the simulation results. The incidence wave vacuum wavelength $\lambda_0 \simeq 0.34$ cm and density scale length at the critical surface is 4.8 cm. The turbulence rms level is $\zeta_{rms} \simeq 0.01$.

uncertainty shown in the figure are from the deviation from the Gaussian shape of the response.

Fig. 7-19 and Fig. 7-20 show the result of reflectometry signal amplitude correlation with turbulence correlation. Fig. 7-19 shows an example of the signal amplitude (A) correlation functions γ_A vs. model density correlation γ_n. Fig. 7-20 shows γ_A vs. γ_n. The figure shows that $L_{r,A} \simeq L_{r,n}$ at the turbulence level $\zeta_{rms} \simeq 0.01$.

Though both $L_{r,\phi}$ and $L_{r,A}$ are close to $L_{r,n}$ for the case of $\zeta_{rms} \sim 0.01$ as shown above, we should also check whether this similarity holds for other turbulence levels, which is shown in next Section.

7.4.3 Reflectometry responses at different turbulence levels

In this study, we run simulations with different turbulence levels $0.02 \leq \zeta_{rms} \leq 0.20$. at a fixed correlation length $L_{r,n} \simeq 0.45$ cm of the modelled density turbulence.

Fig. 7-21 shows the obtained signal amplitude correlation length vs. turbulence

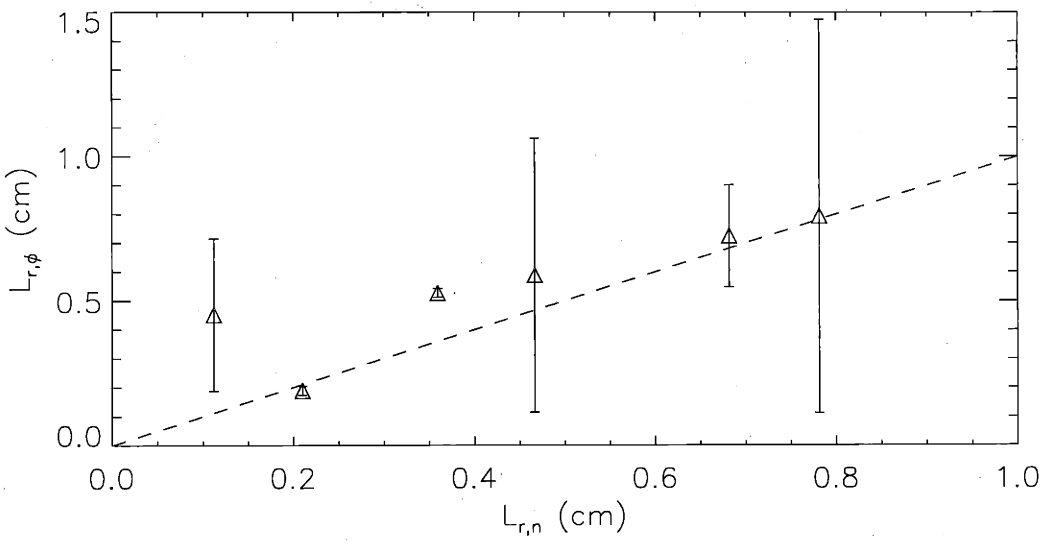

Figure 7-18: Reflectometry $L_{r,\phi}$ vs. turbulence $L_{r,n}$. The figure shows that generally $L_{r,\phi} \simeq L_{r,n}$ in the range $0.1 \leq L_{r,n} \leq 0.8$ cm at the turbulence level $\zeta_{rms} \simeq 0.01$.

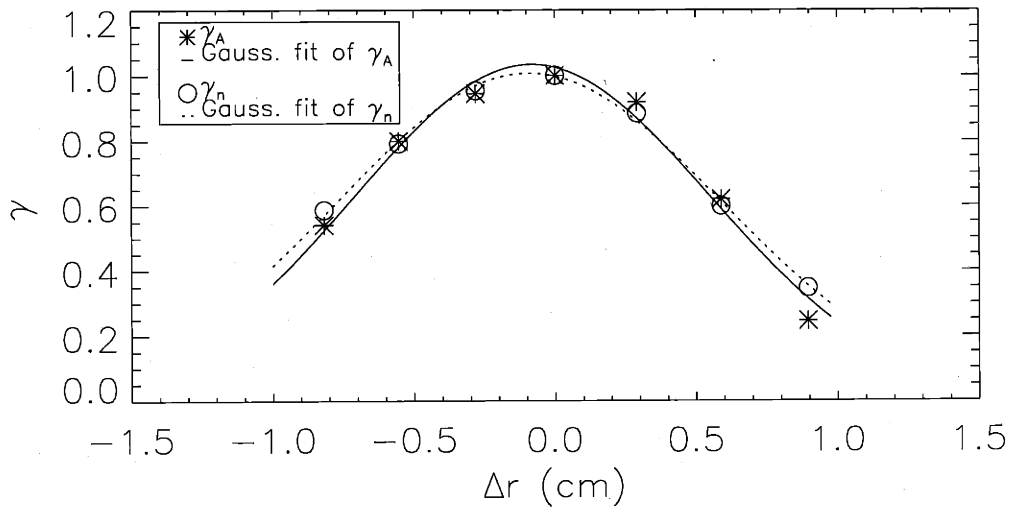

Figure 7-19: Reflectometry amplitude correlation γ_A and turbulence correlation γ_n. Simulation parameters are identical to those in Fig. 7-17.

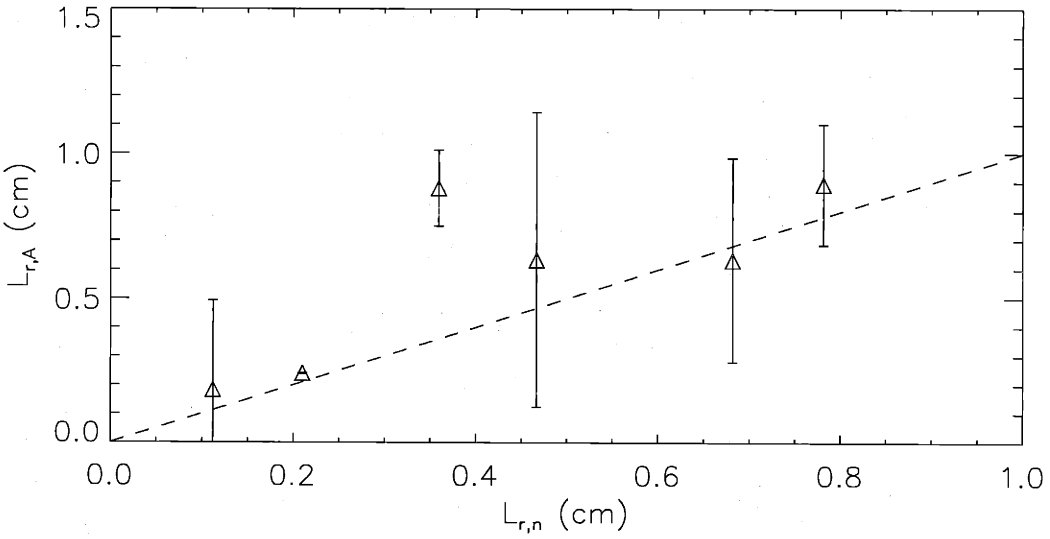

Figure 7-20: Reflectometry $L_{r,A}$ vs. turbulence $L_{r,n}$. The figure shows that generally $L_{r,A} \simeq L_{r,n}$ in the range $0.1 \leq L_{r,n} \leq 0.8$ cm at the turbulence level $\zeta_{rms} \simeq 0.01$.

level. In the range of $\zeta_{rms} \leq 0.1$, $1.0 \leq L_{r,A}/L_{r,n} \leq 1.5$. $L_{r,A}$ is systematically larger than $L_{r,n}$, but it is still reasonably close. For $\zeta_{rms} > 0.1$, the Gaussian fit fails because of significant shape deviation and the reflectometry signal amplitude correlation fails to represent the turbulence correlation.

Fig. 7-22 shows the obtained signal phase correlation length vs. turbulence level. The figure shows that $L_{r,\phi}$ is generally very different than the turbulence correlation $L_{r,n}$. It indicates that it is not reliable to estimate $L_{r,n}$ from $L_{r,\phi}$.

In summary, reflectometry should be able to measure turbulence radial correlation length for typical Alcator C-Mod plasmas provided that the turbulence level is small. The correlation length from the amplitude of the reflectometry signal, $L_{r,A}$, is generally more reliable than that from signal phase correlation, $L_{r,\phi}$, to estimate the correlation length of turbulent density, $L_{n,r}$. Results from this preliminary study are different than those obtained from the much more simplified distorted mirror model (Ref. [57]) (also see Section 3.5). More detailed study in this subject is suggested for future work.

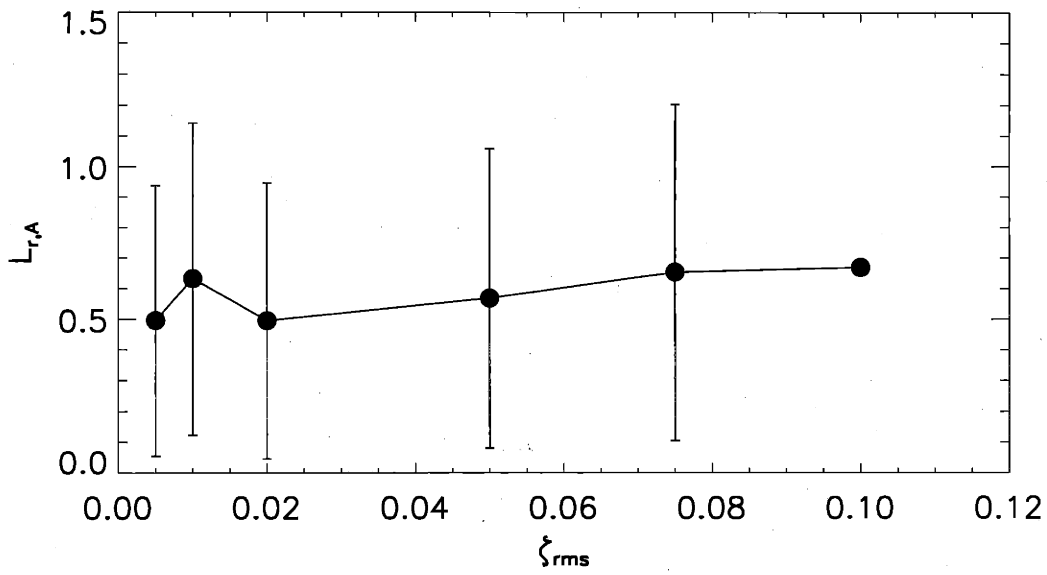

Figure 7-21: Reflectometry $L_{r,A}$ at different turbulence level. Though $L_{r,A}$ is systematically larger than $L_{r,n} = 0.45$ cm for $\zeta_{rms} \leq 0.1$, it is still reasonably close. The Gaussian fit fails for the γ_A at higher turbulence levels $\zeta_{rms} > 0.1$.

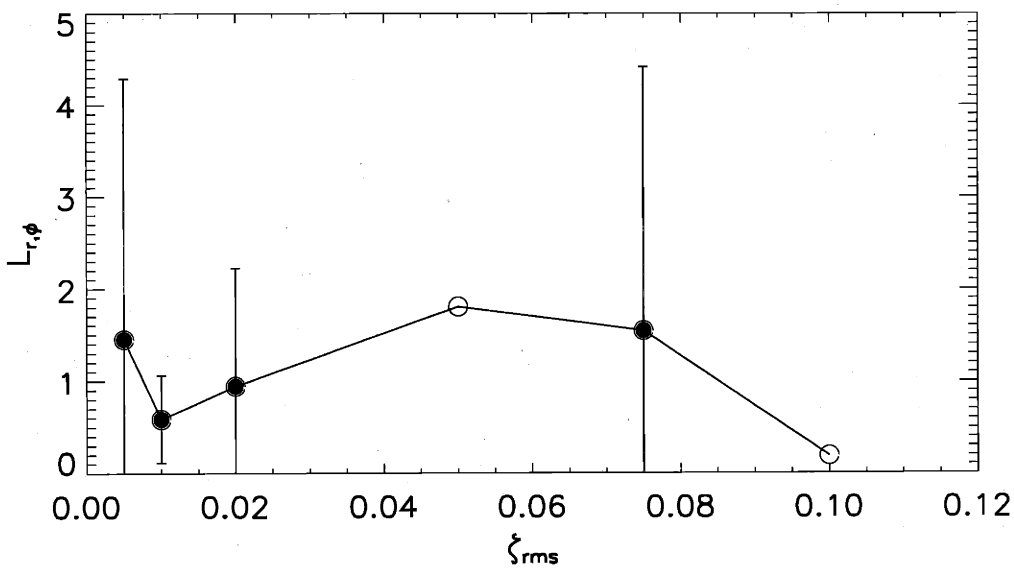

Figure 7-22: Reflectometry $L_{r,\phi}$ at different turbulence level. The empty circles are points that the uncertainty in the Gaussian fit is larger than the plotting range. The figure shows that $L_{r,\phi}$ may not be a reliable quantity to infer the turbulence correlation.

Summary

The 2-D full wave reflectometry simulation code is used to study the QC fluctuation level considering realistic 2-D geometry. The study provides a calibration curve through which we can infer the QC fluctuation level. Plasma curvature is found to significantly extend the microwave reflectometry response to high $k_\perp$ fluctuations when the effective radius of curvature $\rho \ll 2k_0w^2$. The reflectometry responses to high $k_\perp$ poloidal fluctuations may be several orders of magnitude larger than the slab geometry result.

Preliminary numerical studies using the 2-D simulation code on the reflectometry application of turbulence radial correlation measurement indicates that reflectometry should work well for typical Alcator C-Mod plasmas provided that the turbulence level is small. The correlation length from the amplitude of the reflectometry signal, $L_{r,A}$, is generally more reliable than that from signal phase correlation, $L_{r,\phi}$, to estimate the correlation length of turbulent density, $L_{n,r}$.

Chapter 8

Conclusions and future work

In Section 8.1, we draw conclusions from the experimental and numerical study of reflectometry in Alcator C-Mod. In Section 8.2, we briefly describe the design of two higher frequency reflectometry channels (128-136 GHz and 136-144 GHz), which are being installed for the year 2001 campaign. We also discuss some physics issues that can be further pursued using the present reflectometer together with the two higher frequency channels. Further numerical studies using the 2-D full-wave reflectometry simulation code are also discussed.

8.1 Conclusions

The following are conclusions drawn from the experimental and numerical study of reflectometry in Alcator C-Mod:

1. Reflectometer in Alcator C-Mod can continuously measure plasma density profiles and monitor edge density fluctuations. Quasi-coherent continuous edge fluctuations are observed by reflectometer in EDA H-mode periods. These fluctuations are shown to be the signature of the EDA H-mode.

2. Reflectometer data show that the QC fluctuations are localized near the center of the EDA H-mode density pedestal with a small shift toward the lower part of the pedestal. The radial width (FWHM) of these fluctuations, W, is usually

in the range of $0.1 - 0.3$ cm. W increases with the increase of resistivity η at the center of the pedestal. The line-integrated fluctuation level approximately scales with $(\nu^* q_{95}^2)^{0.56}$. The result indicates that higher q_{95}, higher density, and lower temperature are favored for the QC fluctuations. Neither the location nor the width changes significantly in an EDA H-mode period, while the frequency and level vary. Both theoretical models on resistive ballooning mode and drift ballooning mode show promising agreements with experimental results.

3. A 2-D full-wave reflectometry simulation code has been developed to quantitatively interpret O-mode reflectometry fluctuation signals. The code uses finite-difference time-domain methods solving the Maxwell equations in two dimensions under cold plasma assumption. Perfectly matched layers are used as boundary. The Huygens source technique is used to generate Gaussian beam and separate the reflected waves from the total fields. The simulation code is able to simulate realistic 2-D reflectometry geometry.

4. Simulations based on realistic 2-D geometry of the Alcator C-Mod reflectometer provide a calibration curve by which we can relate the QC fluctuations in reflectometry signals to plasma density fluctuations. Results indicate that the line-integrated fluctuation level derived from reflectometry is similar to that measured by PCI. Simulation also finds that the reflectometry geometry affects the measurement. Plasma curvature extends the reflectometry response to fluctuations with high poloidal wavenumber. The 2-D full-wave code has also been used to understand the measurement of radial correlation length of turbulences. For typical Alcator C-Mod plasmas, a preliminary study indicates that we should be able to estimate the correlation length of the turbulence from the reflectometer signal amplitude provided that the fluctuation level is small.

8.2 Future work on the reflectometer

8.2.1 Upgrade to measure radial correlation length

Two higher frequency reflectometry channels with center frequencies 132 GHz and 140 GHz are being installed on Alcator C-Mod in collaboration with PPPL while this dissertation is being written. The major part of these two reflectometry channels were originally installed on TFTR at PPPL. The two channels are able to sweep frequencies, $128 - 136$ GHz and $136 - 144$ GHz respectively. By comparing the signals from the two channels, we can infer the radial turbulence correlation length at the critical surface of $n_c \simeq 2.3 \times 10^{20}$ m^{-3} corresponding to $f \simeq 136$ GHz.

The layout of the mm-wave part of the two channels is shown in Fig. 8-1. There are three Gunn diode oscillators in each channel. One of them is frequency tunable by analogy waveform input. The other two Gunn diode oscillators are used to down-convert the mm-wave into an IF signal: 300 MHz for the 132 GHz channel and 800 MHz for the 140 GHz channel. Broad-band mixers and amplifiers are used to cover the wide frequency range. The IF signals carry density fluctuation information. These signals are measured by the IF system shown in Fig. 8-2.

In the IF system, the two 300 MHz signals from the mm-part of the 132 GHz channel — one is the reference signal, and the other carries plasma information — are converted to a 500 MHz signal, which carries the difference of the two 300 MHz signals. This 500 MHz signal is measured by an I/Q detector, which produces the signal amplitude and phase. The procedure is basically the same for the 800 MHz signals from the 140 GHz channel. The phase difference from these two channels is also measured, which provides one more point of group delay for the density profile measurement. Signals passing through the broad band-pass filter (500 ± 100 MHz) are also connected to a spectrum analyzer so that we can directly detect fluctuation signals at the ion cyclotron frequency ($\simeq 80$ MHz at $B \simeq 5.4$ T), which can arise from the ICRF heating related phenomena.

The mm-wave part of these channels is enclosed in a metal box, and the waveguides are to be connected to those of the present 110 GHz channel. The system will

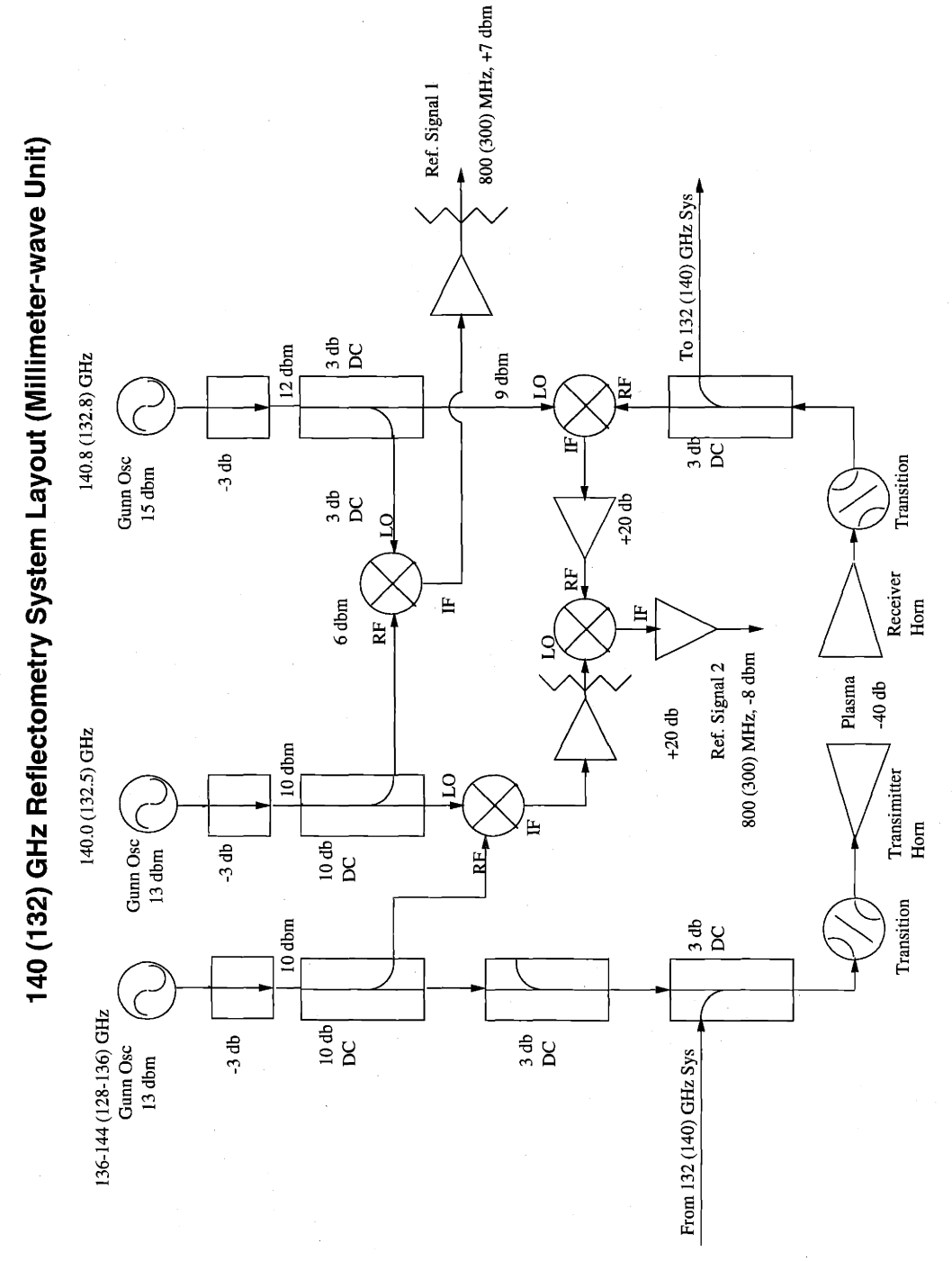

Figure 8-1: Layout of the mm-wave part of 132 GHz and 140 GHz channels (PPPL design).

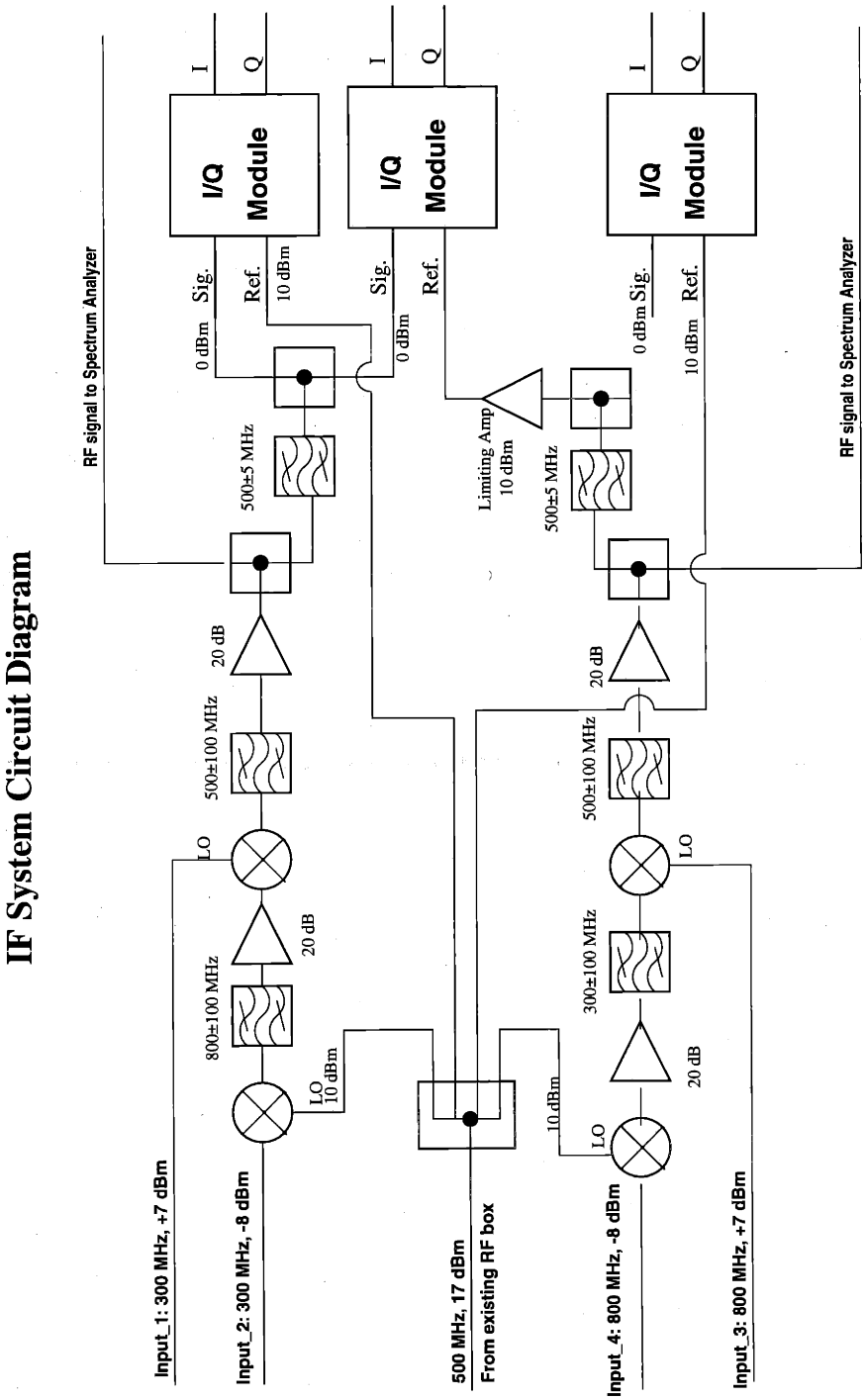

Figure 8-2: Layout of the IF part of the 132 and 140 GHz channels (in collaboration with PPPL).

(temporarily) share the transmitting and receiving lines with the 110 GHz channel.

These two channels can penetrate deeper into the plasma (critical densities $2.0 \times 10^{20} \leq n_c \leq 2.6 \times 10^{20}$ m^{-3}) than the present 5 channels, and they are able to measure turbulence correlation length. Together with the measurements from the present 5 channels, the upgraded reflectometry system will provide important results in many research directions.

8.2.2 Dual O-X mode reflectometry

In Ref. [91], a dual O-X mode reflectometer has been reported. The possibility of measuring magnetic field based on the correlation of turbulence signals from an O-mode reflectometry wave and an X-mode reflectometry wave was explored. It showed that by simultaneously measuring fluctuations of the X-mode wave, which is affected by the magnetic field, and fluctuations of the O-mode wave, which is independent of the magnetic field, we can infer the magnetic field near the critical surface. Therefore, we can potentially use reflectometry to measure the q profile in Alcator C-Mod besides the standard approach of motion stark emission (MSE)[1].

The other advantage of dual O-X mode approach, or equivalently, a polarization rotator as Dr. R. Nazikian of PPPL put it, is the ability to have a larger range of accessibility. Dr. Nazikian has been designing such a polarization rotator system, and it will be installed on Alcator C-Mod in the future.

8.2.3 Reflectometry imaging

A major difficulty in the interpretation of reflectometry fluctuation signals is that the conventional reflectometry process is not always a one to one mapping process. Some studies suggested using reflectometry imaging to obtain a better picture of density fluctuations (for example, Refs. [52] [90]). A novel 3-D reflectometry imaging system has been designed and will be installed in the TEXTOR tokamak (Ref. [92]). An X-mode microwave reflectometry imaging system together with an ECE imaging

[1]The MSE system is under development in collaboration with PPPL.

system are planned to give an instantaneous 3-D view of density and temperature fluctuations (Ref. [93]). However, it is not clear to what extent that reflectometry images can correctly represent a 3-D mapping of density fluctuations. These issues need detailed studies.

The 2-D full-wave reflectometry simulation code described in Chapter 6 can be used to study the imaging process by simply adding numerical lens and aperture in the path of reflected waves. This study should be able to evaluate the validity of this new approach of reflectometry application and interpret the imaging result.

8.3 Future physics studies by reflectometry in Alcator C-Mod

8.3.1 Advanced tokamak physics study

Advanced tokamaks (AT) are tokamaks with higher β, longer energy confinement time τ_E, higher bootstrap current ratio, and longer plasma current duration than traditional tokamaks (Ref. [94]). AT is a cost-effective approach for a reactor-size device. AT study requires particle control, plasma shaping, and current density profile control (for example, Ref. [95]).

A lower hybrid current drive (LHCD) system is being developed for current density profile control in Alcator C-Mod. For the success of LHCD, we must have an accurate measurement of plasma electron density outside the LCFS because the density is critical in determining whether the lower hybrid waves can couple into the plasma. By adding several reflectometry channels at low frequency, we can continuously measure this low density region out of the LCFS.

Using off-axis current drive, we can obtain reversed shear ($s = (r/q)(dq/dr)$) region in the plasma. We expect to routinely see ITBs in the reversed shear region. Reflectometry will be an important tool in characterizing the turbulence suppression in the ITB region (for example, Refs. [96] [97]). ITBs have been observed in Alcator C-Mod in so called enhanced neutron (EN) H-mode (Ref. [98]) and off-axis ICRF

heating (Ref. [29]). Fig. 8-3 shows an ITB in an EN H-mode. The accessibility of the present reflectometry is shown. With the two new high frequency channels, the O-mode reflectometer can reach the ITB region and measure the plasma turbulence level and radial correlation length.

8.3.2 ICRF physics study

In Ref. [99] and Ref. [100], reflectometry was used to study ICRF fast waves in TFTR and DIII-D respectively. By the same token, we can also use the reflectometer to detect ICRF fast waves in Alcator C-Mod. A direct measurement of fast wave level in the plasma should provide key insights for the physics of ICRF heating.

Moreover, the probing waves of reflectometry combined with PCI laser chords can have a very localized density fluctuations measurement. Many ICRF phenomena are spatially localized because of their dependence on the strength of the total magnetic field. For example, the mode conversion from the fast waves to ion Bernstein waves (IBW) is spatially localized at certain major radius (Ref. [101]). Though the PCI system can provide information of line-integrated fluctuations, a cross-examination with reflectometry should be very useful for studies of such spatially localized phenomena.

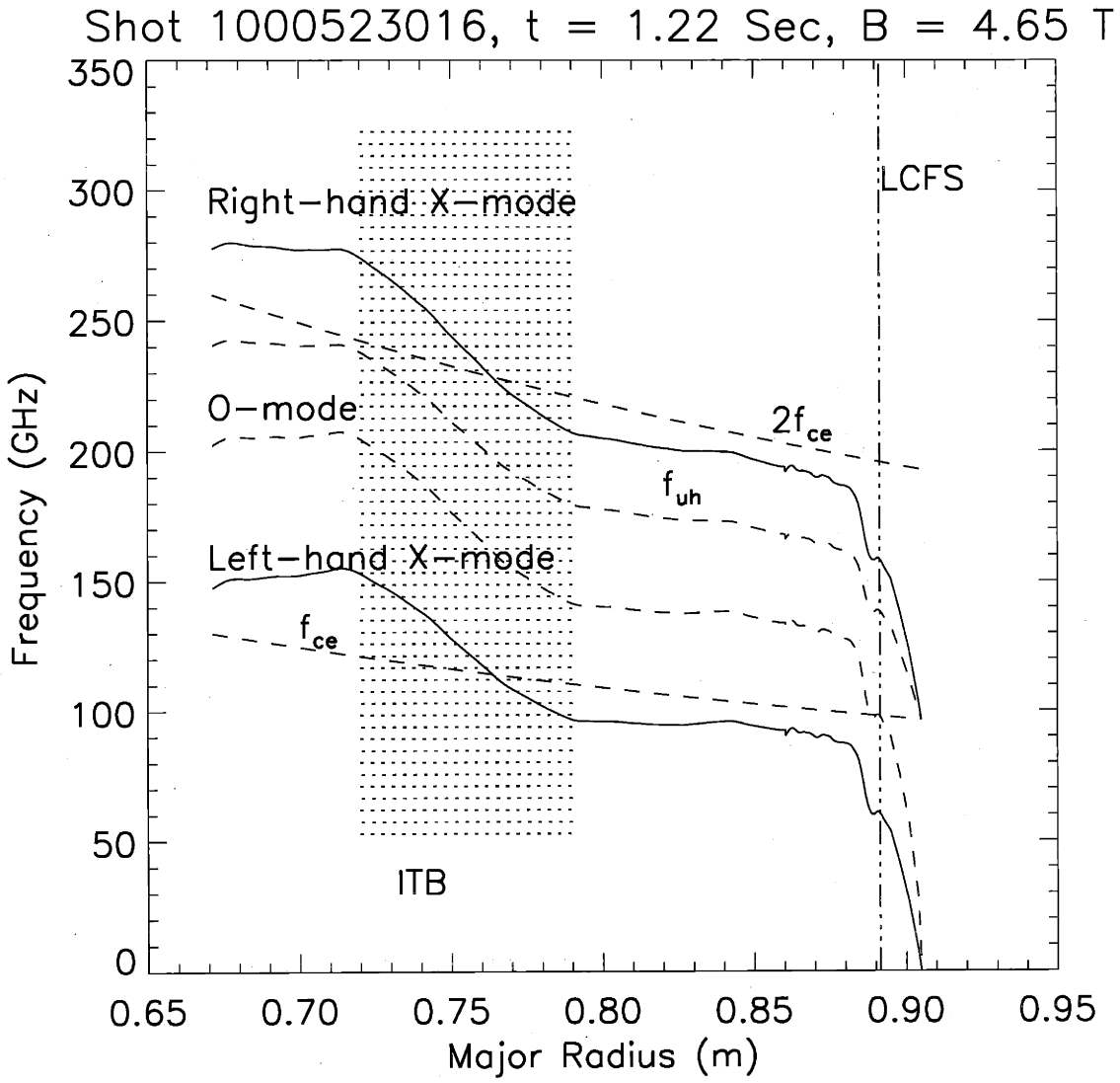

Figure 8-3: Reflectometry accessibility to an internal transport barrier (ITB) in an enhanced neutron H-mode. O-mode waves at the 132 and 140 GHz can access to the ITB region.

Bibliography

[1] J. W. Connor and H. R. Wilson. A review of theories of the L-H transition. *Plasma Phys. Control. Fusion*, 42:R1–R74, 2000.

[2] F. Wagner et al. Regimes of improved confinement and high beta in neutral-beam-heated divertor discharge of the ASDEX tokamak. *Phys. Rev. Lett.*, 49:1408, 1982.

[3] Y. Takase, R. L. Boivin, F. Bombarda, P. T. Bonoli, C. Christensen, C. Fiore, D. Garnier, J. A. Goetz, S. N. Golovato, R. Granetz, M. Greenwald, S. F. Horne, A. Hubbard, I. H. Hutchinson, J. Irby, B. LaBombard, B. Lipschultz, E. Marmar, M. May, A. Mazurenko, G. McCracken, P. O'shea, M. Porkolab, J. Reardon, J. Rice, C. Rost, J. Schachter, J. A. Snipes, P. Stek, J. Terry, R. Watterson, B. Welch, and S. Wolfe. Radiofrequency-heated enhanced confinement modes in the Alcator C-Mod tokamak. *Phys. Plasmas*, 4(5):1647–1653, 1997.

[4] P. C. Stek. *Reflectometry on Alcator C-Mod.* PhD thesis, MIT, Cambridge, MA, 1997.

[5] J. H. Irby, S. Horne, I. H. Hutchinson, and P. C. Stek. 2D full-wave simulation of ordinary mode reflectometry. *Plasma Phys. Control. Fusion*, 35:601–618, 1993.

[6] J. D. Lawson. Some criteria for a power producing thermonuclear reactor. *Proceedings of the Physical Society B*, 70(6), 1957.

[7] B. B. Kadomtsev. *Tokamak Plasma: A Complex Physical System.* Institute of Physics Publishing, Bristol and Philadelphia, 1992.

[8] J. P. Friedberg. *Ideal Magnetohydrodynamics.* Plenum Press, 1987.

[9] I. H. Hutchinson. *Principles of Plasma Diagnostics.* Cambridge University Press, 1987.

[10] F. L. Hinton. In M. N. Rosenbluth and R. Z. Sagdeev, editors, *Handbook of Plasma Physics, Vol. 1.* North Holland, 1983.

[11] R. B. White. *Theory of Tokamak Plasmas.* North Holland, 1989.

[12] ITER Confinement Database and Modelling Expert Group. In *Proceedings of the 16th IAEA fusion energy conference*, Montreal, October 1996.

[13] F. Ryter, W. Suttrop, B. Brusehaber, M. Kaufmann, V. Mertens, H. Murmann, A. G. Peeters, J. Stober, J. Schweinzer, H. Zohm, and ASDEX Upgrade Team. H-mode power threshold and transition in ASDEX Upgrade. *Plasma Phys. Control. Fusion*, 40(5):725–729, 1998.

[14] A. E. Hubbard, R. L. Boivin, J. F. Drake, M. Greenwald, Y. In, J. H. Irby, B. N. Rogers, and J. A. Snipes. Local variables affecting H-mode threshold on Alcator C-Mod. *Plasma Phys. Control. Fusion*, 40(5):689–692, 1998.

[15] D. J. Ward. LH transition theories and theory of H-mode. *Plasma Phys. Control. Fusion*, 38(8):1201–1212, 1996.

[16] E. J. Doyle, G. M. Staebler, L. Zeng, T. L. Rhodes, K. H. Burrell, C. M. Greenfield, R. J. Groebner, G. R. McKee, W. A. Peebles, C. L. Rettig, B. W. Rice, and B. W. Stallard. Observation of simultaneous internal transport barriers in all four transport channels and correlation with turbulence behaviour in NCS discharges on DIII-D. *Plasma Phys. Control. Fusion*, 42(5A):A237–A246, 2000.

[17] M. Greenwald, R. Boivin, F. Bombarda, P. T. Bonoli, C. Fiore, D. Garnier, J. Goetz, S. N. Golovato, M. A. Graf, R. Granetz, S. Horne, A. Hubbard,

I. Hutchinson, J. Irby, B. LaBombard, B. Lipschultz, E. S. Marmar, M. J. May, G. M. McCracken, P. O'Shea, J. Rice, J. Schachter, J. A. Snipes, P. C. Stek, Y. Takase, J. Terry, Y. Wang, R. Watterson, B. Welch, and S. Wolfe. H-mode confinement in Alcator C-Mod. *Nucl. Fusion*, 37(6):793–807, 1997.

[18] H. Zohm. The physics of edge localized modes (ELMs) and their role in power and particle exhaust. *Plasma Phys. Control. Fusion*, 38(8):1213–1223, 1996.

[19] L. L. Lao, H. St. John, R. D. Stambaugh, A.G. Kellman, and W. Pfeiffer. Reconstruction of current profile parameters and plasma shapes in tokamak. *Nucl. Fusion*, 25:1611–1622, 1985. Reconstruct.

[20] S. Wolfe. 2001. Personal communication.

[21] E. S. Marmar, R. L Boivin, C. Fiore, J. Goetz, R. Granetz, M. Greenwald, A. Hubbard, J. Hughes, I. H. Hutchinson, J. Irby, B. Labombard, Y. Lin, B. Lipschultz, A. Mazurenko, D. Mossessian, T. Sunn Pedersen, M. Porkolab, J. Rice, G. Schilling, J. A. Snipes, G. Taylor, J. Terry, S. Wolfe, and S. Wukitch. Enhanced D-Alpha H-modes studies in the Alcator C-Mod tokamak. In *Proceedings of the 18th IAEA fusion energy conference*, number IAEA-CN-77/EX2/5, Sorrento, Italy, October 2000.

[22] Y. Lin, J. Irby, P. Stek, I. Hutchinson, J. Snipes, R. Nazikian, and M. McCarthy. Upgrade of reflectometry profile and fluctuation measurement in Alcator C-Mod. *Rev. Sci. Instrum.*, 70(1):1078–1081, 1999.

[23] A. Mazurenko. *Phase Contrast Imaging on the Alcator C-Mod tokamak.* PhD thesis, MIT, Cambridge, MA, 2001.

[24] M. Greenwald, R. L. Boivin, P. Bonoli, C. Fiore, J. Goetz, R. Granetz, A. E. Hubbard, I. H. Hutchinson, J. Irby, Y. Lin, E. Marmar, A. Mazurenko, D. Mossessian, T. Sunn Pedersen, J. Rice, J. Snipes, G. Schilling, G. Taylor, J. Terry, S. Wolfe, and S. Wukitch. Studies of EDA H-mode in Alcator C-Mod. *Plasma Phys. Control. Fusion*, 42(5A):A263–A269, 2000.

[25] J. A. Snipes, B. LaBombard, M. Greenwald, I. H. Hutchinson, J. Irby, Y. Lin, A. Mazurenko, and M. Porkolab. The quasi-coherent signature of Enhanced D_α H-modes in Alcator C-Mod. *Plasma Phys. Control. Fusion*, 43(4):L23–L30.

[26] A. E. Hubbard. Physics and scaling of the H-mode pedestal. *Plasma Phys. Control. Fusion*, 42(5A):A15–A35, 2000.

[27] J. E. Rice, M. Greenwald, I. H. Hutchinson, E. S. Marmar, Y. Takase, S. M. Wolfe, and F. Bombarda. Observations of central toroidal rotation in ICRF heated Alcator C-Mod plasmas. *Nucl. Fusion*, 38(1):75, 1998.

[28] I. H. Hutchinson, J. E. Rice, R. S. Granetz, and J. A. Snipes. Self-acceleration of a tokamak plasma during ohmic H-mode. *Phys. Rev. Lett.*, 84(15):3334–3337, 2000.

[29] J. E. Rice, R. L. Boivin, P. T. Bonoli, J. A. Goetz, R. S. Granetz, M. J. Greenwald, I. H. Hutchinson, E. S. Marmar, G. Schilling, J. A. Snipes, S. M. Wolfe, S. J. Wukitch, C. L. Fiore, J. H. Irby, D. Mossessian, and M. Porkolab. Observations of impurity toroidal rotation suppression with ITB formation in ICRF and ohmic H mode Alcator C-Mod plasmas. *Nucl. Fusion*, 41(3):277–284, 2001.

[30] F. W. Perkins, R. B. White, P. T. Bonoli, and V. S. Chan. Generation of plasma rotation in a tokamak by ion-cyclotron absorption of fast Alfven wave. *Phys. Plasmas*, 8(5):2181–2187, 2001.

[31] W. L. Rowan, R. D. Bengtson, V. Bravenec, H. He, J. Jagger, D. M. Patterson, D. W., Ross, P. M., Valanju, and A. J. Wootton. Neutral beam diagnostics for Alcator C-Mod. *Rev. Sci. Instrum.*, 68(1):300–303, 1997.

[32] N. A. Krall and A. W. Trivelpiece. *Principles of Plasma Physics.* San Francisco Inc., 1986.

[33] T. H. Stix. *Waves in Plasmas.* American Institute of Physics, 1992.

[34] V. Ginzberg. *Propagation of Electromagnetic Waves in Plasmas.* Gordon and Breach, New York, 1960.

[35] J. J. Sakurai. *Modern Quantum Mechanics.* Addison-Wesley Publishing Company, Inc, Reading, Massachusetts, 1995.

[36] F. Simonet. Measurement of electron density profile by microwave reflectometry on tokamaks. *Rev. Sci. Instrum.*, 56(5):664–669, 1985.

[37] E. Mazzucato. Microwave reflectometry for magnetically confined plasmas. *Rev. Sci. Instrum.*, 69(6):2201–2217, 1998.

[38] L. Zeng, E. J. Doyle, T. C. Luce, and W. A. Peebles. Implementation of reflectometry as a standard density profile diagnostic on DIII-D. *Rev. Sci. Instrum.*, 72(1):320–323, 2001.

[39] C. Laviron, A. J. H. Donné, M. E. Manso, and J. Sanchez. Reflectometry techniques for density profile measurements on fusion plasmas. *Plasma Phys. Control. Fusion*, 38:905–936, 1996.

[40] J. Sánchez, B. Branas, T. Estrada, E. de la Luna, and V. Zhuravlev. Amplitude modulation reflectometry for large fusion devices. *Rev. Sci. Instrum.*, 63(10):4654–4656, 1992.

[41] P. Varela, M. Manso, I. Nunes, J. Santos, F. Nunes, A. Silva, and F. Silva. Automatic evaluation of plasma density profiles from microwave reflectometry on ASDEX upgrade based on the time-frequency distribution of the reflected signals. *Rev. Sci. Instrum.*, 70(1):1060–1063, 1999.

[42] F. D. Nunes, J. Santos, and M. E. Manso. Recursive algorithm for fast evaluation of the abel inversion integral in broadband reflectometry. *Rev. Sci. Instrum.*, 70(1):1047–1050, 1999.

[43] E. Doyle. In S. Stott, editor, *Diagnostics for Experimental Thermonuclear Fusion Reactors.* Plenum, New York, 1996.

[44] D. Pinsonneault, B. Quirion, J. L. Lachambre, and C. Legros. Edge density profile measurements in TdeV using amplitude modulation reflectometry. *Rev. Sci. Instrum.*, 68(1):990–993, 1997.

[45] M. Zerbini, P. Amadeo, and P. Buratti. Experimental results of amplitude modulation reflectometry on the FTU. *Rev. Sci. Instrum.*, 68(1):428–430, 1997.

[46] M. Hirsch, H. J. Hartfuss, T. Geist, and E. de la Luna. Amplitude modulated heterodyne reflectometer for density profile and density fluctuation profile measurements at W7-AS. *Rev. Sci. Instrum.*, 67(5):1807–1813, 1996.

[47] N. Bretz. One-dimensional modelling of the wavelength sensitivity, localization, and correlation in reflectometry measurements of plasma fluctuations. *Phys. Fluids B*, 4:2414–2422, 1992.

[48] C. Fanack, I. Boucher, F. Clairet, S. Heuraux, G. Leclert, and X. L. Zou. Ordinary-mode reflectometry: modification of the scattering and cut-off responses due to the shape of localized density fluctuations. *Plasma Phys. Control. Fusion*, 38:1915–1930, 1996.

[49] R. L. Watterson, R. E. Slusher, and C. M. Surko. Low-frequency density fluctuations in a tokamak plasma. *Phys. Fluids*, 28(9):2857–2867, 1985.

[50] E. Z. Gusakov and M. A. Tyntarev. The two-dimensional theory of reflectometry diagnostics of plasma fluctuations. *Fusion Eng. Des.*, 34–35:501–505, 1997.

[51] Y. Lin, R. Nazikian, J. H. Irby, and E. S. Marmar. Plasma curvature effects in microwave reflectometry fluctuation measurements. *Plasma Phys. Control. Fusion*, 43(1):L1–L8, 2001.

[52] R. Nazikian and E. Mazzucato. Reflectometer measurement of density fluctuations in tokamak plasmas (invited). *Rev. Sci. Instrum.*, 66(1):392–398, 1995.

[53] E. Mazzucato and R. Nazikian. Radial scale length of turbulence fluctuations in the main core of TFTR plasmas. *Phys. Rev. Lett.*, 71(12):1840–1843, 1993.

[54] G. D. Conway. Scattering of reflectometer signals from rippled surfaces. *Rev. Sci. Instrum.*, 64(10):2782–2788, 1993.

[55] G. D. Conway. Beam diameter effects on microwave reflectometer measurements. *Plasma Phys. Control. Fusion*, 39:1261–1265, 1997.

[56] G. D. Conway. Effects of reflectometer asymmetries of fluctuation measurements. *Plasma Phys. Control. Fusion*, 41:65–92, 1999.

[57] G. D. Conway. 2D modelling of radial correlation reflectometry. *Plasma Phys. Control. Fusion*, 39:407–421, 1997.

[58] E. Holzhauer, M. Hirsch, T. Grossmann, B. Branas, and F. Serra. Theoretical and experimental investigation of the phase-runaway in microwave reflectometry. *Plasma Phys. Control. Fusion*, 40:1869–1886, 1998.

[59] G. D. Conway, G. Vayakis, J. A. Fessy, and D. V. Bartlett. A reflectometer for fluctuation and correlation studies on the Joint European Torus tokamak. *Rev. Sci. Instrum.*, 70:3921–3929, 1999.

[60] I. Hutchinson. One-dimensional full-wave analysis of reflectometry sensitivity and correlations. *Plasma Phys. Control. Fusion*, 34:1225–1251, 1992.

[61] E. Z. Gusakov. 2001. Personal communication.

[62] T. L. Rhodes, R. J. Taylor, and W. A. Peebles. Correlation reflectometry: An experimental investigation of measurement capability. *Rev. Sci. Instrum.*, 66(1):824–826, 1998.

[63] M. Gilmore, W. A. Peebles, and X. V. Nguyen. Detailed comparison of plasma turbulence correlation length measurements using microwave reflectometry and a Langmuir probe array. *Plasma Phys. Control. Fusion*, 43(1):L1–L7, 2000.

[64] D. Mossessian, A. E. Hubbard, E. S. Marmar, T. Sunn Pedersen, R. S. Granetz, R. L. Boivin, M. Greenwald, J. Hughes, J. Irby, D. Johnson, B. LaBombard, Y. Lin, A. Mazurenko, R. Nazikian, C. S. Pitcher, G. Taylor, and S. M. Wolfe.

Measurements and scaling of the H-mode pedestal on Alcator C-Mod. *Plasma Phys. Control. Fusion*, 42(5A):A255–A262, 2000.

[65] J. W. Hughes, D. A. Mossessian, A. E. Hubbard, E. S. Marmar, D. Johnson, and D. Simon. High-resolution edge thomson scattering measurements on the Alcator C-Mod tokamak. *Rev. Sci. Instrum.*, 72(1):1107–1110, 2001.

[66] E. S. Marmar, R. L. Boivin, R. S. Granetz, J. W. Hughes, B. Lipschultz, S. McCool, D. Mossessian, C. S. Pitcher, J. E. Rice, and J. L. Terry. High resolution visible continuum imaging diagnostic on the Alcator C-Mod tokamak. *Rev. Sci. Instrum.*, 72(1):940–943, 2001.

[67] K. Shinohara, S. Shiraiwa, K. Hoshino, Y. Miura, K. Hanada, H. Toyama, and JFT-2M group. A new method to analyze density fluctuations by microwave reflectometry. *Jpn. J. Appl. Phys.*, 36:7367, 1997.

[68] A. Ejiri, K. Shinohara, and K. Kawahata. An algorithm to remove fringe jumps and its application to microwave reflectometry. *Plasma Phys. Control. Fusion*, 39:1963–1980, 1997.

[69] T. L. Rhodes, W. A. Peebles, E. J. Doyle, P. Pribyl, M. Gilmore, R. A. Moyer, and R. D. Lehmer. Signal amplitude effects on reflectometer studies of density turbulence in tokamaks. *Plasma Phys. Control. Fusion*, 40:493–510, 1998.

[70] T. L. Rhodes, R. A. Moyer, R. Groebner, E. J. Doyle, R. Lehmer, W. A. Peebles, and C. C. Rettig. Experimental evidence for self-organized criticality in tokamak plasma turbulence. *Phys. Lett. A*, 253:181–186, 1999.

[71] B. Carreras, B. Ph. van Milligen, M. A. Pedrosa, R. Balbin, C. Hidalgo, D. E. Newman, E. Sanchez, M. Frances, I. Garcia-Cortes, J. Bleuel, M. Endler, C. Ricardi, S. Davies, G. F. Matthews, E. Martines, V. Antoni, A. Latten, and T. Klinger. Self-similarity of the plasma edge fluctuations. *Phys. Plasmas*, 5(10):3632–3643, 1999.

[72] M. Greenwald, R. Boivin, P. Bonoli, R. Budny, C. Fiore, J. Goetz, R. Granetz, A. Hubbard, I. Hutchinson, J. Irby, B. LaBombard, Y. Lin, B. Lipschultz, E. Marmar, A. Mazurenko, D. Mossessian, T. Sunn Pedersen, C. S. Pitcher, M. Porkolab, J. Rice, W. Rowan, J. Snipes, G. Schilling, Y. Takase, J. Terry, S. Wolfe, J. Weaver, B. Welch, and S. Wukitch. Characterization of enhanced D_α high-confinement modes in Alcator C-Mod. *Phys. Plasmas*, 6(5):1943–1949, 1999.

[73] A. E. Hubbard, R. L. Boivin, B. A. Carreras, R. S. Granetz, M. Greenwald, J. W. Hughes, I. H. Hutchinson, J. H. Irby, V. Klein, B. LaBombard, Y. Lin, E. S. Marmar, A. Mazurenko, D. Mossessian, E. Nelson-Melby, T. S. Pedersen, M. Porkolab, J. A. Snipes, J. Terry, and S. Wolfe. Pedestal profiles and fluctuations in C-Mod enhanced D-alpha H-modes. *Phys. Plasmas*, 8(5):2033–2040, 2001.

[74] A. Mazurenko, M. Porkolab, X. Q. Xu, and W. M. Nevins. On the physics of quasi-coherent fluctuations in the high density tokamak plasma. 2001. Submitted to *Phys. Rev. Lett.*

[75] P. H. Diamond, P. L. Similon, T. C. Hender, and B. A. Carreras. Kinetic theory of resistive ballooning mode. *Phys. Fluids*, 28(4):1116–1125, 1984.

[76] B. A. Carreras, P. H. Diamond, M. Murakami, J. L. Dunlap, J. D. Bell, H. R. Hicks, J. A. Holmes, E. A. Lazarus, V. K. Pare, P. Similon, C. E. Thomas, and R. M. Wieland. Transport effects induced by resistive ballooning modes and comparison with high-β_p ISX-B tokamak confinement. *Phys. Rev. Lett.*, 50(7):503–506, 1983.

[77] J. W. Connor and R. J. Hastie. Collisionless and resistive ballooning stability. *Phys. Plasmas*, 6(11):4260–4264, 1999.

[78] L. Garcia, B. A. Carreras, and V. E. Lynch. Spatiotemporal structure of resistive pressure-gradient-driven turbulence. *Phys. Plasmas*, 6(1):107–115, 1999.

[79] D. Mossessian. 2001. Personal communication.

[80] R. J. Hastie. 2001. Personal communication.

[81] L. Garcia, B. A. Carreras, and V. E. Lynch. Effect of poloidally asymmetric sheared flow on resistive ballooning turbulence. *Phys. Plasmas*, 6(10):3910–3917, 1999.

[82] B. A. Carreras, L. Garcia, and P. H. Diamond. Theory of resistive pressure-gradient-driven turbulence. *Phys. Fluids*, 30(5):1388–1400, 1987.

[83] A. E. Hubbard, R. L. Boivin, R. S. Granetz, M. Greenwald, I. H. Hutchinson, J. H. Irby, Y. In, J. Kesner, B. LaBombard, Y. Lin, J. E. Rice, T. S. Pedersen, J. A. Snipes, P. C. Stek, Y. Takase, S. M. Wolfe, and S. Wukitch. Measurements of the high confinement mode pedestal region on Alcator C-Mod. *Phys. Plasmas*, 5(5):1744–1751, 1998.

[84] B. Rogers and J. Drake. Diamagnetic stabilization of ideal ballooning modes in the edge pedestal. *Phys. Plasmas*, 6(7):2297–2801, 1999.

[85] W. C. Chew. *Waves and Fields in Inhomogeneous Media.* Van Nostrand Reinhold, New York, 1990.

[86] J. Berenger. A perfectly matched layer for the absorption electromagnetic waves. *J. Comp. Phys.*, 114:185–200, 1994.

[87] R. Holland and J. W. Williams. Total field versus scattered-field finite-difference codes: A comparative assessment. *IEEE Transactions on Nuclear Science*, NS–30(6):4583–4588, 1980.

[88] Y. Lin, J. H. Irby, R. Nazikian, E. S. Marmar, and A. Mazurenko. Two-dimensional full wave simulation on the reflectometry fluctuations measurements in Alcator C-Mod. *Rev. Sci. Instrum.*, 72(1):344–347, 2001.

[89] J. S. Bendat and A. G. Piersol. *Engineering Applications of Correlation and Spectral Analysis.* John Wiley and Sons, New York, 1993.

[90] E. Mazzucato. Numerical study of microwave reflectometry in plasmas with two-dimensional turbulence fluctuations. *Rev. Sci. Instrum.*, 69(4):1691–1698, 1998.

[91] M. Gilmore, W. A. Peebles, and X. V. Nguyen. Dual mode (ordinary-extraordinary) correlation reflectometry for magnetic field and turbulence measurements (invited). *Rev. Sci. Instrum.*, 72(1):293–300, 2001.

[92] C. W. Domier, B. H. Deng, A. J. H. Donn, P. L. Hsu, N. C. Luhmann Jr., E. Mazzucato, H. K. Park, M. J. van de Pol, and J. Wang. Three-dimensional fluctuation imaging diagnostic for TEXTOR (abstract). *Rev. Sci. Instrum.*, 72(1):363, 2001.

[93] B. H. Deng, C. W. Domier, N. C. Luhmann Jr., D. L. Brower, G. Cima, A. J. H. Donne, T. Oyevaar, and M. J. van de Pol. ECE imaging of electron temperature and electron temperature fluctuations (invited). *Rev. Sci. Instrum.*, 72(1):301–306, 2001.

[94] R. J. Goldston et al. Advanced tokamak physics-status and prospects. *Plasma Phys. Control. Fusion*, 36(12B):B213–B227, 1994.

[95] C. C. Petty, T. C. Luce, P. A. Politzer, and M. R. Wade et al. Advanced tokamak physics in DIII-D. *Plasma Phys. Control. Fusion*, 42(12B):75–85, 2000.

[96] P. Thomas. Internal transport barrier in JET optimised plasmas. *Bull. Am. Phys. Soc.*, 44(7):21, 1999.

[97] J. Sanchez-Sanz and T. Estrada. Diagnostic developments for the study of internal transport barriers. *Plasma Phys. Control. Fusion*, 42(12B):341–351, 2000.

[98] C. L. Fiore, J. E. Rice, P. T. Bonoli, R. L. Boivin, J. A. Goetz, A. E. Hubbard, I. H. Hutchinson, R. S. Granetz, M. J. Greenwald, E. S. Marmar, D. Mossessian, M. Porkolab, G. Taylor, J. Snipes, S. M. Wolfe, and S. J. Wukitch. Core internal transport barriers in Alcator C-Mod. *Phys. Plasmas*, 8(5):2023–2028, 2001.

[99] R. Nazikian, R. Maeski, E. Mazzucato, M. McCarthy, H. K. Park, C. K. Phillips, J. H. Rogers, G. Schilling, and G. Taylor. Application of microwave reflectometry to the measurement of fast magnetosonic waves in the Tokamak Fusion Test Reactor. *Rev. Sci. Instrum.*, 68(1):450–453, 1997.

[100] J. H. Lee, E. J. Doyle, N. C. Luhmann Jr., W. A. Peebles, C. C. Petty, R. I. Pinsker, and T. L. Rhodes. Determination of internal radio frequency electric field profiles via millimeter wave reflectometry in the DIII-D tokamak. *Rev. Sci. Instrum.*, 68(1):462–465, 1997.

[101] E. Nelson-Melby. *Observations of Mode-Converted Ion Bernstein Waves in the Alcator C-Mod Tokamak.* PhD thesis, MIT, Cambridge, MA, 2001.